New Concepts
for
Organic Rankine Cycle
Power Systems

Emiliano I.M. Casati

2014

New concepts for organic Rankine cycle power systems

Proefschrift

ter verkrijging van de graad van doctor
aan de Technische Universiteit Delft,
op gezag van de Rector Magnificus prof. ir. K. C. A. M. Luyben,
voorzitter van het College voor Promoties,
in het openbaar te verdedigen op maandag 29 september 2014 om 12.30 uur.

door

Emiliano I.M. CASATI

Energy Engineer–Politecnico di Milano
geboren te Milano, Italië

Dit proefschrift is goedgekeurd door de promotoren:

Prof. dr. P. Colonna

Prof. dr. V. Dossena

Samenstelling promotiecommissie:

Rector Magnificus	voorzitter
Prof. dr. P. Colonna	Technische Universiteit Delft, promotor
Prof. dr. V. Dossena	Politecnico di Milano, Italië, promotor
Prof. dr. F. Scarano	Technische Universiteit Delft
Prof. dr. H. Spliethoff	Technische Universität München, Duitsland
Prof. dr. R. Martinez-Botas	Imperial College London, Verenigd Koninkrijk
Prof. dr. S.J. Song	Seoul National University, Zuid-Korea
Prof. dr. A. Guardone	Politecnico di Milano, Italië

This research is supported by the Dutch Technology Foundation STW, Applied Science Division of NWO, the Technology Program of the Dutch Ministry of Economic Affairs (grant # 11143), and the Italian Ministry of Education, University, and Research.

ISBN 978-94-6259-330-5

Front cover image from: *The Direct Acting Solar Engine*, F. Shuman, 1907 - Review Publishing & Printing Company - Philadelphia.

[1]Author e-mail address: e.i.m.casati@tudelft.nl and emilianocasati@gmail.com

Dedicated to my beloved Alice
we waited long enough
for this book to be
written . . .

Table of Contents

1 Introduction **1**
1.1 Energy Scenario . . . 2
1.2 Thesis Outline . . . 3

I Innovative Concepts **9**

2 ORC Power Systems: from the Concept to Current Applications and an Outlook to the Future **11**
Abstract . . . 12
2.1 Introduction . . . 12
2.2 Evolution . . . 19
2.3 State of the art . . . 28
2.3.1 Technical options . . . 28
2.3.2 Energy conversion applications . . . 32
2.4 Future scenarios . . . 35
2.4.1 Heat Recovery from Automotive Engines . . . 39
2.4.2 Domestic CHP . . . 41
2.4.3 Ocean Thermal Energy Conversion - OTEC . . . 41
2.4.4 Concentrated Solar Power - CSP . . . 42
2.4.5 Other applications . . . 42
2.5 Conclusions . . . 43
Nomenclature . . . 45

3 Centrifugal Turbines for ORC Applications **57**
Abstract . . . 58
3.1 Introduction . . . 58
3.2 Preliminary Design Method . . . 60
3.2.1 Mean-line Design Tool for ORC Turbines . . . 60
3.2.2 Optimization Procedure . . . 61

3.3 Centrifugal Architecture for ORC applications . . . 62
3.4 Analysis of the Centrifugal Architecture . . . 64
3.5 Design of Exemplary 1 MW_e Machines . . . 68
3.5.1 Design Assumptions . . . 68
3.5.2 Design Methodology . . . 69
3.5.3 Results: Transonic Turbine . . . 71
3.5.4 Results: Slightly Supersonic Turbine . . . 73
3.6 Design of Exemplary 10 kW_e Machines . . . 75
3.6.1 Design Assumptions . . . 75
3.6.2 Design Methodology . . . 77
3.6.3 Results: Transonic Turbine . . . 78
3.6.4 Results: Slightly Supersonic Turbine . . . 78
3.7 Conclusions . . . 79
Nomenclature . . . 82

4 Thermal Energy Storage for Solar Powered ORC Engines 89
Abstract . . . 90
4.1 Introduction . . . 90
4.2 Siloxanes: High-Temperature ORC Working Fluids . . . 91
4.3 Concepts of TES Systems for Power Plants . . . 93
4.4 Direct Storage of Working Fluid in Rankine Power Stations . . . 95
4.4.1 Storage Methods . . . 95
4.4.2 Discharge Methods . . . 96
4.4.3 Storage Systems . . . 96
4.5 Case Study . . . 98
4.5.1 Working Principle . . . 98
4.5.2 Flashing Rankine Cycles with Organic Fluids . . . 100
4.5.3 Flashing the Organic Vapor Down to Saturated Conditions 101
4.5.4 Design Analysis Results . . . 101
4.5.5 Dynamic Modelling . . . 102
4.5.6 Control Strategy . . . 102
4.5.7 Dynamic Analysis Results . . . 103
4.6 Conclusions . . . 105
A.1 Comparison Between Flashing and Evaporative Organic Rankine Cycles . . . 106
A.2 Complete Flash Evaporation as a Working Condition for ORC Power Systems . . . 110
A.3 System Components Dynamic Modelling . . . 111
Nomenclature . . . 113

5 Design Methodology for Flexible Energy Conversion Systems Accounting for Dynamic Performance **121**
Abstract . . . 122
5.1 Introduction . . . 122
5.2 Methodology . . . 123
5.2.1 Multi-Objective Design Optimization . . . 123
5.2.2 Assessment of Dynamic Performance . . . 124
5.3 Case of Study . . . 124
5.4 System Modeling . . . 126
5.4.1 Preliminary ORC Power Plant Design . . . 126
5.4.2 Dynamic Modeling . . . 129
5.4.3 Validation . . . 133
5.4.4 The DYNDES Tool . . . 134
5.5 Results and Discussion . . . 139
5.5.1 Multi-objective Design Optimization . . . 139
5.5.2 Assessment of Dynamic Performance . . . 140
5.6 Conclusions . . . 142
Nomenclature . . . 143

6 Design of CSP Plants with Optimally Operated Thermal Storage **149**
Abstract . . . 150
6.1 Introduction . . . 150
6.2 Modeling Framework . . . 153
6.3 Operation Strategy . . . 156
6.3.1 Reference Operation Strategy . . . 156
6.3.2 Optimal Control . . . 156
6.4 Computational Infrastructure . . . 157
6.5 Results & Discussion . . . 157
6.6 Conclusions . . . 162
6.7 Acknowledgements . . . 163
A.1 Solar Fields Design . . . 163
A.2 Financial Analysis . . . 166
A.3 Modelica and Optimica listings . . . 168
Nomenclature . . . 169

II Fundamental Aspects **175**

7 Flexible Asymmetric Shock Tube (FAST): Commissioning of a High Temperature Ludwieg Tube for Wave Propagation Measurements **177**
Abstract . . . 178
7.1 Introduction . . . 178
7.2 Fundamentals . . . 178
7.3 The FAST Set-Up . . . 180
7.3.1 Working Principle . . . 181
7.3.2 Vapour Generator . . . 182
7.3.3 Reference Tube . . . 184
7.3.4 Charge Tube . . . 185
7.3.5 Fast Opening Valve . . . 185
7.3.6 Low Pressure Plenum . . . 185
7.3.7 Condenser and flow return pipe . . . 187
7.4 Data Acquisition and Control system . . . 187
7.4.1 Vapour generator control . . . 187
7.4.2 Reference Tube control . . . 187
7.4.3 Charge Tube control . . . 188
7.4.4 Low Pressure Plenum control . . . 188
7.4.5 Data Acquisition . . . 188
7.5 Validation . . . 188
7.5.1 Tightness characterization . . . 188
7.5.2 Valve Opening Sequence . . . 189
7.5.3 Wave Speed Measurements . . . 193
7.6 Conclusions & Future Work . . . 196
Nomenclature . . . 197

8 Nonclassical Gasdynamics of Vapour Mixtures **203**
Abstract . . . 204
8.1 Introduction . . . 204
8.2 Admissibility Region for Rarefaction Shock Waves in Dense gas Mixtures . . . 206
8.3 Nonclassical Gasdynamics Behaviour of Dense Gas Mixtures . . . 212
8.4 Conclusions . . . 218
A.1 iPRSV-WS Thermodynamic Model . . . 219

9 Conclusions & Perspectives **229**

Summary 235

Samenvatting 239

Acknowledgements 243

About the Author 245

List of publications 247

1

Introduction

1.1 Energy Scenario

Energy provision is one of the major challenges for the Human Society, and it is increasingly clear that the current production/consumption model is not sustainable, due to the wake of consequences induced by the exhaustion of fossil energy resources: global climate change, local pollution, and diffused geopolitical disorders. According to the Energy Technology Perspectives report published by the International Energy Agency in 2012 (ETP-2012)[1], global energy demand has nearly doubled since 1980, driving up energy-related greenhouse gas (GHG) emissions, which amount now to the 68% of the anthropogenic total. If current trends will continue unabated, a further 85% rise is expected by 2050, leading the world down the path towards a 6 ^{o}C rise in average global temperature during the same period, with potentially devastating results regarding climate change, long-term energy security, and, finally, our survival.

The ETP-2012 introduced the so-called 2DS scenario, which identifies technology options and policy pathways ensuring an 80% chance of limiting the global temperature increase to 2 ^{o}C by 2050. According to the study, this figure is compatible with a sustainable future.

Achieving the 2DS will require extensive transformation of the energy system, aiming at cutting energy-related GHG emissions in half by 2050 compared to 2009. The message is clear: different energy systems deliver very different futures. People and governments must choose what future they want, and start building the appropriate energy system now if that future is to be realized.

Furthermore, a collective effort is required in every aspect, since no single fuel, technology or sector can deliver a dominant proportion of the necessary emissions reduction. Accordingly, the 2DS reflects a concerted effort to reduce overall consumption and replace fossil fuels with a mix of renewable and nuclear energy sources. It is discussed how substantial opportunity exists to increase energy savings, efficiency and know-how across sectors and technologies, such as those between heat and electricity, or among transport and industry applications. This sustainable energy system is foreseen to be smarter, more decentralised and integrated.

In the author's opinion, energy conversion systems based on the organic Rankine thermodynamic cycle (ORC) have the potential to play a major role in this envisaged framework. ORC power plants are one of the most proven solutions for the exploitation of external [2] thermal sources in the power-output range from, say,

[1] Energy Technology Perspectives–ETP2012. Technical report, International Energy Agency, 2012.

[2] External with respect to the power system, as opposed to the internal combustion encountered

few kW_E, up to tens of MW_E. Furthermore, the cogeneration of thermal power can usually be accomplished in a fairly straightforward way.

In ORC power converters, a phase-changing organic compound is adopted as the evolving fluid which, following the working principle defining the Rankine cycle, allows to exploit a given source in order to convert part of its energy content into useful outputs, such as, e.g., mechanical, electrical, and thermal energy.

The global diffusion of ORC power systems grew at a fast pace during the last 20 years, primarily thanks to the intense academic research effort which accompanied this idea since its early days. The possibility of tailoring the working fluid and the operating thermodynamic conditions to the application at hand offers important advantages. Higher conversion efficiency, lower cost and improved compactness of the system can be attained by limiting the specific work in the expansion process, and/or by reducing the irreversibility produced during thermal power transfers.

The ORC energy converters are extremely flexible in nature, and able to exploit a virtually infinite variety of thermal sources. At the same time, this poses great challenges from the design point of view. Innovative concepts can be devised drawing from the fundamentals of the working fluid behavior, passing to the component- and up to the system-level of detail, but the corresponding generalized design methodologies have to be concurrently developed and integrated. The work documented in this thesis aims at contributing to these topics, by presenting the original results of numerical and experimental research investigating the potential of molecularly heavy and complex organic compounds as working fluids for the ORC power systems of the future.

1.2 Thesis Outline

This thesis is composed of two main parts, in turn constituted by self-contained chapters, each addressing a specific sub-topic. The collected material forms the basis of several publications on peer-reviewed international journals: five papers are already published, one has been accepted for publication, and two are about to be submitted for publication.

The first part illustrates several advancements in the field of energy conversion systems, with a focus on ORC turbo-generators. A more detailed description of

in, e.g., gas turbines.

the chapters follows.

Chapter 2 presents an introductory review on ORC systems, with an overview of their history, the description of the state-of-the-art from both the academic and the industrial perspective, and an outlook to envisaged paths of development.

The cumulative global capacity of ORC power systems is undergoing a rapid growth, which started a decade ago, in accordance with recent developments in the energy conversion scenario. The potential for the conversion into electricity of the thermal power coming from liquid-dominated geothermal reservoirs, waste heat from primary engines or industrial processes, biomass combustion, and concentrated solar radiation is arguably very large. ORC power systems are one of the most flexible conversion technologies, in terms of capacity and temperature levels, for these energy sources, and are currently often the only applicable conversion technology in many applications. In addition, they can co-generate heating and/or cooling. Related research and development is therefore extremely lively.

Firstly, basic elements on the thermodynamic cycle, working fluid, and design aspects are introduced, together with an evaluation of advantages and disadvantages in comparison to competing power systems. An overview of the long history of the development of ORC technology follows, in order to place the more recent evolution into perspective. A compendium of the many aspects of the state of the art is then illustrated by reviewing the engineering solutions currently adopted in commercial power plants, the main-stream applications, together with information about exemplary installations. An outlook on the many research and development activities is provided, whereby information on new high-impact applications such as automotive heat recovery is included. Possible directions of future developments are highlighted, ranging from efforts targeting volume-produced stationary and mobile mini-ORC systems with a power output of few kW_E, up to large base-load ORC power plants.

Chapter 3 documents the original research conducted in the field of ORC turbo-expanders. As a matter of fact, these are the most critical components when efficient ORC power systems have to be designed. The variety of possible working fluids, the complex gas dynamics phenomena encountered, and the lack of simplified design methods based on experience on similar machines, make the design of efficient ORC turbines a complicated task.

Relevant paths of development may thus be concerned with (i) the development of generalized design methodologies, and (ii) the assessment of non-conventional machine architectures: the research presented in this chapter aims

at exploring both. The first critical evaluation of the centrifugal or radial-outflow turbine (ROT) architecture as a candidate technology for ORC turbo-generators is presented, together with a novel methodological framework for the design of these machines. The developed tools can be of help for the designer of ROT machines, for virtually any power-output.

The first part of the chapter deals with the design of comparably large size turbines, i.e. in the MW_E power output range, which is the power output typical of present industrial applications. The second part of the chapter is devoted to the assessment of the down-scaling potential of the ROT architecture, considering its implementation in the promising field of mini-ORC turbo-generators, i.e., systems with power output of the order of 10 kW_E. The results show that the radial-outflow turbine is a promising concept for future ORC power systems, since it allows for the realization of efficient, compact, and reliable turbo-expanders in the investigated power-output range.

Chapter 4 deals with the assessment of a novel thermal storage system tailored to high-temperature ORC systems for concentrating solar power (CSP) applications, stemming from the observation that the direct storage of the ORC working fluids can be effective thanks to their favourable thermodynamic properties. The feasibility of energy storage is of paramount importance for solar power systems, to the point that it can be the technology enabler. The interest for highly efficient and modular concentrated solar power plants of small to medium capacity (5 kW_E−5 MW_E) is growing: ORC power systems stand out in terms of efficiency, reliability and cost-effectiveness in such power-range.

The concept of complete flashing cycle (CFC) is introduced as a mean of achieving an unmatched system layout simplification, while preserving conversion efficiency. This is a new variant of the Rankine cycle, originally introduced by the presented research, whereby the vapour is produced by throttling the organic working fluid from liquid to saturated vapour conditions.

The discussion of a case study follows: a 100 kW_E CFC turbo-generator with direct thermal energy storage, coupled with state-of-the-art parabolic trough collectors. A dynamic model, developed for the complete system, is used to investigate the performance under extreme transient conditions. By adopting a relatively simple and robust control strategy, the storage system is demonstrated to be effective in decoupling the solar field and the ORC power block, which can thus be operated close to nominal conditions notwithstanding the environmental disturbances. The feasibility of remotely controlled operation is thus positively assessed by means of this preliminary study.

Chapter 5 presents a methodology conceived to help in the definition of the optimal design of power generation systems. The innovative element is the integration of requirements on dynamic performance into the procedure. Operational flexibility is an increasingly important specification of power systems for base- and part-load operation. Thus, it is crucial to discard, in an early phase of the design process, plant configurations which feature unacceptable dynamic performance.

The test case is the preliminary design of an off-grid power plant serving an off-shore platform, where one of the three installed gas turbines is combined with an organic Rankine cycle turbo-generator in order to increase the overall energy efficiency. At the top level of the procedure is a stationary model, capable of performing the on-design thermodynamic cycle calculation, and the design of the main components of the system. The results of these simulations are used within the framework of a multi-objective optimization procedure to identify a number of equally optimal system configurations.

A dynamic model of each of these system designs is automatically parameterized, by inheriting its parameters values from the optimization results. Dynamic simulations of selected reference transients allow then to discriminate among the initial set of solutions, thus providing the designs that also comply with dynamic requirements.

Chapter 6 introduces a new methodology aimed at assessing the potential of optimal control techniques in the context of thermal energy storage management for concentrated solar power (CSP) plants. These systems present the possibility of integrating a thermal energy storage able of sustaining several hours of full-load operation in the absence of solar radiation. However, usually adopted design software tools assume a short-sighted strategy for storage management. The novel design method is applied to a test case, a state-of-the-art central receiver plant with direct storage, using molten salts as working fluid, and operating in a context of variable electricity prices.

The system modelling and optimization problems are formulated and implemented using modern high-level modelling languages, thus demonstrating the potential of the approach. Different operating strategies are compared based on a detailed financial analysis. A wide system design space is considered, and the results are presented for all the foreseeable combinations of solar field size and storage system capacity. The proposed method is an additional decision tool allowing to treat the storage operation strategy as a new relevant variable in the design of next generation energy systems. Notably, this could be of particular interest for

ORC-based CSP systems operating in the envisaged distributed generation scenario, possibly cogenerating thermal power for heating or cooling purposes.

The second part of this thesis presents the contribution regarding the experimental and numerical investigation the non-classical gas dynamics behavior of dense vapors of single- and multi-component organic fluids. A more detailed description of the chapters appearing in this part of the work follows.

Chapter 7 describes the commissioning of the Flexible Asymmetric Shock Tube (FAST) experimental setup designed and built at the Delft University of Technology. The aim of this Ludwieg Tube facility is to measure the speed of propagation of pressure waves in organic vapors, with the final objective of providing the first experimental evidence of the most exotic non-classical gas dynamics phenomenon, i.e., the rarefaction shock wave (RSW) in the dense vapor region of fluids formed by complex organic molecules.

The facility operates at temperatures and pressures of the order of 400° C and 10 bar, respectively. A fast opening valve induces a rarefaction propagation in the tube, which is sensed by using dynamic pressure transducers. The equipment and measurement methodology are described in detail. The fast opening valve is characterized in terms of its opening time, which is proven to be small enough to allow for the detection of the RSW. The results regarding a shock wave forming in air are presented, and used to demonstrate and validate the setup capabilities. Preliminary expansion measurements in D_6 siloxane are also presented, being of special interest to the end of the envisaged non-classical gas dynamics experiments.

Chapter 8 presents the first investigation about the non-classical gas dynamics of binary mixtures of organic fluids in the vapour phase. Differently from mixtures of ideal gases, thermodynamic properties of dense vapours of multicomponent mixtures do not scale linearly with the mole fractions of each compound, as molecular interaction among different molecules plays a major role. The fundamental derivative of gas dynamics Γ, being a derived thermodynamic property, is also affected by non-ideal mixing effects. In addition, experiments on the thermal stability of siloxane mixtures, and a deeper understanding on the chemistry of thermal decomposition of these compounds, show that, at temperatures close to the so-called temperature stability limit, a pure siloxane undergoes a rearrangement transformation, whereby small quantities of other compounds of the same family are formed.

The composition of the mixture is therefore a new relevant variable in the study of BZT fluids, and, importantly, such mixtures are also considered as working fluids for ORC power systems, one of the possible applications of non-classical gas dynamics.

A predictive thermodynamic model is used to compute the relevant mixture properties, including its critical point coordinates and the local value of Γ. The considered model is the improved Peng-Robinson Stryjek-Vera cubic equation of state, complemented by the Wong-Sandler mixing rules. A finite thermodynamic region is found where the non-linearity parameter Γ is negative, and therefore non-classical gas dynamics phenomena are admissible. A non-monotone dependence of Γ on the mixture composition is observed in the case of binary mixtures of siloxane and perfluorocarbon fluids, with the minimum value of Γ in the mixture being always larger than that of its more complex component.

The observed dependence indicates that non-ideal mixing has a strong influence on the gas dynamics behaviour—either classical or non-classical—of the mixture. Numerical experiments of the supersonic expansion of a mixture flow around a sharp corner show the transition from the classical configuration, exhibiting an isentropic rarefaction fan centred at the expansion corner, to non-classical ones, including mixed expansion waves and rarefaction shock waves, if the mixture composition is changed.

Part I

Innovative Concepts

2

ORC Power Systems: from the Concept to Current Applications and an Outlook to the Future

Part of the contents of this chapter will appear in:

"ORC Power Systems: from the Concept to Current Applications and an Outlook to the Future"
P. Colonna, E. Casati, T. Mathijssen, C. Trapp, J. Larjola, T. Turunen-Saaresti, & A. Uusitalo
J Eng Gas Turb Power, Submitted for Publication (2014)

Abstract *The cumulative global capacity of Organic Rankine Cycle (ORC) power systems for the conversion of renewable and waste thermal energy is undergoing a rapid growth, which started a decade ago, in accordance with recent developments in the energy conversion scenario. It is estimated that the power capacity of all these types of power plants currently adds up to at least* $2,000$ MW_E*. The potential for the conversion into electrical or mechanical power of the thermal power coming from liquid-dominated geothermal reservoirs, waste heat from primary engines or industrial processes, biomass combustion, and concentrated solar radiation is arguably very large. ORC power systems are one of the most flexible conversion technologies in terms of capacity and temperature level of these energy sources, and are currently often the only applicable conversion technology for external thermal energy. In addition, they are suitable for the cogeneration of heating and/or cooling, another advantage in the framework of distributed power generation. Related research and development is therefore extremely lively. These considerations motivated the effort documented in this chapter, aimed at providing consistent information about the evolution, state, and likely future of this power conversion system. Firstly, basic theoretical elements on the thermodynamic cycle, working fluid, and design aspects are introduced, together with an evaluation of advantages and disadvantages in comparison to competing technologies. An overview of the long history of the development of ORC power systems follows, in order to place the more recent evolution into perspective. A compendium of the many aspects of the state of the art is then illustrated by reviewing the engineering solutions currently adopted in commercial power plants, the main−stream applications, together with information about exemplary installations. An outlook on the many research and development activities is provided, whereby information on new high-impact applications such as automotive heat recovery is included. Possible directions of future developments are highlighted, ranging from efforts targeting volume-produced stationary and mobile mini−ORC systems with a power output of few* kW_E*, up to large base−load ORC power plants such as, e.g., for ocean thermal energy conversion − OTEC.*

2.1 Introduction

The concept of an engine based on the Rankine thermodynamic cycle, whereby the fluid is an organic compound instead of water (see fig. 2.1a–2.1b) originates from two main observations [1–3]:

- if the selection of the working fluid is an additional degree of freedom for the design of the thermodynamic cycle, the fluid can be chosen such that it

is optimal from both a thermodynamic and a technical point of view. The properties of the fluid, e.g., the properties at the vapor-liquid critical point, the saturation line, and the specific heat directly affect how well the temperature profile of the thermal energy source and sink can be matched by the corresponding cycle heating and cooling processes, see, e.g., figs. 2.1c–2.1d. The conversion efficiency of the power system, aside from the efficiency of the expander, strongly depends on the exergy loss in both the primary heat exchanger and the condenser. Furthermore, cycle configurations that are not possible if water is the working fluid, can be contemplated: the supercritical cycle configuration is possible even if the thermal energy source is at low temperature. As for the advantages with respect to technical aspects, it is notable that: (i) the fluid pressure and density levels within the system can be selected, to a certain extent, independently from the cycle temperatures (for example, relatively low fluid temperature in the evaporator can correspond to high pressure, and vice versa), (ii) effective thermal energy regeneration can be realized by means of one single non-extractive de-superheating process, (iii) for the majority of the organic Rankine cycle (ORC) working fluids, the expansion process is completely dry, thus blade erosion issues in turbines, and inherent expansion inefficiency due to condensation are avoided, (iv) several ORC working fluid are also suitable as a lubricant for rotating machinery, thus further simplifyng the system.

- For low power output, from few kW_E up to few MW_E, the realization of an efficient, reliable, and cost-effective steam expander is challenging: the volumetric flow is extremely small, the expansion ratio comparatively large, and the specific work over the expansion is also very large, thus the design of a simple axial or radial turbine is problematic and the efficiency bound to be low. Steam volumetric expanders in turn must be complex, as challenging lubrication issues must be dealt with, and the net expansion efficiency is heavily affected by blow-by and friction losses. Water cannot effectively lubricate, therefore it must be mixed with a lubricant, which decreases thermodynamic efficiency, and can thermally decompose if it flows through the evaporator. In addition, for several applications, the freezing temperature of water is too high, and the very low pressure in the condenser can lead to unfeasibly large dimensions of this component. If the working fluid is organic, the much smaller enthalpy decrease of the expanding vapor allows to design an expander, be it a turbine [2, 4, 5] or a positive displacement machine (e.g., screw, scroll, vane, or piston expander) [6], featuring a lower rotational speed and higher volumetric flow for a given power output.

Summarizing, the selection of the working fluid affects at the same time the thermodynamic performance of the system, and the design of all its components. For a detailed treatment, the reader is referred to Ref. [7]. For example, if the thermal energy source features a relatively small potential and a rather high-temperature (say 2 MW_T, and $T_{source} > 300$ ^oC), the selection of a fluid formed by complex molecules (large specific heat) yields to a slightly superheated and regenerated cycle as the corresponding optimal cycle configuration. The relatively large volume flow due to the small enthalpy drop over the expansion allows for the design of an efficient and simple turbine, with sufficiently large flow passages. In particular, the small specific expansion work allows also to limit the number of stages (e.g., 2 or 3), and the resulting rotational speed may be 10 – 20 times smaller compared to a steam turbine for the same operating conditions. The dominant need of reducing the number of stages, this increasing their pressure ratios, together with the low values of the sound speed of the expanding organic vapor, leads in most cases to the acceptance of highly supersonic flows, at least in the first stator, which therefore requires special care in the fluid dynamic design. Depending on the condensing temperature, the volume flow at the outlet of the turbine can be large, thus requiring a comparatively bulky regenerator and condenser. As a consequence, cost issues related to the heat transfer equipment might arise. Additional challenges ensue in case vacuum conditions have to be managed. Conversely, the overall low maximum pressures in the system can be beneficial as far as the cost of the evaporator and safety issues are concerned. It is also notable that regeneration positively affects the thermal efficiency of the cycle, but negatively affects the temperature at which the heat source can be cooled (limited by the temperature of state 3 in figure 2.1a), thereby the amount of thermal power that can be converted into mechanical power. Similar reasoning can be applied to other applications, e.g., low- and medium-temperature geothermal energy conversion, leading to different results.

The working fluid is also subjected to a number of other constraints, which can be more or less stringent depending on the application, namely the fluid should be

- non-toxic, non-flammable, non-corrosive, and cost-effective,
- characterized by a low or zero Global Warming Potential (GWP) and Ozone Depletion Potential (ODP),
- thermally stable and compatible with all the containing and sealing materials up to the cycle maximum temperature,
- possibly a good lubricant, featuring also good heat transfer properties,

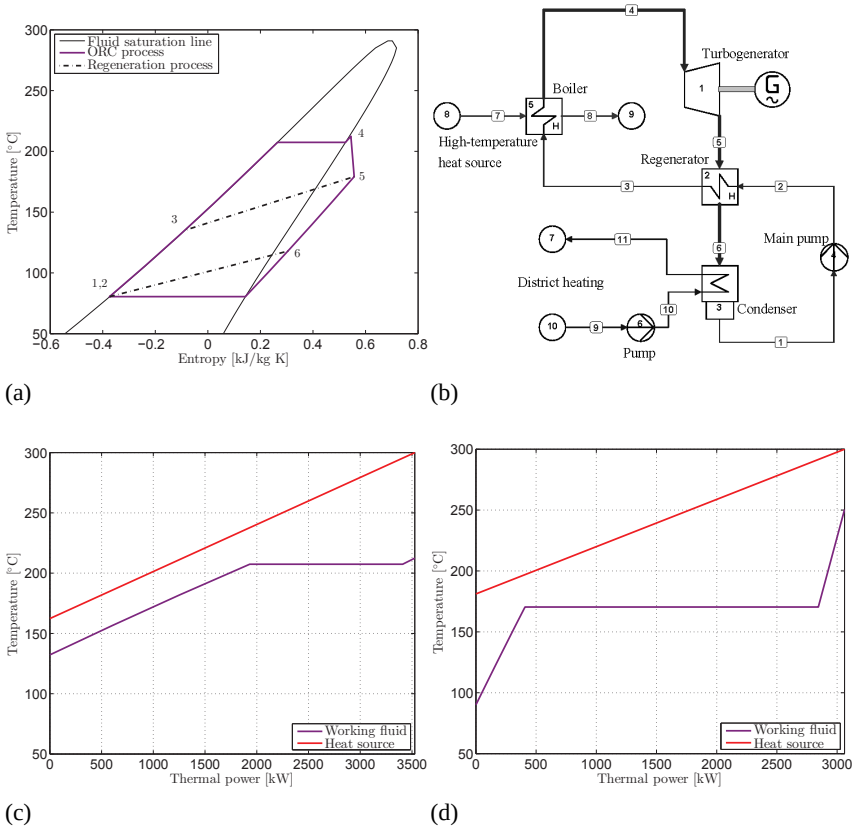

Figure 2.1: The processes forming an exemplary superheated/regenerated Organic Rankine cycle power plant in the $T - s$ thermodynamic plane of the working fluid 2.1a, together with the corresponding process flow diagram 2.1b. 2.1c: $Q - T$ diagram of the ORC evaporator, assuming that the energy source is flue gas at 300 °C, compared to the $Q - T$ diagram of the boiler of a simple steam power plant 2.1d having as energy input flue gas at the same conditions.

- if used for generator cooling, an electrical insulator and compatible with the adopted resin.

With reference to high-temperature applications, one remarkable deficit of currently adopted working fluids (hydrocarbons, siloxanes, perfluorocarbons) is their thermal stability in contact with typical containing materials, which sets the peak cycle temperature threshold at around 350 °C, depending on the specific fluid, and on additional technical, operational and cost-related constraints. These are the frequency of fluid charge substitution, the level of fluid purity, the level of plant sealing, and the dearation requirements in the low-pressure part of the plant. Ideally, an organic fluid which would not thermally decompose (in contact with stainless steel) at temperatures up to 500 – 600 °C would substantially increase the conversion efficiency in some applications. So far the highest thermal stability in realistic operating conditions was reported for a mixture of pentafluorobenzene and hexafluorobenzene [8]. The fluid underwent dynamic thermal tests at temperatures up to 468 °C, and no decomposition was observed during the 532 hour test. The fluid is claimed to feature low toxicity in case of acute and subacute exposures, but products of thermal decompositions of perfluorocarbons are chemically aggressive and possibly highly toxic [9].

These exemplary considerations show that the design of an optimal system is a complex problem, possibly leading to multiple technical solutions, with different equipment selection, each with its advantages and disadvantages. With reference to the example previously illustrated, the selection of a working fluid made of simpler molecules would result in a faster-rotating and smaller turbine, possibly affected by lower efficiency, and requiring reduction or power electronics for the coupling to the electrical generator. In turn, the adoption of such a fluid could eliminate the need for a regenerator, and entail a more compact and super-atmospheric condenser.

One of the main and unique advantages of ORC power systems is that the technology is applicable to virtually any *external* thermal energy source,[1] with temperature differences between thermal source and sink ranging from approximately 30 to 500 °C [10]. ORC systems are therefore technically suitable for the conversion of renewable or renewable-equivalent energy sources such as

- geothermal reservoirs (liquid-dominated or steam-dominated, whereby the steam is too contaminated to be directly expanded in a turbine),
- solar radiation,

[1] External with respect to the power system, as opposed to the internal combustion of reciprocating engines or gas turbines.

- biomass combustion,
- industrial waste heat recovery,
- urban solid waste, and landfill gas combustion,
- heat recovery from other prime movers (reciprocating engines, gas turbines, fuel cells, etc.),
- ocean thermal gradient.

Other advantages of ORC systems are:

- the overall simplicity of the plant configuration,
- the reliability and durability of slow-rotating expansion devices,
- the possibility of using common stainless steel (or in some cases aluminum) as construction material, thanks to the low peak system pressure and temperature, and to the non-corrosive nature of the working fluids. This feature can be compared, for instance, with materials required for high-temperature water, gas turbines, or Stirling engines.

The graph of figure 2.2 synthetically shows the current relation between the temperature of the energy source and the power capacity of ORC power systems vs steam power plants. The graph refers either to systems that are commercially available, or to those currently under development or studied. Notably, the state of the art is quickly evolving, therefore figure 2.2 has been adapted here in order to account for the fact that the boundary of ORC technology applications is expanding toward the region of conventional steam power plant applications. This chart might need to be updated in few years.

If large-capacity high-temperature energy conversion systems are excluded from the comparison (primarily therefore steam power plants), competing technologies for the conversion of the mentioned energy sources are in principle the Stirling engine, the Closed Brayton Cycle (CBC) power plant, and the externally-fired gas turbine (EFGT). For low-temperature energy sources, e.g., geothermal reservoirs or heat recovery, the Kalina cycle power plant [12] is also a potential competitor, though power plants based on this concept are at a lower development stage vs. ORC power systems, and face difficulties due to inherently higher complexity [13].

Conventional Stirling engines can operate at a sufficient level of efficiency only if the thermal energy source is at high temperature (indicatively 700−1100 ^{o}C),

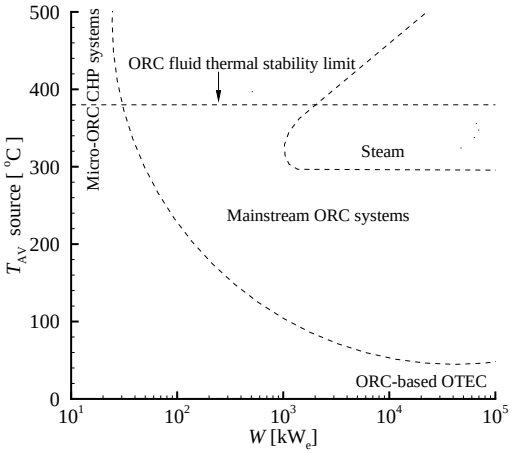

Figure 2.2: Current and future fields of application of ORC vs Steam power systems in terms of average temperature of the energy source, $T_{av.,source}$, and plant power capacity. Boundaries are indicative, and evolving in time. Adapted from Ref. [11].

therefore they are developed mainly for high-temperature solar conversion [14, 15], biomass and biogas combustion [16], and domestic micro-cogeneration [17] for a power range from 1 kW_E up to several tens of kW_E. The necessarily complex kinematic mechanisms, and the challenging high-temperature sealing requirements for the typically leak-prone working fluids (Helium, Hydrogen, Nitrogen, Air) have so far hampered the reliability of the systems being developed. Organic working fluids have been proposed for high-pressure/moderate-temperature Stirling engines [18], but no actual development is known to the authors. High power density, high net conversion efficiency (the world record is 31.25 % [19]) and possibly low cost, if large-series production is envisaged, are positive features of Stirling engine technology.

Developments of medium-capacity CBC power plants are related to systems employing carbon dioxide[2] as working fluid [20], and they have been initially proposed for next-generation nuclear power plants [21]. As previously illustrated, CO_2, being a simple molecule, is arguably unsuitable for the design of low power output expanders. The development of medium-capacity (10 – 50 MW_E) supercritical CO_2 CBC power plants is now actively pursued in combination with high-

[2]Note that Carbon Dioxide is an organic compound, as it contains carbon, therefore systems based on supercritical CO_2 thermodynamic cycles entailing working fluid condensation, as it is the case in some proposed configurations, qualify as supercritical Organic Rankine Cycle systems.

temperature solar tower technology [22], and very high conversion efficiency at moderate peak cycle temperature is possibly attainable (approximately 50 % at 750 °C).

The EFGT concept is proposed for biomass combustion or gasification [23], and for high-temperature solar conversion [24], the main challenge being the high-temperature at which the primary heat exchanger must operate. Prototypes so far achieved limited efficiency, and issues of reliability still need to be solved.

Fossil-fuel fired ORC systems compete with fuel cells, micro-gas turbines, Stirling and reciprocating engines for innovative applications, like micro-cogeneration of heat and power (CHP) for apartments and houses [25]. Domestic cogeneration, that is the use of small CHP systems in place of conventional gas or diesel boilers, can be beneficial in terms of fuel utilization in countries with cold or moderate climate.

Research and development of ORC technology has been receiving an ever increasing impulse starting from the beginning of this century, together with a rapid increase of the installed power capacity, and the number and diversity of applications. This work stems from the need for a reasoned synthesis about the evolution of this technology (sec. 2.2), its state-of-the-art (sec. 2.3), and an outlook toward the future (sec. 2.4), thus providing information on both commercial applications and active research topics.

2.2 Evolution

The idea of using a fluid different from water in a Rankine cycle for power conversion is rather old. As early as 1826, Thomas Howard patented the concept of an engine using ether as the working fluid [26]. Among the low-boiling pressure fluids, several inorganic substances were considered and tested throughout the years, with limited success. This short review is limited to Rankine engines employing organic fluids. Probably the first organic working fluid used commercially in Rankine cycle engines is naphtha. A patent of Franck W. Ofeldt [27] is at the basis of several ORC engines adopting a reciprocating expander fed by a naphtha vaporizer and powering launches, see Fig. 2.3a. Naphtha was used as fuel, working fluid and lubricant, allowing to avoid the cost of the specialized operator needed for steam engines, because of the much lower evaporation pressure in the boiler. The Gas Engine & Power Company of New York claimed in 1890 to have sold five hundred ORC engines based on the Ofeldt design [28].

Simultaneously in Europe (1888), a British inventor by the name of Alfred Yarow also developed a naphtha-based ORC engine for launches [31]. One of

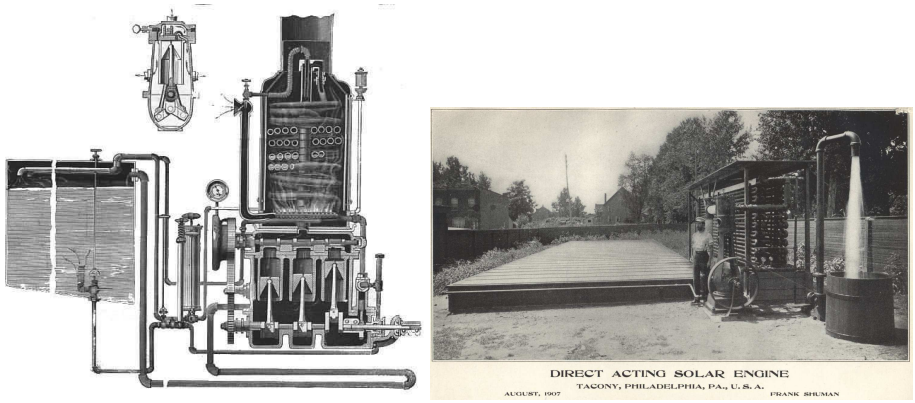

(a) (b)

Figure 2.3: Earliest ORC engines. 2.3a: engine of the Ofeldt naphta launch, 1897. Fuel is pumped from the tank in the bows by air pressure, generated by a hand pump, and passes through a coil boiler. Part of the vapour issuing from the boiler is fed to the burner that heats the boiler itself, and the rest drives a three-cylinder engine. The long U-tube at the bottom is the condenser [29]. 2.3b: Shuman's solar ORC-based pumping system prototype installed in Philadelphia (US-PA), 1907. The the flat solar collector is also visible. It was called *the hot box*, with double glazing containing the blackened pipes acting as the vapor generator [30].

these engines, built by the Swiss company Esher Wyss AG (later to become Sulzer), reached a certain notoriety as it propelled the *Mignon*, the boat that Alfred Nobel launched in 1891 [32]. Even if the boiler was operated at a pressure lower than that of steam engines, the early days of ORC engines were affected by several accidents [33].

Frank Shuman, in 1907, was probably the first who had the idea of a solar ORC engine: he used a flat solar collector of about 110 m^2 to boil ether at temperatures around 120 ^oC and drive a 2.6 kW_M engine, see also Fig. 2.3b [34]. Romagnoli in 1923 used water at 55 ^oC to boil ethyl chloride and run a 1.5 kW_M engine [7, 35].

Professor Luigi D'Amelio (1893-1967), chair of thermal and hydraulic machinery at the University of Naples, is possibly the father of modern ORC technology. In 1936, his work on a solar power plant for irrigation based on an ORC engine using monochloroethane as working fluid [36] won him a prize of 10,000 Lire.[3] A series of 3 cm-deep vessels full of water would receive solar radiation,

[3]The prize was awarded by the Libyan governatorate of Italy and the National Association of Combustion Control. Such solar ORC plant would have been used to pump water in the arid areas of North Africa.

Table 2.1: Specifications of the first solar ORC power plant proposed by Prof. L. D'Amelio in 1935, as reported in Ref. [36].

Working fluid	C_2H_5Cl
Surface of solar collectors	270 m^2
Evaporation temperature	40 ^oC
Evaporation pressure	2.7 bar
Condensation temperature	23 ^oC
Condensation pressure	1.3 bar
Turbine isentropic efficiency	0.65
Net power output	4 kW_M
Net conversion efficiency	0.035

thus heating the water up to about 60 ^oC. The water is circulated to a shell and tube evaporator where the working fluid is heated and evaporated in small pipes at approximately 40 ^oC. The vapor is expanded in an impulse axial turbine stage, and generates mechanical work. The monochloroethane vapor is condensed at 23 ^oC, and the liquid pumped back to the evaporator. The design specifications of the plant are reported in table 2.1. The estimated thermal conversion efficiency was about 3.5 %. The cited monograph outlines for the first time all the main principles of ORC system and turbine design, notably including the selection of the working fluid among several candidates, see also Refs. [37, 38]. In 1939, these ideas were implemented in a 2.6 kW_M prototype for the conversion of low-grade geothermal energy which was commissioned and operated successfully in a laboratory of the University of Naples [39]. The experience gained with the prototype led to the realization of an 11 kW_M geothermal ORC pilot power plant on the island of Ischia in 1940. A second power plant of 250 kW_M based on the same technology was built in 1943 but was never operated [40]. After the second world war, D'Amelio resumed his studies on the ORC concept, and his work presented at the first conferences on solar energy received considerable attention [41, 42].

The first commercially operated geothermal ORC power plant, a so-called binary power plant, was briefly operated at Kiabukwa, in the Democratic Republic of Congo, in 1952 [43]. It featured a power capacity of 200 kW_E, utilized geothermal water at 91 ^oC as heat source, and it supplied power to a mining company. The second oldest geothermal ORC power plant was commissioned at Paratunka in the Kamchatka peninsula in 1967 [43, 44]. It was a pilot plant exploiting geother-

mal water at 85 °C, rated at 670 kW_E, and using refrigerant R12 as the working fluid [45]. It provided a small village with electricity and greenhouses with heating.

Dr. Lucien Bronicki met Prof. D'Amelio during his PhD studies in the late 50's in Paris[4] and started to study the application of the ORC principle to small solar power plants [46]. He and made an important contribution by outlining for the first time the relation between the working fluid and the design of the expander in an article published on an international journal [1]. In the 60's, perfluorocarbons were studied by other authors as working fluids for mini-ORC turbines [47]. Several experimental solar ORC systems have also been reported. These adopted static non-focusing collectors, thus achieving comparatively low maximum cycle temperature (around 100 °C), and solar-to-electric efficiency (typically < 5 %). Furthermore, also during the 60's, few ORC-driven systems for the pumping of water for irrigation or desalination purposes have been documented [34].

In these years, Dr. Bronicki and his group designed, built, and tested several small solar ORC units (2−10 kW_E) with monochlorobenzene as the working fluid. These systems featured inlet fluid temperatures of the order of 150 °C. Some of these plants have been reported as having run for 12 years without repairs [48]. In 1972, they realized a highly unconventional 0.4 kW_E unit powered by a radioisotope, featuring a much higher TIT, and thus a cascaded cycle configuration was adopted, employing different working fluid in the top and bottoming cycle systems [49]. The group then succeeded in deploying the results of these studies in the first commercial application of mini-ORC turbogenerators, i.e., the powering of remote telecommunication stations and of the auxiliaries of gas pumping stations [50]. The most important requirement was reliability in order to allow for a very long operation without maintenance service, while conversion efficiency was not so relevant (about 5 %). The first units of this type (3 kW_E), using monochlorobenzene as the working fluid, were operational in 1961. In the period between 1961 and 1988, thousands of these small ORC turbogenerators were installed. The power capacity ranges from 0.2 to 6 kW_E, the working fluid is commonly dichlorobenzene, or more rarely trichlorobenzene, due to the need of high thermal stability, being the working fluid directly heated by combustion flue gases. These systems pioneered the high-speed hermetic turbogenerator solution: the radial-inflow turbine and the generator are directly coupled and enclosed in a single sealed canister. Journal bearings support the shaft, using the working fluid as a lubricant and coolant, without additives. The generator is a solid-rotor brushless alternator: The three-phase output of the alternator is connected to the

[4] June 2013, personal communication.

rectifier feeding the load. The electrical output terminals reach the outside of the assembly thanks to ceramic feed-throughs. The high boiling point of the working fluid enables returning the condensate by gravity without the need for a feed pump. The stainless steel evaporator is of the once-through type, and the condenser is naturally air-cooled in order to avoid moving parts. The recuperator is tube-in-shell [46, 51]. In more recent years, photovoltaic panels substituted mini-ORC turbogenerators for these applications.

In 1975, Prigmore and Barber presented the first results of a research activity aimed at coupling an array of solar flat-plate collectors, a 1 kW_E ORC turbogenerator using R113 as the working fluid, and a compression chiller for air conditioning. The evaporation and condensation temperatures were equal to 93 and 35 ^oC, respectively, the efficiency of the ORC module was 7 %, and the system overall COP approximately 0.5 [52]. The possibility of reaching maximum cycle temperatures higher than 300 ^oC by adopting focusing collectors (mainly linear), has been investigated in the late 70's: a prototype was tested at Sandia National Laboratories in New Mexico, in combination with parabolic trough collectors to heat a thermal oil loop powering an ORC turbogenerator of 32 kW_E, and also supplying space heating and cooling with an absorption air conditioner [53] . Also in the US, from 1976 to 1984, the Jet Propulsion Laboratory developed a power system using parabolic dishes coupled with an ORC power module. The cavity receiver was designed to heat toluene at approximately 400 ^oC and 42 bar. The rotating parts (single-stage impulse turbine, centrifugal pump, and alternator) were mounted on a single shaft rotating at 60,000 rpm. The same working fluid was also used for bearing lubrication. A solar-to-electric conversion efficiency of 18 % was measured, with a power output of 16 kW_E, thus lower than the design value, due to test conditions [54].

ORC power systems have been adopted also in combination with solar ponds, whereby a temperature gradient is established in a water basin by an artificially induced salinity-gradient. An experimental 5 MW_E Solar Pond Power Plant (SPPP) was operated from 1983 to 1990 in Beit Ha'aravah, Israel [55]. A 200 kW_E SPPP operated from 1986 to 2002 at temperatures as low as 65 ^oC in El Paso, Texas, USA [56].

The first experimental geothermal cascading ORC power plant was called Magmamax, and it was located in East Mesa, Imperial valley, California [43]. Its initial design was very ambitious, as it was based on two interconnected ORC power plants. The topping cycle utilized isobutane as the working fluid, while the bottoming cycle adopted propane. The plant was commissioned in 1979, and was rated at 12.5 MW_E gross power (and 11 MW_E net). Though it went through

a number of operational problems and changes, it paved the way for the following generations of geothermal power plants. After two other small experimental geothermal ORC power plants [56], in 1984 the company founded by Dr. Bronicki commissioned its first commercial ORC power plant for the conversion of geothermal energy in Wabuska, Nevada, featuring a capacity of 700 kW_E [56].

As a consequence of the oil crisis of the late 70's, many other units for geothermal power plants manufactured by several companies followed, while also the capacity of these plants gradually increased toward the multi-MW_E range. The working fluids were mainly light hydrocarbons, chlorobenzenes, and chloro-fluorocarbons (CFC). In this period, few ORC power plants were used also for the conversion of other renewable energy sources, like industrial waste heat and engine exhaust gases. The largest of these plants was built in Japan at Mitsui Engineering & Shipbuilding, featuring a power output of 15 MW_E [57]. As a result of rising concerns about air pollution, followed by rising fuel prices during the oil crisis, investigations on the use of Rankine engines for automobiles started in the 70's [58, 59]. Both steam and organic compounds were considered as working fluids, with either a turbine or a piston expander. A 30 kW_E prototype was successfully tested as bottoming cycle on a long-haul truck [8, 60], but never made it to the commercial market. In the 80's, intense research and development activity occurred also in East Germany, Finland, France, Japan, Israel, Italy, USSR. In the US, notable developments were related to five 600 kW_E units for industrial heat recovery [61], and to a concept for electricity generation for the international space station [62, 63].

Particularly relevant are the studies carried out in Italy during the 60's and the 70's by Prof. Gianfranco Angelino, one of the fathers of modern ORC power systems technology, together with his colleagues at Politecnico di Milano, Prof. Mario Gaia and Prof. Ennio Macchi. Their work was important also because it helped laying the scientific and technical basis for research and development [2]. An example of the application of these investigations is documented in a study presented by Bado and colleagues, a 35 kW_E perfluorocarbon (C_8F_{16}) unit providing a net electric conversion efficiency of 19 % at condensing and collectors cooling loop exit temperature equal to 40 and 300 ^oC, respectively [64]. Such unit was subsequently built and tested, and a net efficiency of 17 % was recorded at a turbine inlet temperature of approximately 270 ^oC [65, 66]. In these first prototypes, axial turbines were directly coupled to an asynchronous generator rotating at 3,000 rpm. Notable is the Borj Cedria 12 kW_E solar power station in Tunisia, which was commissioned in 1983. The working fluid was tetrachloroethylene, and during field tests a net electrical efficiency of 11 % was recorded, with evaporation

and condensation temperatures equal to 84 and 20 ^{o}C, respectively [67]. Based on these studies, a company was established in 1980 by Gaia. The company was initially involved in the realization of experimental solar and geothermal ORC power plants adopting various working fluids and single or multi-stage axial turbine [2]. Studies on the use of siloxanes as working fluids for high-temperature ORC power systems were conducted in collaboration with Angelino and co-workers [63, 68]. The first biomass-fuelled turbogenerator, which was later to determine the commercial success of the company, was commissioned in Bière, Switzerland, in 1998 [11]. It was a skid-mounted 300 kW_E genset, using siloxane MDM as the working fluid, and featuring a 2-stage axial turbine. The plant was ordered by the Swiss army in order to provide electricity and cogenerated heat to a barrack.

In Finland, Prof. J. Larjola led the development of high-speed hermetic turbogenerators in the hundreds kW_E range, in which the turbine, generator and pump share the same shaft. One of the first applications of this type of ORC turbogenerator was the use as the charger of the batteries of a deep-see submersible [69]. The hermetic turbogenerator configuration was similar to the early mini-ORC units for remote power applications [70, 71]. The knowledge acquired with these developments was later utilized in commercial units that were marketed starting from the early 2000's [72].

Information concerning operational ORC power plants referred to the period before 1995 are collected in Ref. [3], containing also data from Ref. [73], which in addition covers earlier years. During the 1980's, however, fossil fuel prices were relatively low: this led to most of the experimental plants being shut down because economics were not attractive. The main data related to the majority of the plants that have been commercially operated after 1995 are shown in Table 2.2. Fig. 2.4 presents a quantitative assessment of the the evolution of installed ORC power plants in the same period, in terms of both cumulated power and number of units.

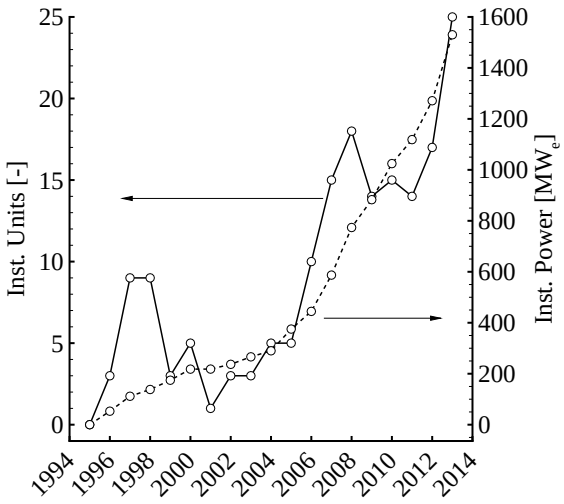

Figure 2.4: Commercial ORC power plants commissioned between 1995 and the end of 2013, based on the data reported in Tab. 2.2: number of units installed (solid line), and cumulated power capacity (dashed line).

Manufacturer	Country	Output kW_E	Out. cogen–T kW_T – °C	Working Fluid	Energy source	Turbine type/N_{stgs}	Turbine inlet T_{max}, °C	Turbine inlet P_{max}, bar	N units	Year commiss.	Ref
Atlas Copco (?)	CA	2100	–	R134a	WH	rad. in/1	na	na	1	2012	
	TR	22500	–	n-Butane	G	rad. in/1	na	na	2	2013	
	DE	3600	–	iso-Butane	G	rad. in/1	na	na	1	2014	
	TR	22500	–	n-Butane	G	rad. in/1	na	na	2	2015	
Exergy (IT)	TR	1000	–	FC	B	rad. out/na	na	na	2	2012	[74, 75]
	IT	1000	–	HC	G,B		na	na	2	2013	
	IT,FR	100 – 1000	–	RE,FC,SIL	WH,B		na	na	4	2014	
	IT,TR	1200 – 12000	–	HC	WH,G	rad. out+axial/na	na	na	7	2015	
GE Energy (US)	na	125	–	R245fa	B	rad. in/1	121	17.2	> 100	2009 – 2011	[76]
GE Oil & Gas (IT)	CA	17000	–	Cyclo-pentane	WH	rad. in/2	250		1	2012	[77, 78]
	BN		–						1	2014	
	CN,TH		–						4	2015	
Ormat (US)	US,Vars.	400 – 3500	–	n-Pentane	G	axial/1 – 4	105 – 170	na	67	1995 – 1999	[79, 80]
		2000 – 15000	–		G,S		140 – 180	na	144	2000 – 2013	
		300 – 6500	–		WH		110 – 180	na	19	1999 – 2013	
Tri-O-Gen (NL)	Vars.	80 – 160	–	Toluene	WH	rad. in/1	325	32	21	2009 – 2013	[72, 81]
		135 – 160	–		B				6	2012 – 2013	

Table 2.2: Overview of the main characteristics of commercial ORC power plants commissioned after 1995, data from official companies' websites and personal communications [TO BE COMPLETED - MISSING DATA]. For older data see, e.g., Refs. [3, 73]. Countries of installation are indicated with ISO 3166 Codes. FC: (per)fluorocarbons, HC: hydrocarbons, RE: refrigerants, SIL: siloxanes. Out. cogen–T: thermal power cogenerated – delivery temperature. Energy source: B = biomass, G = geothermal, S = Solar, and WH = waste heat. N_{stgs}: number of turbine stages. 'Vars' stands for 'various', and 'na' for 'not available'.

2.3 State of the art

A brief description of the most commonly adopted technical options encountered in commercially available systems is provided here. A sequential and iterative design process is often carried out in the order in which these technical solutions are presented. The design of one system component strongly depends on the others, therefore a trend toward an increasingly integrated and automated approach is pursued [82–84]. The number of possible combinations of the technical solutions applicable at system and component level is very large, and it explains why, even for similar specifications, the units that have reached commercial status can differ considerably. As it was in other sectors of the power field, after a period in which a relatively large variety of products compete for the market, evolution may reduce this diversity in the future, at least for a given application.

2.3.1 Technical options

The selection of the available solutions for the design of a system and its components depends on the initial specifications, which most often are:

- Type of thermal energy source, average power capacity, and average temperature
- Available/usable cooling fluid (water or air) and its average temperature

ORC modules can exhibit a certain level of standardization up to a power capacity of $2 - 3$ MW_E, while larger power units, like those of larger geothermal power plants, are highly customized.

Cycle configuration and working fluid

As discussed in Sec. 2.1, the design decision about the cycle configuration and the working fluid is closely coupled, and it has consequences on the choice of the expander and its design [2]. Currently, saturated [5] and superheated cycle configurations are common, while the supercritical cycle configuration has been implemented only in few cases [74, 85]. Two and three pressure levels in the evaporator have been adopted only in large geothermal power plants in order to substantially reduce the average temperature difference between the geothermal

[5] In case the expander is a turbine, a small degree of superheating at the turbine inlet and throughout the expansion is needed in order to avoid droplets impact against the rotor.

and the working fluid [86]. The supercritical cycle configuration might be optimal from a purely thermodynamic point of view, but the power consumption of the main feed pump becomes very large. Table 2.3 lists the working fluids that are most commonly employed, together with their main properties. In general, fluids formed by more complex molecules are suitable for high-temperature applications (e.g. siloxanes, toluene), and small-medium power capacity, while those formed by simpler molecules (e.g. refrigerants, alkanes) are adopted in low-temperature applications, and are suitable also for large power output.

Table 2.3: Main properties of the most diffused working fluids in current ORC plants, see also Tab. 2.2. MW: molecular weight, T_{boil}: normal boiling temperature, $p_{vap@80°C}$: vapour pressure at 80 °C. MDM: octamethyltrisiloxane, MM: hexamethyldisiloxane, PP5: Perfluorodecalin, PP2: perfluoro-methylcyclohexane, r245fa: 1,1,1,3,3-Pentafluoropropane, r134a: 1,1,1,2-tetrafluoroethane. Data from Ref. [87].

Fluid name	Chemical formula	MW [g mol^{-1}]	T_{CR} [°C]	p_{CR} [bar]	ρ_{CR} [kg m^{-3}]	T_{boil} [°C]	$p_{vap@80°C}$ [bar]
toluene	C_7H_8	92.1	318.6	41.26	278.8	110.6	0.389
cyclo-pentane	C_5H_{10}	70.1	238.5	45.15	272.6	49.2	2.522
iso-pentane	C_5H_{12}	72.1	187.2	33.78	215.7	27.8	4.575
iso-butane	C_4H_{10}	58.1	134.7	36.29	224.6	-11.8	13.438
MDM	$C_8H_{24}Si_3O_2$	236.5	290.9	14.15	302.9	152.5	0.091
MM	$C_6H_{18}OSi_2$	162.4	245.5	19.39	292.9	100.2	0.537
PP5	$C_{10}F_{18}$	462.0	291.9	17.88	565.0	140.7	0.133
PP2	C_7F_{14}	350.0	211.9	20.60	574.7	75.8	1.152
r245fa	$C_3H_3F_5$	134.0	154.0	36.51	489.3	15.1	7.893
r134a	$C_2H_2F_4$	102.0	101.1	40.59	545.6	-26.1	26.332

Rotating equipment

In case of larger power plants, one of the advantages related to the selection of an optimal organic working fluid is that it is possible to design an efficient turbine for rotational speeds that allow for direct coupling to a synchronous generator (3,000/1,500 rpm if the grid frequency is 50 Hz, or 3,600/1,800 rpm if it is 60 Hz). If this is not possible or wanted, reduction gears can then be used. The shaft seal demands for special attention, especially if the working fluid is used for lubrication, in order to avoid excessive leakage. Oil is often used in a dedicated bearings system for the shaft, especially in slow-rotating turbines and pumps, whereby mechanical seals are adopted for the shaft. The expander, electrical generator, and feed pump can rotate independently from one another, or, in

some cases and for systems rated at hundreds of kW_E, they can share the same shaft [72, 76, 81]. The so-called high-speed hermetic turbogenerator assembly allows to enclose the rotating equipment into a single casing and use the working fluid as bearings lubricant and generator coolant. In addition, thanks to the use of an inverter, the rotational speed of the turbine can be varied in order to match the machine optimum efficiency at the given operating condition. However, the consequent high-rotational speed of the feed-pump leads to its highly sub-optimal operation.

Expander. ORC expanders are currently dynamic (turbines) in the vast majority of the cases, while volumetric (screw, scroll) expanders are in the pre-commercial or market-introduction phase. Turbo-expanders cover the power capacity (from about 100 kW_M to several MW_M), expansion ratio (approximately from 5 to 100), and inlet temperature ($\approx$ 120 to $\approx$ 350 ^oC) ranges typical of current commercial ORC power systems. Volumetric expanders derived from refrigerant compressors are employed only in the low-temperature and low-capacity power systems (1 to about 100 kW_M) which are now being proposed to the market. An exception are the 1 MW_E screw expanders that have been recently installed in a low-temperature geothermal power plant in New Mexico [88]. The maximum volumetric expansion ratio of volumetric expanders currently prevents their use in high temperature systems. These machines feature lower isentropic efficiency if compared to turbo-expanders, which in turn are not yet available with a power output of few kW_E. Screw and scroll expanders can be cost-effective because they are derived from volume-produced refrigerant compressors. A distinguishing technical feature is that they can tolerate a fraction of liquid working fluid. Ref. [89] provides an overview on the main aspects of volumetric expanders for small ORC power systems. ORC expanders are in general different from other common machines expanding steam, air or other gases, because dense vapor properties deviate largely from ideal gas behavior, thus affecting the design, and because the speed of sound is much lower than in light gases or steam [90–92].

Axial turbines are commonly adopted for medium to large power output ORC systems (several hundreds kW_E to several MW_E) in single or multi-stage arrangement (currently up to four in large-capacity units). The isentropic efficiency in nominal conditions typically goes from 80 % to less than 90 %. In case of smaller-capacity systems (up to 200 kW_E), the radial inflow configuration is preferred because it allows to achieve high efficiency with one single stage, even in case of large expansion ratio/high TIT. The optimal rotational speed in these cases can be of the order of several tens of thousands rpm. A two-stage radial inflow turbine configuration has been recently implemented in a large ORC power plant [77].

Systems based on turbines adopting the multi-stage radial outflow configurations have been recently successfully commercialized [75].

The first ORC scroll expanders proposed to the market are either semi-hermetic or hermetic, the power output varies from 1 to 10 kW_E, the volumetric expansion ratio is at maximum 4-5, while the rotational speed is between 1,500 and 6,000 rpm [93].

Screw expanders are in a slightly more advanced stage of development, and their power output reaches several hundreds kW_E. They feature either the sigle-screw or the double-screw configuration, and the maximum expansion ratio is slightly larger than that of scroll machines (5-6) [89]. Their rotational speed can be as high as 10-12,000 rpm in the smaller machines.

Bearings. Conventional oil bearings are typically used in case the electrical generator is external to the turbine casing. If the working fluid has good lubricant properties, especially designed bearings are adopted, thus simplifying the turbine/generator assembly. These are often of the tilted pad type due to the high rotordynamic stability they offer. The high-speed hermetic turbogenerator assembly configuration also demands for special bearings, either magnetic, or lubricated with pressurized working fluid [57, 76, 94]. Magnetic bearings are utilized in some units that are in the initial commercialization phase with low turbine inlet temperature. The implementation of this technology in higher-temperature systems requires additional study.

Pump. The power consumption of an ORC pump is comparatively larger than that of the pump of a steam power plant, being the ratio of the specific pump work to the specific turbine work larger. For this reason, even though standard centrifugal water pumps are often adapted for the use in mainstream ORC systems, sometimes ad hoc pumps must be employed in order to achieve sufficient compression efficiency. The cost and comparatively low efficiency of multi-stage pumps is one of the main reasons why the supercritical cycle configuration is currently seldom adopted [86].

Heat Exchangers

Evaporator / Primary heater. The primary heat exchanger/evaporator can be of the once through type [2, 72], or the shell and tube type, having the working fluid typically in the shell side [95, 96]. Thermal energy can be transferred directly from the heat source (flue gas, hot waste stream, geothermal reservoir, solar radiation) to the working fluid, or indirectly via an intermediate thermal loop. Direct heating allows for higher temperature and pressure in the evaporator, while indirect heating demands for additional pumping power, thus direct heating implies

higher net conversion efficiency. The choice among the two solutions depends on many aspects: avoidance of hot spots that increase the risk of working fluid decomposition, ease of control, safety regulations, and contractual issues. In case of high-temperature applications, and if the working fluid is more expensive than the diathermal oil, lowering the temperature of the working fluid is a way of decreasing the frequency of working fluid charge substitution, thereby lowering the operating costs.

Regenerator. The adoption of a regenerator depends on the working fluid, and optimal cycle configuration [83]. In some cases, the thermodynamic advantage can be quite limited, but the adoption of the regenerator can help reducing the size of the condenser, which is often a significant cost component. In smaller capacity ORC power plants, the regenerator can be of the finned tube or plate type, thus being very compact. In larger power plants, the regenerator is more often of the shell and tube type. In any case, regenerators selection must account for a limited pressure drop on the vapor side, which directly affects the turbine outlet pressure, and thus its power output. This becomes a critical aspect if the condenser operates at very low pressure.

Condenser. Depending on the availability and regulations, water-cooled condensers are preferred because of the higher achievable net efficiency of the power plant. Wet cooling is also adopted if the ORC power plant cogenerates distric or process thermal energy or if it powers an absorption chiller or refrigerator. Depending on the system capacity, compact heat exchangers are more commonly adopted in low-power output systems, while shell and tube are adopted in larger power plants. Direct air cooling is seldom adopted, because it considerably increases the working fluid inventory, while air-coolers with an intermediate water/glycol loop is the most frequently adopted technical solution.

2.3.2 Energy conversion applications

The current applications of ORC power plants are listed here in order of relevance in terms of presently installed power capacity. ORC power systems are either the preferred or the only technology that can be adopted for the conversion into electricity of several types of relevant thermal renewable energy sources. For example, arguably most of the high temperature vapor-dominated geothermal reservoirs are already exploited, while the potential of liquid-dominated ones is still very large [43]. Similarly, in case of biomass combustion, the optimal plant capacity is mainly limited by the cost of fuel gathering. In both cases, the flexibility in terms of temperatures and scalability makes ORC power systems often more attractive than steam power plants. This is testified by the steadily increasing

number of ORC power plants being commissioned all over the world.

Geothermal Reservoirs

ORC power plants around the world are used mainly for the conversion of liquid-dominated reservoirs at temperature of 120 – 150 ^{o}C, though examples of operational plants fed by a mixture of steam and brine at higher temperature exist (Zunil Guatemala - 20 MW_E, Ribeira Grande I and II in San Miguel, Azores - 14 MW_E, Olkaria III, Kenya - 13 MW_E, and Oserian, Kenya - 1.8 MW_E) [96]. The goethermal fluid usually contains also a substantial amount of incondensible gases, which might form corrosive compounds. In case of two-phase geothermal fluid, the steam and the brine are separated, and the steam is used to evaporate the organic working fluid, while the brine is used for liquid working fluid preheating. The saturated cycle configuration with an alkane as a working fluid is the most common. Sometimes the system includes a regenerator. In case of a steam-dominated geothermal reservoir of large capacity, whereby a steam power plant is used as the high-temperature conversion system, an ORC power plant as bottoming cycle results into an efficient combined cycle configuration [97]. Exemplary plants of this type are the Upper Mahiao, Philippines (125 MW_E), the Mokai 1 and 2, New Zealand (100 MW_E), and the Puna, Hawaii (30 MW_E) [96].

Solid biomass or biogas combustion

High-temperature ORC power plants in the MW_E power range fuelled with various types of solid biomass have been installed at increasing pace in Europe starting from the early 2000's, thanks also to favorable legislation. More than 200 ORC gensets of this type are in operation. Most often these plants are integrated into wood-manufacturing sites, and feature the CHP arrangement, whereby the heat discharged by the ORC unit, at temperatures typically below 100 ^{o}C, is used for process purposes, or district heating. Many of these power systems adopt a superheated and regenerated cycle configuration, indirect heating, two, or in few cases, three-stage axial turbines, and MDM as the working fluid. The rated net electrical efficiency is usually in the 15 – 20 % range, while the total energy efficiency can be as high as 90 %. Information on exemplary biomass CHP power plants of this type can be found in Ref. [98] related to a 1 MW_E power plant in Lienz, Austria, in Ref. [99] for the 1.1 MW_E power plant in Tirano, Italy, and in Ref. [100] for that in Ostrow Wielkopolski, Poland, rated at 1.5 MW_E.

Flue Gas from Gas Turbines or Gas Engines

Several examples of ORC turbogenerators used to recover waste heat from the exhaust of gas engines already exists [77, 78], and the number of these installations is also increasing. In cases in which the reciprocating engine or the gas turbine is fed with biogas, the addition of an ORC heat recovery system is often economically viable because of the subsidized value of the generated electricity.

Industrial Waste Heat

Opportunity for heat recovery in the manufacturing and process industry are countless. The majority of the thermal energy is wasted at temperatures between 60 and 400 ^{o}C, with a capacity that monotonically increases toward vast quantities at low temperature.
Only recently this enormous potential has attracted interest, and few ORC power plants recovering various forms of thermal energy otherwise wasted are now operational, while many feasibility studies are performed.

First examples of industrial waste heat recovery ORC power plants can be found in the cement industry [101]. Throughout the production of cement, about 34 – 40% of the process heat is wasted to the environment, mainly via the exhaust gases from the rotary kiln, coming from the limestone preheaters and also from the ambient air used for clinker cooling [102]. Depending on the cement plant configuration, and the process efficiency, waste heat streams are available at temperatures between 215 and 380 ^{o}C [103, 104]. The first ORC heat recovery system (1.5 MW_E) in a cement factory was commissioned in 1998 at the HeidelbergCement AG plant of Lengfurt, Germany. Other successfull examples are: the 4 MW_E ORC power plant at A.P. Cement Works in India (2007), and the 2 MW_E Ait Baha, Morocco, plant of Italcementi (2010) [101]. Similar plants are under construction or commissioning: a 4 MW_E ORC plant in Alesd (Romania), a 5 MW_E plant in Rohoznik (Slovakia), and a 1.9 MW_E plant in Untervaz (Switzerland).

In comparison to the quite standardized cement production, steel manufacturing requires quite diverse processes. The potential for heat recovery in the steel manufacturing industry by means of ORC power systems has been recently studied, and especially heat recovery from the exhaust gas of Electric Arc Furnaces (EAF) and rolling mills has been found promising [105]. One of the implemented arrangement features an intermediate loop, whereby saturated steam at temperatures around 300 ^{o}C is used in order to transfer the thermal energy of the furnace off-gas to the ORC working fluid [106]. Currently, a 3 MW_E unit is under con-

struction at the EAF of Elbe-Stahlwerke Feralpi in Riesa (Germany) as part of the European H-REII Demo project (Heat Recovery in Energy Intensive Industries).

The glass industry also offers vast opportunities for waste heat recovery by means of indirectly heated ORC power systems. An intermediate heat transfer loop can collect thermal energy from the hot gas exiting the oven that melts and refines the raw materials. The exhaust gas temperatures are relatively high (400 – 500) ^{o}C [101]. Since 2012 one such system (1.3 MW_E) is in operation at the AGC floating glass production site in Cuneo, Italy. Other examples of successful ORC power plant installations for industrial heat recovery are at the urban solid waste incinerator plant in Roeselare, Belgium (3 MW_E), and at the sintered magnesite production site in Radenthein, Germany (1 MW_E). The Roeselare plant receives thermal energy at approximately 180 ^{o}C from a pressurized water loop transferring heat from the incineration furnace, and is a retrofit, because initially the plant was supposed to provide only district heating. The ORC system adopts a saturated configuration, axial turbine, synchronous generator, and Solkatherm as the working fluid.

Concentrated Solar Radiation

The design paradigm of concentrated solar power (CSP) plants based on ORC engines is mainly related to the choice of the maximum plant temperature [107]. High temperature entails increased conversion efficiency, but calls for comparatively expensive solar collecting equipment and power block. The complementary approach consists in selecting a low maximum plant temperature which allows to adopt simpler technological solutions, but leads to lower conversion efficiency, which in turn demands for a larger solar field surface for a given power output. The STORES project, in the US, has investigated a new paradigm for the successful deployment of thermal solar plants: economy of production can be achieved by means of high-volume manufacturing of small-capacity standard and modular systems, suitable for distributed energy conversion, instead of larger centralized power plants. ORC turbogenerators have been identified as the optimal conversion technology in this context, because of their performance and reliability [108, 109]. The main outcome of the study has been the construction of the first solar plant of this kind in the Saguaro Desert, Arizona (US). The plant, entered in operation in 2006, uses pentane as the working fluid and features a nominal power of 1 MW_E, with no need for onsite staff. The cycle efficiency is 21 % with inlet-turbine and condensation temperatures equal to 204 and 15 ^{o}C, respectively. The reported average annual solar conversion efficiency is 12 % [110].

2.4 Future scenarios

Research and development activities are very lively because, together with the constant technological improvement related to current applications, new high-potential ones in the field of renewable energy and waste eat recovery are considered and actively studied and developed. The growth of the scientific and technical interest in ORC power systems is testified by the increase of scientific literature in this field, see Fig. 2.5. The sudden increase of the number of publications related to ORC technology in the 80's and after 2000 can be correlated to the increase of oil prices, though the more recent trend is continuing notwithstanding the decrease and stabilization of oil prices of more recent years. It can be argued therefore that policy and strategic considerations are driving these studies.

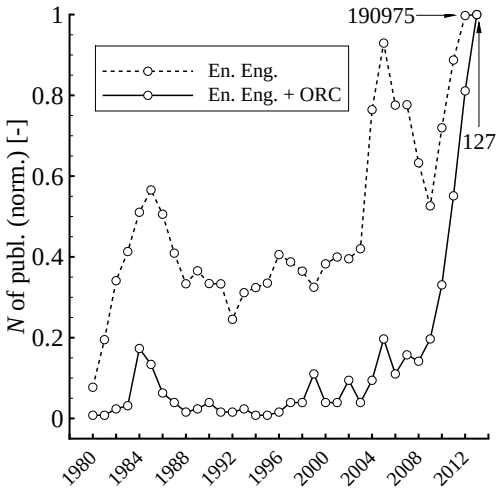

Figure 2.5: Number of published journal articles or conference papers, since 1980, in English. Results within the subject areas *engineering* and *energy* (dashed line) and, among these, works dealing with ORC power systems, i.e., with the acronym ORC appearing in the article title, abstract or among the keywords (solid line). The data series are normalized with respect to the maximum value, which is explicitly indicated in the figure [111].

Nowadays, the application showing the highest growth potential is arguably heat recovery at largely different capacity and temperature levels. All the applications of ORC power systems described in Sec. 2.3.2 are undergoing a fast-pace growth, which will continue in the coming years, given the global turn toward renewable energy, which is also happening in various countries in Asia. Waste heat recovery by means of ORC power systems is actively researched in case of

automotive engines (from few up to 10 – 15 kW_E net power output) and larger stationary reciprocating engines, but also as bottoming units for medium-size industrial gas turbines (up to about 20 MW_E), especially those used as mechanical drive in gas compression stations, and for power generation in the chemical and oil industry.

With reference to fig. 2.2, new applications of ORC power systems are located at the boundaries in terms of temperature and power capacities highlighted in the chart. At power levels of few kW_E, the conversion efficiency of low-temperature ORC systems ($T_{av.,source} \lesssim 130$ °C) is probably inherently too low for economic viability, though the system is feasible.

A number of research efforts are ongoing aimed at developing Rankine cycle-based heat recovery systems for passenger vehicle applications, with a number of studies identifying ORC turbogenerators among the most promising solutions [112–114]. If the energy source is at high temperature, i.e., $T_{av.,source} \lesssim 450$ °C, in the power range starting from hundreds kW_E, both steam and ORC power systems are feasible and various economic and technical consideration drive the selection, though ORC power systems are more often selected. It is only recently that, at this temperature range, ORC power systems are being developed at multi-megawatt capacity level, while for larger power capacity ORC power systems cannot compete with steam power plants. At medium temperatures of the energy source, $T_{av.,source} \lesssim 300$ °C, but large power capacity (> several hundreds MW_E), ORC power plants are studied for the heat recovery from large processing units in the oil and gas industry [105], and other sectors of the chemical industry are also interested. At low temperature level of the heat source, currently the only very large energy source that is driving some developments in the power sector is the thermally stratified water of tropical and equatorial ocean regions, whereby $T_{av.,source}$ is actually extremely low (see sec. 2.4.3).

As for the most relevant research topics, the supercritical cycle configuration is receiving attention because its thermodynamic merit needs careful evaluation, together with implications on turbomachinery design, due to dense-gas effects, and large expansion ratio [82, 83, 115]. The fluid dynamic design of unconventional organic fluid pumps for high pressure levels, and large compression ratio, whereby compressible effects might also play a role, should be considered, though at the moment no study can be found in the literature. In analogy to steam power plants, multiple pressure-level cycles and reheating of expanded vapor have been considered in order to boost efficiency [10, 116]. However, the feasibility of these solutions is challenged by the additional plant complexity they imply. The Lorentz thermodynamic cycle is known to be thermodynamically the best option for the

exploitation of sensible heat sources and, to this end, different solutions adopting organic working fluids in so-called trilateral cycles have been proposed [117–119]. Generally speaking, the criticality with such systems is related with the fully wet expansion process, still posing technological concerns regarding the expanding device, if this should be a turbine [120]. If very high electrical efficiency is sought, the binary (or cascaded) cycle configuration can be attractive and its evaluation has driven some interest, presenting several advantages if compared to a single cycle with large pressure ratio [10, 43, 109, 121].

Research on new working fluids can have a large impact, especially because fluids for high temperature applications that satisfy all requirements do not exist. However, fluid manufacturers are currently refraining from highly targeted development of new working fluids because the dimension of the market would require taking as a risk the large investments needed for R&D activities on new molecules, new synthesis processes, and new production plants. The merit of using fluid mixtures has been addressed already many years ago [122], and still stimulates many theoretical studies.

An innovative idea that very recently sparked some interest is the integration of the selection of the working fluid into the automated cycle optimization procedure [123]. Furthermore, new developments due to the advancements of simulation science promise to overhaul the traditional sequential and iterative design process. The new design paradigm can be termed *virtual prototyping*. The physics involved in an ORC power system is relatively well understood and therefore it can be accurately modeled, The power of modern software and computers are making it possible to develop and use a programming environment in which the entire system and its components can be modeled and simulated to the level of detail that is needed for preliminary design and optimization [124]. Dynamic simulation capabilities allow considering requirements on transient operation and control in this early design stage [84]. Applications that may feature critical control aspects are automotive heat recovery [114], and the conversion of concentrated solar radiation [125].

The fluid dynamic of expanders is often the aspect of an ORC system attracting more research effort. A sizable improvement of the expander performance directly affects the power output and thus the return on investment, more often without affecting the cost of each unit. On the contrary, improvement of the heat exchanging equipment can often be obtained only by increasing the heat transfer surface, therefore the cost of each unit. The fluid dynamics of turbo-expanders and volumetric expanders is intensely studied [126], and the non-conventional features of highly supersonic flows typical of high-temperature ORC turbines has driven

even quite some fundamental studies [127, 128]. Recently, several research efforts have been also devoted to investigate innovative turbine configurations, see, e.g., Ref. [129].

All types of volumetric expanders for mini-ORC power systems are currently studied theoretically and experimentally. Piston expanders would be suitable for high-temperature applications, and they have recently been studied for truck engine heat recovery systems [130], though the need for a lubricant, and the high blow-by losses are difficult challenges to overcome. Predictive models for scroll expanders are actively studied [131, 132], and also experimental activities are pursued [93]. Models of single and twin-screw expanders [133] are also under strong development.

The literature reports very few articles dealing with heat exchangers specifically designed for ORC power systems, see, e.g., Ref. [134] and [135]. However the design of more compact and lighter heat exchanger plays a very important role, particularly in the emerging field of mobile applications. To this end, several heat transfer enhancement techniques are investigated, leading to new concepts such as micro-channel [134, 136, 137] and porous [138, 139] heat exchangers. The addition of nano-particles to the working fluid might be beneficial for ORC power system for which ultra-high heat transfer to and from the working fluid is relevant [140]. Polymeric materials heat exchangers might also be an option in the future [141].

More detailed information on current and possibly future research and development activities is given in the following sections, depending on the specific application. In this respect, one important factor that might influence the level and amount of future research is the recent interest in ORC technology by large global companies. This is testified either by the starting of R&D work devoted to new applications, or by the acquisition of companies that developed ORC techology.

2.4.1 Heat Recovery from Automotive Engines

The potential of recovering heat from the exhaust and the cooling system of automotive engine cannot be understated. The development paradigm of this product is radically different from that of stationary units, that now veers toward that of economy of scale (larger, customized power plants). In case of mini-ORC power systems the paradigm is rather oriented towards an economy of production (large number of standardized units). If this industrial sector is successful, several new large markets for mini-ORC power systems could open up, see, e.g., Sec. 2.4.2.

Recently interest is being revived [142–146], and a considerable research and development effort by original equipment manufacturers (OEM) and tier-one sup-

pliers has been focused especially on the waste heat recovery from long-haul truck engines [130]. In this case, as opposed to car engines [147], the amount of thermal power that can be recovered is arguably enough to allow for the design of an ORC system that does not incur into the limitations inherent to very small expanders and tight space constraints. In addition, the large number of operating hours at cruising speed, plays an important role in the evaluation of the profitability of the investment. Feasibility studies on heat recovery from car engines have unveiled several limitations with current technological and economic conditions.

The first units that will be marketed are likely to be add-ons for existing trucks and their engines, employing ethanol as the working fluid and high-speed turbines. Because the system is designed to fit existing truck frames and engines, strict requirements on the volume occupied by ORC components must be complied with. Designers face the problem of the selection of the working fluid: a simple-molecule compound, even water, allows for the design of a comparatively efficient simple-cycle system without internal regeneration, and compact condenser, thanks to the relatively high pressure. On the other hand, if the expander is a turbine, the small flow passages and the high rotational speed pose technological and efficiency issues. In turn, volumetric expanders likely require a lubrication system, are kinetically complex, and subjected to vibrations. Regulations and requirements on the working fluids for the automotive sector are also quite stringent: aspects like toxicity, flammability, ODP and GWP are regulated. Even though a rational approach would require that these aspects are considered in relation to the corresponding indexes of the fuel, which is transported in quantities that are at least an order of magnitude larger. Very importantly, the freezing point of the working fluid must comply with the typical requirements of the automotive sector, therefore operation of the ORC system should be guaranteed for engine idle and startup temperatures as low as $-40\ ^{o}$C. Another notable difference with stationary applications is that the inherently dynamic operation of the unit [148] demands for advanced control strategies [149], which in turn ask for appropriate dynamic simulation capabilities [150].

An interesting concept that might be successful in the longer run, is the *combined-cycle power train*: in this case the primary engine and its integrated heat recovery system are designed together in order to optimize all critical aspects: efficiency, volume, weigth, reliability, etc. The potential for improvement with respect to the add-on approach can be large, if one thinks to the similarity to the design methodology of combined-cycle power stations. In this case the gas and the steam turbine systems are optimized in an integrated fashion, which often leads to a gas turbine which is less efficient than what is achievable with a simple gas turbine

cycle configuration, because the waste heat can be efficiently recovered, see, e.g., Ref. [151]. In a combined cycle powertrain, also the relatively large amount of thermal energy dissipated by the engine cooling system could be recovered. Given the radical changes with respect to current practice that such a system could impose, it is likely that the whole cab and drivetrain should be designed around the new combined-cycle powertrain. Another interesting possibility is that the combined-cycle powertrain generates electricity to power electric in-wheel motors and batteries [152].

2.4.2 Domestic CHP

The potential advantages of finely distributed cogeneration have been studied [25], especially in case of capillary natural-gas distribution, like in large parts of Europe. Besides the high utilization factor and total system efficiency, there might be a strategic interest in promoting a new business model of distributed power generation, due to the increasing difficulty to locate or refurbish power stations in densely populated areas because of permitting and public acceptance.

Among the technologies that are suitable for small-capacity electrical power conversion and cogeneration of heating, domestic ORC-based CHP units underwent research and development activities [153, 154]. In comparison to Stirling and micro-gas turbine generators, ORC systems display some potential advantages. In case of recent developments, the power capacity is either very small (1 kW_E) [153] or small (10 – 30 kW_E) [154], and the need to keep the cost low, especially in the case of a new application promoted by small companies, resulted in low-temperature cycles and the use of scroll expanders [155], whereby the electric efficiency is bound to be low (5–10 %). In any case, the total energy efficiency can reach values of the order of 90 %. The market for mini-ORC CHP units for domestic use could be very large (e.g., several millions unit per year in Europe only), but the higher investment cost compared to a traditional heater might be a barrier to widespread market introduction. The introduction of mini-ORC power systems for other applications, see Sec. 2.4.1, could boost the development of derived products for this sector.

2.4.3 Ocean Thermal Energy Conversion - OTEC

An ORC power plant could be suitable for the conversion of the energy deriving from the temperature difference between surface and deep ocean water, which is in the range 20 – 25 ^{o}C in various parts of the tropical and equatorial belt. The OTEC concept has been studied for a long time, though no commercial applica-

tion exists, the very low efficiency being the main technical and economic challenge [10]. Recently, experimental research has been resumed and pilot plants have been built, utilizing mainly ammonia as the working fluid in a saturated cycle configuration. ORC systems utilizing a refrigerant or a hydrocarbon as alternative working fluid are being studied [156, 157]. Technical problems related to deep-water pipes and pumps can now be solved thanks to advancements in off-shore technology. Economic viability might be achieved in the future, depending on energy value and policy, arguably only with large installations (many tens to hundreds or more MW_E). The co-production of other goods could also positively influence the economic feasibility. An interesting overview of various aspects related to OTEC power plants can be found in Ref. [10], together with the illustration of a study on the hybridization of an OTEC power plant with the addition of solar concentrators, and the utilization of complex configuration (multiple pressure level) for maximum efficiency.

2.4.4 Concentrated Solar Power - CSP

The majority of the present research efforts are devoted to low-to-medium temperature solar ORC systems, aiming at using comparatively inexpensive solar collectors, and often cogenerating heat and cooling. In the authors' opinion, also considering the promising results achieved in the past [54, 66], the investigation of higher temperature and thus high-efficiency systems is worth more attention. The advantage of solar ORC power systems is arguably the possibility of locally cogenerating heating and cooling power, and still achieving electric efficiency that is competitive with photo-voltaic panels, at the cost of a more complex system, possibly requiring more maintenance. The potential market of distributed solar cogeneration is very large (medium and large building in the solar belt). In this respect, innovative concepts aimed at including thermal storage, while simplifying plant layout and operation, and preserving or improving performance might be successful [120]. The combination of solar power conversion with other functions has also been studied: examples are desalinized water, or combination with cooling by means of absorption chillers [6, 158–161]. Also the hybridization with other energy sources seems promising; this is the case of systems integrating concentrated solar input with biomass combustion [162], industrial waste heat recovery, geothermal energy [163], or ocean thermal energy [10]. As anticipated, the use of small-capacity solar or biomass-fueled ORC modules to power the electrification of remote areas has been envisaged since the first studies on this technology [36, 46], and this research field is still actively investigated [121, 164].

2.4.5 Other applications

Other niche applications attracted some research efforts. An example is the heat recovery from high-temperature fuel cells, which discharge flue gases at temperatures exceeding 400 ^{o}C, and achieve extremely high electrical efficiency (50 % to 60 %, respectively). They have not reached widespread market introduction because of the very high cost per kW_E and because of long-term reliability and maintenance issues. The first commercialized units are in the medium power range (300 kW_E to 3 MW_E), and an ORC power system is the heat recovery system of choice [165–168].

ORC turbogenerators are increasingly studied also as bottoming cycles in combined systems for advanced power conversion facilities. According to several authors, this can be the solution of choice to recover power from the exhaust of high efficiency small and medium-size gas turbines, in order to exceed 50% efficiency at power levels as low as 5 MW_E [169, 170]. Similar systems are being considered also for CBC-based plants proposed for next generation nuclear and CSP applications [171].

Another notable application that has been studied in the past and that might attract attention in the future is the conversion from solar radiation in space. At the time of the initial activities aimed at the development of the International Space Station, together with Stirling engine and Closed Brayton Cycle gas turbine, ORC power systems were intensely studied, also experimentally [63, 172, 173]. It is well possible that the increasing presence of devices orbiting around the earth and further space exploration will drive the development of special solar or nuclear-powered ORC systems, whereby the main advantage with respect to photovoltaic panels could be the possibility of efficiently cogenerating the heat needed for propulsion or for the thermal control of on-board equipment.

2.5 Conclusions

The concept of the organic Rankine cycle (ORC) engine is almost coeval with that of the steam engine and, similarly, the concept has been implemented into actual power systems with an impressive growth of technological sophistication. Arguably, the main cause of the recent success of ORC power systems is their very high flexibility. It is a technology that can be used to convert external sources of thermal energy at widely different temperature levels, and at an equally wide range of capacities. This characteristic places ORC power systems in a prominent position among the technologies that are suitable for renewable of

renewable-equivalent thermal energy conversion (geothermal reservoirs, biomass combustion, concentrated solar radiation, industrial waste-heat recovery, waste heat recovery from reciprocating engines and gas turbines, ocean thermal gradient). ORC power systems can also cogenerate heat and cooling, thus are inherently suitable for distributed energy conversion with unequaled efficiency.

Technical solutions have been developed out of scientific and technical research, and some times quite fundamental investigation paved the way to highly innovative improvements. This is the case, for instance, of the study on new fluids, and their modeling, and the study of the complex gas dynamics of dense vapors and supercritical fluid flows of organic substances. Equally important were technical inventions related to the various components of the system, and the hermetic turbogenerator, or the recently re-descovered radial outflow turbine are good examples. Design problems are quite complex as fundamental aspects, like those related to thermodynamic cycles, and fluid dynamics, cannot be studied without, at the same time, taking into account realistic technical constraints. The development of new technology benefits today from the application of the most advanced engineering methods, like high-fidelity simulations of fluid flows, and complex multi-physics system and component optimization.

The cumulative installed capacity of ORC power plants have been growing at a sustained rate starting from the first years of the new millennium, as well as the number of ORC power systems. The number of vendors is increasing, and large manufactures of conventional power equipment are entering the market, together with several new dynamic enterprises. The analysis of the available information about commercial power plants shows that the range of power outputs of ORC units that enter into operation is expanding towards both larger and smaller units, if compared to few years ago. The application of ORC technology to geothermal heat and biomass combustion conversion, the two applications that sparked the growth of ORC installations, continues the trend, whereby the power output of geothermal ORC power plants is increasing (the plants that were recently commissioned feature capacities from several tens of MW_E up to the last one, which reached almost 100 MW_E). Biomass-fuelled ORC power plants are still spreading in Europe, where policy is favorable, but the situation is not yet equally favorable in other continents. Waste heat recovery from prime movers and industrial processes by means of ORC power plants has also started to grow in recent years, and it is the application with arguably the highest potential in the foreseeable future.

Very recently, a considerable amount of research and development efforts are dedicated to the development of ORC systems for applications suitable for high-volume production, and heat recovery from automotive engines stands out. The

automotive industry is boldly committed to the initiative. Several solutions are investigated, different above all with respect to the expander. Volumetric (piston, screw, scroll) expanders are attractive, as much knowledge from small refrigeration compressors is available, but limitations related to the maximum expansion ratio and inlet temperature are difficult to overcome. High-speed turbines are very promising given their ability to expand vapors from high temperature and to handle large expansion ratio. In addition they potentially offer a high degree of reliability, given their simplicity, as it can be extrapolated from the experience with turbo-chargers. The first models of mini-ORC turbogenerators for heat recovery from the exhaust of truck engines will likely be commercialized in the next few years. If successful, the production of a large number of standardized and cost-effective units could promote the adoption of mini-ORC power systems in many other high-volume applications. Examples are domestic CHP, distributed solar power plants cogenerating heat and/or cooling with thermal storage, and capillary waste heat recovery. The possibility that ORC power blocks will make OTEC plants a viable solution for base-load energy conversion in the tropical oceans is also interesting.

As a final remark, it is worth noting that modern technological progress is often the outcome of strong collaboration between academia and industry. Academics shall continue to strive with their role of looking at high-risk high-reward research, especially now that the technology grew further from its infancy. The level of research and development should reach those of more mature energy conversion technologies, like, e.g., gas turbines or reciprocating engines. The companies that have been on the market since the beginning of the diffusion of ORC power systems, and those that are now entering the market shall therefore maintain or increase their attitude toward research and innovation, without which the solutions needed in order to fulfill the high potential of current and future applications cannot be identified.

Nomenclature

s, p	=	specific entropy [kJ kg^{-1} K^{-1}], pressure [bar]
T, ρ	=	temperature [°C], density [kg m^{-3}]
MW	=	molecular weight [g mol^{-1}]
W, Q	=	Electric power, thermal power [kW]

Subscripts

E, M	=	electrical, mechanical

Acronyms

ORC	=	Organic Rankine Cycle
ROT	=	Radial Outflow Turbine
OTEC	=	Ocean Thermal Energy Conversion
CFC	=	Complete Flashing Cycle
GWP	=	Global Warming Potential
ODP	=	Ozone Depletion Potential
CBC	=	Closed Brayton Cycle
CHP	=	Combined Heat and Power
EFGT	=	Externally Fired Gas Turbine
SPPP	=	Solar Pond Power Plant
EAF	=	Electric Arc Furnace
CSP	=	Concentrated Solar Power

References

[1] H. Tabor and L. Bronicki. Establishing criteria for fluids for small vapor turbine. *SAE Technical Paper*, (640823), 1964.

[2] G. Angelino, M. Gaia, and E. Macchi. A review of Italian activity in the field of organic Rankine cycles. In *VDI Berichte - Proceedings of the International VDI Seminar*, volume 539, pages 465–482, Düsseldorf, 10–12 September 1984. VDI Verlag.

[3] A. W. Adam. *Encyclopedia of Energy Technology and the Environment*, chapter Organic Rankine Engines, pages 2157–2161. John Wiley & Sons, 1995.

[4] E. Macchi. Design criteria for turbines operating with fluids having a low speed of sound. In *Lecture Series 100 on Closed Cycle Gas Tubines, Von Karman Institute for Fluid-Dynamics*, May 1977.

[5] A. Verneau. Supersonic turbines for organic fluid Rankine cycles from 3 to 1300 kW. In *Lecture series 1987-07 Small High Pressure Ratio Turbines*. Von Karman Institute for Fluid Dynamics, June 1987.

[6] Sylvain Quoilin, Martijn Van Den Broek, Sébastien Declaye, Pierre Dewallef, and Vincent Lemort. Techno-economic survey of Organic Rankine Cycle (ORC) systems. *Renewable and Sustainable Energy Reviews*, 22:168 – 186, 2013.

[7] Costante M. Invernizzi. *Closed Power Cycles - Thermodynamic Fundamentals and Applications*. Number 11 in Lecture Notes in Energy. Springer-Verlag, 2013.

[8] L.R. Di Nanno, F.A. Di Bella, and M.D. Koplow. An RC-1 organic Rankine bottoming cycle for an adiabatic Diesel engine. Technical Report DOE/NASA/0302-1, NASA, Lewis Research Center, 1983.

[9] S.H. Fergason, A. Guardone, and B.M. Argrow. Construction and validation of a dense gas shock tube. *Journal of Thermophysics and Heat Transfer*, 17(3):326–333, 2003.

[10] P. Bombarda, C. Invernizzi, and M. Gaia. Performance analysis of OTEC plants with multilevel organic Rankine cycle and solar hybridization. *Journal of Engineering for Gas Turbines and Power*, 135(4), 2013.

[11] M. Gaia. 30 years of ORC development. 2011. Keynote lecture at the ORC2011 - 1st International Seminar on ORC Power Systems - Delft (NL), September 22-23. Available online: www.kcorc.org/en/literature/orc2011-proceedings.

[12] I. A. Kalina. Combined cycle system with novel bottoming cycle. *Journal of Engineering for Gas Turbine and Power*, 106:737–742, 1984.

[13] P. Bombarda, C. Invernizzi, and C. Pietra. Heat recovery from Diesel engines: A thermodynamic comparison between Kalina and ORC cycles. *Applied Thermal Engineering*, 30:212 – 219, 2010.

[14] K.W. Stone, E. Leingang, B. Liden, E. Ellis, T. Sattar, T. Mancini, and H. Nelving. SES/Boeing dish Stirling system operation. In *Proceedings of the ASME International Solar Energy Conference, Washington (US-DC), April 21-25*, pages 105–110, 2001.

[15] W. Reinalter, S. Ulmer, P. Heller, T. Rauch, J. M. Gineste, A. Ferriere, and F. Nepveu.

Detailed performance analysis of a 10 kW dish Stirling system. *Journal of Solar Energy Engineering*, 130(011013), 2007.

[16] H. Carlsen and J. Fentz. Development of a 9 kW Stirling engine. In *Proceedings of the International Gas Research Conference, Vancouver (CA), November*, 2004.

[17] G. Conroy, A. Duffy, and L.M. Ayompe. Validated dynamic energy model for a Stirling engine μ-CHP unit using field trial data from a domestic dwelling. *Energy and Buildings*, 62:18–26, 2013.

[18] G. Angelino and C. Invernizzi. Real gas effects in Stirling engines. In *Proceedings of the* 35^{th} *Intersociety Energy Conversion Engineering Conference & Exhibit (IECEC), Las Vegas (US-NV), July 24-28*, pages 69–75, 2000.

[19] Unknown. Global monitor: Sandia, Stirling energy systems set new world record. *Power*, 152(4), 2008.

[20] G Angelino. Carbon dioxide condensation cycles for power production. *Journal of Engineering for Power*, 10:287–295, July 1968.

[21] V Dostal, P Hejzlar, and M J Driscoll. High-performance supercritical carbon dioxide cycle for next-generation nuclear reactors. *Nuclear Technology*, 154(3):265–282, 2006.

[22] B.D. Iverson, T.M. Conboy, J.J. Pasch, and A.M. Kruizenga. Supercritical CO_2 Brayton cycles for solar-thermal energy. *Applied Energy*, 111:957–970, 2013.

[23] S. Bram, J. De Ruyck, and A. Novak-Zdravkovic. Status of external firing of biomass in gas turbines. *Proceedings of the Institution of Mechanical Engineers, Part A: Journal of Power and Energy*, 219(2):137–145, 2005.

[24] P. Heller, M. Pfänder, T. Denk, F. Tellez, A. Valverde, J. Fernandez, and A. Ring. Test and evaluation of a solar powered gas turbine system. *Solar Energy*, 80(10):1225–1230, 2006.

[25] M. Pehnt, B. Praetorius, K. Schumacher, C. Fischer, L. Schneider, M. Cames, and J.-P. Voß. *Micro Cogeneration: Towards Decentralized Energy Systems*. Springer, 2006.

[26] E. Galloway and L. Hebert. *History and progress of the steam engine: with a practical investigation of its structure and application.* Printed for Thomas Kelly, R. Clay printer, 1836.

[27] Frank W. Ofeldt. Engine. 1898. Patent US611792 A.

[28] K. Durant. *The Naphtha Launch*. Monographs. Adirondack Museum, 1976.

[29] P. Towne. The naphta engine. *Gas Engine Magazine*, October/November 1991.

[30] Frank Shuman. The direct acting solar engine - the prime mover of the immediate future. Technical report, The Sun Power Company, 1907. Review Publishing & Printing Company, Philadelphia (US-PA).

[31] G. Tissandier and H. de Parville. Moteurs a vapeurs volatiles. *La Nature*, (790):113–114, July 21 1888.

[32] Esher Wyss AG. Motorboote und motoryachten. Reprinted by Brian Hillsdon and Jim White in 1982, 1912. Catalogue.

[33] Unknown. Naphta launch ablaze. *The New York Times*, 26 July 1904.

[34] J.T. Pytilinski. Solar energy installations for pumping irrigation water. *Solar Energy*, 21(4):255 – 262, 1978.

[35] L.C. Spencer. A comprehensive review of small solar-powered heat engines: Part I. a history of solar–powered devices up to 1950. *Solar Energy*, 43(4):191 – 196, 1989.

[36] L. D'Amelio. *Impiego di vapori ad alto peso molecolare in piccole turbine e utilizzazione del calore solare per energia motrice*. Industria Napoletana Arti Grafiche, 1935.

[37] L. D'Amelio. La turbina a vapore ed i cicli binari con fluidi diversi dall'acqua fra le isoterme inferiori. *L'Elettrotecnica*, XXIII(9):250–257, 1936.

[38] L. D'Amelio. La turbina a vapore ed i cicli binari con fluidi diversi dall'acqua fra le isoterme inferiori. *L'Elettrotecnica*, XXIII(10):286–292, 1936.

[39] L. D'Amelio. *I combustibili nazionali ed il loro impiego*, chapter Le acque termali come fonti di energia, pages 293–307. Reale accademia delle scienze di Torino, 1939.

[40] M. Dornig. *Trattato generale delle macchine termiche ed idrauliche: Macchine a vapore*, chapter 2, page 246. Libreria editrice politecnica C. Tamburini, 1959.

[41] L. D'Amelio. A steam engine using a mixture of vapours from non-miscible fluids as a solar engine with flat plate collectors. In E. F. Carpenter, editor, *Proceedings of the 1955 International Conference on the Use of Solar Energy - the Scientific Basis. Tucson (US-AZ), Oct. 31 - Nov. 1*. Association for Applied Solar Energy, Arizona Unversity Press, 1958.

[42] L. D'Amelio. Thermal machines for the conversion of solar energy into mechanical power (presented at the United Nations conference on new sources of energy, Rome, 1961, 12 p.). *Solar Energy*, 7(2):82, 1963.

[43] R. Dipippo. *Geothermal Power Plants: Principles, Applications, Case Studies and Environmental Impact*. Butterworth Heinemann, 2nd edition, 2008.

[44] O. Povarov, V. Saakyan, A. Nikolski, V. Luzin, G. Tomarov, and M. Sapozhnikov. Experience of creation and operation of geothermal power plants at Mutnovsky geothermal field, Kamchatka, Russia. In *Proceedings of the International Geothermal Conference*, number S01P52, pages 1–56, 2003.

[45] G. V. Tomarov, A. A. Nikolsky, V. N. Semenov, and A. A. Shipkov. Recent geothermal power projects in Russia. In *Proceedings of the World Geothermal Congress*, pages 1–7, 2010.

[46] H. Tabor and L. Bronicki. Small turbine for solar energy power package. *Solar Energy*, 7(2):82, 1963. Presented at the 1961 United Nations Conference on New Sources of Energy, Rome.

[47] S. K. Ray and G. Moss. Fluorochemicals as working fluids for small Rankine cycle power units. *Advanced Energy Conversion*, 6:89–102, 1966.

[48] L.C. Spencer. A comprehensive review of small solar-powered heat engines: Part II. research since 1950 – "conventional engines" up to 100 kW. *Solar Energy*, 43(4):197 – 210, 1989.

[49] L. Bronicki. The Ormat Rankine power unit. In *Proceedings of IECEC*, pages 327–334, San Diego, USA, September 1972.

[50] Anon. Turbo-generator provides 2,000 watts remote power. *World Oil*, 175(7):67–69, 1972.

[51] L. Bronicki. Ten years of research, development and operation of Rankine cycle power units in Israel. In *Proceedings of IECEC*, Boulder, Colorado, USA, 1968.

[52] Daryl Prigmore and Robert Barber. Cooling with the sun's heat design considerations and test data for a Rankine cycle prototype. *Solar Energy*, 17(3):185 – 192, 1975.

[53] J.P. Abbin. Solar total energy test facility project test summary report: Rankine cycle energy conversion subsystem. Technical Report SAND-78-0396, Sandia Labs., Albuquerque (US-NM), 1978.

[54] Leonard D. Jaffe. Review of test results on parabolic dish solar thermal power modules with dish-mounted Rankine engines and for production of process steam. *Journal of Solar Energy Engineering, Transactions of the ASME*, 110(4):275–281, 1988.

[55] A. Einav. Solar energy research and development achievements in Israel and their practical significance. *Journal of Solar Energy Engineering, Transactions of the ASME*, 126(3):921–928, 2004.

[56] L. Y. Bronicki. Organic Rankine cycles in geothermal power plants: 25 years of Ormat experience. In *GRC transactions*, volume 31, pages 499–502. Geothermal Resources Council,

May 2007.

[57] J. Larjola. ORC power plant based on high speed technology. In *Proceedings of Conference on High Speed Technology*, number ENTE D-15, pages 63–77, Lappeenranta, Finland, 1988.

[58] Ove. B. Platell. Progress of Saab Scania's steam power project. *SAE Technical paper*, 760344, February 1976.

[59] S. Luchter and R.A. Renner. Assessment of the technology of Rankine engines for automobiles. Technical Report ERDA-77-54, US Energy Research and Development Administration, 1977.

[60] Francis A. DiBella, Luco R. DiNanno, and Michael D. Koplow. Laboratory and on-highway testing of Diesel organic Rankine compound long-haul vehicle engine. *SAE Technical paper*, 830122, 1983.

[61] Anil Prasad. Field testing of a 600 kW organic Rankine cycle waste recovery system: Results to date. *Energy Technology: Proceedings of the Energy Technology Conference*, 1:482–494, 1980.

[62] J. E. Boretz. Supercritical organic Rankine engines (SCORE). In *21st Intersociety Energy Conversion Engineering Conference (IECEC)*, volume 3, pages 2050–2054, Washington, DC, August 1986. ACS.

[63] G. Angelino and C. Invernizzi. Cyclic Methylsiloxanes as Working Fluids for Space Power Cycles. *J. Sol. Energ. - Trans. ASME*, 115(3):130–137, 1993.

[64] G. Bado, G. Tomei, G. Angelino, M. Gaia, and E. Macchi. The Ansaldo 35 kW solar power system. In *Sun II, Proceedings of the Silver Jubilee Congress, Atlanta - GA, Vol. 2*, pages 1090–1094. Pergamon Press, May 28-June 1 1979.

[65] G. Angelino, M. Gaia, E. Macchi, A. Barutti, C. Maccio, and G. Tomei. Test results of a medium temperature solar engine. *International Journal of Ambient Energy*, 3(3):115–126, 1982.

[66] A. Barutti, W.G. Pedrick, G. Angelino, M. Gaia, and E. Macchi. Ansaldo solar thermal and photovoltaic plants located at Ballajura, Western Australia. In *Proceedings of the 8th Solar World Congress 1983, Biennial Congress of the International Solar Energy Society, Perth (AU)*, volume 3, pages 1572–1576, 1984.

[67] M. Gaia, G. Angelino, E. Macchi, D. DeHerring, and J.P. Fabry. Experimental results of the ORC engine developed for the Borj Cedria solar plant. In *Proceedings of the 8th Solar World Congress 1983, Biennial Congress of the International Solar Energy Society, Perth, Australia*, volume 3, pages 1460–1464, 1984.

[68] G. Angelino, C. Invernizzi, and E. Macchi. *Organic Working Fluid Optimization for Space Power Cycles*, chapter 16, pages 297–326. Springer New York, 1991.

[69] T. Jokinen, J. Larjola, and I. Mikhaltsev. Power unit for research submersible. In *ElecShip 98, International conference on electric ship*, pages 114–118, Istanbul, Turkey, 1998.

[70] L. Bronicki. Experience with high speed organic Rankine cycle turbomachinery. In *Proceedings of Conference on High Speed Technology*, number ENTE D-15, pages 44–61, Lappeenranta, Finland, 1988.

[71] J. Larjola. ORC-plant with high-speed gas lubricated turbogenerator. In *VDI Berichte - Proceedings of the International VDI Seminar*, volume 539, pages 697–705, Düsseldorf, 10-12 September 1984. VDI Verlag.

[72] J. van Buijtenen, J. Larjola, T. Turunen-Saaresti, J. Honkatukia, H. Esa, J. Backman, and A. Reunanen. Design and validation of a new high expansion ratio radial turbine for ORC application. 2003. 5th European conference on turbomachinery - Prague (CZ), March 18-21.

[73] H.M. Curran. Use of organic working fluids in Rankine engines. *Journal of energy*,

5(4):218–223, 1981.

[74] C. Spadacini, L. Centemeri, L. G. Xodo, M. Astolfi, M. C. Romano, and E. Macchi. A new configuration for organic Rankine cycle power systems. 2011. ORC2011 - 1st International Seminar on ORC Power Systems - Delft (NL), September 22-23. Available online: www.kcorc.org/en/literature/orc2011-proceedings.

[75] C. Spadacini, D. Rizzi, C. Saccilotto, S. Salgarollo, and L. Centemeri. The radial outflow turbine technology. 2013. ASME ORC2013 - 2nd International Seminar on ORC Power Systems - Rotterdam (NL), October 7-8. Available online: www.kcorc.org/en/literature/asme-orc2013-proceedings.

[76] L. Hawkins, Z. Lei, E. Blumber, P. Mirmobin, and R. Erdlac. Heat-to-electricity with high-speed magnetic bearing/generator system. In *Geothermal Resources Council Annual Meeting*, volume 36, pages 1073–1078, 2012.

[77] P. Del Turco, A. Asti, A.S. Del Greco, A. Bacci, G. Landi, and G. Seghi. The ORegen waste heat recovery cycle: Reducing the CO_2 footprint by means of overall cycle efficiency improvement. In *Proceedings of ASME Turbo Expo 2011, Vancouver (CA), June 6-10*, pages 547–556, 2011.

[78] A. Burrato. ORegen™waste heat recovery: Development and applications. 2013. ASME ORC2013 - 2nd International Seminar on ORC Power Systems - Rotterdam (NL), October 7-8. Available online: www.kcorc.org/en/literature/asme-orc2013-proceedings.

[79] L. Bronicki. Short review of the long history of ORC power systems. 2013. Keynote lecture at the ASME ORC2013 - 2nd International Seminar on ORC Power Systems - Rotterdam (NL), October 7-8. Available online: www.kcorc.org/en/literature/asme-orc2013-proceedings.

[80] L. Bronicki. Private discussions. 2013.

[81] J. van Buijtenen, Q. Eppinga, and S. Ganassin. Development and operation of a high temperature high speed organic Rankine cycle system. 2013. ASME ORC2013 - 2nd International Seminar on ORC Power Systems - Rotterdam (NL), October 7-8. Available online: www.kcorc.org/en/literature/asme-orc2013-proceedings.

[82] M. Astolfi, M.C. Romano, P. Bombarda, and E. Macchi. Binary ORC (organic Rankine cycles) power plants for the exploitation of medium-low temperature geothermal sources - Part A: Thermodynamic optimization. *Energy*, 66:423–434, 2014.

[83] M. Astolfi, M.C. Romano, P. Bombarda, and E. Macchi. Binary ORC (organic Rankine cycles) power plants for the exploitation of medium-low temperature geothermal sources - Part B: Techno-economic optimization. *Energy*, 66:435–446, 2014.

[84] L. Pierobon, E. Casati, F. Casella, F. Haglind, and P. Colonna. Design methodology for flexible energy conversion systems accounting for dynamic performance. *Energy*, 68:667–679, 2014.

[85] M. Astolfi, R. Bini, E. Macchi, M. Paci, C. Pietra, N. Rossi, and A. Tizzanini. Testing of a new supercritical ORC technology for efficient power generation from geothermal low temperature resources. 2013. ASME ORC2013 - 2nd International Seminar on ORC Power Systems - Rotterdam (NL), October 7-8. Available online: www.kcorc.org/en/literature/asme-orc2013-proceedings.

[86] L.Y. Bronicki. Organic Rankine cycles in geothermal power plants 25 years of Ormat experience. *Transactions - Geothermal Resources Council*, 31:499–502, 2007.

[87] P. Colonna, T. P. van der Stelt, and A. Guardone. FluidProp (Version 3.0): A program for the estimation of thermophysical properties of fluids, 2012. A program since 2004.

[88] T. Biederman and J Brasz. Geothermal ORC systems using large screw expanders. 2014.

22nd International Compressor Engineering Conference, West Lafayette (US-IN), July 14-17.

[89] V. Lemort, L. Guillaume, A. Legros, S. Declaye, and S. Quoilin. A comparison of piston, screw and scroll expanders for small scale Rankine cycle systems. In *Proceedings of the* 3rd *International Conference on Microgeneration and Related Technologies, Naples (IT), April 5 – 17*, 2013.

[90] P. Colonna and S. Rebay. Numerical simulation of dense gas flows on unstructured grids with an implicit high resolution upwind Euler solver. *Int. J. Numer. Meth. Fl.*, 46(7):735–765, 2004.

[91] P. Colonna, J. Harinck, S. Rebay, and A. Guardone. Real-gas effects in organic Rankine cycle turbine nozzles. *J. Propul. Power*, 24(2):282–294, March–April 2008.

[92] J. Harinck, P. Colonna, A. Guardone, and S. Rebay. Influence of thermodynamic models in 2D flow simulations of turboexpanders. *J. Turbomach.*, 132(1):011001–17, January 2010.

[93] P. Song, M. Wei, L. Shi, S.N. Danish, and C. Ma. A review of scroll expanders for organic Rankine cycle systems. *Applied Thermal Engineering*, 2014. Article in Press.

[94] J. van Buijtenen. The Tri-O-Gen organic Rankine cycle: development and perspectives. *Power Engineer: Journal of the Institution of Diesel and Gas Turbine Engineers*, 13(1), 2009.

[95] R. Bini and E. Manciana. Organic Rankine cycle turbogenerators for combined heat and power production from biomass. In 3rd *Munich Discussion Meeting Energy Conversion from Biomass Fuels Current Trends and Future Systems*, Munich, Germany, 22-23 October 1996.

[96] L. Bronicki. Advanced power cycles for enhancing geothermal sustainability, 1,000 MW deployed worldwide. In *Power and Energy Society General Meeting - Conversion and Delivery of Electrical Energy in the 21st Century, 2008 IEEE*, 2008.

[97] Z. Krieger and Kaplan U. Apparatus and method for producing power using geothermal fluid, January 2000.

[98] P. Thonhofer I. Obernberger and E. Reisenhofer. Description and evaluation of the new 1000 kwel organic Rankine cycle process integrated in the biomass CHP plant in Lienz. *Euroheat & Power*, 10:1–17, 2002.

[99] R. Bini, A. Duvia, A. Schwarz, M. Gaia, P. Bertuzzi, and W. Righini. Operational results of the first biomass CHP plant in Italy based on organic Rankine cycle turbogenerator and overwiev of a number of plants in operation in Europe since 1998. In *Second World Biomass Conference*, pages 1716–1721, Rome, May 2004.

[100] A. Duvia, A. Guercio, and C. Rossi. Technical and economic aspects of biomass fuelled CHP plants based on ORC turbogenerators feeding existing district heating networks. In *17th European Biomass Conference*,, pages 2030–2037, Hamburg, Germany, 2009.

[101] R. Vescovo. ORC recovering industrial heat - power generation from waste energy streams. *Cogeneration and On-Site Power Production*, March-April 2009.

[102] N.A. Madlool, R. Saidur, M.S. Hossain, and N.A. Rahim. A critical review on energy use and savings in the cement industries. *Renewable and Sustainable Energy Reviews*, 15(4):2042 – 2060, 2011.

[103] Tahsin Engin and Vedat Ari. Energy auditing and recovery for dry type cement rotary kiln systems - a case study. *Energy Conversion and Management*, 46(4):551 – 562, 2005.

[104] S. Karellas, A.-D. Leontaritis, G. Panousis, E. Bellos, and E. Kakaras. Energetic and exergetic analysis of waste heat recovery systems in the cement industry. *Energy*, 58(0):147 – 156, 2013.

[105] F. Campana, M. Bianchi, L. Branchini, A. De Pascale, A. Peretto, M. Baresi, A. Fermi, N. Rossetti, and R. Vescovo. ORC waste heat recovery in European energy intensive indus-

tries: Energy and GHG savings. *Energy Conversion and Management*, 76:244–252, 2013.

[106] C. Born and R. Granderath. Analysis of potential and specific problems of heat recovery in the EAF. *Steel Times International*, 35(5):45–48+51, 2011.

[107] H. Tabor. Use of solar energy for production of mechanical power and electricity by means of piston engines and turbines. *Solar Energy*, 6(3):89 – 93, 1962.

[108] H. Price and V. Hassani. Modular trough power plant cycle and system analysis. Technical Report NREL/TP-550-31240, US National Renewable Energy Laboratory, 2002.

[109] E. Prabhu. Solar trough organic Rankine electricity system (STORES) stage 1: Power plant optimization and economics. Technical Report NREL/SR-550-39433, US National Renewable Energy Laboratory, 2006.

[110] S. Canada, D.A. Brosseau, and H. Price. Design and construction of the APS 1-MW_E parabolic trough power plant. In *Proceedings of the ASME International Solar Energy Conference 2006*, volume 2006, Denver, CO, 2006.

[111] Elsevier B.V. Scopus: abstract and citation database of peer-reviewed literature, scientific journals, books and conference proceedings (available online: www.scopus.com), 2014.

[112] R. Saidur, M. Rezaei, W.K. Muzammil, M.H. Hassan, S. Paria, and M. Hasanuzzaman. Technologies to recover exhaust heat from internal combustion engines. *Renewable and Sustainable Energy Reviews*, 16(8):5649 – 5659, 2012.

[113] Alberto A. Boretti. Transient operation of internal combustion engines with Rankine waste heat recovery systems. *Applied Thermal Engineering*, 48(0):18 – 23, 2012.

[114] T.A. Horst, W. Tegethoff, P. Eilts, and J. Koehler. Prediction of dynamic Rankine cycle waste heat recovery performance and fuel saving potential in passenger car applications considering interactions with vehicles' energy management. *Energy Conversion and Management*, 78:438–451, 2014.

[115] Daniel Maraver, Javier Royo, Vincent Lemort, and Sylvain Quoilin. Systematic optimization of subcritical and transcritical organic Rankine cycles (ORCs) constrained by technical parameters in multiple applications. *Applied Energy*, 117(0):11 – 29, 2014.

[116] K.J. DiGenova, B.B. Botros, and J.G. Brisson. Method for customizing an organic Rankine cycle to a complex heat source for efficient energy conversion, demonstrated on a Fischer Tropsch plant. *Applied Energy*, 102(0):746 – 754, 2013.

[117] I.K. Smith and R.Pitanga Marques da Silva. Development of the trilateral flash cycle system. part 2: Increasing power output with working fluid mixtures. *Proceedings of the Institution of Mechanical Engineers, Part A: Journal of Power and Energy*, 208(2):135–144, 1994.

[118] P. Boyle, L. Hays, K. Kaupert, and P. Welch. Performance of variable phase cycle in geothermal and waste heat recovery applications. volume 37, pages 679–685, 2013.

[119] T. Ho, S. Mao, and R. Greif. Comparison of the organic flash cycle (OFC) to other advanced vapor cycles for intermediate and high temperature waste heat reclamation and solar thermal energy. *Energy*, 42(1):213 – 223, 2012.

[120] E. Casati, A. Galli, and P. Colonna. Thermal energy storage for solar-powered organic Rankine cycle engines. *Solar Energy*, 96:205 – 219, 2013.

[121] M. Kane, D. Larrain, D. Favrat, and Y. Allani. Small hybrid solar power system. *Energy*, 28(14):1427 – 1443, 2003.

[122] G. Angelino and P. Colonna. Multicomponent working fluids for organic Rankine cycles (ORCs). *Energy*, 23(6):449–463, 1998.

[123] Matthias Lampe, Joachim Groß, and André Bardow. Simultaneous process and working fluid optimisation for Organic Rankine Cycles (ORC) using PC-SAFT. *Computer Aided Chemical Engineering*, 30:572 – 576, 2014.

[124] The Modelica Association. Modelica - A unified object-oriented language for physical systems modeling - Language specification version 3.2 revision 2. Online - www.modelica.org (Last accessed June 2014), July 30 2013.

[125] E. Casati, A. Desideri, F. Casella, and P. Colonna. Preliminary assessment of a novel small CSP plant based on linear collectors, ORC and direct thermal storage. 2012. Proceedings of the 18th SolarPACES conference, Marrakech (MO), 11–14 September.

[126] J. Harinck, T. Turunen-Saaresti, P. Colonna, S. Rebay, and J. van Buijtenen. Computational study of a high-expansion ratio radial organic rankine cycle turbine stator. *Journal of Engineering for Gas Turbines and Power*, 132(5), 2010.

[127] A. Spinelli, M. Pini, V. Dossena, P. Gaetani, and F. Casella. Design, simulation, and construction of a test rig for organic vapors. *Journal of Engineering for Gas Turbines and Power*, 135(4), 2013.

[128] T. Mathijssen, E. Casati, M. Gallo, N.R. Nannan, C. Zamfirescu, A. Guardone, and P. Colonna. Flexible asymmetric shock tube (FAST): Commissioning of a high temperature Ludwieg tube for wave propagation measurements. *Submitted for publication*, 2014.

[129] E. Casati, S. Vitale, M. Pini, G. Persico, and P. Colonna. Centrifugal turbines for Mini-ORC power systems. *Journal of Engineering for Gas Turbines and Power-Transactions of the ASME*, 2014. In print.

[130] D. Seher, T. Lengenfelder, J. Gerhardt, N. Eisenmenger, M. Hackner, and I. Krinn. Waste heat recovery for commercial vehicles with a Rankine process. In 21st *Aachen Colloquium Automobile and Engine Technology, Aachen (DE)*, 2012.

[131] I.H. Bell, E. A. Groll, J. E. Braun, and W. T. Horton. A computationally efficient hybrid leakage model for positive displacement compressors and expanders. *International Journal of Refrigeration*, 36(7):1965 – 1973, 2013. New Developments in Compressor Technology.

[132] A. Giuffrida. Modelling the performance of a scroll expander for small organic Rankine cycles when changing the working fluid. *Applied Thermal Engineering*, (0):–, 2014.

[133] I.K. Smith, N. Stosic, and A. Kovacevic. *Power recovery from low grate heat by means of screw expanders*. Chandos Publishing, 2014.

[134] H. Wang and R.B. Peterson. Performance enhancement of a thermally activated cooling system using microchannel heat exchangers. *Applied Thermal Engineering*, 31(14-15):2951–2962, 2011.

[135] S. Karellas, A. Schuster, and A.-D. Leontaritis. Influence of supercritical ORC parameters on plate heat exchanger design. *Applied Thermal Engineering*, 33-34(1):70–76, 2012.

[136] C. Harris, K. Kelly, T. Wang, A. McCandless, and S. Motakef. Fabrication, modeling, and testing of micro-cross-flow heat exchangers. *Journal of Microelectromechanical Systems*, 11(6):726–735, 2002.

[137] M.M. Ohadi, K. Choo, S. Dessiatoun, and E. Cetegen. *Next Generation Microchannel Heat Exchangers*. Springer, 2013.

[138] K. Boomsma, D. Poulikakos, and F. Zwick. Metal foams as compact high performance heat exchangers. *Mechanics of Materials*, 35(12):1161–1176, 2003.

[139] A. Muley, C. Kiser, B. Sundn, and R.K. Shah. Foam heat exchangers: A technology assessment. *Heat Transfer Engineering*, 33(1):42–51, 2012.

[140] L. Godson, B. Raja, D. Mohan Lal, and S. Wongwises. Enhancement of heat transfer using nanofluids-an overview. *Renewable and Sustainable Energy Reviews*, 14(2):629–641, 2010.

[141] J.G. Cevallos, A.E. Bergles, A. Bar-Cohen, P. Rodgers, and S.K. Gupta. Polymer heat exchangers-history, opportunities, and challenges. *Heat Transfer Engineering*, 33(13):1075–1093, 2012.

[142] C. Sprouse and C. Depcik. Review of organic Rankine cycles for internal combustion engine exhaust waste heat recovery. *Applied Thermal Engineering*, 51(1-2):711 – 722, 2013.

[143] H. Teng, G. Regner, and C. Cowland. Waste heat recovery of heavy-duty Diesel engines by organic Rankine cycle part I: Hybrid energy system of Diesel and Rankine engines. *SAE Technical paper*, 01-0537, 2007.

[144] H. Teng, G. Regner, and Ch. Cowland. Waste heat recovery of heavy-duty Diesel engines by organic Rankine cycle part II: Working fluids for WHR-ORC. *SAE Technical paper*, 01-0543, 2007.

[145] R. Freymann, W. Strobl, and A. Obieglo. The Turbosteamer: a system introducing the principle of cogeneration in automotive applications. *MTZ*, 5:20–27, 2008.

[146] W. Lang, R Almbauer, and P. Colonna. Assessment of waste heat recovery for a heavy-duty truck engine using an ORC turbogenerator. *Journal of Engineering for Gas Turbines and Power-Transactions of the ASME*, 135(4):042313–1–10, April 2013.

[147] T. Endo, S. Kawajiri, Y. Kojima, K. Takahashi, T. Baba, S. Ibaraki, T. Takahashi, and M. Shinohara. Study on maximizing exergy in automotive engines. *SAE Technical Paper*, (2007-01-0257), 2007.

[148] Mitsuo Kadota and K Yamamoto. Advanced transient simulation on hybrid vehicle using Rankine cycle system. Technical report, SAE Technical Paper, 2008.

[149] Sylvain Quoilin, Richard Aumann, Andreas Grill, Andreas Schuster, Vincent Lemort, and Hartmut Spliethoff. Dynamic modeling and optimal control strategy of waste heat recovery organic Rankine cycles. *Applied Energy*, 88(6):2183 – 2190, 2011.

[150] F. Casella, T. Mathijssen, J. van Buijtenen, and P. Colonna. Dynamic modeling of ORC power systems. *Journal of Engineering for Gas Turbines and Power*, 135(042310), 2013.

[151] P.K. Nag. *Power Plant Engineering*. Tata McGraw Hill Education Private Limited, 3rd edition, 2008.

[152] Chan-Chiao Lin, Huei Peng, and Jessy W. Grizzle. Power management strategy for a parallel hybrid electric truck. *IEEE trans. on control systems technology*, 11(6), November 2003.

[153] R. Dettmer. The mighty micro. *Engineering and Technology*, 5(3):42–45, 2010.

[154] Malick Kane. Micro-cogeneration based organic Rankine cycle (ORC) system in a district heating network: A case study of the Lausanne city swimming pool. 2011. ORC2011 - 1st International Seminar on ORC Power Systems - Delft (NL), September 22-23. Available online: www.kcorc.org/en/literature/orc2011-proceedings.

[155] R. Zanelli and D. Favrat. Experimental investigation of a hermetic scroll expander-generator. In W. Soedel, editor, *12th International Compressor Engineering Conference*, pages 459–464, Purdue, USA, 1994.

[156] Faming Sun, Yasuyuki Ikegami, Baoju Jia, and Hirofumi Arima. Optimization design and exergy analysis of organic Rankine cycle in ocean thermal energy conversion. *Applied Ocean Research*, 35(0):38 – 46, 2012.

[157] Min-Hsiung Yang and Rong-Hua Yeh. Analysis of optimization in an OTEC plant using organic Rankine cycle. *Renewable Energy*, 68(0):25 – 34, 2014.

[158] A. Schuster, S. Karellas, E. Kakaras, and H. Spliethoff. Energetic and economic investigation of organic Rankine cycle applications. *Applied Thermal Engineering*, 29(8-9):1809–1817, 2009.

[159] B.F. Tchanche, G. Lambrinos, A. Frangoudakis, and G. Papadakis. Low-grade heat conversion into power using organic Rankine cycles - A review of various applications. *Renewable and Sustainable Energy Reviews*, 15(8):3963–3979, 2011.

[160] Fredy Vélez, José J. Segovia, M. Carmen Martín, Gregorio Antolín, Farid Chejne, and Ana

Quijano. A technical, economical and market review of organic Rankine cycles for the conversion of low-grade heat for power generations. *Renewable and Sustainable Energy Reviews*, 16(6):4175 – 4189, 2012.

[161] L. Wang, A.P. Roskilly, and R. Wang. Solar powered cascading cogeneration cycle with ORC and adsorption technology for electricity and refrigeration. *Heat Transfer Engineering*, 35(11-12):1028–1034, 2014.

[162] M. Jradi and S. Riffat. Modelling and testing of a hybrid solar-biomass ORC-based micro-CHP system. *International Journal of Energy Research*, 2013. Article in Press.

[163] M. Astolfi, L. Xodo, M.C. Romano, and E. Macchi. Technical and economical analysis of a solar-geothermal hybrid plant based on an organic Rankine cycle. *Geothermics*, 40(1):58–68, 2011.

[164] S. Quoilin, M. Orosz, H. Hemond, and V. Lemort. Performance and design optimization of a low-cost solar organic Rankine cycle for remote power generation. *Solar Energy*, 85(5):955–966, 2011.

[165] G. Angelino and P. Colonna. Air cooled siloxane bottoming cycle for molten carbonate fuel cells. In *Fuel Cell Seminar*, pages 667–670, October 2000.

[166] C. De Servi, S. Campanari, A. Tizzanini, and C. Pietra. Enhancement of the electrical efficiency of commercial fuel cell units by means of an organic Rankine cycle: A case study. *Journal of Engineering for Gas Turbines and Power*, 135(4), 2013.

[167] A.V. Akkaya and B. Sahin. A study on performance of solid oxide fuel cell-organic Rankine cycle combined system. *International Journal of Energy Research*, 33(6):553–564, 2009.

[168] F.A. Al-Sulaiman, I. Dincer, and F. Hamdullahpur. Energy analysis of a trigeneration plant based on solid oxide fuel cell and organic Rankine cycle. *International Journal of Hydrogen Energy*, 35(10):5104–5113, 2010.

[169] R. Chacartegui, D. Snchez, J.M. Mu noz, and T. Sánchez. Alternative ORC bottoming cycles for combined cycle power plants. *Applied Energy*, 86(10):2162 – 2170, 2009.

[170] K. Kusterer, R. Braun, L. Köllen, T. Sugimoto, K. Tanimura, and D. Bohn. Combined solar thermal gas turbine and organic Rankine cycle application for improved cycle efficiencies. In *Proceedings of the ASME Turbo Expo*, volume 4, San Antonio - Texas, USA, 3-7 June 2013.

[171] M.T. Dunham and B.D. Iverson. High-efficiency thermodynamic power cycles for concentrated solar power systems. *Renewable and Sustainable Energy Reviews*, 30:758–770, 2014.

[172] Donald L. Nored and Daniel T. Bernatowicz. Electrical power system design for the US space station. In *Proceedings of the Intersociety Energy Conversion Engineering Conference*, pages 1416–1422, 1986.

[173] F. Farina, C. Mao, and G. Tuninetti. Organic Rankine cycle power conversion systems for space applications. In *Photovoltaic Generators in Space, Proceedings of the Fifth European Symposium*, pages 225–230. European Space Agency, (Special Publication) ESA SP, 1987.

3

Centrifugal Turbines for ORC Applications

Part of the contents of this chapter appeared in:

M. Pini, G. Persico, E. Casati, & V. Dossena
J Eng Gas Turb Power, **135**(4), pp. 042312 – 1 – 9 (2013)

E. Casati, S. Vitale, M. Pini, G. Persico, & P. Colonna
J Eng Gas Turb Power, **136**(12), pp. 122607 – 1 – 11 (2014)

Abstract *A critical component in designing efficient ORC plants is the expander, which is typically a turbine. The variety of possible working fluids, the complex gas dynamic phenomena encountered, and the lack of simplified design methods based on previous experience on similar machines make the design of efficient ORC turbines a complicated task. Relevant paths of research may thus be concerned with (i) the development of generalized design methodologies, and (ii) the assessment of non-conventional machine architectures: this chapter explores both. In particular, the first critical evaluation of the centrifugal or radial-outflow turbine (ROT) architecture as a candidate technology for ORC turbo-generators is presented.*

In the first part of the chapter, starting from basic turbomachinery theory, all the special features involved in ROTs design are enlightened. The main findings being that, in order to design efficient centrifugal turbines, particularly for low power output applications, it is needed that (i) the blade discharge geometric angles, the radial chords, the stage expansion ratios, and the reaction degrees are allowed to vary among each cascade, and (ii) the diameter and the speed of revolution are included among the optimization variables. It is discussed how simplifying assumptions usually adopted in the axial turbines practice are typically not applicable. A novel design methodology is derived and presented for the preliminary sizing of ROTs in the power size range from several MW_E *down to few* kW_E*, i.e., covering most of the applications foreseen today. An original in-house mean-line code coupled to an external optimizer is developed, which allows to determine the preliminary design of ORC turbines of various configurations and working with different fluids. This tool, named* zTurbo*, is adopted to verify the novel method by presenting several exemplary design exercises.*

The second part of the chapter deals with the design of centrifugal machines with 1 MW_E *power output, handling expansion ratios of the order of 60, and rotating at 3000 rpm, thus representative of present industrial applications. Several simplifications derived from the axial-turbines practice are adopted in order to illustrate their consequences. The design of two different turbines is performed with* zTurbo*, a transonic six-stage and a supersonic three-stage ones. It is confirmed that the adopted simplifications lead to unwanted design features, such as converging meridional channels and large flaring angles on the last stages. The predicted fluid-dynamic efficiency for the transonic and the supersonic machine is around 86% and 81%, respectively.*

The third part of the chapter focuses on the assessment of the down-scaling potential of the ROT architecture, considering its implementation in the promising field of mini-ORC turbogenerators. The novel design methodology is applied to the sizing of two 10 kW_E *ROTs, handling an expansion ratio of 45: a 5 stages transonic, and a 3 stages slightly supersonic ones. The proposed design procedure proves valuable in sizing machines with a meridional channel which monotonically diverges maintaining maximum flaring angles lower than 10°. The resulting turbines are projected to exceed a fluid-dynamic efficiency of 79% and 77%, with speed of revolution around 124000 and 15400 rpm, respectively.*

The results show that the ROT architecture is a promising concept for future ORC power systems, which allows for the realization of efficient, compact, and reliable expanders down to a power output of few kW_E*. However, the design of these machines presents several criticality which are unveiled here for the first time.*

3.1 Introduction

As anticipated in Ch. 2, ORC power systems have been demonstrated to be advantageous compared to steam Rankine cycles for a number of applications: this is mainly a consequence of the increase of specific cost of turbomachinery as the scale of the plant reduces. The use of organic fluids, char-

acterized by high molecular weight, make available cost-effective solutions for the turbo-expander [1–4]. The specific enthalpy drop along the turbine expansion line is inversely proportional to the molecular weight of the fluid. This determines two main advantages in case of organic fluids: primarily the relatively small specific work can be disposed in a low number of stages; secondarily, for a target power output, a relatively large mass flow rate is required, resulting in an enlarged size of small-capacity ORC turbines with respect to steam units [2]. On the other hand, the low number of stages leads to high expansion ratios per stage; this, combined with the low speed of sound, leads to the widespread application of transonic and supersonic turbines in ORC systems. As a result, highly dissipative systems of shock waves are commonly found in these machines, complicating their design and the performance of the whole system, particularly during part-load operations [5, 6]. Moreover, part of the expansion process usually occurs in close proximity of the saturated vapour curve, or even close to the critical point. In such thermodynamic conditions complex equations of state are necessary to accurately describe the working fluid behaviour. This design scenario is further complicated by the lack, in the open literature, of experimental data regarding flows of organic fluids [7, 8], specially in the thermodynamic region of interest.

The most successful commercial applications of ORC power plants have been deployed in the power size ranging from hundreds of kW_E up to approximately 5 MW_E, and these systems represent now the state of the art of the ORC technology. Nonetheless, since the first examples of implementation, the ORC technology proved suitable for the conversion of thermal energy into electricity for very low power capacity, down to few kW_E [1, 2, 9]. These small systems are often referred to as mini-ORC (*m*ORC) power plants, and many researchers are still investigating the development of *m*ORC modules, see e.g. Ref. [10] Furthermore, depending on the application, i.e. mainly the temperature levels of the thermal source and of the rejection sink, different working fluids are available in order to better suit the (often conflicting) design requirements [1–4].

Concluding, the potentially infinite variety of power-output and adopted working fluids, together with the thermo- and fluid-dynamic operating conditions typically encountered, make the design of efficient ORC turbines a challenging topic. Furthermore, simplified design methods based on statistical information on similar existing machines are not yet available. Relevant paths of development may be concerned with the development of generalized design methodologies, and the assessment of non-conventional machine architectures: this chapter explores both.

The original in-house mean-line code *zTurbo*, developed to perform the preliminary design of ORC turbines, is described in §3.2. The concept of centrifugal turbine, and its application to ORC power modules are discussed in §3.3. An in-depth analysis of the specific features of centrifugal turbines is thus performed and, in §3.4, it is shown how the relation between the design assumptions and the resulting machine features differs from the axial arrangement. A novel and general methodological framework is developed and presented, which may be of support to the designer of radial-outflow turbines of any power output. The design of several exemplary centrifugal machines is thus presented. Comparably large size centrifugal machines, i.e. in the MW_E power-output range, are dealth with in §3.5, following the work on the same topic published in Ref. [11]. Similarly, §3.6 investigates in detail the down-scaling potential of the radial-outflow turbine architecture, considering its implementation in the 10 kW_E power-output range, following the work on the same topic published in Ref. [12].

3.2 Preliminary Design Method

The preliminary design of a turbine is the phase in which the fundamental machine features, such as the number of stages, the velocity triangles, the speed of revolution, and the blading geometry, are selected. As detailed in the seminal work of Macchi [5], this step is fundamental particularly if no previous experience is available regarding the specific machine to be designed. In other words, although advanced design methods based on computational fluid-dynamics constitute a precious help for the designer, they can yield high turbine performance only if the boundary conditions established in the preliminary design phase allow for it [5]. This is often obtained for conventional turbines by making use of simple rules based on statistical information on existing similar machines [13]. As anticipated, since this is generally not available when designing an expander for an ORC power system, a more general approach must be followed. In particular, a simultaneous optimization process accounting for all the main variables affecting the turbine efficiency is desirable: this is typically achieved by resorting to so-called 0-D mean-line methods [14]. Several studies reported a good agreement between the results of such calculations and measurements, if reliable loss and flow angle correlations are applied [15–17].

The mean-line design code *zTurbo*, specifically conceived for ORC turbines and developed within the present research, is described in §3.2.1. *zTurbo* has been thus introduced in an optimization procedure, in order to automatically determine the optimal design features of the machines, depending on the designer's objective, as detailed in §3.2.2.

3.2.1 Mean-line Design Tool for ORC Turbines

The main aim of this code, whose development has been directly contributed by the author, is to provide a preliminary machine design without any limitation on the adopted working fluid, flow regime, and architecture: axial, radial-inflow, and radial-outflow turbine arrangements can be designed with *zTurbo*. The code is coupled with the *FluidProp* software library, allowing for an accurate evaluation of the working fluid thermophysical properties [18]. The balance equations for mass, energy, and momentum, alongside a loss model to evaluate entropy generation, are written in a generalized formulation, and both subsonic and supersonic flows are properly treated in the stationary and rotating frames of reference. The calculation scheme of a single turbine stage, as performed by *zTurbo*, is briefly summarized in the following:

1. At the beginning, the total upstream thermodynamic conditions, the stage expansion ratio, and the mass flow rate are provided as external inputs (e.g. as outputs of the thermodynamic cycle optimization). This is the case also for several geometric quantities related to manufacturing limits (e.g. trailing-edge thickness, hub/tip clearance, and stator/rotor gap). The values of several design variables are thus initially assumed, among others: the rotational speed, the reaction degree, the blades chords and outlet geometric angles, and the channel minimum width (throat dimension).

2. By assigning the stage reaction degree, the stator outlet velocity and the corresponding isoentropic Mach number can be calculated. If the flow is supersonic, for instance, isentropic expansion is assumed from the inlet section where total conditions are given (e.g. pressure $P_{T,in}$ and temperature $T_{T,in}$), up to the choked throat where sonic conditions are

attained. The system of equations accordingly implemented is

$$\begin{cases} s = s(p_{\mathrm{T,in}}, T_{\mathrm{T,in}}) \\ h_{\mathrm{th}} = h_{\mathrm{T,in}}(p_{\mathrm{T,in}}, T_{\mathrm{T,in}}) - \frac{1}{2} c(h_{\mathrm{th}}, s)^2 \\ \dot{m} = \rho_{\mathrm{th}}(h_{\mathrm{th}}, s) \cdot c(h_{\mathrm{th}}, s) \cdot A_{\mathrm{th}} \ , \end{cases} \tag{3.1}$$

where s is the specific entropy, and the subscript 'th' indicates the (static) thermodynamic conditions in the throat section. Solving the continuity equation appearing in system (3.1), the throat flow passage area A_{th} can be evaluated and, if the throat width is assigned, the blade height can be computed. On the contrary, if subsonic flow occurs at the outlet section, the thermodynamic conditions are obtained by solving the balance equations for the mass and the momentum in the tangential direction, between the geometric throat and the downstream non-bladed zone, as detailed in Ref. [17]. In both cases the flow angle is calculated starting from the blade geometric angle (BDA) by applying a proper deviation correlation. The blade number is evaluated by applying the Zweifel load criterion [19], which provides the optimal solidity as a function of the flow deflection across the cascade. It should be noted that a proper selection of solidity and blade loading would need a specific aerodynamic optimization, which is beyond the intrinsic limitations of a mean-line approach.

3. The initial isentropic design represents the first guess for an iterative procedure to estimate the cascade losses. Several loss-prediction methods are available within *zTurbo*, such as those proposed by Ainley & Mathieson [20], Craig & Cox [15], and Traupel [21]. Alternatively, user-defined loss coefficients can be specified. The estimation of losses allows to correct the flow velocities and the blades height previously estimated (see point 2 above). The choice of a suitable model is critical, since its accuracy becomes questionable for flow conditions departing from the validity range of the method [22]. In the case at hand, the situation is further complicated by i) the fact that the machine arrangement is not axial, ii) the different fluids and thermodynamic operating conditions, iii) the onset of post-expanded and supersonic flows, and vi) the possibly low scale dimensions of the machines, that may induce a stronger interaction among different loss mechanisms (e.g., profile and tip-leakage losses) which is unlikely to be properly captured by the models.
4. A similar methodology (i.e. points 1 to 4), implementing the conservation of rothalpy, is employed for the calculation across the rotor in the rotating frame of reference.

The outputs of the procedure outlined above (relative to a single stage) are: i) the velocity diagrams, ii) the meridional channel shape, and iii) the performance parameters (efficiency, loss coefficients, etc.). For multi-stage turbines, such procedure is applied stage-by-stage, assuming a value for the number of stages. The repartition of the expansion among the stages is a critical aspect, particularly when dealing with turbines elaborating large expansion ratios with few stages [5].

3.2.2 Optimization Procedure

The methodology described in §3.2.1, once implemented in the framework of an optimization procedure, allows to search for the optimal machine design [5, 23]. The optimization of a turbomachinery is typically aimed at the maximization of its fluid-dynamic efficiency, which may be formulated in general terms as:

$$\eta_{\mathrm{T}\chi} = f(\Psi, \phi, M, Re, sh, \chi) = \frac{\Delta w}{\Delta h_{\mathrm{TS}} - \chi \frac{C_{\mathrm{out}}^2}{2}} \ , \tag{3.2}$$

The subscript 'Tχ' clarifies that the ideal total-to-static enthalpy drop used to calculate the efficiency is reduced by a fraction (in the range $0 < \chi < 1$) of the discharge kinetic energy, supposing this can be recovered downstream of the last stage. In other words, $\eta_{T\chi} = \eta_{TT}$ if $\chi = 1$, and $\eta_{T\chi} = \eta_{TS}$ if $\chi = 0$; the choice of a value for χ has a deep influence on the turbine design, as shown in Ref. [5]. The functional dependence of η from the work and flow coefficients Ψ and ϕ, and the Mach and Reynolds numbers M and Re, is expressed by the first equality in Eq. (3.2). This dependence includes also the term sh, synthetically indicating the turbine shape and accounting for the influence of geometrical parameters such as the solidity, the blade angles, the ratio of the trailing-edge thickness and of the tip clearances with respect to the blade chord, etc. From a mathematical point of view, several main aspects have to be taken into account: i) the definition of a suitable objective function to be maximized or minimized, ii) the independent variables and their range of variation within the design space, iii) the geometrical and fluid-dynamics constraints bounding the space of solutions, and iv) the algorithm to be used to search the design space for the optimal solution.

In this chapter the efficiency defined in Eq. (3.2) is chosen as the objective function, with $\chi = 0.5$. This assumption implies that a diffuser is used downstream of the last rotor, and is able to recover half of the kinetic energy of the exiting flow. Concerning the optimization strategy, a flexible and non-intrusive approach is desirable in order to leave to the user the choice of the independent variables, the constraints, and the search algorithm. Therefore, *zTurbo* is coupled to a well known open source external optimization software *Dakota* [24]. An evolutionary optimization strategy, based on a single-objective genetic algorithm, is adopted in the present analysis. For a single objective optimization, the application of a gradient-based algorithm would require a lower computational effort. However, due to the possibly highly non-regular behavior of the fitness function, local optima may be found during the search. Genetic algorithms span the whole design space, and have therefore the advantage of being more robust under this respect, proceeding towards the global optimum [25].

In particular, the adopted optimization method is the single objective version of the multi-objective elitist genetic algorithm proposed in [26] and implemented in [24], based on binary encoding and dynamic memory allocation.

3.3 Centrifugal Architecture for ORC applications

Some critical challenges encountered in the design of efficient vapour turbines are a consequence of the large variation of the volumetric flow rate over the expansion. The low speed of sound characterizing ORC working fluids further complicates the design of the expander, leading to supersonic regime within the flow passages [5]. In the centrifugal architecture, the fluid enters the machine close to the rotational axis, and flows outward in the radial direction (see fig. 3.1). This is advantageous primarily because it provides a natural increase of the passage area along the flow path. Another major advantage is the possibility of implementing multi-stage arrangements in a comparatively easy way [27, 28]. The counter-rotating centrifugal steam turbine was proposed by Ljüngstrom in the early 20th Century and widely adopted until the Sixties [29]. The limits of the Ljüngstrom turbine emerged for large-capacity machines, resulting in a maximum power capacity of about 65 MW_E per unit. This is mainly due to the difficulty, for larger output, of elaborating the corresponding volumetric flow rates in a single-casing arrangement. Eventually, the requirement of two counter-rotating electrical generators determined the success of the axial-flow concept [29]. Notably, none of these issues applies in the ORC context and, as such, several studies have discussed the potential merits of these machines in this field [5, 30, 31]. These characteristics have recently driven also the industrial interest towards centrifugal ORC turbines, which have been thus

successfully introduced in the market. Summarizing:

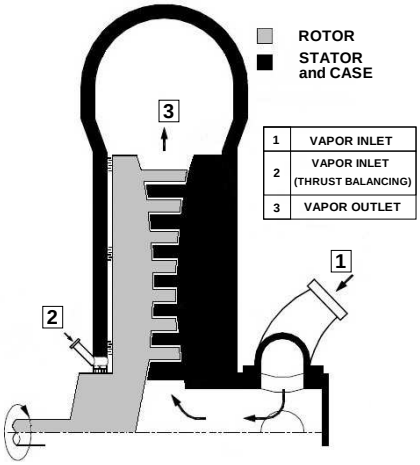

Figure 3.1: Centrifugal turbine schematic, adapted from [32]

1. The low specific expansion work typical of ORC fluids allows to i) adopt the stator-rotor arrangement (radial sequence of stators and rotors), and ii) maintain a relatively low peripheral speed, which is typically well below the mechanical stress limit.
2. The peripheral speed of the blades does not change along the blade span, and no radial equilibrium establishes in the span-wise direction [16]. This results in a design and manufacturing simplification, since the velocity diagrams can be chosen such that the reaction degree and work coefficient at midspan are optimal. These conditions are maintained all along the span of the (untwisted) blades. Notably, a mean-line method is thus expected to yield more accurate predictions in this case.
3. The relatively small temperature variation across an ORC turbine, typically of the order of 100 ^{o}C), makes the thermal gradient acting on adjacent blade rows far less critical than in steam machines; as a result, all blade rows can be installed as well as machined on the same disk.
4. Full admission inlet stages can be adopted: the first rows, characterized by a low volumetric flow rate, can be placed where the rotor diameter is smaller, thus allowing for comparatively larger blade height. The simplicity of the multi-stage assembly allows to maintain tight clearance between moving parts, thus reducing leakages. In addition, disc-friction losses are comparatively low.

Notably, these last aspects regard loss mechanisms which are particularly severe for small turbines[2, 9, 27].

3.4 Analysis of the Centrifugal Architecture

An in-depth analysis of the specific features of centrifugal turbines is performed here, following Ref. [12]. The aim of the treatment is, starting from the design procedures proposed in the literature,

to derive a novel methodological framework which may be of support to the designer. It is in fact shown how, in the general case, the relation between the design assumptions and the resulting machine features differs from the axial arrangement case. This, in turn, makes the development of design procedures specific for the radial-outflow turbine architecture necessary, in particular as the machine power output is reduced.

Most of the available works on the subject of radial-outflow centrifugal turbines (ROTs) deal with the design of large power output machines and, usually, simplified procedures are borrowed from the vast literature available in the field of axial turbines, lacking specific treatments. A typical assumption is therefore that all the rows feature the same geometrical blade discharge angles (BDA) [11, 27, 28, 32]. Referring to Fig. 3.2, this implies that, for all the N stages of the machine, the

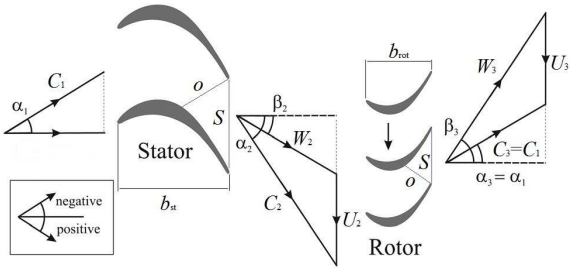

Figure 3.2: Schematic of the two-dimensional flow through a turbine stage of the repeating type. All the rows feature the same geometrical angles (BDA). The peripheral velocity is assumed to be constant along the machine, i.e., $U_2 \overset{N}{=} U_3$. The stage reaction degree is 0.5, and the velocity triangles are thus symmetrical. The sign convention for the flow angles is also reported, adapted from [22]

following holds

$$\alpha_1 \overset{N}{=} -\beta_2, \text{ and } \alpha_2 \overset{N}{=} -\beta_3. \tag{3.3}$$

Usually also the blade chords are kept equal, i.e.

$$b_{st} \overset{N}{=} b_{rot}. \tag{3.4}$$

Other simplifying assumptions are commonly introduced regarding the distribution of the total expansion among the stages, and among stator and rotor in each stage (i.e. the stage degree of reaction R). For instance, these quantities can be kept constant among the stages, i.e.,

$$\left(\frac{p_{out}}{p_{in}}\right)_{stg} \overset{N}{=} \left(\frac{p_{out}}{p_{in}}\right)_{total}^{1/N}, \tag{3.5}$$

$$R \overset{N}{=} a, \text{ with } (0 < a < 1). \tag{3.6}$$

Eq. 3.5 indicates that the total load is divided such that each stage features the same expansion ratio. Similarly, Eq. 3.6 bounds the value of the stage reaction to be the same for all the stages. A typical design choice in the case of axial turbine stages is to impose that the reaction degrees is around 50% ($a = 0.5$ in Eq. 3.6), i.e., a value ensuring close-to-optimal stage efficiency [17], Eq. 3.3. By assuming that the variation of the mean-line peripheral velocity is negligible and that the axial

velocity component conserves throughout the expansion, the so-called repeating-stage arrangement is obtained, see, e.g., Fig. 3.2. Repeating stages are usually characterized by similar stator and rotor blades, namely

$$\alpha_3 \overset{N}{=} \alpha_1, W_3 \overset{N}{=} C_2, W_2 \overset{N}{=} C_3. \tag{3.7}$$

Notably, these conclusions rest on assumptions that can only be partly realized in radial machines, since the peripheral speed varies in the stream-wise direction. Proper design rules are therefore to be established if centrifugal turbine arrangements are of interest. Even if the constraints imposed by the repeating stage approach are neglected, radial outflow machines dimensioned on the basis of common axial turbine design criteria, i.e., fulfilling Eq. 3.3, 3.4, 3.5, and 3.6, may show i) different velocity triangles per-stage, notwithstanding the geometrical similarity of the stages, and ii) a characteristic meridional channel shape, which tends to be convergent in the first stages while becoming divergent in the last stages, see, e.g., § and Refs. [11, 32].

A converging-diverging meridional shape of the flow channel is typically an undesirable feature, particularly in case of mini-ORC turbines, since i) the blade height might already be insufficient at the inlet (a full-admission first stage is preferable as far as efficiency is concerned), and ii) large variations of the meridional channel lead to span-wise velocity components which, even though not captured by a mean-line analysis, deteriorate the performance of the turbine.

In a radial turbine, contrary to what happens in axial turbines, the stage chord has an influence on the distribution of the stage diameters along the machine, and thus on the work extraction process. This is in turn governed by the variation of peripheral speed, being

$$D_{\text{out}} = D_{\text{in}} + b, \tag{3.8}$$

$$w \propto U^2 = \omega^2 \, D_{\text{out}}^2. \tag{3.9}$$

This feature has an impact also on the variation of the volumetric flow rate, and consequently of the flow passage area A_{out} needed to accommodate the flow along the expansion. For instance, by applying the continuity equation to the outlet section of the bladed region of a subsonic row, see, e.g., Fig. 3.2, such area may be expressed as

$$A_{\text{out}} = H_{\text{out}} \, o = \frac{\dot{m}}{\rho_{\text{out}} \, V_{\text{out}} \, N_{\text{blds}} \, \epsilon}, \tag{3.10}$$

where H_{out} and o are the blade height and the channel outlet section width (normal to the flow) at the outlet of the channel, respectively, and V_{out} is the corresponding flow velocity magnitude. N_{blds} is the number of blades, while ϵ accounts for possible correction factors (e.g., that for blocking effects due to the boundary layer or the blade section). Assuming a rectilinear suction blade end-side, the relation among the outlet section width o and the blade geometric discharge angle BDA is expressed as

$$o = S \, cos(\text{BDA}), \tag{3.11}$$

where the blade pitch S is evaluated according to the equation

$$S = \pi \, D_{\text{out}} \, N_{\text{blds}}^{-1}. \tag{3.12}$$

Finally, in order to express the blade height H_{out}, Eq. 3.10 may be rearranged into

$$H_{\text{out}} = \frac{\dot{m}}{\rho_{\text{out}} \, V_{\text{out}} \, cos(\text{BDA}) \, D_{\text{out}} \, \pi \, \epsilon}. \tag{3.13}$$

This last variable greatly affects the meridional channel shape, which may be characterized by the so-called flaring angle δ, i.e., the ratio between the blade height at the outlet and at the inlet of a given row. Assuming a constant span among subsequent rows, the blade height at every row inlet may be specified as equal to that at the outlet of the previous row, i.e., for every row 'i' apart for the first stator (for which i=1), the equality $H_{in}^{i} = H_{out}^{i-1}$ holds. This leads to the following expression for the flaring angle of the i^{th} row

$$\delta^{i} \approx \left.\frac{H_{out}}{H_{in}}\right|^{i} \propto \underbrace{\frac{\rho_{out}^{i-1}}{\rho_{out}^{i}}}_{A} \cdot \underbrace{\frac{V_{out}^{i-1}}{V_{out}^{i}}}_{B} \cdot \underbrace{\frac{cos\left(BDA^{i-1}\right)}{cos\left(BDA^{i}\right)}}_{C} \cdot \underbrace{\left(\frac{D_{in}}{D_{in}+b}\right)^{i}}_{D}. \tag{3.14}$$

Terms A and B in Eq. (3.14) are determined by the expansion process across the machine, i.e., by the distribution among the stages of the loading and of the reaction degree R. If simplifying assumptions are adopted, by assigning, for instance, common values to every stage as in Eqs. 3.6 and 3.5, both A and B may be considered approximately the same for all the stages. Referring to Fig. 3.2, and using V to indicate the velocity magnitude of the flow discharged by a generic row, it can be noted that $V_{out}^{i} = C_{out}^{i}$ and $V_{out}^{i-1} = W_{out}^{i-1}$ if the i^{th} row is a stator. Conversely, $V_{out}^{i} = W_{out}^{i}$ and $V_{out}^{i-1} = C_{out}^{i-1}$ if the i^{th} row is a rotor. This implies that, if the reaction degree in around 0.5, $B \approx 1$, being $C_{out}^{i} = W_{out}^{i-1}$ for a stator, and $W_{out}^{i} = C_{out}^{i-1}$ for a rotor. Hence, the influence of term B on δ vanishes. In radial-outflow turbines B tends to be lower than one as a consequence of the increasing peripheral speed that, in turn, increases also the rotor outlet velocity. This fact can be handily explained by resorting to the energy balance in the relative frame of reference, which states the conservation of rothalpy rt across the rotating cascade, i.e. referring to Fig. 3.2

$$rt = h_2 + \frac{{W_2}^2}{2} - \frac{{U_2}^2}{2} = h_3 + \frac{{W_3}^2}{2} - \frac{{U_3}^2}{2}, \tag{3.15}$$

which leads to

$$W_3 = W_{out}^{i} = V_{out}^{i} = \sqrt{2(rt - h_3 + \frac{{U_3}^2}{2})}. \tag{3.16}$$

Compared to an axial stage having the same features, i.e., the same stator outlet velocity V_{out}^{i-1}, inlet rothalpy and expansion ratio (which leads to a similar value of static outlet enthalpy h_3), a centrifugal stage is affected by a greater W_3 due to the larger kinetic term $U_3^2/2$, In these conditions B has an adverse effect on the flaring angle, and this can be compensated only by acting on the other terms of Eq. (3.14).

Regarding term C, assuming that all the blades have the same value of BDA according to Eq. 3.3, the equality $C = 1$ is obtained. The meridional channel shape becomes therefore primarily a function of terms A and D.

The quantity represented by term D, i.e., the row diameters ratio, is plotted against the row inlet diameter in Fig. 3.3, considering different values of the radial chord. It can thus be seen how, for radial stages placed at progressively larger diameters, D tends to unity, i.e., its potential influence on δ vanishes. In other words, as expected, centrifugal stages characterized by small values of the ratio b/D_{in} tend to behave like axial stages, with the chord size having little influence in determining the meridional channel shape, which is rather determined by the expansion process, i.e., by term A in Eq. (3.14). This is the case of the ROTs described in Ref. [28], and proposed for Rankine cycle power systems working with potassium and ranging in size from 20 up to 200 MW_M. In the case small of ROT's, however, the low mass flow rate leads to comparatively large b/D_{in} ratios, due primarily to the need of obtaining acceptable blade height at the turbine inlet. The design is therefore

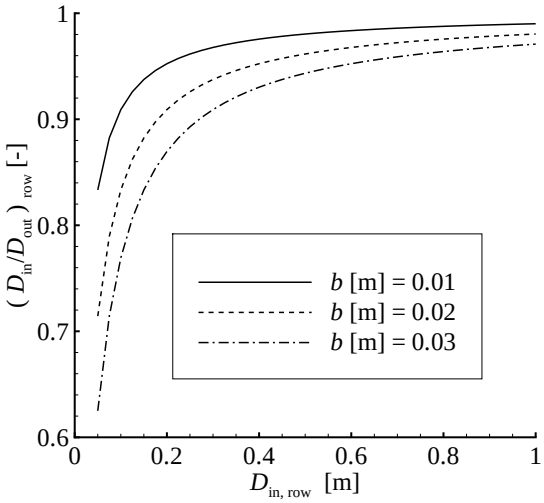

Figure 3.3: Diameters ratio for a centrifugal row $(D_{in}/D_{out})_{row}$, i.e. term D in Eq. (3.14), as a function of the row diameter $D_{in,\,row}$ and of the radial chord b.

likely to include rows characterized by a $(D_{in}/D_{out})_{row}$ value smaller than unity, i.e., $D < 1$, see Fig. 3.3. For this condition, if the simplifying design assumptions previously described are adopted, a convergent meridional channel is likely to be obtained since $A, B \approx$ const. and $C \approx 1$. This is the case of the preliminary fluid dynamic designs presented in §3.5, and of the 240 MW_M ROT described in Ref. [32]. As anticipated, however, this is not a suitable solution, specially for small power-output machines. The present treatment demonstrates therefore that, although useful in reducing the complexity of the preliminary design, the simplifying assumptions usually adopted, e.g. Eqs. 3.3-3.6, are not applicable in general in the ROT field. A novel design methodology is thus necessary, following two main guidelines, i.e.

1. the blade discharge geometric angles, the radial chords, the stage expansion ratio, and the reaction degrees are allowed to vary among each cascade,
2. the diameter and the speed of revolution are included among the optimization variables.

In particular, this last choice stems from the difficulty of providing an *a priori* estimation for the design quantities at hand, e.g. based on statistical information regarding existing machinery, as done in the turbomachinery practice [13, 33]. As a consequence, all the afore-mentioned quantities add to the independent variables involved in the optimization problem. This will be discussed further, with the help of several examples, in the next sections.

3.5 Design of Exemplary 1 MW_e Machines

The purpose of this section is to clarify the procedure presented in §3.4, by performing the design of two exemplary centrifugal turbines in the MW_E power-output range. The tool adopted for the preliminary design is the in-house software *zTurbo*, presented in §3.2.1. The treatment follows the

work documented in Ref. [11], which constitutes also the first published investigation of the use of the ROT architecture in the ORC field. The main design assumptions adopted are detailed in §3.5.1.

3.5.1 Design Assumptions

The results of the thermodynamic cycle analysis provide the needed inputs to the turbine preliminary design procedure. Operating conditions typical of an industrial high-temperature ORC turbogenerator are considered here. The main characteristics of this cycle, resumed in Tab. 3.1, are common to all the machines designed in the present section. The working fluid is siloxane MDM, whose T–s diagram is represented in Fig. 3.4. The outlet pressure corresponds to a condensation temperature of about 95 °C, which frequently occurs in ORC power plants co-generating electricity and thermal power to be used, e.g., for district heating. The mass flow rate value is imposed in order to obtain a power-output close to the target one of about 1.2 MW_M. It can be noted that the first

Fluid	MDM
$\dot{m}_{flow}$ [kg s^{-1}]	22
$T_{T,in}$ [°C]	274
$p_{T,in}$ [bar]	10
z_{in}	0.61
p_{out} [bar]	0.17
$\frac{p_{T,in}}{p_{out}}$	59
$\frac{\dot{V}_{out}}{\dot{V}_{in}}\Big\vert_s$	85

Table 3.1: Thermodynamic cycle parameters assumed for the preliminary design of the turbines presented in this section, after [11]. The last two terms indicate the pressure and the isoentropic volumetric flow rate ratios across the turbine expansion. The working fluid is siloxane MDM (octamethyltrisiloxane, $C_8H_{24}O_2Si_3$): MW = 236.53 [g mol^{-1}], T_{CR} = 290.9 [°C], p_{CR} = 14.15 [bar], ρ_{CR} = 302.9 [kg m^{-3}].

part of the expansion takes place in the so-called dense gas region, where the compressibility factor is significantly lower than unity, i.e. $z_{in} < 1$. In these conditions relevant real gas effects occur, and accurate thermodynamic models must be adopted in order to obtain a meaningful turbine design [6]. As anticipated, the software library presented in Ref. [18] is adopted to this end.

As a common feature of comparatively low-output power generating systems, ORC turbogenerators are likely to work in off-design conditions for a large part of their operative life-time. Thus, preserving a reasonably good turbine efficiency in a wide operating range is of paramount importance. This can be better accomplished by using transonic or slightly supersonic machines, i.e. with maximum flow Mach numbers lower than approximately 1.4. Additionally, the condition of subsonic flow at the rotors inlet (in the relative frame of reference) is imposed. These configurations, where the stages can be constituted of converging-only blades, are able to handle load variations by adapting to the new conditions through post-expansion phenomena. If the load change produces a post-expanded flow with Mach number not exceeding about 1.4, the induced efficiency losses are comparatively limited [17]. On the contrary, if Mach numbers larger than 1.4 are attained already in design conditions, the onset of dissipative shock patterns is expected to strongly affect the turbine

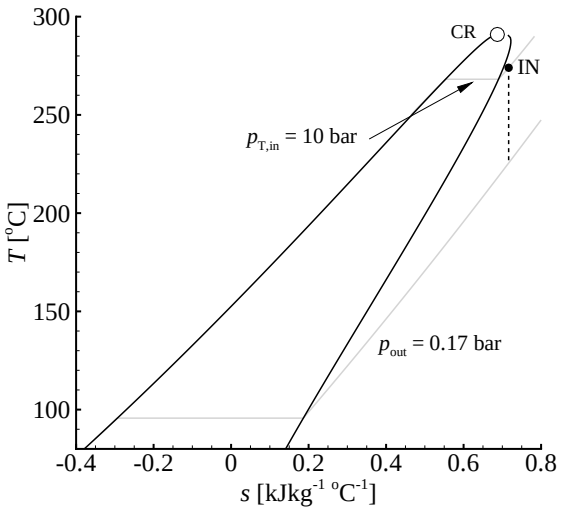

Figure 3.4: Saturation curve of siloxane MDM in a T-s diagram, showing the thermodynamic boundary conditions for the turbine design, i.e. the inlet total conditions, point IN, and the discharge pressure. Point CR indicates the liquid-vapour critical point of the fluid.

efficiency, in particular during off-design operations [6, 17]. However, the choice of dealing with highly supersonic flows is typically justified by the opportunity of minimizing the number of stages [9]. As mentioned in §3.3, however, the adoption of the centrifugal architecture allows to increase the number of stages with relative ease, thus relaxing this constraint.

Therefore, all the machines whose design is proposed in the following belong to one of these general classes, i.e., they are either transonic or slightly supersonic ones. To this end, it is possible to tentatively vary the number of stages, or to include also this among the optimization variables. In the present case, the designs of a subsonic six-stage turbine, and of a three-stage transonic one featuring supersonic post-expanding flows are presented.

The losses-estimation method proposed by Craig & Cox is adopted here [15], see §3.2.1, and the only losses modelled are the profile, and the secondary ones.

3.5.2 Design Methodology

The variables and parameters involved in the design are collected in Tab. 3.2, see also §3.2.1. Primarily, the rotational speed ω is constrained to the value of 3000 rpm, in order to directly couple the turbine and the electrical generator. This, in fact, adds an important economic benefit to the resulting machine, in that electronic converters are not required. Both the tip clearance t_{cl} and the trailing-edge thickness t_e are set to minimum values, related to mechanical resistance or manufacturing limits, and common to all the rows [5, 23]. The radial clearance cl, i.e. the gap between the cascades, is also assigned a fixed value, since a proper optimization of this parameter is outside the capabilities of a generalized mean-line approach. However, considering its strong impact on the performance of axial turbines [34], an even larger influence may be expected in radial machines. In centrifugal turbines, in fact, the radial gap directly affects the variation of the radial coordinate and,

Common parameters			
ω [rpm]	3000	t_{cl} [mm]	0.1
t_e [mm]	0.1	cl [mm]	1
H_{min} [mm]	10	δ_{max} [°]	±30

6-stage Machine

Design Variables	**LB**	**UB**
D_{in} [mm] (x 1)	200	–
$(p_{T,in}/p_{S,out})_{stg}$ (x 1)	1.97	1.97
R (x 1)	0.4	0.6
BDA [°] (x 1)	65	75
b [mm] (x 1)	25	40

3-stage Machine

Design Variables	**LB**	**UB**
D_{in} [mm] (x 1)	150	–
$(p_{T,in}/p_{S,out})_{stg}$ (x 3)	3.5	5
R (x 3)	0.1	0.6
BDA [°] (x 6)	60	75
b [mm] (x 6)	25	60

Table 3.2: Design variables, with relative lower (LB) and upper (UB) bounds, and parameters involved in the proposed design methodology as applied to a N-stages centrifugal turbine.

hence, may induce a diffusion effect due to the increase of passage area in the flow direction. The minimum blade height H_{min} constitutes a critical parameter as the size of the machine is reduced and, in the present case, it is assigned a value of 10 mm. The flaring angle δ, i.e. the angle between the end-wall contour and the radial direction, is constrained in the typical range adopted for axial machines of $\pm 30\,^{\circ}$ [5, 23]. The lower constraint on the inlet diameter D_{in} may be tentatively determined in order to be compatible with the minimum blade height, keeping however in mind that, owing to the possibility of a converging meridional channel, this does not necessarily occur in the first stage, see §3.4.

Regarding the 6-stage machine, the design assumption of repeating stages (§3.4) is adopted in order to illustrate its consequences on the result. Coherently, the main variables of the problem, i.e. the pressure drops, the degrees of reaction, the radial chords, and the blades outlet geometric angles, are assumed to be the same for all the stages. In particular, the blades angles, which are given values typical for turbine cascades, are opposite in sign between stators and rotors. The global total-to-static pressure ratio is evenly distributed among the stages, i.e. $(p_{\text{T,in}}/p_{\text{S,out}})_{\text{stg}} = (p_{\text{T,in}}/p_{\text{S,out}})^{1/N_{\text{stgs}}}$. The reaction degree is left to vary between 0.4 and 0.6, in a region of high stage-performance. This allows also to split almost equally the expansion ratio between the stator and the rotor, thus limiting the maximum Mach number within the stage. The constraints imposed on the radial chord are selected in order to preserve acceptable blade aspect ratios and to limit the turbine dimension, i.e. its maximum diameter.

In the 3-stage machine, due to the increased stage-loading, all the preceding simplifications are removed in order to limit the maximum Mach number to 1.4 and to respect the constraint on the maximum flaring angle. In particular, the pressure drops, the degrees of reaction, the radial chords, and the blades outlet geometric angles are allowed to assume values differing among the stages, according to the novel design procedure introduced at the end of §3.4.

3.5.3 Results: Transonic Turbine

The main features of the optimized 6-stage turbine are shown in Tab. 3.3. The optimal velocity triangles are shown in Fig. 3.5a and, as expected (§3.4), there is no similarity among them, notwithstanding the design assumption of repeating-stages. Another expected feature of the machine is the shape of the meridional channel, see Fig. 3.5b, which appears to be slightly convergent in the first stages, while in the last one the flaring angle reaches the prescribed upper limit of $30\,^{\circ}$. This trend is strictly combined to the other quantities of the problem, and more insight may be gained by considering again Eq. (3.14).

An increase in the flow passage area is required along the stream-wise direction, in order to accommodate for the considerable growth of the volumetric flow rate as the expansion process proceeds. Being the blades angle and the radial chord values constrained to be the same in this case, the only free variable that can be exploited to this end is the flaring angle. In the first stages, where the increase in passage area determined by the diameter increase is comparatively large, the meridional channel tends to be convergent. On the contrary, an increasing divergence is needed in the subsequent stages.

The adoption of a comparably large number of stages reduces the blade aerodynamic loading, which is an interesting quantity for underlying differences and analogies with respect to the axial architecture. In axial machines, this quantity is normally proportional to the stage specific work w. Conversely, for radial outflow configurations, the reduction of the the aerodynamic load-

P_m [MW]	1.27	δ_{max} [°]	30
D_{in} [m]	0.2	D_{out} [m]	0.98
H_{min} [mm]	8.2	H_{max} [mm]	147
R	0.47	BDA [°]	66
b [mm]	30		
$\eta_{T\chi=0.5}$	0.87	M_{max}	1.16
$\eta_{T\chi=0.5,CFD}$	0.86	$M_{max,CFD}$	0.99

Table 3.3: Main results for the 6-stage 1 MW_M transonic turbine.

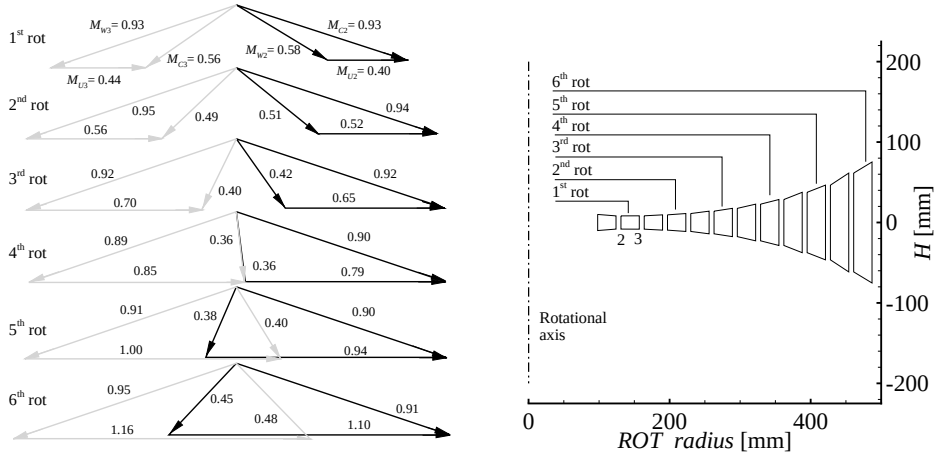

Figure 3.5: Design results for the 6-stage transonic 1 MW_M turbine, following the repeating-stage assumption, adopting the boundary conditions reported in Tab. 3.1, and the Craig & Cox loss estimation method [15]. Fig. 3.5a shows the velocity triangles, in black those referring to the rotor inlet section, in grey to the rotor outlet. The Mach numbers corresponding to the different velocity components are also detailed. The meridional section is depicted in Fig. 3.5b.

ing, expressed by the work coefficient Ψ, does not imply a direct decrease of w, as shown in Fig. 3.6a. In fact, by assuming the definition typical of axial turbines, i.e. $\Psi = w_{stg}/2\overline{U}^2$, with $\overline{U} = (U_{in} + U_{out})_{stg}/2$, can be noted how Ψ can lower throughout the expander, notwithstanding the fact that $\Delta h_{TT,\,stg}$, i.e. the specific work extracted, increases. This results in the initial stages being characterized by a lower specific work, but larger blade deflections and aerodynamic loadings, which cause the profile losses to increase. The trend is thus strictly correlated to the constraints imposed on the geometry.

The loss-estimation method of Craig & Cox [15] predicts a significant variation of the losses

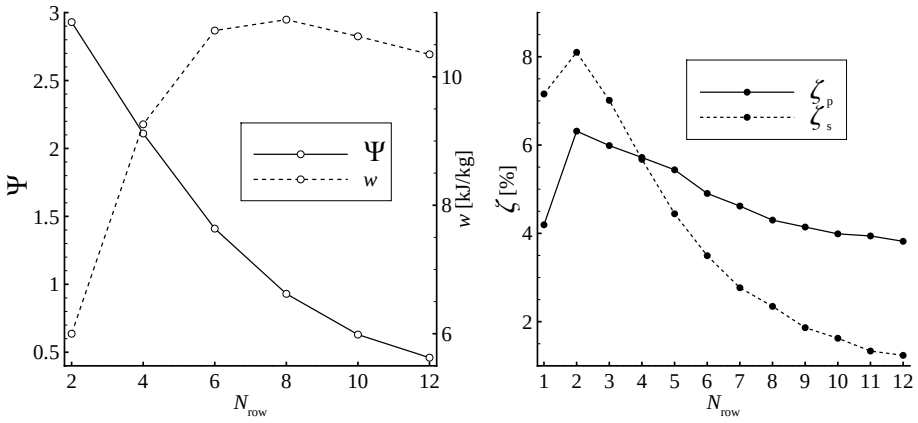

(a) (b)

Figure 3.6: Design results for the 6-stage transonic 1 MW_M turbine of Fig. 3.5. 3.6a: evolution of the load distribution among the stages, in terms of the aerodynamic loading expressed by Ψ (solid line), and of the stage specific work w (dashed line). 3.6b: row-by-row evolution of the kinetic energy loss coefficients ζ_p (solid line), and ζ_s (dashed line) accounting for profile-, and secondary-losses. The presented results are obtained with the Craig & Cox model [15].

throughout the machine, as shown in Fig. 3.6b. This is a direct consequence of the turbine configuration, featuring stages characterized by very different geometrical quantities (e.g. solidity, aspect ratio etc.). In particular, end-wall loss coefficients are found to be more influential in the first stages, characterized by lower blades aspect-ratios. The same trend characterizes also the profile losses, which assume larger values in the high deflection blades of the first stages. As a result, the stage efficiency increases along the machine, passing from about 75% in the first stage to about 95% in the last one.

3.5.4 Results: Slightly Supersonic Turbine

The main features of the optimized 3-stage turbine are shown in Tab. 3.4. The increased aerodynamic loading lead to an efficiency penalty with respect to the 6-stage machine. The optimal velocity triangles are shown in Fig. 3.7a and, as expected (§3.4), the optimized blades geometrical angles vary along the machine in this case.

It can be noted that the application of the design procedure proposed in §3.4 allows to avoid any converging part in the meridional channel, as shown in Fig. 3.7b. At the same time, the constraint on the maximum flaring angle is respected notwithstanding the fact that the same expansion is performed with three stages only. This is achieved by an increase of the chords in the last stages, accompanied by a reduction of the deflection and a consequent increase of the radial velocity component.

P_m [MW]	1.22		
M_{max}	1.36	δ_{max} [°]	30
D_{in} [m]	0.29	D_{out} [m]	0.85
H_{min} [mm]	7.1	H_{max} [mm]	153
$\eta_{T\chi=0.5}$	0.84	M_{max}	1.36
$\eta_{T\chi=0.5,CFD}$	0.81	$M_{max,CFD}$	1.40
		Stage	
	1st	**2**nd	**3**rd
$(p_{T,in}/p_{S,out})_{stg}$	3.7	4.7	4.8
R	0.23	0.35	0.40

Table 3.4: Main results for the 3-stage supersonic turbine.

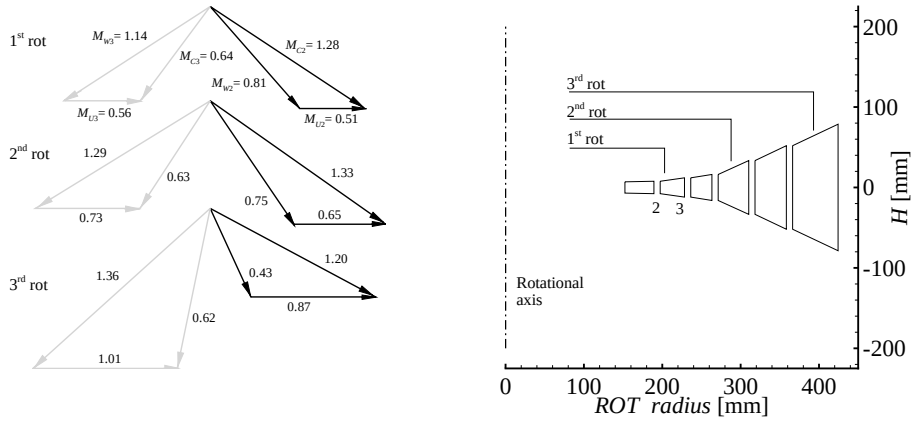

(a) (b)

Figure 3.7: Design results for the 3-stage supersonic 1 MW_M turbine, following the repeating-stage assumption, adopting the boundary conditions reported in Tab. 3.1, and the Craig & Cox loss estimation method [15]. Fig. 3.7a shows the velocity triangles, in black those referring to the rotor inlet section, in grey to the rotor outlet. The Mach numbers corresponding to the different velocity components are also detailed. The meridional section is depicted in Fig. 3.7b.

3.6 Design of Exemplary 10 kW_e Machines

The purpose of this section is to further clarify the procedure presented in §3.4 by presenting the design of two exemplary centrifugal turbines in the 10 kW_E power-output range. The tool adopted for the preliminary design is the in-house software *zTurbo*, presented in §3.2.1. The treatment

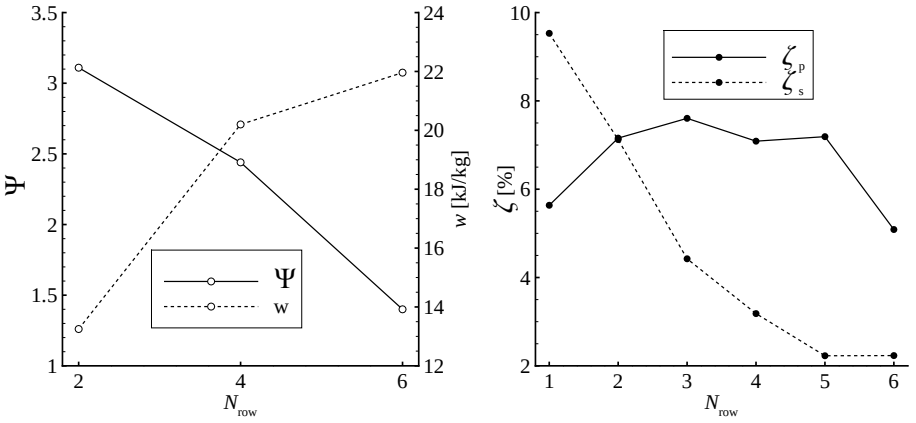

(a) (b)

Figure 3.8: Design results for the 3-stage supersonic 1 MW_M turbine of Fig. 3.7. 3.8a: evolution of the load distribution among the stages, in terms of the aerodynamic loading expressed by the work coefficient Ψ (solid line), and of the stage specific work w. 3.8b: row-by-row evolution of the kinetic energy loss coefficients ζ_p (solid line), and ζ_s (dashed line) accounting for profile-, and secondary-losses. The presented results are obtained with the Craig & Cox loss model [15].

follows the work documented in Ref. [12], which constitutes also the first assessment of the down-scaling potential of the ROT architecture, considering its implementation in the field of low power-output mini-ORC turbo-generators. The modelling framework resembles closely the one presented in §3.5.1, and is discussed in §3.6.1.

3.6.1 Design Assumptions

The results of the thermodynamic cycle analysis provide the needed inputs to the turbine preliminary design procedure. The solution presented by Lang [35] for an ORC turbo-generator recovering thermal power from the exhaust of an heavy-duty truck engine is adopted here. The main characteristics of this cycle, resumed in Tab. 3.5, are common to all the machines designed in the present section. The working fluid is siloxane D_4, whose $T-s$ diagram is represented in Fig. 3.9. The outlet pressure corresponds to a condensation temperature of about 100 °C. The mass flow rate value is imposed in order to obtain a power-output close to the target one of about 10 kW_M. Also in this case the first part of the expansion takes place in the so-called dense gas region, where the compressibility factor is lower than unity, see also Tab. 3.5. Relevant real gas effects are therefore expected, and accurate thermodynamic models are needed [6, 18].

For the reasons detailed in §3.5.1, two machine configurations are presented: a five-stage transonic turbine, and a three-stage one, which is slightly supersonic.

The loss estimation method adopted is the one proposed by Traupel [21]. However, as already mentioned, the predictive capability of these models is expected to decrease as the flow Mach numbers increase, and as the size of the machine is reduced. Thus, a comparison among different models is presented for the three-stage expander, by re-designing the same machine using the Craig

Fluid	D_4
$\dot{m}_{flow}$ [kg s^{-1}]	0.266
$T_{T,in}$ [°C]	242.5
$p_{T,in}$ [bar]	3.9
z_{in}	0.80
$p_{S,out}$ [bar]	0.087
$\frac{p_{T,in}}{p_{S,out}}$	45
$\left.\frac{V_{out}}{V_{in}}\right\|_S$	53

Table 3.5: Thermodynamic cycle parameters assumed for the preliminary design of the turbines presented in this section, after [35]. The last two terms indicate the pressure and the isoentropic volumetric flow rate ratios across the turbine expansion, respectively. The working fluid is siloxane D_4 (octamethylcyclotetrasiloxane, $C_8H_{24}O_4Si_4$): MW = 296.62 [g mol^{-1}], T_{CR} = 313.3 [°C], p_{CR} = 13.32 [bar], ρ_{CR} = 301.3 [kg m^{-3}].

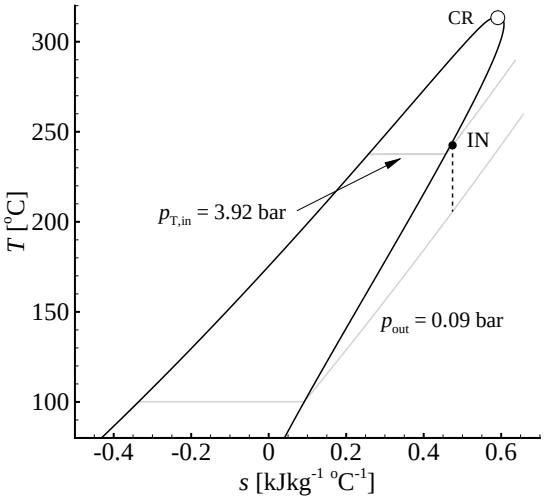

Figure 3.9: Saturation curve of siloxane D_4 in a T-s diagram, showing the thermodynamic boundary conditions for the turbine design, i.e. the inlet total conditions, point IN, and the discharge pressure. Point CR indicates the liquid-vapour critical point of the fluid.

& Cox model [15]. Beside the estimation of profile and secondary losses, also those due to tip-leakage are considered in this case, being an increasingly significant contribution for comparatively small machines. The modeled physical phenomena account for the reduction of the useful mass flow rate, and for a larger flow angle deviation downstream of the cascade [36]. In particular, tip-leakage losses are assumed to be null across the stator, owing to the possibility of using an almost hermetic sealing on the turbine shaft [5]. On the contrary, unshrouded rotor crowns are assumed,

and the associated tip leakage losses estimated. Shrouded rows are generally preferred in small turbines in order to reduce tip-leakages [37] but, in the present chapter, greater importance has been attributed to easy the machine realization, see e.g. §3.3.

3.6.2 Design Methodology

The design of the machines considered here, given their comparatively low power-output, is performed following the novel design procedure purposely introduced at the end of §3.4. In particular, the pressure drops, the degrees of reaction, the radial chords, and the blades outlet geometric angles are allowed to assume different values among the stages. The variables and the geometric parameters needed to perform the turbine design, see e.g. §3.2.1, are collected in Tab. 3.6. The design framework is similar to the one described in §3.5.4, and all the quantities are described therein. As anticipated, both the inlet diameter D_{in} and the speed of revolution ω appear in this case among the variables to be optimized, see e.g. §3.4. For the blade height H, which is a critical quantity given the low power-output, the minimal value compatible with mechanical resistance and manufacturing limits is assigned as the lower bound [5, 23]. Further analysis conducted on the machines presented in §3.5 by means of CFD tools highlighted that, for centrifugal turbines, is beneficial for the machine performance to adopt maximum flaring angles lower than those suggested from the axial turbines practice [11]. Following this results, the range of variation of the flaring angle δ is now reduced to $\pm 12°$.

Common parameters			
t_{cl} [mm]	0.1	t_e [mm]	0.1
cl [mm]	1	H_{min} [mm]	2
δ_{max} [°]	±12		
Design Variables	**LB**	**UB**	
D_{in} [mm] (x 1)	20	100	
ω [krpm] (x 1)	5	20	
$(p_{T,in}/p_{S,out})_{stg}$ (x N_{stgs})	2	5	
R (x N_{stgs})	0.1	0.6	
BDA [°] (x N_{rows})	55	75	
b [mm] (x N_{rows})	2	12	

Table 3.6: Design variables, with relative lower (LB) and upper (UB) bounds, and parameters involved in the proposed design methodology as applied to a N-stages centrifugal turbine.

3.6.3 Results: Transonic Turbine

The main features of the optimized 5-stage *m*ROT are shown in Table 3.7. Is to be noted that the optimal angular velocity, i.e. 12400 rpm, is considerably lower than the values encountered for traditional axial or centripetal machines designed for a comparable application and power output, see e.g. [35]. The optimal velocity triangles are shown in Fig. 3.10a and, as expected, the blades

P_m [kW]	10.6	$\eta_{T\chi=0.5}$	0.79
M_{max}	0.98	ω [rpm]	12400
D_{in} [mm]	53	D_{out} [mm]	180
H_{in} [mm]	2	H_{out} [mm]	15
δ_{max} [°]	9.0		

	Stage				
	1st	**2nd**	**3rd**	**4th**	**5th**
$(p_{T,in}/p_{S,out})_{stg}$	2.2	2.5	2.6	2.4	2.3
R	0.31	0.36	0.39	0.40	0.40

Table 3.7: Main results for the 5-stage 10 kW_M transonic turbine.

geometrical angles vary along the machine, suggesting that customized geometry configurations are needed in order to achieve highly efficient *m*ROTs.

As already observed in §3.5.4, the proposed design procedure proves successful in obtaining a smooth increase of the blade heights along the machine, with the concurrent increase of the radial chords. The resulting meridional contour is depicted in Fig. 3.10b. The maximum flaring angles, of the order of 9° are, are located on the last stage.

The relation between the stages aerodynamic loading, the imposed deflections, and the corresponding profile losses, is similar to what already observed and discussed in the previous sections. In particular, the specific work elaborated by the stages decreases along the machine, while the deflections and consequently the losses tend to follow an opposite trend, as shown in Fig. 3.11. As a result, also in this case the stage efficiency increases along the machine, passing from about 72% in the first stage to about 88% in the last one. As expected, tip leakages heavily affect the performance, and the associated loss coefficient reaches maximum values in the first two rotors, characterized by larger tip clearance/blade-height ratios. Notably, tip-leakage losses are comparable in magnitude with profile and secondary ones.

3.6.4 Results: Slightly Supersonic Turbine

The main features of the slightly supersonic 3-stage design are shown in Table 3.8. As anticipated, the design is performed adopting two different loss-estimation methods, i.e. the Craig & Cox [15], and the Traupel one [21]. The comparison among the predictions of such models is included in all the figures presenting the outcome of the design. It can be concluded that the obtained turbine design is scarcely dependent from the adopted loss prediction method.

Coherently with the similarity theory [13], stating that the smaller the machine, the higher the speed of revolution needed to achieve better performance, the three-stage turbine rotates at 15400 rpm. The optimal velocity triangles are shown in Fig. 3.12a and, also in this case, the blades geometrical angles vary along the machine. The meridional channel of the optimal design is depicted in Fig. 3.12b, and its appearance is similar to that of the 5-stage machine.

With respect to the transonic machine, the use of only three stages increases the blade aerodynamic loading, as shown in Fig. 3.13a, thus lowering the overall turbine efficiency. The main sources of loss are reported in Fig. 3.13b, from where it can be noted that the major differences

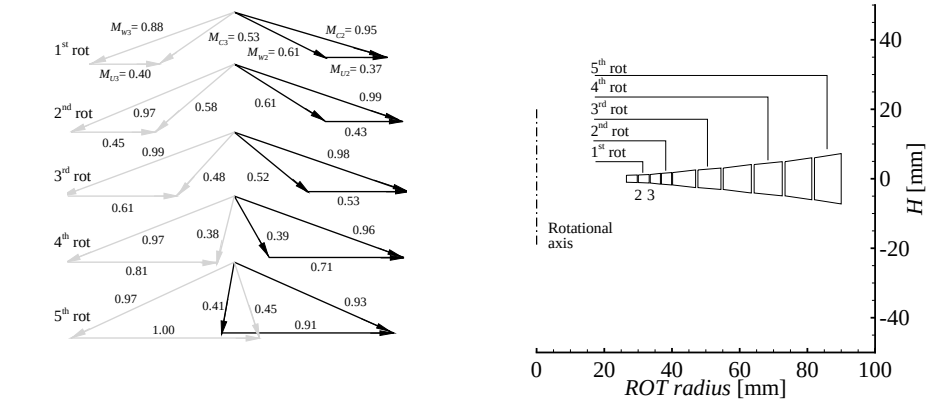

(a) (b)

Figure 3.10: Results for the design of the 5-stage transonic 10 kW_M turbine designed following the novel methodology presented in this chapter, adopting the boundary conditions reported in Tab. 3.7, and the Traupel loss estimation method [21]. Fig. 3.10a shows the velocity triangles, in black those referring to the rotor inlet section, in grey to the rotor outlet. The Mach numbers corresponding to the different velocity components are also detailed. The meridional section is depicted in Fig. 3.10b.

among the two models are found in the predictions of the secondary loss coefficient in the first stages, characterized by aspect ratios close to one. From this perspective, the Craig & Cox model resulted to be somehow more conservative.

3.7 Conclusions

The first critical evaluation of the centrifugal or radial-outflow turbine (ROT) architecture as a candidate technology for ORC turbo-generators is presented. All the special features involved in ROTs design are enlightened, the main findings being that, in order to design efficient centrifugal turbines it is needed that i) the blade discharge geometric angles, the radial chords, the stage expansion ratios, and the reaction degrees are allowed to vary among each cascade, and ii) the diameter and the speed of revolution are included among the optimization variables.

It is discussed how simplifying assumptions usually adopted in the axial turbines practice are typically not applicable. A novel design methodology is derived and presented for the preliminary sizing of ROTs in the power size range from several MW_E down to few kW_E. The in-house mean-line optimization code *zTurbo*, which allows to determine the preliminary design of ORC turbines of various configurations and working with different fluids, is presented and adopted to verify the novel method by presenting several exemplary design exercises.

First, the design of two 1 MW_E centrifugal turbines is presented, a transonic six-stage and a supersonic three-stage machines. These expanders handle an expansion ratio of 60, and rotate at 3000 rpm. Simplifications derived from the axial-turbines practice are adopted in order to illustrate

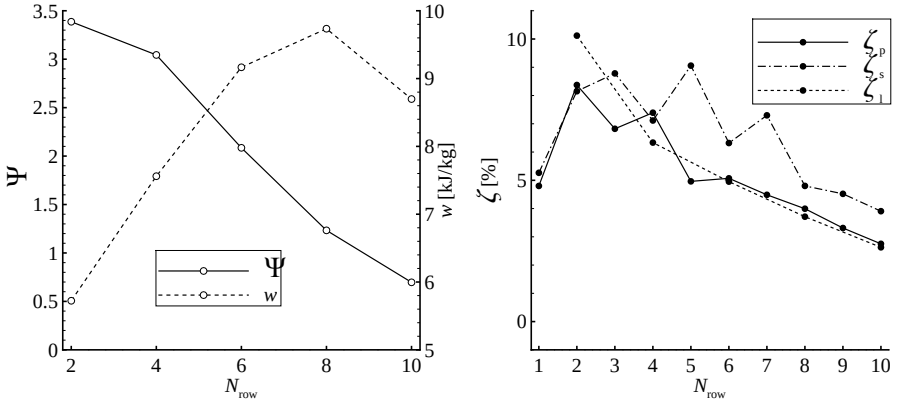

Figure 3.11: Design results for the 5-stage transonic 10 kW_M turbine of Fig. 3.10. 3.11a: evolution of the load distribution among the stages, in terms of the aerodynamic loading expressed by the work coefficient Ψ, and of the stage specific work w. 3.11b: row-by-row evolution of the kinetic energy loss coefficients ζ_p (solid lines), ζ_s (dash dotted lines), and ζ_l (dashed lines) accounting for profile-, secondary- and tip leakage-losses. The presented results are obtained with the Traupel loss estimation model [21].

their consequences. The results of the design exercises, carried out with *zTurbo*, confirm that the adopted assumptions lead to unwanted design features, such as converging meridional channels and large flaring angles on the last stages. The predicted fluid-dynamic efficiency for the transonic and the supersonic machine is around 86% and 81%, respectively.

Thus, the down-scaling potential of the centrifugal architecture is assessed, by applying the novel design methodology to the sizing of two 10 kW_E ROTs, handling an expansion ratio of 45. The design of a 5 stages transonic turbine, and of a 3 stages slightly supersonic one is presented. The proposed design procedure proves valuable in overcoming the criticality previously highlighted. In particular, the resulting meridional channel monotonically diverges maintaining maximum flaring angles lower than 10°. The resulting turbines are projected to exceed a fluid-dynamic efficiency of 79% and 77%, with speed of revolution around 124000 and 15400 rpm, respectively.

This research therefore demonstrates that the ROT architecture is a promising concept for future ORC power systems, capable of preserving its features and performance when downscaled, for both transonic and slightly supersonic configurations. In particular, transonic machines are expected to outperform the supersonic one during partial load operations, thus contributing to significantly enhance the average efficiency of the ORC turbo-generator which, in the typical case, is called to work within a wide range of operating conditions. The detailed part-load modeling tool necessary to assess and quantify this last point will be developed as one of the next steps of the present research. Finally, CFD-based tools have a demonstrated their strong potential in deepening the results of the mean-line analyses presented here, and they will be therefore further developed in the future.

Nomenclature

P_m [kW]	10.3	$\eta_{T\chi=0.5}$	0.77
M_{max}	1.33	ω [rpm]	15400
D_{in} [mm]	57	D_{out} [mm]	162
H_{in} [mm]	2	H_{out} [mm]	18
δ_{max} [°]	11.8		

	Stage		
	1st	**2**nd	**3**rd
$(p_{T,in}/p_{S,out})_{stg}$	3.6	4.1	4.5
R	0.25	0.37	0.42

Table 3.8: Main results for the 3-stage 10 kW_M supersonic turbine.

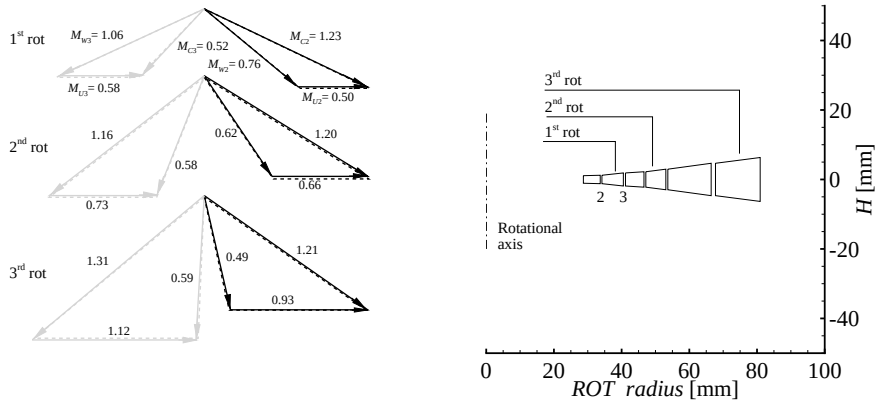

(a) (b)

Figure 3.12: Results for the design of the 3-stage supersonic 10 kW_M turbine designed following the novel methodology presented in this chapter, adopting the boundary conditions reported in Tab. 3.5. Fig. 3.12a shows the velocity triangles, in black those referring to the rotor inlet section, in grey to the rotor outlet. The Mach numbers corresponding to the different velocity components are also detailed. The solid lines represent the results obtained with the Traupel model [21], while the dashed ones those pertaining to the Craig & Cox one [15]. The corresponding meridional section is depicted in Fig. 3.12b. In this case, the results of the two models are not distinguishable.

s, p	=	specific entropy [kJ kg^{-1} K^{-1}], pressure [bar]
T, h	=	temperature [°C], specific enthalpy [kJ kg^{-1}]
ρ, c	=	density [kg m^{-3}], speed of sound [m s^{-1}]
MW, z	=	molecular weight [g mol^{-1}] , compressibility factor

A, $\dot{m}$	=	flow passage area [m^2], mass flow rate [kg s^{-1}]
$\dot{V}$	=	volumetric flow rate [m^3 s^{-1}]
$R = \Delta h_{SS,rot}/\Delta h_{TS,stg}$	=	stage reaction degree
Re, M	=	Reynolds and Mach numbers
Sh, rt	=	shape factor, rothalpy [kJ kg^{-1}]
w, P	=	specific work [kJ kg^{-1}], power [kW]
C, W, U	=	absolute, relative, and rotational speed [m s^{-1}]
$\overline{U} = (U_{in} + U_{out})_{stg}/2$	=	average stage peripheral velocity [m s^{-1}]
BDA	=	blade geometric discharge angle [°]
V	=	mean flow velocity magnitude [m s^{-1}]
D, S	=	cascade diameter [m] and pitch [m]
H, b	=	blade height and chord [m]
cl, t_{cl}	=	inter-row radial and tip clearance [m]
o, t_e	=	throat width and trailing-edge thickness [m]
N_x	=	cardinality of quantity x

Greek symbols

χ	=	recovery fraction of discharged kinetic energy
η	=	efficiency
Ψ, Φ	=	work and flow coefficients
α, β	=	absolute and relative flow angles [°]
Δx	=	finite difference for quantity x
ω	=	angular speed of revolution [rpm]
δ	=	row flaring angle [°]
ϵ	=	correction factor for blocking effects
$\zeta = \frac{\Delta h_{S,loss}}{V_{out}^2/2}$	=	loss coefficient ($\Delta h_{S,loss}$ is the static enthalpy drop due to the considered loss, velocity $V = C$ for the stators, and $V = W$ for the rotors)

Subscripts

E, M	=	electrical, mechanical
min, max	=	minimum, maximum value
CR	=	critical thermodynamic conditions (liquid-vapour)
T, S	=	total and static thermodynamic conditions
th, in, out	=	sonic throat, inlet, and outlet sections
r	=	radial direction
st, rot, row, stg(s), bld(s)	=	stator, rotor, row, stage(s), blade(s)

Acronyms

ORC	=	Organic Rankine Cycle
ROT	=	Radial Outflow Turbine

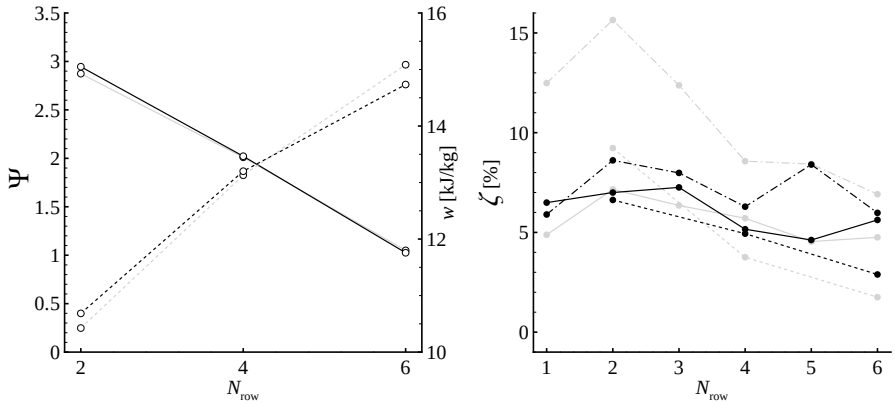

Figure 3.13: Design results for the 3-stage supersonic 10 kW_M turbine of Fig. 3.12. 3.13a: evolution of the load distribution among the stages, in terms of the aerodynamic loading expressed by the work coefficient Ψ, and of the stage specific work w. 3.13b: row-by-row evolution of the kinetic energy loss coefficients ζ_p (solid lines), ζ_s (dash dotted lines), and ζ_l (dashed lines) accounting for profile-, secondary- and tip leakage-losses. The black lines represent the results obtained with the Traupel model [21], while the gray ones those pertaining to the Craig & Cox one [15].

References

[1] L. D'Amelio. *Impiego di vapori ad alto peso molecolare in piccole turbine e utilizzazione del calore solare per energia motrice [On the use of high molecular weight vapors in small turbines and solar energy conversion into mechanical work]*. Industria Napoletana Arti Grafiche, 1935.

[2] H. Tabor and L. Bronicki. Establishing criteria for fluid for small vapor turbine. In *SAE National Transportation, Powerplant, Fuels, and Lubricants Meeting*, number 640823, Baltimore - MD, October 19-23 1964.

[3] G. Angelino, M. Gaia, and E. Macchi. A review of Italian activity in the field of organic Rankine cycles. In *VDI Berichte - Proceedings of the International VDI Seminar*, volume 539, pages 465–482, Düsseldorf, 10–12 September 1984. VDI Verlag.

[4] Costante M. Invernizzi. Closed power cycles - thermodynamic fundamentals and applications. In *Lecture Notes in Energy*, number 11. Springer-Verlag, 2013.

[5] E. Macchi. *Lecture series 100 on Closed-Cycle gas turbines*, chapter Design criteria for turbines operating with fluids having a low speed of sound. Von Karman Institute for Fluid Dynamics, 1977.

[6] P. Colonna, J. Harinck, S. Rebay, and A. Guardone. Real-gas effects in organic Rankine cycle turbine nozzles. *Journal of Propulsion and Power*, 24(2):282–294, 2008.

[7] P. Colonna, A. Guardone, N.R. Nannan, and C. Zamfirescu. Design of the dense gas flexible asymmetric shock tube. *Journal of Fluids Engineering, Transactions of the ASME*, 130(3):0345011–0345016, 2008.

[8] A. Spinelli, M. Pini, V. Dossena, P. Gaetani, and F. Casella. Design, simulation, and construction of a test rig for organic vapors. *Journal of Engineering for Gas Turbines and Power*, 135(4), 2013.

[9] A. Verneau. *Lecture series 1987-07*, chapter Small high pressure ratio turbines. Supersonic turbines for organic Rankine cycles from 3 to 1300 kW. Von Karman Institute for Fluid Dynamics, 1987.

[10] Sylvain Quoilin, Martijn Van Den Broek, Sébastien Declaye, Pierre Dewallef, and Vincent Lemort. Techno-economic survey of Organic Rankine Cycle (ORC) systems. *Renewable and Sustainable Energy Reviews*, 22(0):168 – 186, 2013.

[11] M. Pini, G. Persico, E. Casati, and V. Dossena. Preliminary design of a centrifugal turbine for organic Rankine cycle applications. *Journal of Engineering for Gas Turbines and Power-Transactions of the ASME*, 135:042312–1–9, 2013.

[12] E. Casati, S. Vitale, M. Pini, G. Persico, and P. Colonna. Centrifugal turbines for Mini-ORC power systems. *Journal of Engineering for Gas Turbines and Power-Transactions of the ASME*, 136(12):122607–1–11, 2014.

[13] O.E. Baljé. A study on design criteria and matching of turbomachines: Part A-similarity relations and design criteria of turbines. *Journal of Engineering for Gas Turbines and Power-Transactions of the ASME*, 84(1):83–102, 1962.

[14] J.J. Adamczyk. Aerodynamic analysis of multistage turbomachinery flows in support of aerodynamic design. *Journal of Turbomachinery*, 122(2):189–217, 2000.
[15] H.R.M. Craig and H.J.A. Cox. Performance estimation of axial flow turbines. *Proceedings Institution of Mechanical Engineers*, 185-32/71:407–424, 1971.
[16] D.G. Wilson. *The design of high–efficiency turbomachinery and gas turbines*. The MIT press (Cambridge, MA), 1984.
[17] S. L. Dixon and C. A. Hall. *Fluid Mechanics and Thermodynamics of Turbomachinery*. Elsevier Inc., 6th edition, 2010.
[18] P. Colonna, T. P. van der Stelt, and A. Guardone. FluidProp (Version 3.0): A program for the estimation of thermophysical properties of fluids, 2012. A program since 2004.
[19] O. Zweifel. The spacing of turbo-machine blading especially with large angular deflection. *Brown Boveri Review*, 32(1):436–444, December 1945.
[20] D. G. Ainley and G. C. R. Mathieson. A method of performance estimation for axial-flow turbines. Technical Report R&M 2974, British Aeronautical Research Council, 1957.
[21] W Traupel. *Thermische Turbomaschinen*. Springer-Verlag, Berlin, 1977.
[22] J.D. Coull and H.P. Hodson. Blade loading and its application in the mean-line design of low pressure turbines. *Journal of Turbomachinery*, 135(2), 2013.
[23] E. Macchi. Design limits: Basic parameter selection and optimization methods in turbomachinery design. volume 97 Av 2, pages 805–828, Izmir, Turk, 1985. Martinus Nijhoff Publ., Dordrecht, The Netherlands.
[24] Sandia National Laboratories. The Dakota project - Large Scale Engineering Optimization and Uncertainty Analysis, 2012. dakota.sandia.gov/software.html (last accessed September 2013).
[25] Kalyanmoy Deb. *Multi-objective optimization*. John Wiley & Sons, Inc., 2001. ISBN: 9780470743614.
[26] J. Eddy and K. Lewis. Effective generation of Pareto sets using genetic programming. In *Proceedings of the ASME Design Engineering Technical Conference*, volume 2, pages 783–791, Pittsburgh - PA, September 9-12 2001.
[27] Energy Technology incorporated. Study of advanced radial outflow turbine for solar steam Rankine engines. under contract den 3-86, National Aeronautics and Space Administration, Lewis Research Center, 1979.
[28] E.P. Coomes, R.E. Dodge, D.G. Wilson, and S.J. McCabe. Design of a high-power-density Ljüngstrom turbine using potassium as a working fluid. 1986. Proceedings of the Intersociety of Energy onversion Engineers Conference – San Diego (US-CA), August 25-29.
[29] F. Ljüngstrom. The development of the Ljüngstrom steam turbine and air preheater. *Proceedings of the Institute of Mechanical Engineers*, 160:211–223, 1949.
[30] A. Mobarak, N. Rafat, and M. Saad. Turbine selection for small capacity solar power generation. *Desalination*, 3:1351–1367, 1980.
[31] C. D'Amelio, M. Blasi, and R. Tuccillo. Study of low power engines: Thermodynamic conversion of solar energy. In D.O. Hall and J. Morton, editors, *Proceedings of the ISES Solar World Forum*, volume 4, pages 2983–2992, Brighton, UK, August 23-28 1982.
[32] G. Cerri, L. Battisti, and G. Soraperra. Non conventional turbines for hydrogen fueled power plants. In *Proceedings of the ASME Turbo Expo 2003*, number GT2003-38324, Atlanta, GA, June 16-19 2003.
[33] O.E. Baljé. A study on design criteria and matching of turbomachines: Part B-compressor and pump performance and matching of turbocomponents. *Journal of Engineering for Gas Turbines and Power-Transactions of the ASME*, 84(1):103–114, 1962.

[34] P. Gaetani, G. Persico, and C. Osnaghi. Effects of axial gap on the vane-rotor interaction in a low aspect ratio turbine stage. *Journal of Propulsion and Power*, 26(2):325–334, 2010.

[35] W. Lang, R. Almbauer, and P. Colonna. Assessment of waste heat recovery for a heavy-duty truck engine using an ORC turbogenerator. *Journal of Engineering for Gas Turbines and Power-Transactions of the ASME*, 135(4):042313–1–10, 2013.

[36] J.D. Denton. Loss mechanisms in turbomachines. *Journal of Turbomachinery*, 115(4):621–656, 1993.

[37] G. Lozza, E. Macchi, and A. Perdichizzi. Investigation on the efficiecny potential of small steam turbines of various configurations. In *Proceedings of the* 21st *Intersociety Energy Conversion Engineering Conference*, pages 1367–1373, San Diego-CA, USA, August 25-29 1986. ACS, Washington-DC, USA.

4

Thermal Energy Storage for Solar Powered ORC Engines

Part of the contents of this chapter appeared in:

E. Casati, A. Galli, & P. Colonna
Solar Energy **96**(0), 205-219 (2013)

E. Casati, A. Desideri, F. Casella, & P. Colonna
Proceedings of the 18th *IEA SolarPACES Conference, Marrakech - MA (2012)*

Abstract *The feasibility of energy storage is of paramount importance for solar power systems, to the point that it can be the technology enabler. Regarding concentrated solar power (CSP) systems, the implementation of thermal energy storage (TES) is arguably a key advantage over systems based on photovoltaic (PV) technologies. The interest for highly efficient and modular CSP plants of small to medium capacity (*5 kW_E–5 MW_E*) is growing: organic Rankine cycle (ORC) power systems stand out in terms of efficiency, reliability and cost-effectiveness in such power-range.*

In this chapter, a thorough investigation on thermal storage systems tailored to high-temperature ORC power plants is addressed first, stemming from the observation that the direct storage of the ORC working fluid is effective thanks to its favorable thermodynamic properties. The concept of complete flashing cycle (CFC) is then introduced as a mean of achieving an unmatched system layout simplification, while preserving conversion efficiency. This is a new variant of the Rankine cycle, originally introduced by the presented research, whereby the vapor is produced by throttling the organic working fluid from liquid to saturated vapor conditions.

The presentation and discussion of a case study follows: a 100 kW_E *CFC system with direct thermal energy storage, coupled with state-of-the-art parabolic trough collectors. The proposed turbogenerator achieves an estimated 25% efficiency, which corresponds to a value of 18% in design conditions for the complete system. With siloxanes as working fluids, the estimated values of storage density are around 10* $kWh_E\ m_{ST}^{-3}$*, without considering additional filling materials.*

A dynamic model, developed and for the complete system, is used to investigate the performance under extreme transient conditions. By adopting a relatively simple and robust control strategy, the storage system is demonstrated to be effective in decoupling the solar field and the ORC power block, which can thus be operated close to nominal conditions notwithstanding the environmental disturbances. The feasibility of remotely controlled operation is thus positively assessed by means of this preliminary study.

4.1 Introduction

The debate over the advantages and disadvantages of various solar technologies is lively [1, 2]. Peters and colleagues compared PV- and CSP-based systems for large-scale solar power plants (> 50 MW_E), and concluded that the cost and efficiency of storing energy can turn the competitiveness in favor of CSP systems [3]. Another potentially important benefit of CSP systems integrating TES, along with dispatchability, is their ability to provide grid flexibility: this feature might enable higher overall penetration of other variable-generation technologies such as those based on PV cells and wind turbines [4].

Recent studies have underlined the techno- and socio-economic opportunity of shifting toward a global energy system which is more integrated and complex than presently, and which heavily relies on distributed generation [5]. Within the same context, also small-size CSP power plants in the 100 kW_E–5 MW_E power range have been investigated [6, 7]. It has therefore been argued that the new development paradigm of "getting bigger by going smaller" could provide a path to viability for CSP technologies in general, through modularity and economy of production, thus overcoming the bankability issue which is negatively affecting the sector [8].

Another notable advantage of thermal CSP plants for distributed generation is the possibility of co-generating electricity and useful thermal output for maximum energy utilization and flexibility. The thermal energy discharge from the primary mover can either be used for industrial or domestic purposes on-site, or/and drive an absorption chiller for air-conditioning or process cooling [9, 10].

Among the technologies suitable for high-efficiency conversion of thermal power into electricity and heat in this range of capacity, ORC turbogenerators stand out in terms of reliability and

cost-effectiveness, see, e.g., Ref. [11]. ORC power plants are steadily adopted for the increasing exploitation of geothermal reservoirs, while the growth of the number of ORC power systems for the thermal conversion of biomass fuel and industrial waste heat is remarkable [12]. ORC-based CSP plants have been widely studied, and prototypes were put into operation already several years ago [13, 14]; commercial power plants went recently on-line [15], and new ones are planned or are currently under construction.

To the knowledge of the author, however, no research has been published on TES systems specifically conceived to be integrated into ORC power plants. The study documented here stems from the need of a thorough investigation on thermal storage systems tailored to ORC power plants, and from the observation that the direct storage of high-temperature ORC working fluids is effective thanks to its high heat capacity and other favorable thermodynamic properties.

The chapter is structured as follows: in §4.2 the organic fluids of the class of siloxanes are briefly introduced; these compounds are widely used as working media for high temperature ORC power systems. Is to be noted that the addition of storage filling materials other than the working fluids itself is not considered at this stage of the research. In §4.3 a brief overview of TES-systems integration in power stations is reported. §4.4 deals in detail with the proposed technical solutions for the direct thermal storage of working fluid, discussing their applicability to ORC systems. A case study illustrating the application of one of the proposed storage systems is treated in §4.5. §4.6 summarizes the conclusions and the foreseen developments.

4.2 Siloxanes: High-Temperature ORC Working Fluids

The ORC working fluids considered in this study belong to the family of siloxanes, see table 4.1. These light silicon oils are already employed in commercial high-temperature ORC applications since they are non-toxic, environmentally friendly, low-flammable, bulk-produced and highly thermally stable; mixtures of siloxanes are widely employed as heat transfer fluids (HTF) in multiple fields, comprising the CSP industry [16, 17]. Multiparameter equations of state, employing the

Table 4.1: Main properties of the fluids considered in this work. MW: molecular weight, T_{boil}: normal boiling temperature, $p_{\text{vap@80°C}}$: vapour pressure at 80 °C.

Fluid	MW [g mol^{-1}]	T_{CR} [°C]	p_{CR} [bar]	ρ_{CR} [kg m^{-3}]	T_{boil} [°C]	$p_{\text{vap@80°C}}$ [bar]
Water	18.0	373.9	220.64	322.4	100.0	0.474
D_6	444.9	372.7	9.61	246.8	245.0	0.002
D_4	296.6	313.3	13.32	301.3	175.3	0.035
MDM	236.5	290.9	14.15	302.9	152.5	0.091

Span-Wagner functional form [18], have been recently developed for these fluids [19, 20]. These thermodynamics models, implemented in a software library, are adopted throughout this work [21, 22]. The specific thermophysical properties of the working fluids heavily affect the design of the most critical components, namely the turbine and the heat exchangers. Other fluids may be preferred for the same application, based upon multiple considerations, see e.g. Refs. [11, 23].

Figure 4.1 illustrates the thermodynamic features of interest in this case for siloxane D_4 and water using the T–s state diagram. A typical analysis of thermodynamic cycles is presented here, whereby the cycle minimum and maximum temperature are fixed, and different working fluids are evaluated in terms of obtainable conversion efficiency and other technological aspects. Note that fixing the

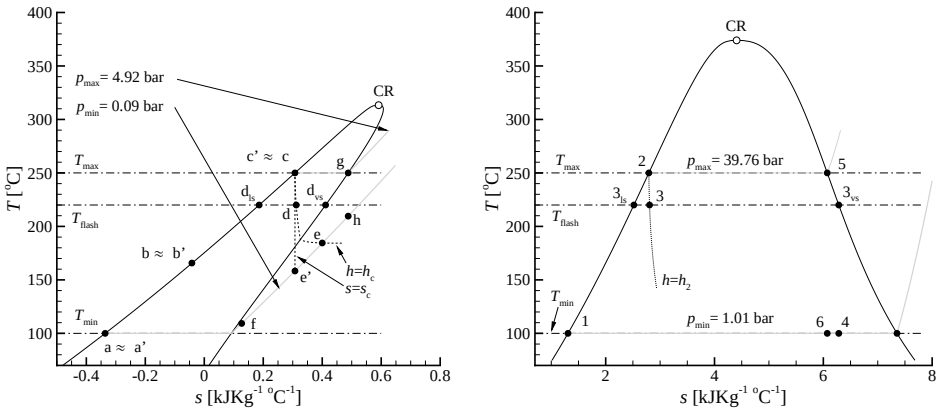

(a) Siloxane D_4 (b) Water

Figure 4.1: Comparison between the T–s thermodynamic diagram of D_4 and that of water: the highlighted temperature levels, resulting from the studied application and thus common to both fluids, are $T_{min} = 100°C$, $T_{max} = 250°C$, and $T_{flash} = 220°C$ (dash-dotted black lines). CR: liquid–vapour critical point, solid-black line: saturation line enclosing the VLE region, solid-grey: isobaric lines, dashed-black: iso-enthalpy lines. Note that the scale of the specific entropy in diagram (a) is different from that in diagram (b).

minimum and maximum cycle temperature results also in the specification of the minimum and maximum cycle (saturation) pressure for the considered fluid. The expansion ratio available for work extraction is thus also fixed.

From these preliminary considerations, the comparison of the thermodynamic features of molecularly complex fluids with those of water along expansions yields interesting conclusions:

I A consequence of the large complexity of the fluid molecular structure, thus of the high value of the specific heat capacity, is the so-called retrograde shape (positive slope) of the bubble line in the T–s diagram of the fluid, which helps visualizing how the expansion of the saturated vapor is inherently dry, see, e.g., Ref. [24]. This thermodynamic feature implies, contrary to what can be observed for a simple-molecule fluid like water, that for a complex organic fluid

   (a) Starting from saturated liquid conditions, see state c in fig. 4.1a, an isenthalpic pressure-reduction representative of a flashing process can result in the fluid being in a saturated–vapor state (process $c \rightarrow d$, whereby $q_d = 1$). If the pressure is further reduced, also superheated-vapour states are attainable.

   (b) The previous observation, applies also to an isentropic pressure-reduction process ($c \rightarrow e'$).

(c) An isentropic expansion starting from saturated vapour conditions always evolves towards superheated–vapour states ($d_{vs} \rightarrow e$).

(d) Furthermore, the temperature of the superheated vapor at the end of the expansion may be so high that internal heat-regeneration is mandatory if high cycle efficiency is required [25].

II Mainly as a consequence of the higher molecular weight, a lower specific enthalpy drop is associated with the given expansion. Thus, the working fluid mass-flow through the expander must be larger for the same power output. In combination, the low specific enthalpy drop and the higher mass-flow rate allow for the realization of comparatively simple and efficient turbines even for low or very low power outputs [14, 23].

III The saturation pressure corresponding to the maximum cycle temperature is lower (e.g., 4.9 bar for D_4 versus 39.8 bar for water): this is a major advantage if TES is of interest. Conversely, very low condensation pressure (e.g., 0.09 bar for D_4 versus 1.01 bar for water) entails technological challenges for other components (e.g., turbines and condenser), see Refs. [11, 26].

4.3 Concepts of TES Systems for Power Plants

The basic principle of storage system integration into power plants is the so-called flow-storage, whereby the TES gets its charge according to several main concepts, corresponding to the plant configurations summarized in fig. 4.2a. In solar power plants, storage systems deal with secondary energy since, as opposed to fuelled thermal plants, storage on the primary energy side (fuel storage) is not possible. Fuel control would be feasible (defocusing of heliostats or collectors) but it is avoided because of the energy loss. Energy storage integrated into the primary heat transfer loop,

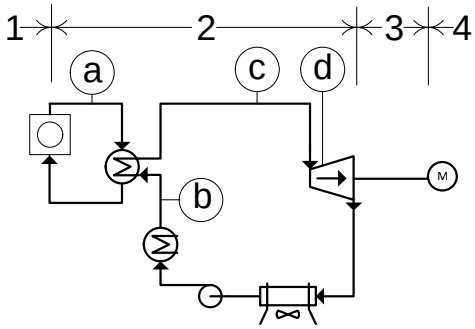

(a) Basic schemes for secondary energy storage in Rankine power plants: 1) primary energy, 2) secondary energy, 3) mechanical energy, 4) electrical energy. The tags a, b, c and d help identifying several so-called flow-storage options, adapted from [27].

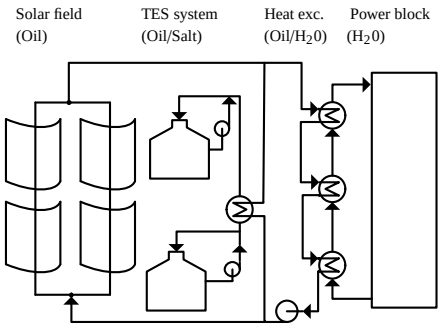

(b) State of the art: simplified process flow diagram of the Andasol solar power plant, adapted from [28].

Figure 4.2: Thermal energy storage in Rankine-cycle power plants.

see case *a* of fig. 4.2a, is the most adopted concept in commercial CSP plants. In this case, sensible heat is accumulated into a liquid, which can be thermal oil and/or molten salt [29]; in so-called *direct systems* the heat transfer fluid serves also as storage medium, while in *indirect systems* a separated system is used to store thermal energy, see fig. 4.2b.

The Spanish Andasol solar power plants, which are in operation since 2009, are representative of the state-of-the-art for technology based on parabolic troughs [30]. They adopt an indirect thermal storage system whereby thermal oil transfers the energy collected from the solar field to molten salt contained in two tanks, see fig. 4.2b; such layout, involving multiple subsystems with different working fluids, is arguably unfeasible for small-scale solar power plants due to complexity and cost.

Other concepts, see cases *b*, *c*, and *d* in fig. 4.2a, are based on the storage of energy in the working fluid itself, and have been implemented in steam power plants. Thermal storage can be used to make pre-heated feed water available to the steam generator (*b*), mainly for peaking purposes, in power plants with regenerative feed-water heating [31]. The storage vessel can also supply the turbine with steam in saturated or superheated state, at both live-steam (*c*) or medium/low pressure (*d*) conditions. Also in these cases both indirect and direct system concepts can be implemented.

Indirect systems for working fluid storage are extensively investigated as TES for direct steam generation (DSG) power plants [28]. Direct systems have been successfully used for decades, and also recently built CSP plants adopt this TES configuration. A direct system for the accumulation of working fluid is often called *steam accumulator* [27, 29]. The main advantage of steam accumulators is that they are simpler than indirect systems, in that no intermediate fluid loop and the related heat exchangers are needed; §4.4 treats in detail these concepts.

The evaluation of the profitability of energy systems is a complicated task, involving a number of considerations from different domains. Among the main elements of the evaluation one needs to consider the projected investment cost and efficiency of the complete system, possible environmental hazards, operation strategy, O&M cost, and the local regulatory framework, i.e., tariffs and/or incentives [32]. In particular, when newly proposed concepts are considered, the uncertainty related to equipment costs has a large impact on the reliability of such evaluation [33]. Also for this reason, an exhaustive economic evaluation is beyond the scope of the present work, which in turn is aimed at the thermodynamic and technical assessment of a new concept for thermal energy storage suitable for small solar-powered ORC plants. The analysis identifies and discusses the factors affecting the performance and the projected costs of the considered systems, such as their efficiency, the temperature and pressure levels in the storage system, the volumetric expansion ratio across the turbine, and the pressure level in the condenser.

The typical thermodynamic performance parameters for a TES system integrated into a thermal power plant are

1. the storage density ρ_{ex} [$kWh_M\ m_{ST}^{-3}$], which is useful to evaluate the size of the storage unit and, thus, to give a first estimate of its cost. Since thermal energy is stored for subsequent conversion into work, density of available energy (exergy) has to be considered [34]. The parameter EEED (Equivalent Electrical Energy Density [$kWh_E\ m_{ST}^{-3}$]), accounting for the subsequent conversion into electricity, is also introduced here. This value quantifies the equivalent electrical energy stored as thermal energy into one cubic meter of liquid at the storage conditions. For a given size of the storage in terms of equivalent hours of storage $h_{eq,st}$, the value of the EEED of a certain TES concept allows for a preliminary estimation of the storage volume and of the required mass of fluid.
2. The turnaround efficiency ξ_{turn}, which accounts for exergy losses along the entire charge-standstill-discharge cycle, and depends both on design and on operational parameters. ξ_{turn} is typically chosen as the objective variable for the thermodynamic optimization of a storage

system [35]. Systems implementing the direct storage of the working fluid attain the highest levels of ξ_{turn}, namely up to 95%, mainly as a consequence of the absence of any heat exchange process external to the storage vessel [27].

4.4 Direct Storage of Working Fluid in Rankine Power Stations

The concepts originally proposed and adopted in steam power plants are introduced here, and their extension to ORC systems is discussed. Being direct storage systems highly integrated into the power plant, both the storage concept and its discharge mode have to be considered in order to properly characterize the system. Three main storage concepts and three discharge methods have been introduced in the past [27]: these are described in §4.4.1 and §4.4.2 respectively. §4.4.3 treats their combination to form several possible storage systems, refer to figure 4.3.

4.4.1 Storage Methods

The working fluid is typically stored in the liquid phase, in order to exploit its greater storage density.

A STORAGE AT CONSTANT PRESSURE
It entails the storage of sensible heat in liquids, usually at atmospheric pressure. Two-tank arrangements, as well as single-tank systems exploiting the thermocline effect (displacement storage) are feasible [36, 37]. Silicon oils have been already adopted as the storage fluid in these systems [38]. If the direct-storage configuration is adopted, pressurization is needed in order to prevent boiling, and an external pressurizer may be needed in this case. Hot pressurized fluid can thus be extracted from the storage vessel at constant pressure, and this is the main advantage in power generation applications.

B EXPANSION STORAGE AT ALMOST CONSTANT PRESSURE
In this case liquid and vapour working fluid are stored in thermodynamic equilibrium at the saturation temperature. A “vapour cushion” is present at all times in the upper part of the storage tank. Hot saturated liquid is extracted from the bottom of the vessel, causing the vapour volume to increase. Additional vapour is produced by evaporation of a small part of the liquid volume, thus causing the pressure to decrease slightly. The drains coming back from the working fluid loop have to be collected and stored in a separate cold-storage vessel, which, being at lower temperature and pressure, is also relatively inexpensive. With respect to the displacement storage solution (A), the complications related to pressurization and thermocline promotion can be avoided and the vessel does not have to withstand severe thermal gradients during the charge-discharge phases.

C SLIDING PRESSURE STORAGE (RUTHS ACCUMULATOR)
In analogy with method B, liquid-vapour equilibrium is maintained in the storage vessel. In this case, however, not the liquid but the vapour forming the cushion is extracted during the discharge phase. The wide pressure swing during the discharge phase, a characteristic of this method, is a major drawback as far as power production is concerned [39]. The main advantage of this storage method is the fast reaction time, allowing for high discharge-rates of saturated steam.

4.4.2 Discharge Methods

1. VAPOR GENERATION BY FLASH EVAPORATION
   Internal flashing in the vessel pertains to the sliding pressure method of storage. In external flash processes the liquid is extracted from the storage tank, and thus throttled; processes featuring multiple flashing steps are also conceivable. The obtained vapour stream can be sent directly to a turbine.
   In case water is the working fluid, flashing systems require the adoption of so-called wet-turbines, which imply well-known technical challenges and rather low efficiency [40]. However, in case the working fluid is an organic compound, the flashed saturated vapour can be directly fed to a high efficiency "dry" turbine (see Sec. 4.2, point Ic). The so-called retrograde characteristic of the working fluid allows also for the complete evaporation of the liquid stream by throttling (see Sec. 4.2, Ia). The phase-separator and the relative liquid-drain circuit are therefore, in principle, unnecessary.
2. FEED WATER STORAGE
   In case of conventional thermal power stations, thermal storage upstream of the steam generator is a proven solution for peak-load generation. With such a method, peak-load can be sustained to an extent limited by the amount of power to be gained by cutting-off all the regenerative bleeds, and by the overload capacity of the main turbine generator set [27]. In the case of ORC power systems, extractive regeneration is never employed, therefore the peaking potential would be due exclusively to the overload capacity.
   This discharge method is not applicable to solar steam power plants as the only storage system; in periods with low solar radiation, feeding the turbine only with steam can become impossible [41].
3. CASCADING STORAGE
   A combination of method 1 and method 2 provides more flexibility for the complete system.
   In case the working fluid is formed by complex molecules, a fourth discharge method can be identified, namely
4. DIRECT LIQUID EXPANSION
   The liquid extracted from the pressurized storage vessel can be directly fed to an expander. If the working fluid is a complex organic molecule, the so-called wet-to-dry expansion process becomes possible (see Sec. 4.2, Ib). Wet-to-dry expanders have been proposed and tested with promising results [40, 42]. However, since none of them has reached technological maturity, wet-to-dry expansion has not been considered in this study, despite its notable potential.

4.4.3 Storage Systems

Figure 4.3 shows the main possible system configurations obtained by combining the storage methods described in Sec. 4.4.1 (A, B, and C), and the discharge methods treated in Sec 4.4.2 (1, 2, and 3), see Ref. [27]. The configurations C2 and C3 are not realizable, while configuration B and C may be combined: vapor may be taken from an expansion storage vessel in addition to liquid (shown by the lines for configurations B2/C1 and B3/C1).

The A1 scheme has been proposed for nuclear power plants [27], while the B2/C1 scheme for CSP plants [41]. The A3 scheme gained acceptance in the late 1920s: the displacement storage plant of the coal-fired power station in Mannheim, Germany, is well known [39]. The C1 scheme (pure sliding pressure) found wider application, mainly as a solution for buffer-storage. Within

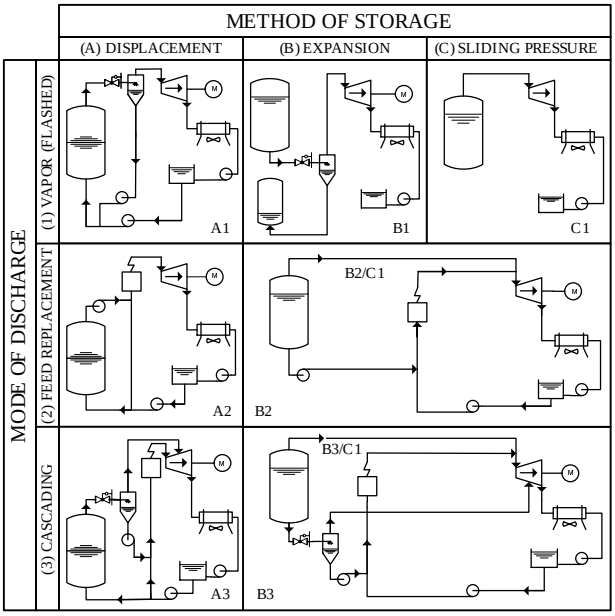

Figure 4.3: Main configurations of direct storage systems for steam power plants, as a combination of storage methods and discharge modes. Labels correspond to those adopted for the description in §4.4.1 and §4.4.2. For the sake of simplicity, only single-stage flash ORC systems are considered, without internal regeneration. Adapted from [27].

the island grid of Berlin, the 50 MW_E Charlottenburg plant - built in 1929 - has been operated with steam accumulators of 67 MWh_E storage-capacity for more than 60 years. Sliding-pressure systems have recently been realized [43], and this concept has been proposed as a solution to supply DSG plants with buffer-storage capabilities [44]. Two-phase refrigerant accumulators working according to this principle are key components in automotive air conditioning systems [45].

It can thus be concluded that all the above mentioned concepts are applicable in principle to ORC power systems. However, applying the very same concepts for thermal energy storage to ORC power plants leads to EEED levels (see Sec. 4.3) which are lower than those of direct water-steam systems, and also of state-of-the-art indirect systems (see Sec. 4.5). In case the working fluid is a siloxane, for a given power output, the same thermal storage capacity requires a larger vessel, if compared to a steam power plant.

It is worth noting that the problems related to fluid containment at concurrently high-pressure and high-temperature levels, which have ultimately hindered the diffusion of water-steam storage systems, are reduced in case working fluid is an organic compound (sec. 4.2, III). Beside the vessel volume and the pressurization level, also the cost of the fluid largely contributes to the total investment cost of the storage system. At present, siloxanes are approximately two times more expensive than synthetic oils (typically mixtures of diphenyl-diphenyl ether), in terms of cost per unit of thermal energy delivered [32]. However, contrary to synthetic oils, siloxanes are classified as non-hazardous materials. Such classification is expected to play an important role if the proposed technology will be applied, particularly if the distributed energy scenario is considered.

The cost of the storage system is however only a fraction of the final investment for a power plant. The case study presented in §4.5 shows that the direct-storage configuration allows for a substantial simplification of the overall layout of the plant, with a beneficial effect on its initial cost.

4.5 Case Study

In order to evaluate the proposed integrated TES system for small-scale solar ORC power plant, the system of figure 4.4a ($\dot{W}_{net}$=100 kW_E) has been studied.
The ORC working fluid is circulated and heated in the SF, which is composed of parabolic trough collectors with evacuated absorber tubes: the feasibility of such concept has been preliminarily assessed in a recent study [46]. The main novelty is the adoption of one of the TES systems introduced in sec. 4.4: the working fluid serves also as the storage medium, making the configuration completely of the *direct* type. The selected TES system is based on a displacement-type storage, with vapour generation through external flashing (type A1 in fig. 4.3).

The concept is aimed at maximizing the simplicity of the plant layout, since lowering of initial cost and maintenance requirements, as well as ease and safety of remotely controlled operation, are considered as key aspects for distributed power applications.

The design data adopted here are reported in table 4.2: the general specifications are common to all the ORC plants modelled in this study (see also A.1 and A.2). A relatively high value of the condensing temperature T_{cond} is chosen, since avoiding excessively low vacuum levels in the condenser is mandatory in high temperature applications, because the presence of air due to inward leaking accelerates the thermal degradation of the working fluid.

The data specific to the proposed exemplary system in terms of fluid and operating conditions, have been determined based on the treatment described in A.1 and A.2, where the main trade-off existing between system efficiency, plant simplification, and components design are discussed in detail. Realistic assumptions regarding both the design of the dry air-cooled condenser and of the plates-regenerator are considered. This information has been obtained from the preliminary design of these components, performed with a commercial package for heat exchanger design [51].

4.5.1 Working Principle

In nominal conditions, the temperatures at the outlet of the solar field $T_{out,SF}$, and in the hot region of the storage vessel $T_{ST,hot}$ (which, in turn, equals that of the fluid fed to the ORC system), are considered to be both equal to T_c. For modelling purposes this is chosen as the main operating variable (see A.1 and A.2), while p_c is supposed to be maintained at a level higher than the corresponding vapour pressure, by an external pressurizer (1 bar in design conditions).

Cold fluid is extracted from the vessel (*b*) and pumped through the SF: under normal operating conditions the mass flow is controlled by acting on the pump in order to maintain a set outlet temperature T_c. Also in this case the temperature at the outlet of the regenerator $T_{ORC,out}$, and that of the stored cold fluid $T_{ST,cold}$, are assumed to be equal to T_b. The hot fluid extracted from the storage vessel (*c*) is externally flashed to saturated vapour conditions, before being fed to the ORC turbogenerator (*d*, with q_d = 1, see Sec. Ia). The superheated vapour leaving the turbine enters the regenerator (*e*), and then the condenser (*f*). The fluid, in saturated liquid conditions (*a*), is then pumped back, through the regenerator, to the bottom part of the storage vessel (*b*).

The mass flow circulating in the SF is determined by the available irradiation together with the area of the collectors which, in turn, is related to the chosen solar multiple (SM). Optimal combi-

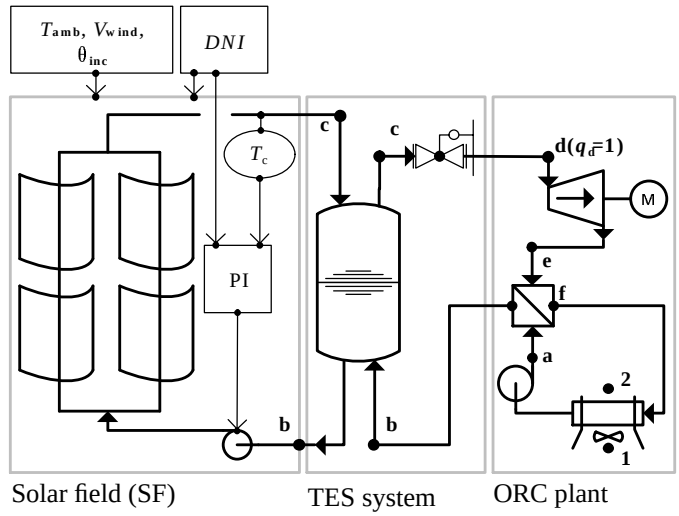

(a)

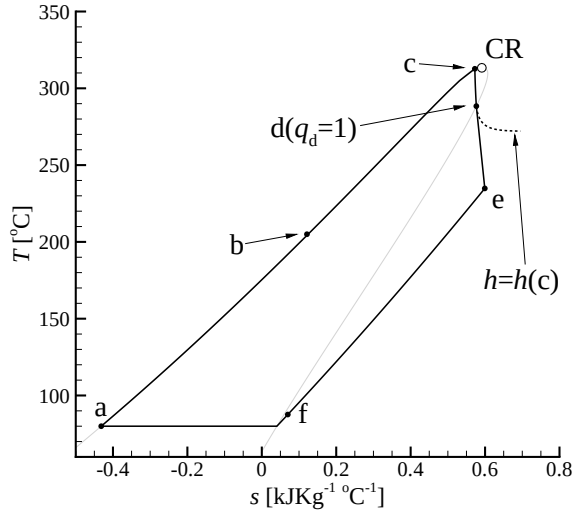

(b)

Figure 4.4: (a) simplified plant layout of a CSP ORC power plant working according to the single-stage flash process, integrating a direct TES system based of the displacement-storage type, from [47]. (b) cycle state points in the T–s thermodynamic diagram of D_4 (black points and solid-black lines). CR: liquid–vapour critical point, solid-gray line: contour of the vapor-liquid equilibrium region, dashed: iso-enthalpy line.

nations of SM and storage-vessel size can be determined only through detailed techno-economic

Solar field design data			
HCE	Schott PTR-70	SCA	ET-150
$\eta_{opt,p}$	0.75	DNI_{des} [W m^{-2}]	850
θ_{inc} [°]	0	T_{amb} [°C]	25
V_{wind} [m s^{-1}]	0	$\Delta p_{b'c'}$ [bar]	1
SM	1		
Main design data for the ORC plants			
$\dot{W}_{net}$ [kW_E]	100	$h_{eq,st}$ [hours]	4
T_{cond} [°C]	80	$\Delta_{pp,cond}$ [°C]	15
ϵ_{reg}	0.85	$\eta_{s,turb}$	0.85
$\eta_{s,pumps-fans}$	0.75	η_{M-E}	0.97
Δp_{ef} [$\%p_{cond}$]	50	Δp_{fa} [$\%p_{cond}$]	10
$\Delta p_{a'b}$ [bar]	0	Δp_{fan} [Pa]	50
Design data for the exemplary system			
Fluid	D_4	p_{cond} [bar]	0.035
$T_{R,c} = T_{R,st}$	0.998	$T_c = T_{ST}$ [°C]	312.6
$p_c = p_{ST}$ [bar]	14.2		
Calculated design performance of the exemplary system			
$\dot{m}_{fluid}$ [kg s^{-1}]	1.81	$\dot{m}_{air}$ [kg s^{-1}]	8.61
η_{ORC}	0.251	$\eta_{SF,glob}$	0.71
$\eta_{SYS,glob}$	0.18	$A_{mirrors}$ [m^2]	704
VR_{turb}	246	EEED [kWh_E m^{-3}_{ST}]	6.2
V_{ST} [m^3]	65	$m_{fluid,st}$ [kg]	$3E^4$

Table 4.2: Design data for steady-state modelling, common to all the simulated systems (see also A.1 and A.2). For a detailed description of the adopted HCE and SCA technologies, see Refs. [48, 49]. $\Delta p_{b'c'}$: pressure drop in the SF, $\Delta_{pp,cond}$: pinch point temperature difference in the condenser, ϵ_{reg}: regenerator effectiveness [50], η_{M-E}: electro-mechanical efficiency of the generator and of all the electrical motors. Δp_{ef}, Δp_{fa}, $\Delta p_{a'b}$, and Δp_{Fan} : pressure drops in the regenerator (vapour side), in the condenser (process side), in the regenerator (liquid side), and in the condenser (static, air side) respectively.

optimization [41, 52]. The values adopted here have therefore to be considered as indicative.

4.5.2 Flashing Rankine Cycles with Organic Fluids

The main implication of the working principle presented in Sec. 4.5.1 is that the plant *always* operates according to a thermodynamic cycle which includes a flashing evaporation process while,

usually, the flash process is adopted only when the storage is being discharged [27]. Referring to figure 4.1, the "flashing cycle" (FC) of the working fluid in the temperature-entropy diagram is identified by the state points *a*, *b*, *c*, *d* (with $q_d = 1$), *e*, *f* ($1, 2, 3, 3_{vs}, 4$ for water). When evaluated for the exploitation of thermal energy sources whose thermal capacity can be assumed as infinite, such power cycles feature an inherently lower efficiency compared to the corresponding evaporative cycle operating between the same maximum and minimum temperature (state points *a*, *b*, *c*, *g*, *h*, *f*, and $1, 2, 5, 6$ for water) [40]. However, if the working fluids is an organic compound, it can be shown that the efficiency penalty affecting the flashing cycle may be comparatively low. A detailed treatment is reported in A.1. Flashing ORC power systems for waste-heat recovery applications have been recently investigated by Ho and colleagues [53].

The flashing cycle boasts notable benefits in case of a solar ORC power system with thermal storage: i) it avoids phase transition in the SF, with major advantages [46, 54, 55]; ii) it decouples the SF and the ORC power block by means of a suitable direct thermal storage system, see figure 4.4a. A minor efficiency reduction can thus be accepted, in view of the substantial simplification it allows for, both in terms of plant layout and operation.

4.5.3 Flashing the Organic Vapor Down to Saturated Conditions

A further simplification of the plant configuration derives from the possibility of reaching complete vaporization of the working fluid by flashing (see sec. 4.2, point Ia). In this way several components become redundant, namely the flashing vessel and the liquid drain circuit. More details are provided in A.2. To the authors' knowledge, ORC power systems working according to the flashing cycle principle, whereby the working fluid is throttled down to saturated vapour conditions before entering the turbine, refer to figure 4.4b, have not been considered before, thus this concept is named here *complete flashing cycle* (CFC).

4.5.4 Design Analysis Results

The steady state modeling of the system is performed with an in-house code implemented in a well known computer language for technical computing [56], coupled with an in-house library for the accurate estimation of the thermophysical properties of the fluids [21]. The calculated performance is reported in table 4.2, while table 4.3 shows the thermodynamic properties of the state points of the thermodynamic cycle. Notwithstanding the selected high design value for T_{cond}, the calculated efficiency of the ORC power system exceeds 25% which, combined with the efficiency of the SF, yields a global efficiency in design conditions close to 18%. This value can be compared to the measured values of recently-built state-of-the-art CSP plants. These steam power plants are much larger, and adopt an indirect storage system with synthetic oil as HTF, and their efficiency is of the order of 22% [57].

Even if no index of annual performance has been estimated yet, ORC power systems are characterized by excellent off-design performance. This characteristic can partially overcome the lower design efficiency in a highly dynamic application such as CSP [46].

The calculated values of equivalent electrical energy density (EEED) storage are lower than those characterizing traditional TES solutions, and this holds for all the considered working fluids (see fig. 8). The proposed system approaches, for the EEED, the limiting value of 6.2 [$kWh_E\ m_{ST}^{-3}$], see table 4.2, assuming that the storage vessel delivers its full energy content without any variation in the discharged fluid properties (conditions corresponding to state *c*). Thermal losses, as well as exergy losses due to deterioration of the stratification [58] are thus neglected: such simplifications

Table 4.3: Thermodynamic properties of the state points of the ORC system. State labels refers to the layout of fig. 4.4a and to the T–s diagram of figure 4.1a. States 1 and 2 refer to the cooling air stream.

state	T [°C]	p [bar]	v [$m^3\ kg^{-1}$]	h [$kJ\ kg^{-1}$]	s [$kJ\ kg^{-1}\ k^{-1}$]	q [$kg_{sv}\ kg_{tot}^{-1}$]
a	80.0	0.04	0.001	-172.6	-0.43	0
b	205.6	14.20	0.001	59.1	0.12	-
c	312.7	14.20	0.002	291.8	0.56	-
d	283.2	8.49	0.011	291.8	0.57	1
e	234.9	0.06	2.489	233.6	0.59	-
f	87.6	0.04	2.551	4.5	0.07	-
1	30.0	1.01	0.880	0.0	-	-
2	67.0	1.01	1.052	37.2	-	-

are typically justified for daily charge-discharge cycles (relatively short standstill times). A recently designed displacement storage system using synthetic oil as HTF, and proposed as an add-on to the APS Saguaro ORC-based CSP plant [15], reaches the value of approximately 15 [$kWh_E\ m_{ST}^{-3}$] [59]. The lower value calculated for the proposed system is mainly due to the low specific work extracted from the turbine, which causes the fluid to be injected back in the storage vessel at high temperature ($T_b \equiv T_{ORC,out}$).

4.5.5 Dynamic Modelling

In order to study the dynamic performance of the plant and its control system, a modular dynamic model has been developed using the *Modelica* object-oriented modelling language [60]. The models of the ORC plant components have been taken from the recently developed *ORC* library [61], which is in turn based on the *ThermoPower* library [62, 63], while the models for the TES system and for the solar field were developed specifically for this work, possibly in combination with existing library models (as in the case of the solar collectors). The momentum equation is always implemented in the stationary form, being the propagation of pressure disturbances much faster than the process of mass and energy transport. Pressure and specific enthalpy are selected as state variables, and all closure equations (pressure loss, heat transfer models, and fluid properties) are expressed as a function of (p, h). All the needed fluid properties (and their derivatives) are computed with the *ExternalMedia* library [64] coupled to *Fluidprop* [21]. The dynamic models of the system components, as shown in figure 4.4a, are shortly described in A.3.

4.5.6 Control Strategy

As mentioned in §4.5.5, the models of a few components in the system implicitly account for ideal control of some local quantity by appropriate means, as detailed in A.3. The solar field pump model incorporates an ideal mass flow controller (e.g., by acting on the pump rotational speed or on a throttling valve), while the component modelling the flashing valve an ideal controller of the outlet

steam quality. Both the model of the dry condenser and of the stratified storage tank embed an ideal pressure controller, i.e. able of maintaining always the imposed pressure value without any dynamic characteristic. This is appropriate for the level of detail of the present study, where the main focus is on the dynamics of the temperatures in the solar field and in the storage tank.

The control strategy selected in this preliminary study aims at keeping the temperature at the outlet of the SF ($T_{out,SF}$) close to the nominal value under transient conditions. This ensures that the storage tank is always loaded from the top with fluid at the design temperature, thus avoiding as much as possible mixing phenomena that could reduce the efficiency of the downstream ORC system.

The open-loop dynamic response of $T_{out,SF}$ to variations of the pump flow rate strongly depends on the value of DNI: at low irradiation, the flow rate must be reduced to keep the outlet temperature constant, so the system dynamics become slower. However, the analysis of a linearized simplified model of this system (which is beyond the scope of this chapter) shows that its frequency response does not change much with DNI in a frequency range slightly above τ^{-1}, where τ is the residence time of the fluid in the solar field at nominal DNI. This allows to tune a fixed-parameters proportional-integral (PI) controller with a crossover frequency $\omega_c = 2\tau^{-1}$ in that particular frequency range.

In order to further improve the control performance, feed-forward compensation of the effects of DNI has been added to the controller output. The computation follows the assumption of negligible heat losses from the SF to the ambient; this of course relies on the possibility that DNI readings from an accurate pyrheliometer are available to the control system.

Finally, a lower saturation limit has been applied to the controller output, in order to prevent the flow rate from becoming too small for very low DNI, which could be dangerous in case of abrupt solar irradiance increases such as, e.g., when a cloud leaves the field. For the present study, the low limit is set at 1.0 kg s^{-1}, with the nominal value being 2.7 kg s^{-1} and the maximum value being 4.5 kg s^{-1}.

4.5.7 Dynamic Analysis Results

The complete model introduced in sec. 4.5.5, and controlled according to the scheme described in sec. 4.5.6, is used to study the dynamic performance of the case-study plant working as outlined in sec. 4.5.1. As anticipated, the main goal is to assess if the whole system can be safely and efficiently operated through automatic control procedures.

From the point of view of safe operation, the main concern regards the possibility of thermal decomposition of the working fluid to occur: for D_4 the limit is close to 400°C $= T_{max}$ [16].
Due to the favourable properties of silicon oils, the corresponding heat transfer coefficient is large enough to prevent, under all the foreseeable operating conditions, the wall temperature to exceed T_{max} [46].
However, as a consequence of the adopted control strategy, a drop in the mass flow circulating in the SF follows a reduction of the solar input: a subsequent sharp increase in the DNI may thus cause the limit of T_{max} to be exceeded somewhere along the absorber, on the internal wall surface (T_{wall}).

From the efficiency point of view, keeping the outlet temperature from the SF $T_{out,SF}$ close to the nominal value allows to preserve the stratification in the storage vessel: the turnaround efficiency of the TES system is consequently increased, and the power block can be operated in conditions close to the design ones for a larger number of hours.

The virtual plant is thus tested under a situation representative of extreme working conditions [65], whereby a series of clouds (3 in this example) causes the solar input to periodically drop,

and than sharply return to the nominal value. This effect is modelled by applying a signal with subsequent ramps to the DNI input of the solar field model (see fig. 4.5): the DNI is supposed to drop down to 10% of its nominal value, perturbing the initial steady state condition (design point, storage fully charged). The monitored quantities are the electrical power $\dot{W}_{E,net}$, the mass flow circulating in the SF $\dot{m}_{SF}$, the temperatures $T_{out,SF}$ and $T_{ST,hot}$, and the maximum wall temperature along the absorber $T_{wall,max}$.

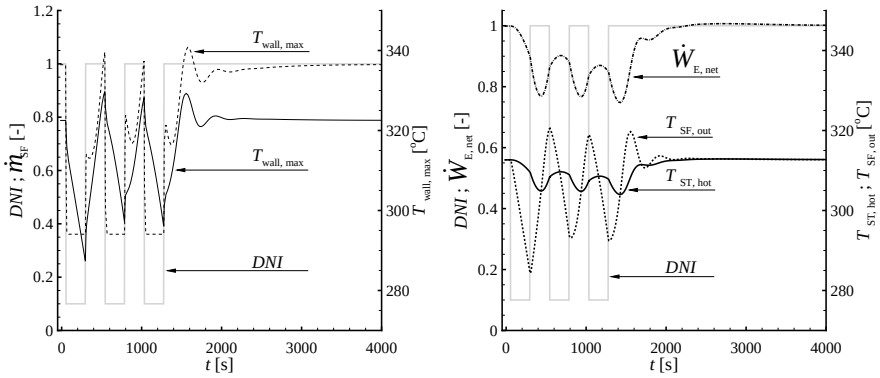

(a) (b)

Figure 4.5: Dynamic simulations results, for the virtual solar ORC plant, under time-varying solar input. The black dotted line represents the non dimensional DNI (with respect to its nominal value): it drops to 10% its nominal value in 5 s, remains constant for 240 s, then returns to its nominal value in 5 s; the interval between two subsequent drops is approximately 230 s. 4.5a black solid line: $\dot{m}_{SF}$; red dash-dotted line: $T_{wall,max}$. 4.5b black solid line: $\dot{W}_{E,net}$; red solid line: $T_{out,SF}$; red dashed line: $T_{ST,hot}$.

From the results reported in figure 4.5, it appears that the virtual plant is characterized by time constants which are large enough to lead to an overlapping effect of the disturbances, as already noted in previous works [65].

The variation of the controlled variable $\dot{m}_{SF}$ is shown in figure 4.5a. The ability of the simulated control system to maintain $T_{out,SF}$ close to its nominal value is proved: the maximum predicted range of oscillation around the design value is 25 °C (fig. 4.5b).
Also the temperature $T_{wall,max}$, which occurs in the last segment of the discretized collector for all the simulated conditions, remains within safe values and, in particular, it is always lower than its design value, see fig. 4.5a.
The effectiveness of the TES system in decoupling the ORC power block from the SF is assessed (fig. 4.5b): the oscillations in $T_{ST,hot}$ (corresponding to the turbine inlet temperature) are substantially damped with respect to those in $T_{out,SF}$: a maximum difference of about 10 °C is predicted. As a consequence, the maximum drop in the delivered power $\dot{W}_{E,net}$ is approximately 20%.

4.6 Conclusions

This chapter documents a study about extending direct flow-storage methods applicable to steam power plants to ORC power systems. So-called direct thermal storage systems are feasible, whereby the same fluid is circulated in the heat source, serves as thermal storage medium, and is also the working fluid of the ORC turbogenerator. A case study regarding a 100 kW_E solar plant implementing such concept is presented: the proposed system features a constant-pressure thermocline storage system, with vapour generation through external flashing of the liquid extracted from the storage vessel.

The thermal storage system can be integrated into the plant, thus decoupling the thermal energy source from the ORC power block: the system can be classified as *constant-parameters storage*, whereby the fluid enters and leaves the vessel (in principle) in the same thermodynamic condition, see states *c* and *b* in fig. 4.4a. Apart from a substantial simplifications in terms of both plant layout and operational strategy, this configuration ensures high exergetic performance of the thermal charge and discharge processes [27].

The power cycle operates according to a newly conceived variant of the Rankine cycle, whereby a flashing evaporation process precedes the power-generating expansion. The properties of the adopted complex-molecule working fluids are such that flashing can lead to saturated or superheated vapor conditions. This characteristic implies further simplifications of the system if compared to conventional steam power plant system with thermal storage. The efficiency of an ORC power plant working according to the newly introduced complete flashing cycle (CFC) may be, under the described assumptions, comparable to that of a conventional evaporative ORC power system.

A design value of the solar-to-electric efficiency of 18% is calculated for the exemplary 100 kW_E solar ORC power system with direct thermal storage and the flashing cycle configuration. The storage density values obtained with siloxanes as the working fluids are of the order of 10 kWh_E per m^3 storage, i.e. around half of what is typically achieved with the storage of diathermic oils. The advantages in terms of simplification of the plant layout could overcome the relatively low values of storage densities, the need of pressurization, and the specific cost of the fluids. To be noted also that the addition of storage filling materials, not considered in this work, is expected to be advantageous under these aspects.

A dynamic model, developed for the complete system, is used to investigate the performance under extreme transient conditions: the reaction to the passage of subsequent clouds, causing the solar input to drop to 10% of its nominal value, is simulated. A relatively simple and robust control strategy allows to maintain the working fluid temperature at the outlet of the solar field approximately constant, without risking thermal decomposition of the fluid itself. The storage system is demonstrated to be effective in decoupling the solar field and the ORC power block, which can thus be operated close to nominal conditions notwithstanding the environmental disturbances. The feasibility of remotely controlled operation is thus positively assessed by means of this preliminary study.

A detailed techno-economic analysis of the proposed system aimed at clarifying these open questions will be developed as the next step of the project. In order to improve system performance, particularly in terms of storage density, it might be worth investigating the binary cycle configuration, whereby direct thermal storage is implemented in the topping cycle.

A.1 Comparison Between Flashing and Evaporative Organic Rankine Cycles

This section presents the thermodynamic evaluation of the steady-state evaporative (EC) and flashing (FC) cycle configurations, as introduced in sec. 4.5. The effect of different working fluids is also addressed. The general design data, common to all the modeled ORC systems, are those reported in table 4.2, and figure 6 shows the conceptual plant layouts of the considered systems. The working principle is the same described in sec. 4.5, whereby the ORC power block shown in fig. 4.4a has been lumped here into a single component, and no storage system is considered. The thermody-

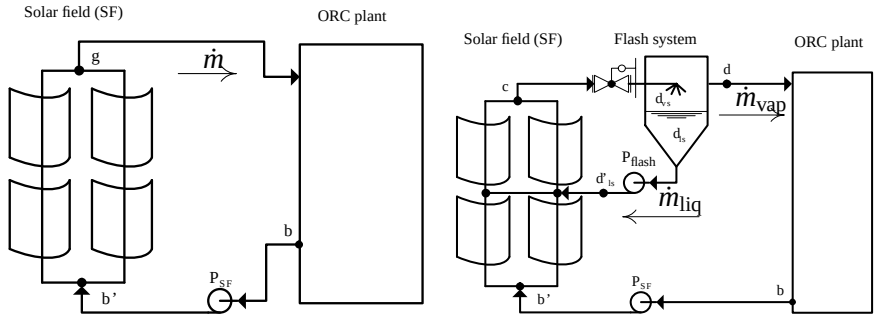

(a) EC (b) FC

Figure 6: (a) simplified plant layouts of ORC power systems working according to the conventional evaporative cycle, and (b) single-stage flash cycle. State points correspond to those in the T–s chart of fig. 4.1a.

namic evaluation is carried on by varying the maximum temperature of the cycle, which is kept the same, i.e., $T_{max} \equiv T_c = T_g$. It is further assumed that:

1. In the EC the working fluid exits from the thermal energy source (the solar field) as saturated vapor at T_{max}, i.e., state point g in fig. 6a;
2. In the FC the working fluid exits from the thermal source (c) in the state of saturated liquid at T_{max}, and then undergoes the flashing process. It is assumed here that the flash evaporation leads to saturated vapor conditions at the outlet of the flashing subsystem (process $c \rightarrow d$, where $q_d = 1$): a critical assessment of this assumption is presented in A.2. As a consequence, no liquid drains from the flash vessel have to be recirculated ($\dot{m}_{liq} = 0$).

From these assumptions follows that, for each value of T_{max}, all the state points defining the two thermodynamic cycles can be determined for a given working fluid. Note that the condensation temperature T_{cond} is fixed and specified. The results of the steady state simulations, performed with an in-house code implemented in a well-known language for technical computing [56], are presented in figures 7 and 8.

The main term of comparison is the global system efficiency $\eta_{SYS,glob}$, i.e. the solar-to-electric efficiency, defined as

$$\eta_{SYS,glob} \equiv \eta_{ORC} \cdot \eta_{SF,glob}, \tag{1}$$

where

$$\eta_{ORC} \equiv \dot{W}_{net}/\dot{Q}_{ORC,in} \tag{2}$$

is the thermal efficiency of the ORC system. $\dot{W}_{net} = \dot{W}_{turb} - \dot{W}_{aux}$ is the electrical power output of the plant, decreased of the power consumption for auxiliaries; $\dot{W}_{net}$ is constrained to be the same for all the simulated cases. $\dot{W}_{aux}$ is obtained by summing the power consumption of all the pumps (subscripts P in eq. 3) and the fans in the system and it is therefore evaluated as

$$\dot{W}_{aux} = \dot{W}_{P_{ORC}} - \dot{W}_{P_{SF}} - \dot{W}_{P_{flash}} - \dot{W}_{Fan}. \tag{3}$$

$\dot{W}_{P_{flash}}$ in eq. 3 is zero for both the EC and the FC systems (in this last case by virtue of assumption 2), since no liquid drains from the flash are present. $\dot{Q}_{ORC,in}$ is the thermal power supplied to the ORC system and, for the FC, it reads

$$\dot{Q}_{ORC-FC,in} = \dot{m}_{vap} \cdot (h_c - h_{b'}) + \dot{m}_{liq} \cdot (h_c - h_{d'_{is}}). \tag{4}$$

Here the 2nd term in the right-hand side vanishes because of assumption (2). In the EC case, equation 4 becomes

$$\dot{Q}_{ORC-EC,in} = \dot{m} \cdot (h_g - h_{b'}). \tag{5}$$

The global efficiency of the solar field is

$$\eta_{SF,glob} = \dot{Q}_{ORC,in}/\dot{Q}_{av}, \tag{6}$$

and it accounts for the optical and thermal efficiency. The thermal power made available by the direct radiation of the sun at the given design point is given by

$$\dot{Q}_{av} = DNI_{des} \cdot A_{SF}. \tag{7}$$

The area of the solar field A_{SF} can be evaluated as

$$A_{SF} = \dot{W}_{net}/[\eta_{ORC}(\dot{q}_{abs} - \dot{q}_{hl} - \dot{q}_{piping})] \tag{8}$$

All the terms of the denominator in eq. 8 represent thermal power specific to the m^2 of SF aperture area. $\dot{q}_{abs} = DNI_{des} \cdot \eta_{opt}$ is the thermal power absorbed by the collectors. Having assumed a null incidence angle for design calculations, the optical efficiency η_{opt} is equal to the peak value $\eta_{opt,p}$ [66]. $\dot{q}_{piping}$ accounts for thermal losses in the piping subsystem of the SF, and a value of 10 W/m^2 is assumed here [67]. $\dot{q}_{hl} = \mathcal{F}(T_{in,SF}, T_{out,SF}, \theta_{inc}, V_{wind})$ accounts for the thermal efficiency of the solar absorbers, and is evaluated according to the detailed procedure presented in Ref. [49][1].

Figure 7a shows $\eta_{SYS,glob}$ (eq. 1) as a function of T_{max}. In order to better compare different working fluids, reduced temperatures are used ($T_{R,max}$). As a consequence of the critical temperature increase with molecular weight (table 4.1), and being the condensing temperature the same for all the simulated cycles, more complex fluids attain higher efficiencies for a given $T_{R,max}$. As expected, being throttling a purely dissipative process, the FC efficiency for a given $T_{R,max}$ is always lower than that of the corresponding EC for the same working fluid. For all the fluids this penalty decreases for increasingly higher $T_{R,max}$, and tends to vanish with larger molecular complexity of the fluid.

It can thus be concluded that, if siloxanes are adopted as high temperature working fluids, and if the maximum cycle temperature is close to the fluid's critical temperature, the flash cycle configuration does not imply severe efficiency losses with respect to the traditional evaporative cycle solution.

[1]The coefficients adopted in the correlation proposed in the reference have been slightly modified, as a consequence of the different fluids and flow regimes, as discussed in Ref. [46].

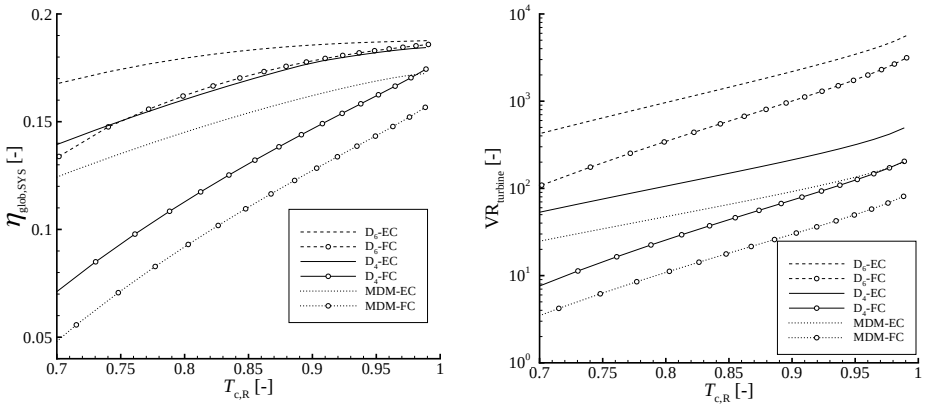

(a) Global system efficiency $\eta_{SYS,glob}$ as a function of $T_{R,max}$.

(b) Turbine volumetric expansion ratio VR_{turb} as a function of $T_{R,max}$.

Figure 7: Elements for comparison between corresponding evaporative and flashing ORC systems for different working fluids. In case of flash cycles, throttling down to saturated vapor conditions is assumed.

The quantity $\eta_{SYS,glob}$ can be considered as the key merit parameter in the comparison, since it is directly related with the area of the solar field and, thus, to the main cost-driver of any CSP installation [68]. However, also considerations about other critical components, such as the turboexpander and the storage system, should be accounted for in order to better define a suitable working fluid and the operating conditions for the given application. In particular the specific cost of the turbine, for small-scale ORC systems, strongly influences the cost of the power block. Figure 7b shows the turbine volumetric expansion ratio ($VR_{turb} = (\dot{V}_{in}/\dot{V}_{out})_{turb}$) as a function of maximum cycle reduced temperature $T_{R,max}$. The volumetric expansion ratio strongly influences the design/complexity of the expander and therefore its cost [69]. For a given fluid and $T_{R,max}$, the expansion due to the throttling process causes the enthalpy drop across the expander and VR_{turb} to be significantly lower in the FC than in the EC case. Smaller expansion specific work and smaller volumetric expansion ratio allow for the design of a more efficient turbine in the FC case than in the EC case, if the level of technology (therefore cost) is to be the same. Note that if higher turbine efficiency for the FC case is accounted for, the differences in $\eta_{SYS,glob}$ shown in figure 7a between the FC and EC configurations would be further reduced.

In case flashing is considered as the discharge method of an hypothetical storage system (see sec. 4.4.2), state *c* can be regarded as the state of the fluid extracted from the storage vessel, such that $T_{max} \equiv T_c = T_{ST}$. This holds for the case-study presented in §4.5, whose storage density EEED (see sec. 4.3) can be evaluated as

$$\text{EEED} = \frac{\dot{W}_{net}}{\dot{m}_{vap} + \dot{m}_{liq}} \cdot \frac{\rho_{ls}}{3600} \qquad [\text{kWh}_E\ \text{m}_{ST}^{-3}] \tag{9}$$

In this case, $\dot{m}_{liq}$ becomes zero because of assumption 2. This simplified approach assumes that the storage, initially fully charged with fluid in conditions corresponding to state *c*, delivers its full energy content without any variation in fluid properties. Thermal losses, as well as exergy losses

due to deterioration of the stratification [58] are thus neglected. Such simplifications are typically justified for daily charge-discharge cycles, that is for relatively short standstill times. The EEED

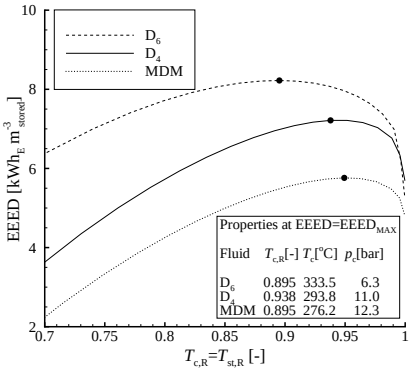

Figure 8: Comparison between flashing organic Rankine cycles for different working fluids. Throttling down to saturated vapour conditions is assumed. Equivalent electric energy density EEED as a function of maximum cycle reduced temperature $T_{R,max}$.

reaches a maximum value for all the working fluids considered here. This maximum value does not correspond to the maximum storage temperature; furthermore, the EEED line is quite flat in the region where the maximum is reached. The differences among fluids are comparatively large, as well as the conditions of the stored fluid in terms of pressure and temperature. In absolute terms, the reached values of EEED, of the order of 10 kWh_E m_{ST}^{-3}, are around half of what is typically achieved with the storage of diathermic oils [32, 59] but, as anticipated, no additional filling material is considered in this study.

In order to summarize these results, table 4 reports the main values obtained with the simulations that are needed to select the working fluid, if D_6 and D_4 are considered. Only these fluids are evaluated here since they allow for higher $\eta_{SYS,glob}$ values. The comparison is then carried on, aiming at the same value of $\eta_{SYS,glob}$, which is taken equal to the maximum value reached in case D_4 is the working fluid. Storing D_6 at higher temperature is not considered here given the corresponding extremely high values of VR_{turb}, though it allows for the higher values of $\eta_{SYS,glob}$ (up to 0.185).

As expected, the two working fluids allow attaining the same efficiency at almost the same value of T_c, which however corresponds to a storage pressure p_c 2.2 times larger in case D_4 is the working fluid. On the other hand, the condensing pressure in case D_6 is the working fluid is 16 times lower. Its very low value constitutes a design criticality for the condenser and the turbine. The volumetric expansion ratio of the turbine, for instance, is almost 4 times larger in case D_6 is the working fluid, whereby the inlet volumetric flows are similar.
The value of EEED is nonetheless 25% lower if D_4 is the working fluid, and the corresponding specific mass of fluid is 12% larger: these effects, combined with the higher pressure needed, would make D_6 the preferred working fluid if only the benefits for the thermal storage are considered.

	Fluid	
	D_6	D_4
$\eta_{SYS,glob}$	0.178	0.178
$T_{R,c}$	0.895	0.998
T_c [°C]	333.6	312.7
p_c [bar]	6.3	14.2
p_{cond} [bar]	0.002	0.035
VR_{turb}	954	246
EEED [$kWh_E\ m_{ST}^{-3}$]	8.2	6.2
m_{fluid} [$kg\ kWh_E^{-1}$]	66	74

Table 4: Main information needed to compare solar ORC power systems with thermal storage operating according to the flashing cycle, in case siloxane D_6 and D_4 are considered as the working fluids.

A.2 Complete Flash Evaporation as a Working Condition for ORC Power Systems

The analysis of the performance of a flashing ORC, see fig. 6b, as a function of the flashing conditions is presented in this section. Only the results for working fluid D_4 are reported, since they are representative of all the other investigated systems featuring siloxanes as working fluid. The system performance is evaluated according to the procedure and the parameters defined in A.1; in this case, however, no simplifying assumption based on the absence of liquid drains can be applied (see eq. 3 and 4): the liquid drains from the flashing vessel have to be compressed and circulated back to the heat source, see figure 6b. This stream is supposed to merge with the main one in the solar field, such that temperature equality between the flows is ensured, while the vapor is delivered to the ORC turbogenerator.

Figure 9a and 9b show the trends of the quantities of interest as a function of the flashing temperature $T_{flash} = T_d$, and the corresponding vapour pressure $p_{flash} = p_d$. Each curve corresponds to a given maximum temperature which, as discussed in A.1, can also be seen as the storage temperature $T_{max} \equiv T_c = T_{ST}$; the storage pressure is assigned a value of 1 bar higher than the corresponding vapor pressure ($p_{max} \equiv p_c = p_{ST}$). For each value of T_{max}, the value of T_d whereby complete flashing evaporation is reached (T_d for which $q_d = 1$) is also plotted (flash evaporation is considered as an isenthalpic process).

Figure 9a shows how, for each maximum temperature T_{max} , the system efficiency $\eta_{SYS,glob}$ initially grows for decreasing T_d until it reaches a relative maximum ($\eta_{SYS,glob,max}$): this is a consequence of the total mass flow which need to be circulated, see fig. 9b, and the corresponding power consumption of the auxiliary components.

As it is characteristic of CSP power systems, the thermal efficiency of the solar field $\eta_{SF,glob}$ is a decreasing function of the temperature of the fluid flowing in the collector. Since the value of $\eta_{SYS,glob}$ includes this effect, lower storage temperature (and pressure) levels lead to comparatively higher values of $\eta_{SF,glob}$; such an effect, however, does not counterbalance the concurrent decrease of η_{ORC}.

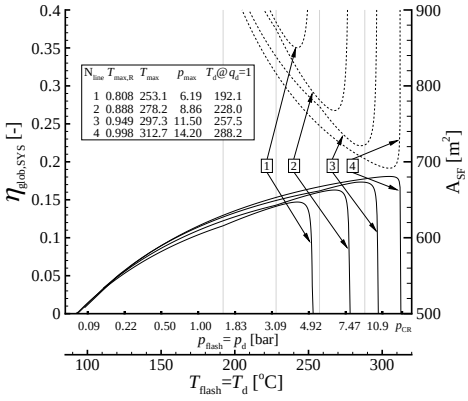

(a) Solid black lines: global system efficiency. Dashed black lines: area of the solar field.

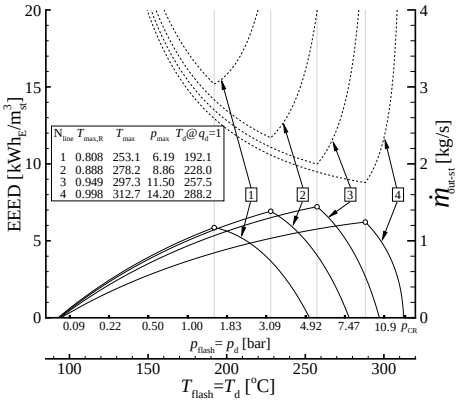

(b) Solid black lines: equivalent electrical energy density. Dashed black lines: total mass flow entering the flashing subsytem (i.e., extracted from the storage vessel)

Figure 9: Detailed analysis of the performance of a flashing-cycle ORC system, in case D_4 is the working fluid. For different maximum temperature levels ($T_{max} \equiv T_c = T_{ST}$), the quantities of interest are plotted as a function of the flashing temperature ($T_{flash} = T_d$); The corresponding vapor pressure is also indicated. For each value of T_{max}, the value of T_d whereby complete flashing evaporation is reached (T_d for which $q_d = 1$) is plotted as a solid grey line.

For increasingly higher T_{max}, the corresponding $\eta_{SYS,glob}$ values tend to become constant in the region where $\eta_{SYS,glob,max}$ occurs. This implies that, for higher values of T_{max}, extending the throttling down to saturated vapour conditions leads to a comparatively low efficiency decrease with respect to $\eta_{SYS,glob,max}$. Figure 9a shows the variation of the SF area A_{SF}, which, having imposed the system net power output, is directly related with $\eta_{SYS,glob}$.

If EEED (eq. 9) is considered, figure 9b shows how strongly this quantity is dependent upon T_d. The figure displays that a relative maximum of the EEED corresponds to the situation whereby the working fluid is flashed down to saturated vapor conditions. The locus of such maxima, for varying T_{max}, corresponds to the line for D_4 of fig. 8. Since this operating condition allows for important advantages (such as maximum storage density for the given T_{max}, and simplification of the flashing system layout), without implying noteworthy efficiency penalties, it can be considered as a reasonable working condition for a system implementing the FC configuration, especially when storage temperatures close to the critical temperature of the working fluid are considered.

A.3 System Components Dynamic Modelling

The dynamic models of the system components, as shown in figure 4.4a, are described in this section, following the treatment presented in Ref. [47].

SOLAR FIELD

The solar field is modelled as a single loop of parabolic collectors connected in series: the large ratio between length and diameter allows a one-dimensional (1D) discretization of the absorber tube. The finite-volume approach with an upwind scheme for mass flow and specific enthalpy is used [65]. The model is implemented connecting 2 sub−components: the *Flow1D* model available from the *ThermoPower* library [62], and the newly developed *SolAbs* model , which interacts through a distributed thermal connector [63].

Flow1D models the working fluid flow through the absorber, or heat collecting element (HCE), accounting for friction losses. The flow regime in the HCE is always turbulent, and the fluid-wall convective heat transfer coefficient U [$\mathrm{kW_T\ m^{-2}\ ^\circ C^{-1}}$] is modelled, in off-design condition, according to the relation $U = U_{\mathrm{des}} \cdot (\dot{m}_{\mathrm{fluid}}/\ \dot{m}_{\mathrm{fluid,des}})^{0.65}$.

SolAbs models the dynamic 1D thermal energy balance on a HCE cross section. It accounts for conduction and storage in the metal pipe, convection and radiation in the vacuum chamber between the glass envelope and the metal pipe, conduction and storage in the glass envelope, convection and radiation transfers with the ambient air [67]. *SolAbs* implements the relations between the environmental parameters (DNI, θ_{inc}, T_{amb}, and V_{wind}), and the axial temperature distribution along the absorber. Both the thermal power lost to the environment $\dot{q}_{\mathrm{hl}}$ (see A.1), and the power transferred to the fluid can thus be evaluated.

The pump circulating the fluid through the solar field is modelled by prescribing the flow rate passing through the machine (see also sec. 4.5.6), and by neglecting the specific enthalpy change across it. This follows the assumption that the dynamics of the recirculation pump is negligible compared to that of the solar collector, and that local flow controllers will be used in the solar field. The complete solar collector model has been validated with reference data from [67].

STORAGE SYSTEM

The thermocline storage is modelled following a 1D, finite volumes approach: the tank, supposed cylindrical, is discretized along its axis [70]. As anticipated, constant pressure is prescribed in the tank, thus implicitly accounting for an ideal pressurization system. The model evaluates changes in the volume of fluid, as a consequence of thermal expansion and mass balance. The implemented dynamic mass and energy balance equations account for the conductive heat transfer in the fluid and in the metal wall (along the vessel height), and the heat transfer between the wall and the fluid. Thermal energy storage in the metal wall is neglected, and three constant overall heat transfer coefficients are defined to model the thermal power lost to the environment from the top roof, the foundation, and the lateral walls of the tank. The four connecting flanges have a fixed position: the first volume to the top is linked to the outlet of the SF and to the inlet of the flashing valve, and the last volume to the bottom is connected to the outlet of the regenerator and to the inlet of the solar field pump. The turbulence mixing effects due to the introduction of the fluid on the stratification in the tank are neglected. Due to the numerical diffusion of the finite volume method, it is necessary to employ a fairly high number of nodes (at least $N = 30$) in order to model the thermocline that develops in the tank. Also note that the delay between the temperature changes at the top inlet and the corresponding changes at the top outlet is represented in the model as the dynamics of a well-stirred volume having $(1/N)^{\mathrm{th}}$ of the total volume, and is thus typically underestimated for such large values of N. This represents a worst-case scenario in terms of the burden imposed on the ORC system controllers by the fast variations of the SF outlet temperature. Since it is very hard to represent this dynamics accurately (detailed 3D CFD models would be required), this approximation is arguably the safest for a system-level dynamic model. The thermocline storage model has been validated based on experimental data from the open literature [70].

The valve performing the flashing process is modelled assuming ideal control of the thermo-

dynamic conditions at the outlet. More specifically, the pressure loss across the valve is implicitly determined by the following equation in the model: $h_{vs}(p_d) = h_c$, i.e., by assuming an isoenthalpic transformation such that the outlet conditions correspond to saturated steam ($h_{vs}(p)$ is the dew-point specific enthalpy as a function of pressure).

ORC POWER BLOCK

The turbogenerator model is implemented connecting the *ChockTurb* model [71], and the *ElecGen* model from *ThermoPower*. *ChockTurb* models a supersonic turbine as a *de Laval* nozzle, assumed to be chocked in all operating conditions. The result of the design calculation is the critical nozzle area (where sonic conditions occur) and, for off-design conditions, the relation between mass flow and inlet pressure is implemented (considering the expansion as isentropic). *ElecGen* only models the electrical generator, without accounting for any dynamics. Both the turbine isentropic efficiency, and the generator electro-mechanical efficiency, are considered constant.

The *PlateHXC* component models a counter−current plate heat exchanger: it is implemented connecting different sub−models from [62]: two *Flow1D* components, representing the fluid flow in the two sides of the exchanger, two *ConvHT* components modelling the convective heat transfer between the two streams and the interposed metal wall, and a *MetalWall* component modelling the heat conduction and the storage of energy in the metal parts.

The *DryCond* component models a condenser with ideal pressure control and negligible sub-cooling. This prescribes both the pressure and temperature on the main pump side, and the pressure at the regenerator side.

The pump of the ORC power block is equivalent to that of the solar field, previously described. In this case however, the circulating mass flow rate imposed to the pump is determined by the *ChockTurb* model.

The complete dynamic model of the ORC power block has been validated by comparison to transient data collected during a recent experimental campaign [61].

Nomenclature

s, p	=	spec. entropy [kJ kg^{-1} K^{-1}], pressure [bar]
T, h	=	temperature [°C], spec. enthalpy [kJ kg^{-1}]
u, ρ	=	spec. int. energy [kJ kg^{-1}], density [kg m^{-3}]
v, q	=	spec.volume [m^3 kg^{-1}], vapour quality [kg$_{sv}$ kg$_{tot}^{-1}$]
V, m	=	volume [m^3], mass [kg]
$h_{eq,st}$	=	equivalent hours of storage

Greek symbols

θ_{inc}	=	incidence angle [°]
ξ_{turn}	=	TES turnaround efficiency
$\eta_{opt,p}$	=	peak opt. efficiency
η_s	=	isoentropic efficiency
$\eta_{SF,glob}$	=	global solar field efficiency
$\eta_{SYS,glob}$	=	global (i.e. solar-to-electric) system efficiency
ω_c	=	crossover frequency

Subscripts

E, T	=	electric, thermal
M, des	=	mechanical, design conditions
CR	=	critical thermodynamic conditions (liquid-vapour)
R	=	Reduced (w/r to critical value)
amb	=	ambient conditions
sv, sl	=	saturated vapour, saturated liquid
turb, cond	=	turbine, condenser

Acronyms

TES	=	Thermal Energy Storage
CSP	=	Concentrated Solar Power
ORC	=	Organic Rankine Cycle
PV	=	Photovoltaic
HTF	=	Heat Transfer Fluid
DSG	=	Direct Steam Generation
O&M	=	Operations and Maintenance
VLE	=	Vapour Liquid Equilibrium
SF	=	Solar Field
ST	=	STorage
SYS	=	System
SM	=	Solar Multiple
HCE	=	Heat Collecting Element
SCA	=	Solar Collector Assembly
DNI	=	Direct Normal Irradiation [W m^{-2}]
EEED	=	Equiv. Elec. En. Density[kWh_E m_{ST}^{-3}]
VR	=	turbine Volumetric expansion Ratio
EC	=	Evaporative Cycle
FC	=	Flashing Cycle
CFC	=	Complete Flashing Cycle
CFD	=	Computational Fluid Dynamics

References

[1] V. Fthenakis, J.E. Mason, and K. Zweibel. The technical, geographical, and economic feasibility for solar energy to supply the energy needs of the US. *Energy Policy*, 37(2):387–399, 2009.

[2] PriceWaterHouseCoopers. 100 % renewable electricity – a roadmap to 2050 for Europe and North Africa. Technical report, 2010.

[3] M. Peters, T.S. Schmidt, D. Wiederkehr, and M. Schneider. Shedding light on solar technologies-a techno-economic assessment and its policy implications. *Energy Policy*, 39(10):6422–6439, 2011.

[4] P. Denholm and M. Mehos. Enabling greater penetration of solar power via the use of CSP with thermal energy storage. Technical Report NREL/TP-6A20-52978, National Renewable Energy Laboratory, 2011.

[5] IEA. Energy technology perspectives 2012. Technical report, International Energy Agency, 2012.

[6] H. Price and V. Hassani. Modular trough power plant cycle and system analysis. Technical Report NREL/TP-550-31240, National Renewable Energy Laboratory, 2002.

[7] E. Prabhu. Solar trough organic Rankine electricity system (STORES) stage 1: Power plant optimization and economics. Technical Report NREL/SR-550-39433, National Renewable Energy Laboratory, 2006.

[8] A. Skumanich. CSP at a crossroads: The first solar electric power plants are still proving their worth after three decades, so why aren't we seeing more CSP reach the development stage? *Renewable Energy Focus*, 12(1):52–55, 2011.

[9] C.A. Balaras, G. Grossman, H.-M. Henning, C.A. Infante Ferreira, E. Podesser, L. Wang, and E. Wiemken. Solar air conditioning in Europe-an overview. *Renewable and Sustainable Energy Reviews*, 11(2):299–314, 2007.

[10] F.A. Al-Sulaiman, F. Hamdullahpur, and I. Dincer. Trigeneration: A comprehensive review based on prime movers. *International Journal of Energy Research*, 35(3):233–258, 2011.

[11] G. Angelino, M. Gaia, and E. Macchi. A review of Italian activity in the field of organic Rankine cycles. In *VDI Berichte - Proceedings of the International VDI Seminar*, volume 539, pages 465–482, Düsseldorf, 10–12 September 1984. VDI Verlag.

[12] I. Obernberger and M. Gaia. Biomass-power-heat coupling based on the ORC process - state-of-the-art and possibilities for process optimization. *VDI Berichte*, (1891):131–148, 2005.

[13] L. D'Amelio. *Impiego di vapori ad alto peso molecolare in piccole turbine e utilizzazione del calore solare per energia motrice [On the use of high molecular weight vapors in small turbines and solar energy conversion into mechanical work]*. Industria Napoletana Arti Grafiche, 1935.

[14] Alain Verneau. Application of organic fluids in solar turbines [l'emploi des fluides organiques dans les turbines solaires]. *Entropie*, 14(82):9–18, 1978.

[15] S. Canada, D.A. Brosseau, and H. Price. Design and construction of the APS 1-MW_E

parabolic trough power plant. In *Proceedings of the ASME International Solar Energy Conference 2006*, volume 2006, Denver, CO, 2006.

[16] G. Angelino and C. Invernizzi. Cyclic methylsiloxanes as working fluids for space power cycles. *Journal of Solar Energy Engineering, Transactions of the ASME*, 115(3):130–137, 1993.

[17] DOW. SYLTHERM 800 Heat Transfer Fluid - Product Technical Data. Technical report, Dow Corning Corporation, 2012.

[18] R. Span and W. Wagner. Equations of state for technical applications. I. simultaneously optimized functional forms for nonpolar and polar fluids. *International Journal of Thermophysics*, 24(1):1–39, 2003.

[19] P. Colonna, N. R. Nannan, A. Guardone, and E. W. Lemmon. Multiparameter equations of state for selected siloxanes. *Fluid Phase Equilibria*, 244(2):193–211, 2006.

[20] P. Colonna, N. R. Nannan, and A. Guardone. Multiparameter equations of state for siloxanes: $[(CH_3)_3\text{-Si-}O_{1/2}]_2\text{-}[O\text{-Si-}(CH_3)_2]_{i=1,\dots,3}$ and $[O\text{-Si-}(CH_3)_2]_6$. *Fluid Phase Equilibria*, 263(2):115–130, 2008.

[21] P. Colonna, T. P. van der Stelt, and A. Guardone. FluidProp (Version 3.0): A program for the estimation of thermophysical properties of fluids, 2012. A program since 2004.

[22] E.W. Lemmon, M.L. Huber, and M.O. McLinden. NIST standard reference database 23: Reference fluid thermodynamic and transport properties-REFPROP, version 9.0. National Institute of Standards and Technology, Standard Reference Data Program, Gaithersburg, 2010.

[23] H. Tabor and L. Bronicki. Establishing criteria for fluids for small vapor turbines. In *SAE National Transportation, Powerplant, and Fuels and Lubricants Meeting*, October 1964.

[24] Costante M. Invernizzi. Closed power cycles - thermodynamic fundamentals and applications. In *Lecture Notes in Energy*, number 11. Springer-Verlag, 2013.

[25] C. Invernizzi, P. Iora, and P. Silva. Bottoming micro-Rankine cycles for micro-gas turbines. *Applied Thermal Engineering*, 27(1):100–110, 2007.

[26] A. Uusitalo, T. Turunen-Saaresti, J. Honkatukia, P. Colonna, and J. Larjola. Siloxanes as working fluids for a mini-ORC systems based on high-speed turbogenerator technology. *Journal of Engineering for Gas Turbines and Power-Transactions of the ASME*, 135(4):042305–1–9, April 2013.

[27] G. Beckam and P.V Gilli. *Thermal Energy Storage*. Springer–Verlag, 1984.

[28] J.F. Feldhoff, K. Schmitz, M. Eck, L. Schnatbaum-Laumann, D. Laing, F. Ortiz-Vives, and J. Schulte-Fischedick. Comparative system analysis of direct steam generation and synthetic oil parabolic trough power plants with integrated thermal storage. *Solar Energy*, 86(1):520–530, 2012.

[29] M. Medrano, A. Gil, I. Martorell, X. Potau, and L.F. Cabeza. State of the art on high-temperature thermal energy storage for power generation. part 2-case studies. *Renewable and Sustainable Energy Reviews*, 14(1):56–72, 2010.

[30] Solar Millenium. The parabolic trough power plants Andasol 1 to 3: The largest solar power plants in the world. Technical report, 2009.

[31] P.V. Gilli and G. Beckmann. Thermal energy storage for non–fossil power plants. In USA J. Silverman, University of Maryland, editor, *Energy Storage: a vital element in mankind's quest for survival and progress*. Pergamon Press, 1980.

[32] Pilkington Solar International GmbH. Survey of thermal storage for parabolic trough power plants. Technical Report NREL/SR-550-27925, National Renewable Energy Laboratory, 2000.

[33] S. Henchoz, F. Buchter, D. Favrat, M. Morandin, and M. Mercangöz. Thermoeconomic anal-

ysis of a solar enhanced energy storage concept based on thermodynamic cycles. *Energy*, 45(1):358–365, 2012.

[34] A. Bejan. *Entropy Generation Trough Heat and Fluid Flow*. John Wiley, 1982.

[35] R.J. Krane. A second law analysis of the optimum design and operation of thermal energy storage systems. *International Journal of Heat and Mass Transfer*, 30(1):43–57, 1987.

[36] A. M. Kandari. Thermal stratification in hot storage-tanks. *Applied Energy*, 35(4):299 – 315, 1990.

[37] D. Brosseau, J.W. Kelton, D. Ray, M. Edgar, K. Chrisman, and B. Emms. Testing of thermocline filler materials and molten-salt heat transfer fluids for thermal energy storage systems in parabolic trough power plants. *Journal Solar Energy Engineering*, 127:109–116, 2005.

[38] A. Gil, M. Medrano, I. Martorell, A. Lzaro, P. Dolado, B. Zalba, and L.F. Cabeza. State of the art on high temperature thermal energy storage for power generation. part 1-concepts, materials and modellization. *Renewable and Sustainable Energy Reviews*, 14(1):31–55, 2010.

[39] W. Goldstern. *Steam Storage Installation*. Pergamon Press, Oxford, 1970.

[40] R. Dipippo. *Geothermal Power Plants: Principles, Applications, Case Studies and Environmental Impact*. Butterworth Heinemann, 2^{nd} edition, 2008.

[41] P.V. Gilli and G. Beckam. Design and economy of solar plants with integrated thermal energy storage. In World Meteorological Organization, editor, *Proceedings of the Unesco/WMO Symposium on Solar Energy*, September 1976 1977.

[42] D.G. Elliott. Theory and tests of two-phase turbines. Technical report, Jet Propulsion Laboratory, California Institute of Technology, Pasadena, CA, 1982.

[43] EU. Final technical progress report of the European project NNE5-1999-356: Ps10 – 10 MW solar thermal power plant for Southern Spain. Technical report, European Union, 2006.

[44] W.-D. Steinmann and M. Eck. Buffer storage for direct steam generation. *Solar Energy*, 80(10):1277–1282, 2006.

[45] B. Li, S. Peuker, P.S. Hrnjak, and A.G. Alleyne. Refrigerant mass migration modeling and simulation for air conditioning systems. *Applied Thermal Engineering*, 31(10):1770–1779, 2011.

[46] E. Casati, P. Colonna, and N. R. Nannan. Supercritical ORC turbogenerators coupled with linear solar collectors. In *Proceedings of the* 30^{th} *ISES Biennial Solar World Congress 2011*, volume 5, pages 4056–4067, Kassel, 28 Aug.-2 Sept. 2011.

[47] E. Casati, A. Desideri, F. Casella, and P. Colonna. Preliminary assessment of a novel small CSP plant based on linear collectors, ORC and direct thermal storage. In *Proceedings of the* 18^{th} *SolarPACES conference*, 2012.

[48] A. Fernández-García, E. Zarza, L. Valenzuela, and M. Pérez. Parabolic-trough solar collectors and their applications. *Renewable and Sustainable Energy Reviews*, 14(7):1695–1721, 2010.

[49] F. Burkholder and C. Kutscher. Heat loss testing of schott's 2008 PTR70 parabolic trough receiver. Technical Report NREL/TP-550-45633, National Renewable Energy Laboratory, 2009.

[50] F. P. Incropera, D. P. DeWitt, T. L. Bergman, and A. S. Lavine. *Fundamentals of Heat and Mass Transfer*. John Wiley & Sons, Inc., 6 edition, 2007.

[51] Aspen Technology Inc. *Exchanger Design and Rating, ver. 7.2*. 2007. www.aspentech.com.

[52] J.M. Cabello, J.M. Cejudo, M. Luque, F. Ruiz, K. Deb, and R. Tewari. Optimization of the size of a solar thermal electricity plant by means of genetic algorithms. *Renewable Energy*, 36(11):3146 – 3153, 2011.

[53] T. Ho, S. Mao, and R. Greif. Comparison of the organic flash cycle (OFC) to other advanced vapor cycles for intermediate and high temperature waste heat reclamation and solar thermal

energy. *Energy*, 42(1):213 – 223, 2012.
[54] S.D Odeh, M. Behnia, and G.L. Morrison. Hydrodynamic analysis of direct steam generation solar collectors. *Journal of Solar Energy Engineering, Transactions of the ASME*, 122(1):14–22, 2000.
[55] M. Eck, W.-D. Steinmann, and J. Rheinländer. Maximum temperature difference in horizontal and tilted absorber pipes with direct steam generation. *Energy*, 29(5-6):665–676, 2004.
[56] The MathWorks Inc. *Matlab, ver. 7.13.0.564*. 2011. http//:www.TheMathworks.com.
[57] A. Giostri, M. Binotti, M. Astolfi, P. Silva, E. Macchi, and G. Manzolini. Comparison of different solar plants based on parabolic trough technology. *Solar Energy*, 86(5):1208–1221, 2012.
[58] M.Y. Haller, E. Yazdanshenas, E. Andersen, C. Bales, W. Streicher, and S. Furbo. A method to determine stratification efficiency of thermal energy storage processes independently from storage heat losses. *Solar Energy*, 84(6):997–1007, 2010.
[59] G.J. Kolb and V. Hassani. Performance analysis of thermocline energy storage proposed for the 1 MW Saguaro solar trough plant. In *Proceedings of the ASME International Solar Energy Conference*, volume 2006, Denver, CO, 2006.
[60] S. E. Mattsson, H. Elmqvist, and M. Otter. Physical system modeling with Modelica. *Control Engineering Practice*, 6(4):501–510, 1998.
[61] F. Casella, T. Mathijssen, P. Colonna, and J. van Buijtenen. Dynamic modeling of ORC power systems. *Journal of Engineering for Gas Turbines and Power*, 135:1–12, 2012.
[62] F. Casella and A. Leva. Modelica open library for power plant simulation: Design and experimental validation. In Peter Fritzson, editor, *Proceedings 3rd International Modelica Conference*, pages 41–50, Linköping, Sweden, Nov. 3–4 2003. Modelica Association.
[63] F. Casella and A. Leva. Modelling of thermo-hydraulic power generation processes using Modelica. *Mathematical and Computer Modeling of Dynamical Systems*, 12(1):19–33, Feb. 2006.
[64] F. Casella and C. Ritcher. ExternalMedia: a library for easy re-use of external fluid property code in Modelica. In B. Bachmann, editor, *Proceeding of the 6th International Modelica Conference*. Modelica Association, 2008.
[65] M. Eck and T. Hirsch. Dynamics and control of parabolic trough collector loops with direct steam generation. *Journal of Solar Energy*, 81:268–279, 2006.
[66] J.A. Duffie and W.A. Beckam. *Solar Engineering of Thermal Processes*. John Wiley & Sons, Inc., 3^{rd} edition, 2006.
[67] R. Forristall. Heat transfer analysis and modeling of a parabolic trough solar receiver implemented in engineering equation solver. Technical Report NREL/TP-550-34169, National Renewable Energy Laboratory, october 2003.
[68] R. Pitz-Paal, J. Dersch, B. Milow, F. Téllez, A. Fernere, U. Langnickel, A. Steinfeld, J. Karni, E. Zarza, and O. Popel. Development steps for parabolic trough solar power technologies with maximum impact on cost reduction. *Journal of Solar Energy Engineering, Transactions of the ASME*, 129(4):371–377, 2007.
[69] E. Macchi and A. Perdichizzi. Efficiency prediction for axial-flow turbines operating with nonconventional fluids. *Journal of engineering for power Transactions of the ASME*, 103(4):718–724, 1981.
[70] Y.H. Zurigat, K.J. Maloney, and A.J. Ghajar. Comparison study of one-dimensional models for stratified thermal storage tanks. *Journal of Solar Energy Engineering, Transactions of the ASME*, 111(3):204–210, 1989.
[71] F. Casella, T. Mathijssen, P. Colonna, and J. van Buijtenen. Dynamic modeling of orc power

systems. *Journal of Engineering for Gas Turbines and Power*, 2012. Accepted for publication.

5

Design Methodology for Flexible Energy Conversion Systems Accounting for Dynamic Performance

Part of the contents of this chapter appeared in:

L. Pierobon, E. Casati, F. Casella, F. Haglind, & P. Colonna
Energy **68**, 667-679 (2014)

Abstract *This chapter presents a methodology to help in the definition of the optimal design of power generation systems. The innovative element is the integration of requirements on dynamic performance into the system design procedure. Operational flexibility is an increasingly important specification of power systems for base- and part-load operation. Thus, it is crucial to discard, in an early phase of the design process, plant configurations which feature unacceptable dynamic performance. The test case is the preliminary design of an off-grid power plant serving an off-shore platform where one of the three gas turbines is combined with an organic Rankine cycle turbo-generator to increase the overall energy efficiency. At the core of the procedure is a stationary model, capable of performing the on-design thermodynamic cycle calculation, and the design of the components of the system. The results of these simulations are used within the framework of a multi-objective optimization procedure to identify a number of equally optimal system configurations. A dynamic model of each of these systems is automatically parameterized, by inheriting its parameters values from the design model. Dynamic simulations allow then to discriminate among the initial set of solutions, thus providing the designs that also comply with dynamic requirements.*

5.1 Introduction

The recent liberalization of the electricity markets, along with the rapid expansion of the utilization of non-dispatchable renewable energy sources, such as wind and solar radiation, is stressing the necessity-opportunity of improving the flexibility of power generation systems [1]. New power technologies play therefore a significant role in providing such flexibility, and the electricity industry has acknowledged that this need will increase in the near future [2]. In the case of base-load power plants, changes to the scheduling procedures are leading to the latest combined-cycle gas turbine units being designed to operate efficiently and reliably under a wide range of rapidly varying conditions. Furthermore, both new coal and nuclear power plants are conceived with increased capability of operating under fast-load variations. In addition, older power stations are retrofitted in order to increase dynamic operation performance [3]. Operational flexibility is mandatory for off-grid power systems, and often preserving high energy conversion efficiency is also demanded. The electrification of remote areas is widely studied [4], together with the powering of industrial installations with systems operating in island [5].

In this context, system dynamic modeling and simulation is becoming a powerful design tool, especially if the level of detail of system and component models can be tuned to the design needs. In a recent work, Garcia and colleagues investigated options to increase the robustness of energy networks, by simulating energy flow scenarios in which multiple forms of energy commodities, such as electricity and chemical products, may be exchanged [6]. They studied the interactions between the grid and such advanced hybrid energy systems, by using dynamic models of various units and simulating their operation. Concerning the detailed study of advanced power systems, Zhu and colleagues analyzed distributed combined cycle plants based on micro gas turbines and fuel cells, with the aim of reducing the costs related to ancillary services in a deregulated market [7]. A detailed model of a complete combined cycle, based on a steam Rankine unit cascaded to a gas turbine, developed in order to study and optimize its start-up procedure is presented in Ref. [8]. Model-based control techniques for the same type of power plant are dealt with in Ref. [9].
Notwithstanding the mentioned advancements, to the knowledge of the author the integration of dynamic performance analysis into the design process has not been considered yet.

Discarding plant configurations featuring unacceptable dynamic performance (e.g., ramp-up and -down time) at a very early design phase can be very valuable. A traditional design approach, mainly aimed at increasing steady-state efficiency, might lead to systems that cannot comply with

dynamic requirements, even if aggressive control strategies are pursued.

This chapter is aimed at the development of an automated preliminary design methodology in which system transient performance can be seamlessly evaluated together with other typical design requirements. In order to test the automated design tool, a relevant test case has been selected, namely the power plant of an off-shore oil and gas platform in the North Sea, operating off-grid. The problem consists in evaluating if it is possible to increase the efficiency of the three gas turbines (GTs) by installing an organic Rankine cycle (ORC) turbo-generator powered by the exhaust gases of one of the GTs, and still comply with stringent dynamic requirements.

This chapter is structured as follows: the novel design methodology is outlined in §5.2, while §5.3 deals with the description of the case study. A detailed description of the models is presented in §5.4. The results are thus reported and discussed in §5.5. Concluding remarks are given in §5.6.

5.2 Methodology

The objective of this study is to develop and demonstrate a methodology for the preliminary design of power generation systems that integrates the fulfilling of dynamic requirements into the automated procedure. This goal is attained by performing two main steps.

In the first step, N performance metrics are selected (e.g., the thermal efficiency, the overall system volume, the net present value), and a multi-objective optimization problem is solved in order to find a set of preliminary system designs which lead to optimal performance of the system at the rated operating point. The outcome is an N-dimensional Pareto front of system designs, which are optimal with respect to different objectives. In the second step, the dynamic performance of the system is assessed by simulating critical transients for each design on the Pareto front, and by verifying whether requirements and constraints involving dynamic variables are met or not. System designs which do not meet the dynamic requirements are discarded.

The end-result of the procedure is a reduced set of optimal system designs complying with the trade-offs between different objectives, while ensuring proper system operation during critical transients. Based on this result, properly informed decisions about the final system design can be taken, thus avoiding the risk of discovering criticalities of transient operation at later project stages, i.e., during detailed design, or even commissioning, when corrective action might be very expensive or impossible.

5.2.1 Multi-Objective Design Optimization

The design methodology utilized in the present chapter is described in detail in Ref. [10], where it is applied to the exemplary case of an ORC power system. The design algorithm is implemented using the Matlab language; several new features were added in the present thesis to the previous version of the program. The design procedure is briefly summarized here for the sake of completeness.

First of all, boundary conditions, which hold for all designs, are defined. For example, in the case of an ORC heat recovery system, these are the mass flow rate, temperature and composition of the flue gas source, the selection of the working fluid, and the choice of the components, such as once-through boiler, shell and tube recuperator, and condenser. The thermodynamic states at the inlet and outlet of each component can thus be identified by applying basic energy and mass balances. Subsequently, the design of the plant equipment, e.g., the number, length, and diameter of tubes in the heat exchangers, or the turbine flow coefficient, is carried out automatically, ultimately leading to the evaluation of the chosen performance metrics. An iterative procedure then explores the de-

sign space, looking for optimal design configurations. The multi-objective optimization approach based on a genetic algorithm (GA) is adopted in this case.

Such design procedure takes care of the typical trade-offs, such as, for example, the one existing between the improvement of turbine performance, i.e., by reducing pressure losses in the recuperator (counter-pressure at the turbine discharge), and the reduction of thermodynamic irreversibility in the heat exchangers. The first goal might be obtained by reducing the heat transfer surface without altering the flow velocity. However, such surface reduction would lead to a deterioration of the heat exchange (larger irreversibility), due to the larger temperature difference between the hot and the cold stream.

5.2.2 Assessment of Dynamic Performance

The set-up of the second step of the design procedure requires to identify critical scenarios involving system transients, e.g. sudden load changes, load rejections, or unit trips. Requirements on critical variables are formulated, such as rise time, settling time, damping, maximum deviation, maximum or minimum allowed value during the transient, etc.

A nonlinear dynamic model of the plant based on first principles is needed, in such a way that it can be parameterized starting from the detailed design data obtained from the first step of the procedure. An effective way to build such model is to use the fully modular approach of the equation-based, object-oriented modeling language Modelica [11]. On the one hand, this allows to carry out the modeling task reliably and in a short time, by leveraging on existing and well-tested libraries of reusable component models. On the other hand, the equation-based approach of the language makes it possible to easily customize the models for the specific requirements of the design problem at hand.

In most cases, the system dynamics is the result of the interaction between the inherent plant dynamics and the control system action, with the controller often playing a crucial role. The definition of the design parameters cannot be complete without the values of the controller parameters. It is then necessary to define control system tuning criteria leading to desirable or optimal performance, which can be applied automatically given the specific values of the design parameters. The assessment of dynamic performance can then be carried out automatically for each design point on the Pareto front, by first running the simulation code generated from the Modelica model with the specific choice of parameters and then checking if all the requirements on critical variables are met.

5.3 Case of Study

Off-shore oil and gas platforms are a proper case of study to incorporate the dynamics of the power generation system directly in the design phase, as they are typically equipped with stand-alone (island) power generation systems. Moreover, in off-shore applications, preventing a failure of the power generation system is crucial as it may cause a loss of oil and gas production and a drop of the economic revenue.

The case of study is the power generation system installed on the Draugen oil and gas off-shore platform, located 150 km off-shore from Kristiansund, in the Norwegian Sea. The platform, operated by A/S Norske Shell, produces natural gas, exported to Kårstø (Norway) via the Åsgard gas pipeline, and oil, which is first stored in tanks at the bottom of the sea and then exported via a shuttle tanker once every 1-2 weeks. Three Siemens SGT-500 gas turbines are installed on the platform, supplying an electrical base load of 19 MW_E. The power demand is increased up to 25 MW_E (peak load) during oil export. In order to guarantee a high reliability of the power generation system, two

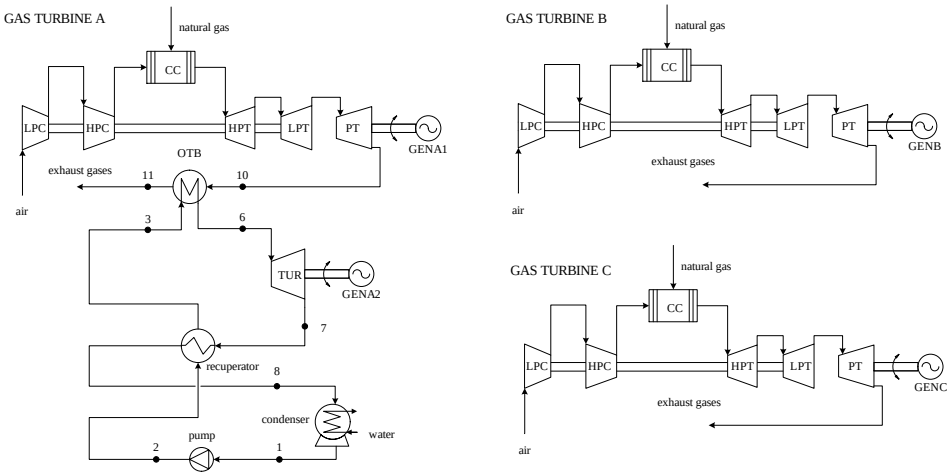

Figure 5.1: Simplified layout of the power generation system on the Draugen off-shore oil and gas platform. The organic Rankine cycle module is added to recover part of the thermal power released with the exhausts of turbine A.

turbines are kept in operation at all times, each covering 50% of the load, while the third is kept on stand-by, allowing for maintenance work. Despite the low energy conversion efficiency, this strategy ensures the necessary reserve power for peak loads, and the safe operation of the engines.

The design point specifications for the Siemens SGT-500 gas turbine are listed in Table 5.1 as provided by the manufacturer. The twin-spool engine employs two coaxial shafts coupling the low pressure compressor (LPC) with the low pressure turbine (LPT) and the high pressure compressor (HPC) with the high pressure turbine (HPT). The power turbine (PT) transfers mechanical power through a dedicated shaft to the electric generator (GEN).

Table 5.1: Design point specifications for the Siemens SGT-500 industrial twin spool gas turbine installed on the Draugen off-shore oil and gas platform.

Turbine inlet temperature [^{o}C]	850
Exhaust gas temperature [^{o}C]	379.2
Exhaust gas mass flow [kg s^{-1}]	91.5
Electric power output [MW$_E$]	16.5
Thermal efficiency [%]	31.3
Fuel	Natural gas

The performance of the power generation system may be enhanced by harvesting part of the exhaust thermal power from one or more engines, by means of an ORC unit [10]. Figure 5.1 shows the layout of the power generation system considered in this chapter. Preliminary calculations suggest that incrementing the installed power by adding two or three ORC units (one for each gas turbine) is not economically feasible. In fact, the utilization factor of the whole plant decreases in this case,

if compared to the layout given in Fig. 5.1. Therefore, only one ORC unit is considered as the bottoming unit for gas turbine A. Due to the relatively low temperature of the gas turbine exhaust (see Tab. 5.1), its thermal energy can be transferred directly to the ORC unit through the once-through boiler (OTB), without the need of an intermediate oil loop. Thus, the working fluid is first expanded in the ORC turbine (TUR), and subsequently cooled down in the recuperator. In this way the inlet temperature in the OTB may be increased by recovering energy from the superheated vapor exiting the turbine. The ORC fluid is then condensed and pumped up to the highest pressure level through the recuperator, thus closing the cycle. Based on the analysis performed in Ref. [10], the selected ORC working fluid is cyclopentane. This compound is already adopted for operating ORC systems in this range of temperature, see Ref. [12]. For the steady state calculations, thermodynamic and transport properties of cyclopentane are calculated according to the model implemented in a well-known program [13]. The same thermodynamic library is linked to the dynamic modeling tool by means of a specific interface for the Modelica language [14], and to the general interface to fluid property libraries Fluidprop [15].

It is assumed that in the new power generation system the base-load power demand (19 MW_E) is shared between the combined cycle (gas turbine A and ORC) and one gas turbine, while the other engine is on stand-by. As a net power output up to 6.4 MW_E can be harvested by the ORC turbo-generator, the load is split so that the combined cycle provides 13 MW_E and the remaining 6 MW_E are supplied by gas turbine B [10]. Note that the combined cycle alone could potentially cover the entire base-load power demand with a higher efficiency; however, this option is discarded since the necessary reserve power for peak loads would not be immediately available during normal operation, as it would require the ignition of one of the gas turbines. Moreover, the proposed configuration allows to stop the combined cycle for maintenance by running gas turbine B and C, each supplying 50% of the load.

5.4 System Modeling

5.4.1 Preliminary ORC Power Plant Design

As described in §5.2.1, the design procedure starts with the calculation of the thermodynamic states of the working fluid at the inlet/outlet of each component, see Fig. 5.1, by solving mass and energy balances, complemented by constitutive equations; the details of the non-linear system of equations can be found in Ref. [10]. At this stage, the gas turbine is modeled as a lumped thermal source, whose output constitutes the main input for the ORC turbo-generator design optimization. The characteristics assumed for the gas turbine exhaust stream are reported in Tab. 5.1. Figure 5.2 illustrates the T–s diagrams of two ORC power unit candidates obtained via the multi-objective optimization approach described in §5.5.1, while the results of the thermodynamic states calculation are listed, for one such candidate designs, in table 5.2.

HEAT EXCHANGERS

The heat exchange equipment is designed following the well-established standard procedure detailed in Ref. [16]. Compared to the work carried out in the previous work by Pierobon and colleagues [10], a new model of a once-through boiler has been developed and implemented. Moreover, since finned tubes have been foreseen in order to enhance the heat transfer process, specific correlations are utilized to evaluate the heat transfer coefficients and the pressure drops outside the tubes.

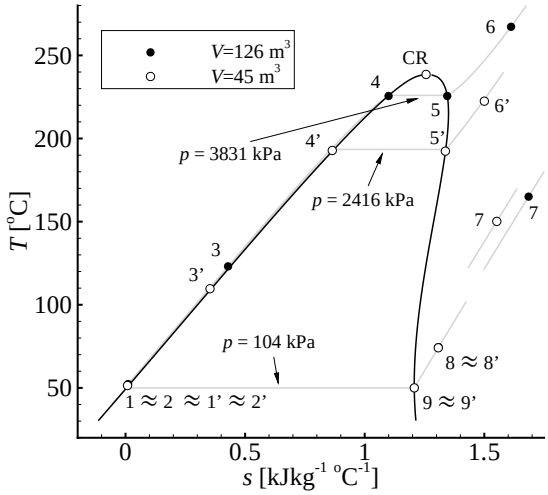

Figure 5.2: Saturation curve (black line) and cycle state points represented in the $T - s$ diagram of the working fluid cyclopentane (C_5H_{10}): MW = 70.1 [g mol^{-1}], T_{CR} = 238.5 [°C], P_{CR} = 4515 [kPa], ρ_{CR} = 272.6 [kg m^{-3}]. The states relative to two exemplary ORC systems are reported, characterized by a volume of 126 m^3 (filled dots) and 45 m^3 (empty dots). The gray lines represent selected isobars.

Table 5.2: Results of the thermodynamic states calculation for one exemplary ORC system characterized by a volume of 45 m^3.

state	T [°C]	P [kPa]	h [kJ kg^{-1}]	s [kJ kg^{-1} k^{-1}]	ρ [kg m^{-3}]	q [kg$_{sv}$ kg$^{-1}_{tot}$]
1	50.0	104.0	1.4	0.004	714.9	0
2	51.4	2416.0	5.9	0.008	716.2	-
3	104.9	2416.0	117.5	0.326	657.3	-
4	193.9	2416.0	348.4	0.871	511.4	0
5	193.9	2416.0	567.2	1.340	67.7	1
6	229.7	2416.0	659.8	1.531	53.4	-
7	143.0	104.0	535.4	1.600	2.1	-
8	74.1	104.0	423.8	1.308	2.6	-
9	50.0	104.0	390.0	1.207	2.8	1

The basic design procedure of heat exchangers requires determining the surface area by evaluating, through an iterative procedure, the overall heat transfer coefficient U_{out} defined as

$$\frac{1}{U_{out}} = \frac{1}{h_{out}} + \frac{1}{h_{out,f}} + \frac{D_{out} \log \frac{D_{out}}{D_{in}}}{2\lambda_{tubes}} + \frac{D_{out}}{D_{in}} \frac{1}{h_{in}} + \frac{D_{out}}{D_{in}} \frac{1}{h_{in,f}} , \tag{5.1}$$

where h is the convective heat transfer coefficient, and D is the tube diameter. λ_{tubes} is the thermal conductivity of the tubes material, while "f" refers to the fouling factor.

Regarding the once-through boiler, due to the high thermal resistance of the exhaust gases flowing outside the tubes, finned tubes are selected in order to enhance h_{out}. This is modelled by replacing the heat transfer and the fouling coefficients outside the tubes in Eq. (5.1) with a term involving the fins area and their effectiveness. Since the heat transfer occurs in both the single- and the two-phase region, specific equations must be adopted. In case of subcooled liquid and superheated vapor, the heat transfer coefficient inside the tubes is evaluated with the correlations proposed by Gnielinski [17]. The pressure drops related to single-phase flow are estimated using the method described in Ref. [16]. The heat transfer coefficient in the two-phase region is evaluated by discretizing the tubes into finite segments (typically 50) and thus applying the method proposed by Shah [18]. The gas-side heat transfer coefficient is evaluated through the approach proposed in Ref. [19], and the correlation derived therein for the air-side Nusselt number in a finned-tubes heat exchanger reads

$$Nu = 0.22\, Re^{0.6}\, Pr^{1/3}\, (A/A_{tubes})^{-0.15} , \tag{5.2}$$

where A is total heat transfer area and A_{tubes} is the outside tubes surface area including the fins.

The recuperator is considered to be of the shell-and-tube type, and modelled accordingly, by following Ref. [16]. The tubes are equipped with external fins, in order to enhance the heat transfer coefficient on the shell side, where the fluid is in the superheated vapour state. The corresponding Nusselt number is evaluated as

$$Nu = 0.134\, Re^{0.681}\, Pr^{1/3}\, ((p_{fin} - t_{fin})/l_{fin})^{0.2}\, (p_{fin}/t_{fin})^{0.1134} , \tag{5.3}$$

where p_{fin}, t_{fin}, and l_{fin} are the fin pitch, thickness, and length, respectively. The pressure drops on both sides for the single-phase regions within the tubes are estimated according to Ref. [16].

The total pressure drops occurring in the two-phase flow are estimated by dividing them into three contributions: the static one, vanishing for the proposed configuration (horizontal tubes), the kinematic one, and the one due to viscous friction. The last two terms are evaluated according to the methods proposed in Refs. [20, 21]. For the pressure drops outside the finned tubes the correlation presented in Ref. [22] is adopted. The equation is valid for banks of tubes in cross flow configuration, with plain transverse fins, and it can be used for both staggered and in-line arrangement.

SUPERSONIC TURBINE

The modeled expander is a turbine, which is usually the choice for ORC plants of the considered power capacity. These are usually one- or two-stage axial machines, leading to large pressure ratios across each stage; as a consequence, the flow is usually supersonic at the outlet of the first stator. The expander is therefore modeled as an equivalent choked de Laval nozzle, whose throat flow passage area is the sum of the throat areas of the nozzles constituting the first stator row.

Isoentropic expansion is assumed from the inlet section, where total conditions (i.e. total pressure $P_{T,6}$ and total temperature $T_{T,6}$) are assumed to be known by virtue of the thermodynamic state calculation, to the throat, where sonic conditions are attained, i.e., the flow speed equals the speed

of sound c. The corresponding equations are:

$$\begin{cases} s_6 = s(P_{T,6}, T_{T,6}) \\ h_{th} = h_{T,6}(P_{T,6}, T_{T,6}) - \frac{1}{2}c(h_{th}, s_6)^2 \\ \dot{m} = \rho_{th}(h_{th}, s_6) \cdot c(h_{th}, s_6) \cdot A_{th} \ , \end{cases} \tag{5.4}$$

where s_6 is the specific entropy at the turbine inlet, and the subscript "th" indicates the sonic throat section. The continuity equation relates the mass flow rate through the nozzle $\dot{m}$ to the density ρ_{th} and the flow passage area A_{th} in the throat section. By solving system (5.4) for given design conditions in terms of thermodynamic state and mass flow rate at the turbine inlet, the total nozzle throat area A_{th} can be evaluated.

5.4.2 Dynamic Modeling

The dynamic model of the combined cycle system is developed by using components from existing Modelica libraries. The gas turbine sub-system model is built by utilizing basic components included in the ThermoPower library [23], while the ORC system model adopts component models from the Modelica ORC library [24], with suitable adaptations regarding the heat transfer coefficients in the 1D once-through boiler model.

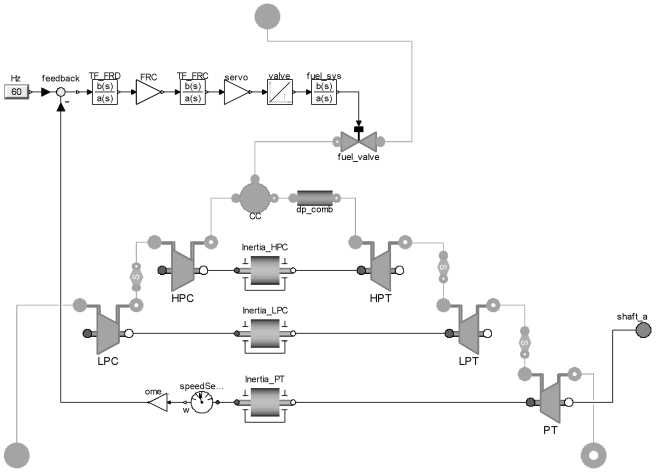

Figure 5.3: Object diagram of the gas engine sub-system.

Figure 5.3 shows the Modelica object diagram of the GT sub-system, which has fluid connectors for air intake, fuel inlet, and exhaust gas, and one mechanical connector for the power turbine shaft. Figure 5.4 shows the Modelica object diagram of the entire combined cycle system. Note that, according to object-oriented modeling principles, a-causal physical connections belonging to different domains (mechanical, thermo-hydraulic, electrical) are made between the different objects; input-output connections are only used for the control systems, which are inherently causal.

GAS TURBINE ENGINE

The low and high pressure compressors are described by quasi-static models, employing the maps

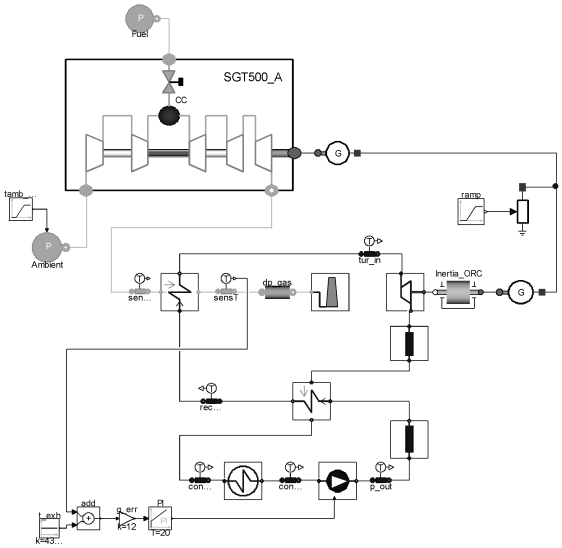

Figure 5.4: Object diagram of the entire combined cycle system.

of axial compressors provided with a commercial software [25]. The compressor maps used here are those originally presented in Ref. [26]. These maps are represented by tables reporting values for reduced flow, pressure ratio, isoentropic efficiency and speed of revolution for the complete operating range of the component. Following the methodology proposed in Ref. [27], the maps are scaled so that they can represent the part-load characteristic of the axial compressors of the SGT-500 gas turbine. For all the turbines, which have many stages, the Stodola equation is used to express the relation between inlet and outlet pressure, the mass flow rate and the inlet temperature in off-design operating conditions [28]. In order to predict the turbines off-design efficiency, the correlation relating the isoentropic efficiency and the non-dimensional flow coefficient proposed in Ref. [29] is utilized. The part-load performance of the electric generator is modeled using the equation proposed by Haglind [30].

The model of the combustion chamber assumes that the mixing and the combustion processes take place inside a constant volume. The mass and the internal energy of the volume are calculated using the thermodynamic properties of the combustion products exiting the combustion chamber. Mass and energy dynamic balances are formulated, by assuming complete combustion and no heat loss to the environment (adiabatic process). The pressure drops are lumped at the outlet of the combustion chamber and are estimated by assuming a quadratic dependency with respect to the volumetric flow. The Modelica mechanical connections between the compressors, shaft inertias, turbines, and generator connector allow to compute the variation of the angular speed of the low pressure, high pressure and power turbine shaft. The values of the inertia of the rotating masses (shaft, blades, generator) and the volume of the combustion chamber are set according to data provided by the gas turbine manufacturer.

ORC SYSTEM

The once-through boiler, which is one of the components of the object diagram of Fig. 5.4, is

implemented by combining basic ThermoPower modules, see Fig. 5.5: 1D flow models for the gas side (top) and fluid side (bottom of the figure), and the 1D thermal model for the tube bundle (middle). The exchange of thermal power is modeled with so-called 1D thermal ports (in orange in the figure); the counter-current model establishes the topological correspondence between the control volumes on the tube walls, and the control volumes on the gas flow model.

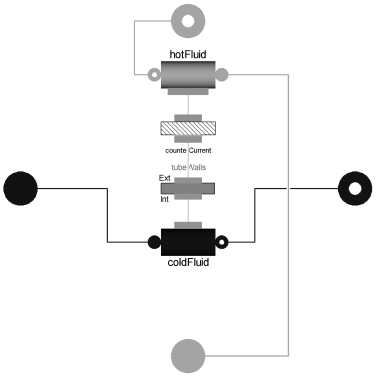

Figure 5.5: Modelica object diagram of the once-through heat exchanger model

The tube metal wall is modeled by a 1D dynamic heat balance equation, discretized by finite volumes. The flow models contain one-dimensional dynamic mass and energy balance equations, discretized by the finite volume method, assuming a uniform pressure distribution; the relatively small friction losses are lumped in an external component model. Here, the pressure drops in off-design conditions are estimated assuming a quadratic dependency from the volumetric flow, with the design point value set from the results of the detailed design step described in §5.4.1.

Since the focus of the dynamic analysis is to evaluate the plant performance during critic transients, the models for the convective heat transfer are simplified in comparison to the ones adopted for the heat exchangers design (see §5.4.1). Due to their relatively small contributions, the thermal resistance in the radial direction and thermal diffusion in the axial direction are thus neglected in the dynamic models. The heat transfer coefficient between the gas and the outer pipe surface is much lower than the one between the inner pipe surface and the ORC working fluid flow. Therefore, the overall heat transfer is essentially dependent on the flue gas side only, and the working fluid temperature is always close to the inner surface temperature of the pipe.

The heat transfer coefficient at the interface between the flue gas and the metal wall, in off-design conditions, is evaluated with the relation presented in Ref. [31], i.e.

$$\epsilon = \epsilon_{\text{des}} \left(\frac{\dot{m}}{\dot{m}_{\text{des}}} \right)^{n} , \tag{5.5}$$

where ϵ is the heat transfer coefficient, $\dot{m}$ the mass flow rate, and the exponent n takes the value 0.6. The thermal interaction between the wall and the working fluid is described by specifying a sufficiently high constant heat transfer coefficient, so that the fluid temperature is close to the wall temperature, and the overall result is dominated by the gas side heat transfer.

The model of the ORC turbine is the same as that employed in the design procedure (see Equations (5.4)). In this case, the throat passage area A_{th} is a fixed parameter obtained from the

design calculation. Hence, Equation (5.4) states the relation between mass flow rate and turbine inlet conditions, during off-design operation. The off-design isoentropic efficiency is expressed as a function of the flow coefficient $\Phi = \omega / \sqrt{2\Delta h_s}$, with ω being the speed of revolution, and Δh_s the isoentropic enthalpy drop across the expansion [29].

The recuperator is modeled by the counter-current connection of 1D ThermoPower modules, much as the once-through boiler, see Fig. 5.5. The heat transfer on the vapor side dominates, therefore the overall heat transfer coefficient is taken equal to that at the interface between the working fluid and the metal wall. Both the overall heat transfer and the pressure drops, in off-design conditions, are modelled as already detailed for the once-through boiler.

The condenser is trivially modeled as a fixed pressure component. This is justified considering the large availability of cooling sea-water, which allows the cooling circuit to be controlled in such a way that the condenser pressure is nearly constant. For simplicity, the condensate is assumed to leave the component in saturated conditions (no subcooling) with no pressure losses.

The pump model is based on a head-volume flow curve derived by fitting the data of an existing centrifugal pump designed for similar volumetric flows and heads. The curve is given as a function of $\alpha = \dot{m}\, \dot{m}_{\text{des}}^{-1} \cdot \rho_{\text{des}}\, \rho^{-1}$, and can be expressed as

$$H = H_{\text{des}} \cdot (b_1 + b_2\, e^{\alpha}) \cdot \left(\frac{\omega}{\omega_{\text{des}}} \right)^2 , \tag{5.6}$$

where H is the head and, in the present case, the coefficients assume the values $b_1 = 2.462$ and $b_2 = -0.538$. The monotonic exponential functional form increases the model robustness compared to typically adopted polynomial expressions. The isoentropic efficiency of the pump is expressed as a function of $\chi = \alpha \cdot \omega_{\text{des}}\, \omega^{-1}$, following Ref. [32].

The off-design electric efficiency of the ORC generator is calculated as for the case of the gas turbine generator, while the electro-mechanic efficiency of the pump motor is evaluated by assuming a quadratic dependency on the ratio between the actual the nominal load value.

CONTROL SYSTEMS

As explained in §5.3, the system under consideration operates off-grid. The alternating current (AC) grid-system of the off-shore platform is powered by the two synchronous generators connected to the gas and ORC turbines, which can be assumed to rotate at the same speed, as the electrical connections are very short. The gas turbine features the fastest load response, so it is used to control the network frequency (or, equivalently, the shaft rotational speed). As the low pressure and high pressure compressor are not equipped with variable inlet guide vanes, the load can only be controlled by opening or closing the fuel valve. The feedback controller included in the gas turbine sub-system (see Fig. 5.3) replicates the functional model provided by the gas turbine manufacturer, including the controller transfer function, and a simplified model of the fuel-system dynamic response, also given as a transfer function. Note that this controller is embedded in the GT unit and its parameters cannot be changed by the end-user, so the controller parameters are taken as they are in the context of this study.

The goal of the ORC control system is to target the maximum possible heat recovery from the GT exhaust, while ensuring that no acid condensation takes place, which might be particularly dangerous since also heavy fuels can be fed to the turbine combustor. This goal is attained by using the feed pump speed to control the temperature of the exhaust gases exiting the OTB at the design point value, which is as low as possible, yet high enough to avoid condensation. During stationary operation, the design of the heat exchanger is such that the highest temperature of the organic fluid, at the turbine inlet, is lower by a safety margin with respect to the thermal decomposition

temperature of the working fluid. In addition, the control system must ensure that this temperature does not exceed the safety limit anywhere in the high-temperature part of the ORC power plant during system transients.

The most critical operational transient from this point of view is the trip of gas turbine B: when this happens, the network frequency drops, so the GT controller reacts by opening the fuel valve to regain the set-point frequency. Consequently, the GT exhaust flow rate and temperature increase, leading to an increase of the OTB exhaust gases temperature, which is then counteracted by the ORC controller by increasing the feed flow to the OTB and thus, eventually, also the share of the load generated by the ORC system.

Preliminary simulations carried out with different designs of the system showed that, as expected, the dynamic response of the ORC system is much slower than the response of the GT system, even for aggressive designs of the temperature controller. This leads to significant and potentially unacceptable overshoot of the pump speed during the transient. This means that the peak value of the turbine inlet temperature (which is one of the critical variables of the process) is almost insensitive to the tuning of the ORC system controller. Such peak is quickly reached due to the fast response of the GT compared to the ORC system. In particular, the response time of the ORC power system is comparatively long since the flow rate through the turbine, and thus the generated power, change very slowly with the OTB pressure. This means that the contribution of the ORC controller to the limitation of the frequency undershoot is marginal.

Based on these considerations, the ORC Proportional-Integral (PI) controller was tuned in order to obtain the minimum possible settling time of the controlled variable, while avoiding the overshoot of the pump speed during the trip response transient and obtaining well-damped responses for all involved variables. The simulations showed that this is possible by setting the proportional gain to a value that is proportional to the heat exchanger volume, thus accounting for the process gain variability with the design parameters, while keeping the integral time at a suitable constant value.

5.4.3 Validation

The shell and tube heat exchanger design model, described in §5.4.1, was validated using an example proposed in Ref. [16]. The differences between the simulation results and the data reported in the reference are within 1% in terms of both overall heat transfer coefficient and pressure drops. For the once-through boiler it is verified that the heat transfer coefficients and the pressure drops related to both singe- and two-phase flow are within the range of values specified in Ref. [33].

The off-design, steady-state simulation results of the gas turbine model presented in §5.4.2 were compared to the partial load characteristics given by the gas turbine manufacturer in the 10%-100% range. Exhaust gas mass flow rate and temperature, fuel mass flow rate, and pressure in the combustion chamber were checked. The quantity showing the larger mismatch is the fuel mass flow: the relative error is about 3% for loads larger than 60%, and increases up to about 15% if the load decreases down to 10%.

The dynamic model of the gas turbine was validated by comparison with simulation results of the reference model provided by the gas turbine manufacturer, which is based on proprietary experimental data. The validation scenario assumes that the three GT units initially share a total load of 24 MW_E, delivering 8 MW_E each. At some point in time, one unit trips, so the other two ramp up their load in order to match the total power demand, with a transient reduction of the network frequency. The result of the simulations are compared in Fig. 5.6, which shows the normalized network frequency and the load of unit B. At time $t = 50$ seconds, one of the gas turbines trips; subsequently, the reference model predicts a minimum normalized frequency drop of

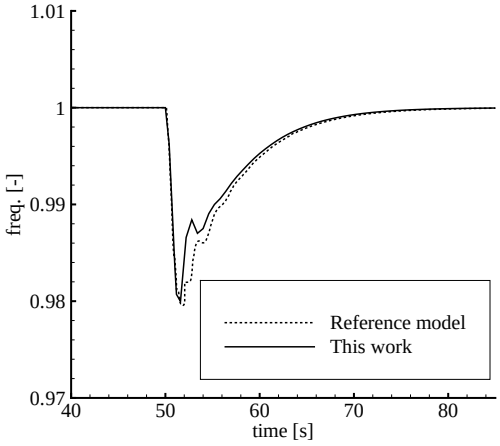

Figure 5.6: Dynamic validation results, normalized frequency vs time. Comparison between the reference model provided by the gas turbine manufacturer and the model developed in the present chapter.

0.0206 and a rise time of 5.5 s, while the model presented here gives a normalized frequency drop of 0.0202 and a rise time of 6.0 s. Based on this results, it is possible to conclude that the gas turbine dynamic model developed in the present chapter is able to reproduce both the steady-state and the dynamics of the gas turbine with reasonable accuracy, over the entire range of loads encountered during real operation.

The model of the ORC system is composed of software objects taken from a library that was developed in order to model a 150 kW ORC system using toluene as the working fluid, and successfully validated for transient operation against experimental data [24]. The developed models are therefore deemed reliable, considering the similarity of the application at hand with the one presented in the cited reference. Furthermore, it has been verified that the on-design and off-design steady-state operating points predicted by the ORC system model are consistent with those computed by the design tool described in §5.4.1.

5.4.4 The DYNDES Tool

The DYNDES computer tool couples steady state and the dynamic software models in order to provide an integrated program for the optimal design of power generation systems, including dynamic criteria. The two computer programs are interfaced by means of shared files and command scripts. More in detail, the results of the multi-objective design optimization is saved in an appropriate file, then the dynamic simulation program is run in command-line mode to: i) extract information from the design results file (e.g. the optimal design data relative to the geometry of the once-through boiler), ii) convert such data into parameters and inputs for the dynamic models, iii) run the simulations, and iv) save quantities of interest for further post-processing. Figure 5.7 shows the flowchart of the DYNDES tool.

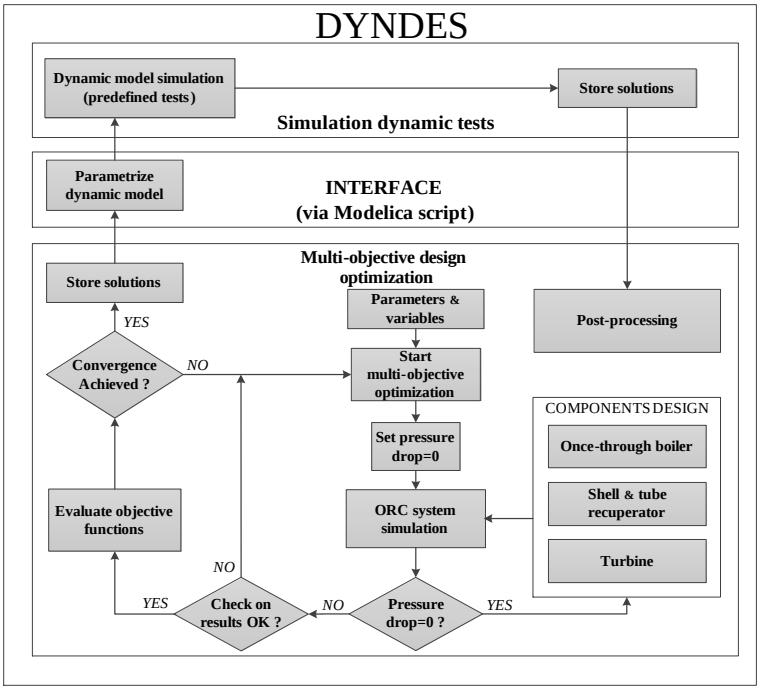

Figure 5.7: Architecture of the DYNDES design tool. The results of the multi-objective design optimization are utilized as inputs for the dynamic simulations of the power generation system. The software integrates the steady state and the dynamic model via a scripting command.

Starting from the same computing environment that is used for the steady-state model, the available multi-objective optimizer runs by first acquiring the array of the parameters and of the upper and lower bounds for the vector of the optimization variables $\bar{X}$, which in the case at hand reads

$$\bar{X} = [P_6, \Delta T_{\text{rec}}, \Delta T_{\text{OTB}}, T_{11}, D_{\text{OTB,in}}, t_{\text{OTB}}, l_{\text{OTB}}, u_{\text{exh}}, D_{\text{rec,in}}, t_{\text{rec}}, l_{\text{rec}}, p_{\text{rec}}, l_{\text{rec,b}}], \tag{5.7}$$

where P_6 is the turbine inlet pressure, $\Delta T_{\text{rec}} = T_8 - T_2$ the minimum temperature difference in the recuperator, and ΔT_{OTB} the temperature difference between the two streams in the once-through boiler, at the location where the ORC fluid is in saturated liquid condition. Note that this does not necessarily correspond to the so-called *pinch-point* of the heat exchanger, since the minimum temperature difference between the two streams in the OTB might also be located at its inlet. T_{11} is the lower temperature reached by the exhaust, see Fig. 5.1. The variables u_{exh}, $D_{\text{OTB,in}}$, t_{OTB} and l_{OTB} are the velocity of the exhaust gases, the inner diameter, the thickness and the length of the tubes of the once-through boiler. Similarly, $D_{\text{rec,in}}$, t_{rec}, and l_{rec} refer to the same quantities in the recuperator, while p_{rec} is the tubes pitch. The variable $l_{\text{rec,b}}$ indicates the baffle spacing given as a percentage of the shell diameter.

The objective functions chosen in the present analysis are collected in the array $\bar{J}$, i.e.

$$\bar{J} = [-\dot{W}_{\text{net,ORC}}, V_{\text{OTB}} + V_{\text{rec}}], \tag{5.8}$$

where $\dot{W}_{\text{net,ORC}}$ is the net power output of the ORC power unit, and the second metric accounts for the total ORC module volume which is determined by the more bulky components, i.e. the heat exchangers. The first term is selected in order to maximize the power output of the combined cycle plant while the latter term is added to the objective function since compactness represents a crucial design requirement in the considered application. The integration of dynamic simulations into the the automated design procedure allows to discard unfeasible designs. Since the dynamics of the condenser can be neglected for the reasons explained in §5.4.2, the volume of the condenser is not included in the second term of the objective function, see Equation 5.8.

The multi-objective optimization uses a controlled elitist genetic algorithm (GA) to search for solutions which minimize simultaneously the two objective functions [34]. Compared to gradient-based methods, a GA is less prone to converge to local minima of the problem. This typically comes at the cost of an increased computational cost, due to the large number of evaluations of the objective functions [34]. The GA parameters are specified as follows: population size equal to 200, generation size equal to 100, crossover fraction equal to 0.8, and migration fraction equal to 0.2. These numerical values are selected in order to ensure the repeatability of the solution when different simulations are performed, and are selected as suggested in Ref. [34].

Table 5.3 lists the upper and lower bounds utilized for the optimization variables, according to the limits reported in Ref. [16]. As the SGT-500 engine can operate on a wide range of both liquid and gas fuels, the limit temperature of the flue gas at the outlet of the OTB is set to 140 °C, in order to prevent the condensation of corrosive compounds. Supercritical cycle configurations are not considered here, and the upper bound for the turbine inlet pressure is thus set equal to 90% of the critical pressure of cyclopentane.

Table 5.4 lists the parameters which are kept constant during the multi-objective optimization. The fin profile and the configuration of the once-through boiler and of the recuperator are retrieved from Refs. [16, 33]. The condensing pressure of the working fluid is fixed to 1 bar, corresponding to a temperature of 50 °C, in order to avoid inward air leakage into the condenser.

Referring to Fig. 5.7, the calculation loop regarding the ORC module determines the thermodynamic states at the inlet and at the outlet of each component, as detailed in Ref. [10]. The pressure drops in the heat exchangers are initially set to zero. At this point the design procedure

Table 5.3: Design variables involved in the multi-objective optimization, with relative upper (UB) and lower (LB) bounds. The bounds relative to the tubes inlet diameter D_{in}, length l, and thickness t are assumed equal for the design of the once-through boiler and of the recuperator.

Variable	LB	UB
Turbine inlet pressure P_6 [bar]	5	41.1
Pinch point recuperator ΔT_{rec} [°C]	10	40
Temperature difference OTB ΔT_{OTB} [°C]	10	80
Exhaust gas temperature T_{11} [°C]	140	180
Inlet diameter of the tubes D_{in} [mm]	16	50
Length of the tubes l [m]	1.83	7.32
Thickness of the tubes t [mm]	1.6	3.2
Tube pitch p_{rec} [-]	1.1	1.3
Baffle spacing $l_{rec,b}$ [%]	20	100
Gas velocity u_{exh} [m s^{-1}]	10	70

of the once-through boiler and of the recuperator (see §5.4.1) is started, obtaining as outputs both the pressure drops and the design parameters of the components, which are then stored. The model of the ORC system is thus run again, but in this case the pressure losses in the OTB and in the recuperator are included in the computation. The results are then checked with respect to the second principle of Thermodynamics. It is also verified that the velocity in the tubes and on the shell side of the recuperator lies within the ranges specified in [16]. The process is repeated until the average change in the spread of the Pareto front is lower than the specified tolerance, which is assumed here equal to 10^{-3}. When the multi-objective optimization terminates, the inputs of the dynamic models are stored in a file that is then used by the dynamic simulator as previously explained.

The dynamic models are parametrized using the data for the heat exchangers and the turbine corresponding to the optimal ORC modules, as determined by the multi-objective optimization procedure. These models are then used to predict the dynamics of the complete system in a predefined transient scenario. Note that the number of dynamic simulations to be performed is equal to the number of points of the Pareto front.

The dynamic test, conceived to assess the dynamics of the complete system, consists in the simulation of the failure of a gas turbine unit. This has been defined according to the specifications of the platform owner, and represents the worst scenario the power system can possibly undergo without compromising the platform functionality. The same dynamic test is thus applied to all the design candidates previously defined.

It is assumed that the combined cycle (gas turbine A and ORC) and the gas turbine B are providing the normal load (13 and 6 MW_E each) while at time t_0 gas turbine B trips. Hence, the combined cycle undergoes a load increment of $\approx$ 1.2 MW_E s^{-1} (e.g. 6 MW_E in 5 s, see Figs. 5.8b and 5.10a) and must take over the entire power demand, until gas turbine C is ignited. The process ends by storing the desired outputs of the dynamic analysis (e.g., the maximum undershoot of the electrical network frequency) for each choice of system design. Finally, post-processing is performed within the software environment for scientific computing.

Table 5.4: Parameters assumed for the multi-objective optimization.

Parameter	Value
Organic Rankine cycle	
Working fluid	cyclopentane
Pump isoentropic efficiency [%]	72
ORC turbine isoentropic efficiency [%]	80
Electric efficiency of the generator [%]	98
Condensing pressure [bar]	1.04
Once-through boiler	
Layout	in-line [16]
Material	stainless steel
Longitudinal pitch [mm]	83
Transversal pitch [mm]	83
Fin pitch [mm]	1.5
Fin thickness [mm]	1
Fin height [mm]	24
Fin efficiency [%]	95
Recuperator	
Layout	triangular pitch [16]
Material	cupro-nickel
Fin pitch [mm]	2
Fin thickness [mm]	1
Fin height [mm]	12
Fin efficiency [%]	95

5.5 Results and Discussion

5.5.1 Multi-objective Design Optimization

Table 5.5 lists the results of the multi-objective optimization procedure applied to the test case. The arithmetic mean average (AMA), the percentage relative standard deviation (RSD), and the minimum and maximum values of the optimized variables are reported. A low RSD means that the variable does not change significantly with the optimal configurations of the ORC unit. The pinch point, the tube diameter and the tube pitch of the recuperator present the lowest RSDs. As a practical implication, table 5.5 provides the designer with the optimal geometry of the heat transfer equipment; the closest available standardized values can then be selected for the design of the actual equipment.

Figure 5.8a shows the two-dimensional Pareto front which relates the net power output of the ORC module with the sum of the volumes of the once-through boiler and of the recuperator. The Pareto front is formed by 70 optimal solutions, ranging from a net ORC power of 3.9 MW_E up to 5.8 MW_E. The trend of the volume vs. the net power output is approximately hyperbolic. The total net power output and the thermal efficiency of the combined cycle unit range from 20.4 MW_E to 22.3 MW_E and from 38.7% to 42.2%. Due to space constraints on the Draugen platform, design points with a volume higher than 100 m^3 are discarded from the Pareto front (triangular dots in Fig. 5.8a).

Table 5.5: Results of the multi-objective optimization. Maximum, minimum, arithmetic mean average, and relative standard deviation of the optimized variables. The values are relative to the 70 points of the Pareto front.

Variable	Max	Min	AMA	RSD [%]
P_6 [bar]	38.3	24.1	34.3	15.0
ΔT_{rec} [°C]	23.0	22.1	22.6	1.0
ΔT_{OTB} [°C]	58.7	43.0	52.0	12.6
T_{11} [°C]	158.6	142.7	148.1	4.2
$D_{OTB,in}$ [mm]	47.0	23.5	29.9	18.8
t_{OTB} [mm]	3.0	1.9	2.2	11.6
l_{OTB} [m]	6.8	5.7	6.4	5.6
u_{exh} [m s^{-1}]	64.2	55.6	62.5	3.5
$D_{rec,in}$ [mm]	18.7	16.6	17.9	1.7
t_{rec} [mm]	3.0	2.2	2.5	7.7
l_{rec} [m]	4.3	3.8	4.0	3.8
p_{rec} [-]	1.29	1.19	1.27	2.1
$l_{rec,b}$ [%]	80.1	68.1	76.9	4.6

5.5.2 Assessment of Dynamic Performance

As far as the results of the analysis of the system dynamics are concerned, Fig. 5.8b illustrates the transient response of the system for two points of the Pareto front (i.e., those corresponding to the designs with the largest and the smallest volume). The influence of the ORC power module design on the network frequency transient is clearly visible: the lower the volume, the larger the undershoot and the overshooting of the frequency. On the contrary, large values of the volume limit the frequency drop, by increasing the thermal inertia of the system.

Figure 5.9a relates the volume to the minimum frequency reached during the transient, for each point of the Pareto front. The curve presents a highly non-linear trend, with the magnitude of the frequency variations increasing more sharply for decreasing volume. According to the standards for power quality adopted by the platform owner, the frequency undershoot must not exceed 4% of the nominal value. Thus, as results from the dynamic analysis, ORC power modules characterized by overall volume V_{ORC} lower than 50 m^3 violate this constraint. These designs are therefore identified as unfeasible, and marked with the hollow square (□) symbol in Figs. 5.8a and 5.9a. Figure 5.9b reports the rise time as a function of volume. The rise time is defined here as the time required for the frequency to return back to 99% of the value at steady state. The trend of the curve is also non-linear with a minimum of approximately 14 s at 65 m^3.

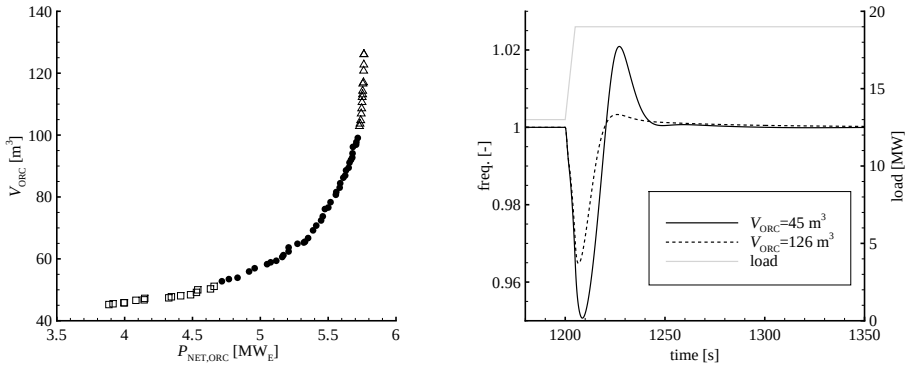

(a) (b)

Figure 5.8: 5.8a multi-objective optimization results, Pareto front showing the relation between the objective functions, e.g. the ORC system net power and the volume of the heat transfer equipment V_{ORC}. The designs identified by the □ symbol are discarded due to the unacceptable frequency undershoot, while those marked with △ due to volume limitations. The other designs (filled circles) are deemed acceptable. 5.8b results of the dynamic test, the grey line represents the corresponding load variation. Normalized frequency and combined cycle load vs time for the two designs characterized by the maximum and minimum values of V_{ORC}.

Figure 5.10a shows the time evolution of the temperature at the inlet of the ORC turbine T_6, together with that of the exhaust gases exiting the gas turbine T_{10} for three points of the Pareto front. As the load of the gas turbine undergoes a sharp variation, the temperature and the mass flow of the exhaust gases entering the OTB rise. As anticipated in §5.4.2, the dynamics of T_6 is much slower than that of T_{10}. The two major contributions to the delay are the inertia of the metal walls

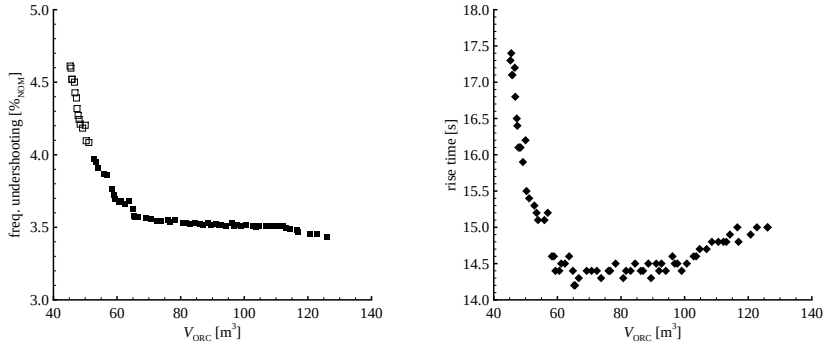

(a) (b)

Figure 5.9: Results of the dynamic test. 5.9a frequency undershoot vs volume V_{ORC}, all the points of the Pareto front are reported. The designs identified by the □ symbol are discarded due to the unacceptable frequency undershoot (> 4%). 5.9b rise time vs V_{ORC}, all the points of the Pareto front are reported.

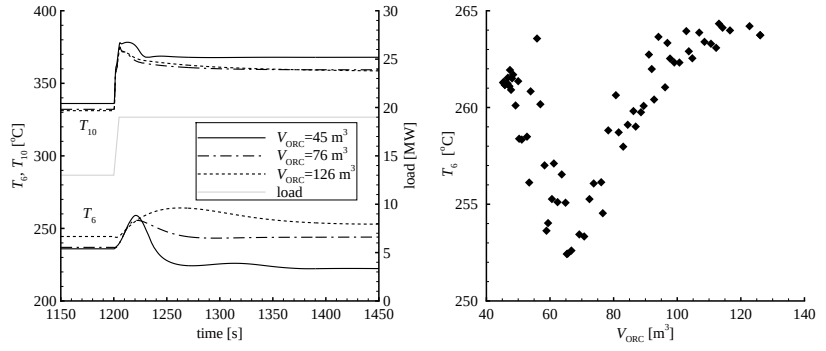

(a) (b)

Figure 5.10: Results of the dynamic test, the grey line represents the corresponding load variation. 5.10a turbine inlet temperature T_6, and exhaust gases temperature at the once-through boiler inlet T_{10} vs time for three selected designs corresponding to points of the Pareto front (the two designs characterized by the maximum and minimum volume of the heat exchanging equipment V_{ORC}, together with an intermediate value). 5.10b maximum turbine inlet temperature vs V_{ORC}, all the points of the Pareto front are reported.

and of the working fluid in liquid phase contained in the heat exchangers. Note that, while the mass of the exhaust gases is negligible, that of the liquid cyclopentane contained in the OTB and in the recuperator is approximately 15 times larger than its mass in the vapor phase.

The peak of T_6 is reported as a function of volume in Figure 5.10b. This value is of paramount importance, being closely related to the maximum temperature reached by the ORC working fluid. This is eventually encountered in the fluid layer close to the metal wall in the boiler (OTB) but, as a consequence of the approximations introduced in §5.4.2, the accurate evaluation of its value is presently beyond the capability of the developed models. As a rough estimation, design point calculations using the methodology outlined in §5.4.1 indicate that the wall temperature of cyclopentane in the hotter part of the OTB is expected to be 10-30 °C higher than the corresponding bulk value. As the thermal stability of the working fluid is a major concern in the design of ORC systems, the minimum risk of decomposition should be ensured. In a recent work, Ginosar and colleagues identified 300 °C as the upper temperature limit for safe operations of an ORC system working with cyclopentane [35]. Therefore, a maximum temperature at the turbine inlet of 270 °C can be accepted, which is also in agreement with other published information, see e.g. Ref. [12].

The dynamic analysis allows to identify a clear minimum for T_6 which, for the considered case, lies at around 250 °C, with a volume of 65 m^3. Values close to 265 °C are achieved for both smaller and larger volumes. Even though the estimated safety limit is not exceeded, the designs characterized by values of volume ranging from 60 to 80 m^3 may be deemed preferable in the light of the present analysis, as they are located in vicinity of the minimum T_6.

5.6 Conclusions

The design of innovative energy conversion systems conceived for flexible operation needs to take into account dynamic requirements on critical transient scenarios as early as possible in the design cycle, in order to avoid costly design changes in later phases, or sub-optimal system performance. The methodology and tools presented in this chapter constitute a first step in this direction.

The design tool DYNDES presented here demonstrates the potential of this preliminary automated design method, if the main design objectives are aspects such as system performance, compactness and flexibility. The software utilizes the multi-objective optimization approach to search for optimal designs with potentially conflicting objectives, which the user can select based on the specific requirements of the system under investigation. As the routine optimizes the geometry of the heat transfer equipment, such a procedure bridges the gap between the mere optimization of the thermodynamic cycle and the preliminary design of system components that constitutes the first step towards the realization of power systems. The system response during transients becomes one of the crucial design criteria, leading to the exclusion from the optimal solutions of several designs which do not satisfy dynamic requirements, e.g., the tolerance on network frequency variations.

The proposed methodology has been applied to the case study of an ORC-based combined cycle power plant for an off-grid oil platform. The test cases demonstrates how dynamic analysis enables to exclude those system configurations which, although potentially more efficient or compact, may lead to unacceptable frequency fluctuations, or increase the risk of decomposition of the working fluid.

The proposed methodology and tools are readily applicable to other systems combining gas turbines and ORC power modules, and it can also be extended to cover other cases of advanced energy conversion systems with demanding dynamic requirements, such as off-grid energy conversion systems, heat recovery in automotive engines, solar thermal plants, etc.

Acknowledgments

The funding from the Norwegian Research Council through Petromaks with project number 203404/E30 is acknowledged. We also acknowledge the kind support from Siemens Industrial Turbomachinery AB, Finspång, Sweden for providing the dynamic model of the SGT-500 gas turbines and the necessary technical documentation.

Nomenclature

s, P	=	specific entropy [kJ kg^{-1} K^{-1}], pressure [kPa]
T, h	=	temperature [°C], specific enthalpy [kJ kg^{-1}]
c, MW	=	speed of sound [m s^{-1}], molecular weight [g mol^{-1}]
A, $\dot{m}$	=	area [m^2], mass flow rate [kg s^{-1}]
u, V	=	velocity [m s^{-1}], volume [m^3]
Re, Pr, Nu	=	Reynolds, Prandtl, and Nusselt numbers
D, p, l, t	=	diameter [mm], pitch [mm], length [m], and thickness [mm]
ω, $\dot{W}$	=	speed of revolution [RPM], power
$\Phi = \omega / \sqrt{2\Delta h_s}$	=	turbine flow coefficient

Greek letters

ρ	=	density [kg m^{-3}]
Δx	=	finite difference for quantity x
λ	=	thermal conductivity [W m^{-1} K^{-1}]
ϵ	=	heat transfer coefficient [W m^{-2} K^{-1}]

Subscripts

E, M	=	electrical, mechanical
des, s	=	design, isoentropic process
exh	=	exhaust gases
fin, b	=	fin, baffle
f, rec	=	fouling, recuperator
min, max	=	minimum, maximum value
CR	=	critical thermodynamic conditions (liquid-vapour)
T, S	=	total and static thermodynamic conditions
th, in, out	=	sonic throat, inlet, and outlet
tot, sv	=	total, saturated vapour conditions

Acronyms

AC	=	Alternating Current
AMA	=	Arithmetic Mean Average
CC	=	Combustion Chamber
LPC	=	Low Pressure Compressor
LPT	=	Low Pressure Turbine

GA	=	Genetic Algorithm
GEN	=	Electric Generator
GT	=	Gas Turbine
HPC	=	High Pressure Compressor
HPT	=	High Pressure Turbine
ORC	=	Organic Rankine Cycle
OTB	=	Once Through Boiler
PI	=	Proportional Integral
PT	=	Pressure Turbine
RSD	=	Relative Standard Deviation
TUR	=	Turbine

References

[1] Wietze Lise, Jeroen van der Laan, Frans Nieuwenhout, and Koen Rademaekers. Assessment of the required share for a stable EU electricity supply until 2050. *Energy Policy*, 59(0):904 – 913, 2013.

[2] Ed Bancalari and Pedy Chan. Adaptation of the SGT6-6000G to a dynamic power generation market. In *Proceedings of the 2005 Power-Gen International Conference*, pages 6–8, Las Vegas, Nevada, 2005.

[3] P. Keatley, A. Shibli, and N.J. Hewitt. Estimating power plant start costs in cyclic operation. *Applied Energy*, 111:550–557, 2013.

[4] J. Lin, Y. Sun, Y. Song, W. Gao, and P. Sorensen. Wind power fluctuation smoothing controller based on risk assessment of grid frequency deviation in an isolated system. *IEEE Transactions on Sustainable Energy*, 4(2):379–392, 2013.

[5] Wei He, Gunnar Jacobsen, Tiit Anderson, Freydar Olsen, Tor Hanson, Magnus Korpoas, Trond Toftevaag, Jarle Eek, Kjetil Uhlen, and Emil Johansson. The potential of integrating wind power with offshore oil and gas platforms. *Wind Engineering*, 34(2):125–138, March 2010.

[6] H.E. Garcia, A. Mohanty, W.-C. Lin, and R.S. Cherry. Dynamic analysis of hybrid energy systems under flexible operation and variable renewable generation - Part I: Dynamic performance analysis. *Energy*, 52:1–16, 2013.

[7] Y. Zhu and K . Tomsovic. Development of models for analyzing the load-following performance of microturbines and fuel cells. *Electric Power Systems Research*, 62:1–11, 2002.

[8] Falah Alobaid, Ralf Postler, Jochen Ströhle, Bernd Epple, and Hyun-Gee Kim. Modeling and investigation start-up procedures of a combined cycle power plant. *Applied Energy*, 85(12):1173 – 1189, 2008.

[9] Rodrigo Lopez-Negrete, Fernando J. D'Amato, Lorenz T. Biegler, and Aditya Kumar. Fast nonlinear model predictive control: Formulation and industrial process applications. *Computers & Chemical Engineering*, 51(0):55 – 64, 2013.

[10] Leonardo Pierobon, Tuong-Van Nguyen, Ulrik Larsen, Fredrik Haglind, and Brian Elmegaard. Multi-objective optimization of organic Rankine cycles for waste heat recovery: Application in an offshore platform. *Energy*, 58(0):538 – 549, 2013.

[11] P. Fritzson. *Principles of Object-Oriented Modeling and Simulation with Modelica 2.1*. John Wiley & Sons, Inc., Piscataway, United States of America, 2003. ISBN: 9780470937617.

[12] P. Del Turco, A. Asti, A.S. Del Greco, A. Bacci, G. Landi, and G. Seghi. The ORegen waste heat recovery cycle: Reducing the CO_2 footprint by means of overall cycle efficiency improvement. In *Proceedings of ASME Turbo Expo 2011*, pages 547–556, Vancouver, Canada, June 2011.

[13] E.W. Lemmon, M.O. McLinden, and M.L. Huber. Refprop: Reference fluid thermodynamic and transport properties. *NIST standard reference database*, 23(8.0), 2007.

[14] Francesco Casella and Christoph C. Richter. ExternalMedia: a library for easy re-use of exter-

nal fluid property code in Modelica. In Bernhard Bachmann, editor, *Proceedings 6th International Modelica Conference*, pages 157–161, Bielefeld, Germany, Mar. 3–4 2008. Modelica Association.

[15] P. Colonna, T. P. van der Stelt, and A. Guardone. FluidProp (Version 3.0): A program for the estimation of thermophysical properties of fluids, 2012. A program since 2004.

[16] J.M. Coulson, J.F. Richardson, and Backhurst J.R. *Coulson and Richardson's Chemical Engineering*. Chemical engineering. Butterworth-Heinemann, Oxford, Great Britain, 1999.

[17] V. Gnielinski. On heat transfer in tubes. *International Journal of Heat and Mass Transfer*, 63(0):134 – 140, 2013.

[18] MM Shah. Chart correlation for saturated boiling heat transfer: equations and further study. *ASHRAE Transaction*, 88(1):185–196, 1982.

[19] Verein Deutscher Ingenieure. *VDI-Wärmeatlas: Berechnungsblätter für den Wärmeübergang*. Springer-Verlag, Berlin, Germany, 1953. ISBN: 9783540412014.

[20] Lutz Friedel. Pressure drop during gas/vapor-liquid flow in pipes. *International Chemical Engineering*, 20(3):352–367, 1980.

[21] S Zia Rouhani and Eva Axelsson. Calculation of void volume fraction in the subcooled and quality boiling regions. *International Journal of Heat and Mass Transfer*, 13(2):383–393, 1970.

[22] Siegfried Haaf. Wärmeübertragung in luftkühlern. In *Wärmeaustauscher*, pages 435–491. Springer Verlag, Berlin, Germany, 1988. ISBN: 9783540154778.

[23] Francesco Casella and Alberto Leva. Object-oriented modelling & simulation of power plants with modelica. In *Proceedings 44th IEEE Conference on Decision and Control and European Control Conference 2005*, pages 7597–7602, Seville, Spain, Dec. 12–15 2005. IEEE, EUCA.

[24] F. Casella, T. Mathijssen, P. Colonna, and J. van Buijtenen. Dynamic modeling of ORC power systems. *Journal of Engineering for Gas Turbines and Power*, 135:1–12, 2012.

[25] Joachim Kurzke. *Component map collection 2, Compressor and turbine maps for gas turbine performance computer programs. Germany; 2004, www.gasturb.de/. [accessed: 19/09/2013]*, 2004.

[26] F. Carchedi and G. R. Wood. Design and development of a 12:1 pressure ratio compressor for the Ruston 6-MW gas turbine. *Journal for Engineering for Power*, 104:823 – 831, 1982.

[27] Joachim Kurzke. How to create a performance model of a gas turbine from a limited amount of information. In *Proceedings of ASME Turbo Expo 2005*, pages 145–153, Reno-Tahoe, Nevada, June 2005.

[28] A. Stodola. *Dampf- und Gasturbinen: Mit einem Anhang über die Aussichten der Wärmekraftmaschinen*. Springer Berlin, Berlin, Germany, 1922. ISBN: 7352997563.

[29] Meinhard Schobeiri. *Turbomachinery flow physics and dynamic performance*. Springer Berlin, Berlin, Germany, 2005. ISBN: 9783540223689.

[30] F. Haglind and B. Elmegaard. Methodologies for predicting the part-load performance of aero-derivative gas turbines. *Energy*, 34(10):1484 – 1492, 2009.

[31] Frank P. Incropera, David P. DeWitt, Theodore L. Bergman, and Adrienne S. Lavine. *Fundamentals of Heat and Mass Transfer*. John Wiley & Sons, Inc., Jefferson City, United States of America, 6 edition, 2007. ISBN: 9780470501979.

[32] J. P. Veres. Centrifugal and axial pump design and off-design performance prediction. Technical report, NASA, Sunnyvale, United States of America, 1994. Technical Memorandum 106745.

[33] Marie-Nolle Dumont and Georges Heyen. Mathematical modelling and design of an advanced once-through heat recovery steam generator. *Computers & Chemical Engineering*, 28(5):651

– 660, 2004.

[34] Kalyanmoy Deb. *Multi-objective optimization using evolutionary algorithms*. John Wiley & Sons, Inc., West Sussex, Great Britain, 2001. ISBN: 9780470743614.

[35] Daniel M Ginosar, Lucia M Petkovic, and Donna Post Guillen. Thermal stability of cyclopentane as an organic Rankine cycle working fluid. *Energy & Fuels*, 25(9):4138–4144, 2011.

6

Design of CSP Plants with Optimally Operated Thermal Storage

Part of the contents of this chapter will appear in:

"Design of CSP Plants
with Optimally Operated Thermal Storage"
E. Casati, F. Casella, & P. Colonna
Solar Energy, Accepted for Publication (2014)

Abstract *Concentrated solar power plants are increasingly considered worldwide, in order to meet the demand for renewable power generation. A distinctive feature of these plants is the possibility of integrating thermal energy storage such that full-load operation can be sustained for several hours in the absence of solar radiation. A number of design software tools are available for sizing the plant and evaluating the return on investment. These usually assume a short-sighted strategy for storage management. This work presents a new methodology aimed at assessing the potential of optimal control techniques when applied to the operation of energy storage systems in general. The design method is applied to a test case, a state-of-the-art central receiver plant with direct storage, using molten salts as working fluid, and operating in a context of variable electricity prices. The system modelling and optimization problems are formulated and implemented using modern high-level modelling languages, thus demonstrating the potential of the approach. Different operating strategies are compared based on a detailed financial analysis. A wide system design space is considered, and the results are presented for all the foreseeable combinations of solar field size and storage system capacity. A potential increase of the order of 5% in terms of yearly revenue is estimated, in case improved control strategies are adopted. This figure translates into an increase of more than 10% of the investment profitability by considering over-life financial figures. It is further shown how, in case of state-of-the-art systems, it is always profitable to adopt optimal control to the end of increasing electricity production. However, the potential of these techniques is discussed also under the point of view of investment cost reduction, since the same yearly revenue can be harvested with smaller energy storage, if optimally operated. This aspect, unveiled here for the first time, might become significant in case technologies with different cost structure are of interest, i.e., in case the storage cost constitutes a comparatively large part of the total investment. The novel method is thus an additional decision tool allowing to treat the storage operation strategy as a new relevant design variable for next generation energy systems.*

6.1 Introduction

Evolving towards a society not depending on fossil fuels is becoming a matter of the greatest interest, as it is increasingly clear that the current energy consumption and generation trend is not sustainable, due to the exhaustion of fossil fuel resources and its effects on climate change [1, 2]. Devices to convert concentrated solar energy into useful work have been designed for over a century [3–5]. The oil crisis triggered substantial R&D on solar energy conversion, and pilot plants were built during the 1980s. In recent years, renewed interest in concentrated solar power (CSP) plants has sparked a new surge in investments; in 2011 the power capacity of the CSP plants that were operational worldwide totalled 1.3 GW_E, that of plants under construction amounted to 2.3 GW_E, while that of planned plants added up to 31.7 GW_E [6]. A very relevant advantage of CSP power plants compared to other renewable energy conversion options is that the installation can integrate a comparatively inexpensive thermal energy storage system (TES), enabling power to be generated when the sun is not shining, and contributing to their distinctive ability to provide dispatchable electricity. Recent research aimed at quantifying the added values of CSP dispatchability, the key findings being: i) the dispatchability of CSP adds quantifiable economic benefits, ii) the flexibility of CSP can aid the integration in the grid of other renewable energy technologies, such as solar photovoltaics [7].

Of all CSP technologies available today, that of central receiver systems (CR, also known as solar towers) is moving to the forefront, and it might become the technology of choice. The interested reader is referred to Ref. [8] for a thorough review of the history of this technology, the state of the art, and the ongoing R&D efforts. State-of-the-art CR systems use molten salts as the

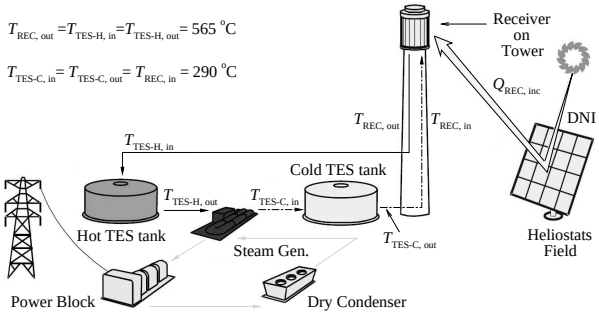

Figure 6.1: Schematic layout of the Gemasolar 20 MW_E solar tower plant, capable of 15 hours of full-load off-sun operation thanks to the storage system, adapted from [11]. The main simplification adopted in the model presented here, i.e., the neglection of thermal losses in all the subsystems apart from the receiver (see §6.2), is also made explicit.

working fluid in both the solar receiver and the storage subsytems, i.e., they implement the so-called direct TES concept [9], which may be sized such that it provides several hours of nominal operation without solar radiation [10]. The schematic layout of the first commercial plant of this type, operating in Spain since 2011, is shown in Fig. 6.1.

The storage unit completely decouples the power block from the variable solar energy source, which is beneficial for both plant efficiency and reliability: in order to achieve better overall performance during the day, the control techniques for CSP systems usually aim at maintaining the solar receiver outlet temperature close to its nominal value, by varying the heat transfer fluid (HTF) mass flow rate. However, in the absence of significant energy storage, the operating point of the power block needs to follow the variations of the solar radiation, as discussed in Refs. [12, 13]. On the contrary, the integraton of a direct TES system into the power plant allows to use an additional control variable, i.e., the mass flow rate from the storage tank to the primary heat exchanger (steam generator). Thus, the receiver outlet temperature and the power delivered to the conversion cycle can be controlled independently. This makes it possible to sustain constant power output during short transients (e.g., clouds passage), or to shift the production to better meet variable-price tariffs.

In the present work, according to a scheme currently adopted mainly in the USA, the produced electricity is supposed to be sold to a utility company at the previously negotiated power purchase agreement (PPA) bid price, multiplied by time-of-day (TOD) factors pre-defined by the applicable tariff, which account for the higher value that the produced power has during peak hours. The PPA price is thus negotiated by the producer in order to balance the investment and operational costs, and hopefully make a profit. For a detailed description of the PPA approach and how this allows to overcome the shortcomings of the other commonly adopted metric, i.e., the levelized cost of electricity (LCOE), the interested reader is referred to the works of Ref. [14] and [15].

The availability of a TES system coupled with variable energy prices demands for an optimized operation of the plant, maximizing the revenues by exploiting the TES ability to shift the production to higher priced time slots. This problem has been considered by many authors in recent times, see, e.g., [16–18]. With reference to real-time operation, Ref. [19] discusses the potential of weather forecast-based operation of CSP plants, stressing the importance of forecast quality. In Refs. [20, 21], a methodology to maximize the revenues for a plant operating in a free energy

market is presented; the CSP plant is run with a price-driven strategy and, based on electricity pricing and weather forecasting, an economically optimized bidding strategy for the day-ahead energy market is determined. The authors identify a period comprising the next one or two trading days as a reasonable optimization horizon, considering the trade-off between profit gain and forecast quality. More recently, the authors of Ref. [22] assessed the potential of a solar-thermal generation system in a fluctuating electricity prices context, by considering the innovative CSP technology proposed in Ref. [23]. Ref. [24] investigated the influence of the operation strategy, focusing on the charge/discharge process for a thermocline storage, on the yearly production of a parabolic trough CSP plant.

The research work documented here stems from the need of generalizing the analysis on optimized dispatching strategies for CSP plants, by considering the whole design-space of present-days systems, e.g., in terms of storage capacity and solar multiple. Furthermore, a novel assessment of how different control procedures can influence the design of the plant and the financial performance of the project is presented. When a new CSP plant is being considered for construction at a specific location, models and tools are needed to assess the potential of eneregy production, and thus eventually compute the PPA price level that can repay for the investment within the specified time. A widely adopted, publicly available software tool for this purpose is the System Advisory Model (SAM) [10, 25, 26], which is assumed as a reference in this work. The TES control strategy assumed by SAM is such that, for each hourly interval of operation, the controller tries to use all the available thermal power from the solar field and from the TES to drive the power block at the maximum possible load. This strategy is clearly sub-optimal when the TOD factor shows significant variations during peak hours, so it can be safely assumed that the plant being evaluated will eventually be operated using some kind of optimal control that will try to maximize the economic revenue by exploiting the available storage instead of the strategy assumed by SAM. In order to make correct decisions in terms of plant sizing and design would be therefore advantageous to include optimal control even at this very early stage.

To this end, the method presented here is based on a dynamic model of the plant, replicating the basic modelling assumptions of the SAM software, which is then employed to formulate and solve a dynamic optimization problem in order to give a credible estimation of the potential of a future CSP plant, assuming optimal control is used for its operation. Since the full details of the real-time implementation of the optimal controller cannot be available at this very early design stage, it is reasonable to consider an idealized set-up of the control problem, assuming perfect matching between the model and the plant dynamics, and perfect knowledge of the future solar irradiation. The attained performance represents therefore the theoretical limit of the operation of a real-time optimal controller, which in reality will have to face modelling errors, unmodelled disturbances, and uncertain weather forecasts. Although the obtained results will be slightly optimistic, they will represent controlled plant operation in a much more credible way than those obtained with the short-sighted control policy usually assumed. Modern object-oriented languages and simulation tools are used in order to concisely formulate and solve the optimal control problem with minimal implementation effort.

The main goal of the work is to show that, by means of these techniques and tools, the noteworthy advantages offered by optimal operation procedures can be easily unveiled and taken into account during the earliest design stages. The chapter is structured as follows. The CSP plant model, replicating the main features of the SAM model, is introduced in §6.2. The reference control strategy and the optimal control problem are formulated in §6.3. The computational infrastructure is discussed in §6.4, while the main results are presented and discussed in §6.5. §6.6 illustrates the main conclusions and an outlook to future work.

6.2 Modeling Framework

The CSP plant selected as a test case is a state-of-the-art 100 MW_E molten salts plant with direct storage, whose schematic layout is shown in Fig. 6.1. The general modelling framework closely follows the one used by SAM, as described in [26], therefore the following main simplifying assumptions hold:

1. the HTF temperature at the receiver outlet is assumed to be always kept at its nominal value $T_{\text{REC, out}}$. Also the temperature of the HTF exiting the steam generator, i.e., $T_{\text{TES-C, in}}$, is assumed to be constant within the considered operating range. The heat losses in the piping are neglected, leading to the equalities $T_{\text{REC, out}} = T_{\text{TES-H, in}}$ and $T_{\text{REC, in}} = T_{\text{TES-C, out}}$. Furthermore, also the storage tanks are supposed to be adiabatic, that is, perfectly thermally insulated, such that $T_{\text{TES-H, in}} = T_{\text{TES-H, out}}$, and $T_{\text{TES-C, in}} = T_{\text{TES-C, out}}$. As a consequence, only two temperature levels are present in the system model, as indicated in Fig. 6.1.
2. Parasitic losses introduced to account for energy storage in the semi-steady framework of the SAM program have not been modelled: this is the case of the energy consumptions and time delays associated with the start-up and shut down of all the subsystems [26];
3. energy storage is explicitly modelled only in the TES tanks, since the (controlled) dynamics of the receiver system and power block is much faster;
4. the temperature dependency of the thermodynamic properties of the HTF, i.e., density and specific heat, is neglected;
5. perfect knowledge of future solar irradiation values is assumed, based on customarily adopted weather data files such as those described in [27].

As shown in the following, these assumptions can enormously reduce the complexity of the design problem, while preserving the consistency of the results with respect to a corresponding omni-comprehensive SAM model.

For simplicity and numerical robustness, all the power variables are normalized with respect to the nominal power block thermal power, all the mass flow rate variables to the corresponding mass flow rate, and the TES tank level to its nominal height. Notably, following the above mentioned assumptions and simplifications, the equalities $m_{\text{PB}} = Q_{\text{PB}}$ and $m_{\text{HTF}} = Q_{\text{HTF}}$ hold, relating the circulating mass flow rate of HTF through the power block and the receiver to the thermal power transferred within the same subsystems. The general design data considered, i.e., the variables which are fixed in this work, are collected in Tab. 6.1. The operating limits regarding the receiver and the power block are expressed in terms of minimum/maximum fractions (i.e., $f^{\text{min}}/f^{\text{max}}$) of the relative design values for the incident radiative power $Q_{\text{REC,inc}}$, and for the mass flow rate fed to the steam generator m_{PB}. Similarly, the maximum storage level is equal to the nominal tank height, while the minimum value is given an absolute value.

Based on all the above mentioned assumptions, the system model contains a single dynamic equation, describing the state of charge of the TES, and several algebraic equations, describing the power block and the TES operation set points. The solar input can be defined in terms of the power available to the receiver $Q_{\text{REC,inc,av}}$ (i.e., the total radiative flux which may reach the receiver if the solar field is fully focused) as

$$Q_{\text{REC,inc,av}} = \text{DNI}(t, \text{loc})\, A_{\text{SF}}\, \eta_{\text{opt}}(t, \text{loc, SF})\, \epsilon_{\text{avail}}\, \epsilon_{\text{refl}} \quad . \tag{6.1}$$

In Eq. 6.1, the functional dependence of DNI and of the field optical efficiency η_{opt} from the time-varying weather conditions (t), and from the plant location (loc), is made explicit. As anticipated,

Table 6.1: General design data adopted for the 100 MW_E (nominal) solar tower system considered here, after Refs. [10, 25, 26]. The plant is assumed to be located in Daggett (CA), latitude 34.9°, longitude −116.8°, average direct normal irradiation (annual) 2791 kWh m^{-2}. η_{PB} is the power block thermal efficiency, $\eta_{REC,th}$ and α_{REC} the receiver thermal efficiency and absorptivity, respectively. ϵ_{avail} and ϵ_{refl} refer to the heliostats availability and reflectivity, both values accounting for the average field performance.

$W_{el,\,gross}$ [MW_E]	115	η_{PB} [%]	40
α_{REC} [%]	94	$\eta_{REC,th}$ [%]	88
ϵ_{avail} [−]	0.99	ϵ_{refl} [−]	0.90
$f^{min}_{Q_{REC,inc}}$ [−]	0.25	$f^{max}_{Q_{REC,inc}}$ [−]	1.2
$f^{min}_{m_{PB}}$ [−]	0.25	$f^{max}_{m_{PB}}$ [−]	1
$x_{TES,min}$ [m]	1	$f^{max}_{x_{TES}}$ [−]	1

weather data in the TMY3 format, containing data for various locations with an hourly sampling, are considered in this work. The value of η_{opt} is evaluated hourly as a function of the solar position but, as shown in Eq. 6.1, it is also dependent on the solar field characteristics (SF). The same is obviously true for the total reflective area A_{SF}.

The dimension of the solar field can be better expressed in terms of the solar multiple (SM) value, that is, the ratio of the receiver design thermal output to the power block design thermal input. As the solar field size is increased, there will be a growing number of hours throughout the year whereby the available solar power exceeds the power block design power. In these conditions, the TES system is used to harvest (part of) the exceeding energy, until defocusing (part of) the heliostats migh become necessary. Thus, a techno-economic optimal combination of the solar field size and of the storage capacity has to be determined for the given plant and location [28]. In particular, the solar power harvesting system constituted by the solar field, the tower, and the receiver, is the most capital intensive part of any solar energy project, and its optimization is therefore critical for the minimization of the overall costs [8, 10, 29]. The SM is thus used as the key parameter in the following analysis, and four solar fields characterized by SM = 1.5, 2, 2.5, and 3.5 are designed for the same hypothetical plant, i.e., starting from the specfications reported in Tab. 6.1.

Apart for the nominal characteristic indicated by the SM, however, the detailed design of the components involved is necessary in order to define both A_{SF} and the $\eta_{opt}(t, \mathrm{loc}, \mathrm{SF})$ relation appearing in Eq. 6.1. In the present work, the PTGen program available within SAM [25, 26], and based on the DELSOL3 code [30, 31], is adopted to this end. Solar fields with a surround radially-staggered layout are considered. Even though several other geometries have been proposed in the literature [8], this arrangement is chosen here for the sake of simplicity. The solar field modelling assumptions adopted in this study, together with the resulting designs, are reported in A.1.

Summarizing, since all the computations involved by Eq. 6.1 can be carried out off-line once the solar field has been designed, $Q_{REC,inc,av}$ is eventually computed as a known, time-varying input for the plant model.

Also the price of the produced electricity P depends on known hourly TOD factors, in turn determined by the selected tariff, on the hour of the day, on the day of the week, and on the season,

according to

$$P = \mathrm{TOD}(t)\ \mathrm{PPA}. \tag{6.2}$$

The power actually reaching the receiver $Q_{\mathrm{REC,inc}}$ may then be calculated as

$$Q_{\mathrm{REC,inc}} = Q_{\mathrm{REC,inc,av}} - Q_{\mathrm{def}}\ , \tag{6.3}$$

where Q_{def} is the power dumped by defocusing heliostats, which is a control variable of the problem. The following (normalized) equations

$$Q_{\mathrm{REC,abs}} = Q_{\mathrm{REC,inc}}\ \alpha_{\mathrm{REC}}\ , \tag{6.4}$$
$$Q_{\mathrm{HTF}} = Q_{\mathrm{REC,abs}}\ \eta_{\mathrm{REC,th}}\ , \tag{6.5}$$
$$m_{\mathrm{HTF}} = Q_{\mathrm{HTF}}\ , \tag{6.6}$$
$$W_{\mathrm{PB}} = m_{\mathrm{PB}}\ \eta_{\mathrm{PB}}\ , \tag{6.7}$$
$$h_{\mathrm{TES}}\ \frac{\mathrm{d}x_{\mathrm{TES}}}{\mathrm{d}t} = m_{\mathrm{HTF}} - m_{\mathrm{PB}}\ , \tag{6.8}$$
$$x_{\mathrm{TES}}(0) = x_{\mathrm{TES,0}}\ , \tag{6.9}$$

complete the model. Eq. (6.4) gives the thermal power absorbed in the receiver $Q_{\mathrm{REC,abs}}$ and Eq. (6.5) the power Q_{HTF} transferred to the HTF. Eq. (6.6) relates the mass flow rate of HTF through the receiver m_{HTF} to Q_{HTF}, while Eq. (6.7) establishes the relation between W_{PB}, m_{PB}, and the power block efficiency η_{PB}, which is assumed to be linear in this work. Finally, the differential equation (6.8) describes the dynamics of the TES system, where h_{TES} is the capacity of the storage tank in terms of hours of operation at nominal power block load. The corresponding initial conditions for the state variable are explicitly defined by Eq. (6.9).

Several constraints need to be enforced in order to ensure feasible operation, namely

$$Q_{\mathrm{REC,inc}} \leq f^{\max}_{Q_{\mathrm{REC,inc}}}\ , \tag{6.10}$$
$$0 \leq Q_{\mathrm{def}} \leq Q_{\mathrm{REC,inc,av}}\ , \tag{6.11}$$
$$0 \leq m_{\mathrm{PB}} \leq 1\ , \tag{6.12}$$
$$x_{\mathrm{TES,min}} \leq x_{\mathrm{TES}} \leq f^{\max}_{x_{\mathrm{TES}}}\ . \tag{6.13}$$

The first inequality states the maximum power that can be handled by the receiver, calling for a partial defocusing of the heliostat field if the available power $Q_{\mathrm{REC,inc,av}}$ becomes too high; the defocused power Q_{def} (second inequality) is non-negative and less than the available power. The normalized flow rate of HTF to the power block is comprised between 0 and 1 per unit (third inequality), while the storage tank state of charge x_{TES} is limited between a lower and an upper bound. Furthermore, both the solar field thermal power $Q_{\mathrm{REC,inc}}$ and the power block HTF flow m_{PB} have a minimum operating load, and need to be turned off if the desired load level is lower than that. The first constraint is enforced by substituting $Q_{\mathrm{REC,inc,av}} = 0$ whenever $Q_{\mathrm{REC,inc,av}} \leq f^{\min}_{Q_{\mathrm{REC,inc}}}$, which is done as a pre-processing task. The second constraint is handled by introducing extra terms in the optimization problem, see §6.3.2.

The resulting model has two known, time-varying inputs $Q_{\mathrm{REC,inc,av}}(t)$ and $f_{\mathrm{TOD}}(t)$, and two control variables $m_{\mathrm{PB}}(t)$ and $Q_{\mathrm{def}}(t)$. The model is readily encoded using the equation-based, object-oriented language Modelica [32], see also §6.4 and listing 1 in A.3.

6.3 Operation Strategy

6.3.1 Reference Operation Strategy

The model described in §6.2 can be used to predict the performance of the considered solar tower plant when the reference operation strategy, defined following Refs. [25, 26] is applied. This approach aims at satisfying the nominal power cycle demand, by making use of the available resources, namely of the solar field (SF) and the TES system, in a prioritized order. A sequence of logical statements is used to determine whether the power cycle demand can be met with only the SF, or with the SF and the TES, always in this order, while ensuring that the operative constraints (Eqs. 6.10-6.13) are satisfied. In other words, the algorithm aims at running the power block at the maximum possible load for every time step, defocusing the solar field when its output $Q_{\mathrm{REC,inc,av}}$ exceeds the sum of the nominal thermal power input of the power block and of the maximum storage charging rate that fulfills the capacity limits over a one-hour horizon. In this way, the values of the decision variables m_{PB} and Q_{def} are determined disregarding any information about the electricity price and of future availability of solar irradiation.

The SAM software approximates the differential-algebraic equations of the model by assuming that all variables are constant within each hour of operation, i.e., by using the forward Euler's method. As there is no feedback from x_{TES} to any other variable of the model, the forward and backward Euler's methods give the same results in this case, only shifted by one time step, which is irrelevant when determining yearly revenues.

6.3.2 Optimal Control

The model described in §6.2 can be adopted to assess the potential of an optimized operation strategy for the considered plant, aimed at maximizing the revenue deriving from the sold electricity. The control objective is an integral cost to be minimized over the integration interval from time t_{in} to t_{fin}, i.e.,

$$\min \int_{t_{\mathrm{in}}}^{t_{\mathrm{fin}}} -W_{\mathrm{PB}}\, P + c \left(\frac{\mathrm{d}u}{\mathrm{d}t}\right)^2 + g\, s\, (u - f_{m_{\mathrm{PB}}}^{\mathrm{min}})\, \mathrm{d}t\,. \tag{6.14}$$

The first term in the integral accounts for the normalized instantaneous revenue from the sale of electricity. The second term, with $c > 0$, is introduced to penalize fast changes and oscillations of the control variable, as well as repeated re-starts of the plant during the same day. This provision, which aims at avoiding stressful operating regimes for the power block, is implemented in order to coherently follow the approach programmed into SAM. The third term, with $g > 0$, is introduced to avoid power block operation below the minimum load, along with the additional constraints

$$u = m_{\mathrm{PB}} + s\,, \tag{6.15}$$

$$0 \le s \le u\,. \tag{6.16}$$

The free control variable u, which is the output of the dynamic optimization problem together with Q_{def}, is the unconstrained normalized value of the HTF flow to the power block, while s is a slack variable. If $u > f_{m_{\mathrm{PB}}}^{\mathrm{min}}$, the term is minimized by taking the lowest possible value of s ($s = 0$), so that $m_{\mathrm{PB}} = u$. Conversely, if $u < f_{m_{\mathrm{PB}}}^{\mathrm{min}}$, the term is minimized by taking the highest possible value of s ($s = u$), so that $m_{\mathrm{PB}} = 0$. The values of c and g are empirically chosen to be the smallest possible, which actually succeeds at avoiding control oscillation, restarting of the power block in the same day, and operation below the minimum load, while perturbing as little as possible the optimization of the first term, i.e., the economic revenue of the plant. An additional constraint might be added to

obtain a specific value of the storage at the end of the operational period; this can be instrumental in comparing the performance of the optimal control to that of the original control strategy on equal grounds. The above-described optimal control problem can be readily encoded using the Optimica language [33], an extension of Modelica that also allows to specify the control objective and the constraint equations, see also §6.4 and listing 2 in A.3.

6.4 Computational Infrastructure

Traditional codes for plant design and optimization are written from scratch in programming languages such as Fortran or C++, which is tedious and error-prone. The approach proposed in this work leverages on modern, high-level modelling languages for the problem formulation, and on software tools that automatically transform this description of the problem into low-level code that can be coupled with state-of-the-art numerical solvers.

The model is encoded using the Modelica language [32, 34], which is a high-level, non-proprietary, equation-based language for the modelling of systems described by differential-algebraic equations, while the optimization problem is encoded using the Optimica extension to the Modelica language [35]. The Modelica/Optimica language is supported by different tools, each implementing alternative strategies for the solution of the dynamic optimization problem [36, 37].

The tool described in [36] was used in the work described here. A collocation method was adopted in order to solve the problem [38, 39]: the time-varying variables of the problem are approximated by Lagrange polynomials, that define the values of the variable in the optimization interval $t_{in} \leq t \leq t_{fin}$ as a direct function of the values at a finite set of nodal points, which become the unknowns of the problem. In this way, the infinite-dimensional optimal control problem stated in §6.3.2 is transcribed into a large, finite-dimensional nonlinear programming (NLP) problem, which is then solved by an open-source NLP solver [40].

In order to directly compare the results with those obtained by the SAM program, which solves the differential equation by Euler's method, 0-order polynomials (i.e., piecewise constant functions) were used, with one-hour time intervals. It is worth pointing out that the proposed approach easily allows to use more accurate interpolations, simply by changing the set-up of the problem transcription. It is also easy to experiment with alternative solution strategies (e.g., multiple-shooting instead of collocation), as well as with different techniques to reduce the size of the NLP by means of symbolic manipulation, in order get the best performance in terms of convergence robustness and CPU time. In all these cases, the high-level formulation of the problem remains the same, only the choice of the tool and its configuration need to change, thus avoiding problem-specific low-level programming.

Last, but not least, the computational framework used to obtain the results presented in this chapter has been entirely built using open-source software and open standards. It is then possible to use it as the foundation of extensions to publicly available tools such as the SAM program, without any issue that might arise from the use of commercial software.

6.5 Results & Discussion

The first analysis aims at assessing the performance of the model developed in this work, see §6.2, by comparing its predictions to the yearly simulation results yielded by a reference SAM model (i.e., with all the main settings keeping their default values). The simulation is performed with a control algorithm emulating the SAM control strategy, see §6.3. The results are shown in Fig.

6.2a, whereby the yearly revenue (Rev) is shown as a function of the TES system capacity h_{TES}, for several SM values. As expected, the revenue increases for larger SM values (larger solar fields) and,

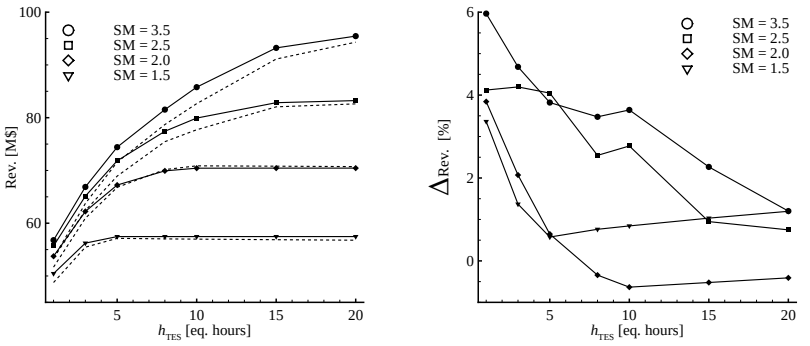

(a) (b)

Figure 6.2: Yearly simulation results in terms of revenue from electricity placement on the market (i.e., Rev, ordinates axis). The results are shown as a function of the TES system capacity (i.e. h_{TES}, abscissae axis). The symbols refer to the SM values. 6.2a comparison between the reference SAM model (dashed lines) and the Modelica model documented in this work (solid lines). 6.2b percentage differences between the two models predictions.

for a given SM value, tends to grow as the size of the storage is increased, that is, as the amount of energy which needs to be dumped through defocusing is reduced. On the other hand, a maximum revenue is reached for each SM value, beyond which an increase of h_{TES} does not influence further the revenue.

As reported in Fig. 6.2b, the predictions of the two models are in close agreement. Furthermore, the larger deviations, of the order of 5%, are encountered for plant layouts of negligible practical interest, i.e., those characterized by large solar fields and comparatively small storage capacity. It is therefore proved that the adopted assumptions allow to develop a comparatively simple model, able of accurately predict the yearly system performance.

This simplified model is thus used to carry on the comparison between the reference and the optimized operation strategy, see §6.3. In order to provide the first insight, the results regarding a 10-days summer period are presented in Fig. 6.3. The considered tariff was adopted by the utility company *Pacific Gas and Electric* in 2011, as defined in SAM [26]. The observed system is characterized by a comparatively small storage capacity with respect to the field size. The time period starts with a week-end, which has a different f_{TOD} schedule. In order to perform the comparison on a fair basis, the initial and final state of the TES in the optimization problem are constrained to be the same as they are in the simulation using the SAM control.

First of all, it can be noted from Fig. 6.3a that the use of optimal control allowed to increase the revenue of the period of about 7%, from 2.92 to 3.13 M$. The defocusing operation, envisaged in both cases, is managed differently, affecting the mass flow rate through the receiver, see, e.g., Fig. 6.3b. The same graph shows how the power block operation varies as a consequence of the

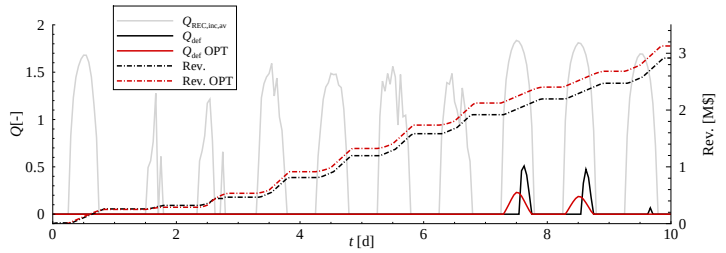

(a)

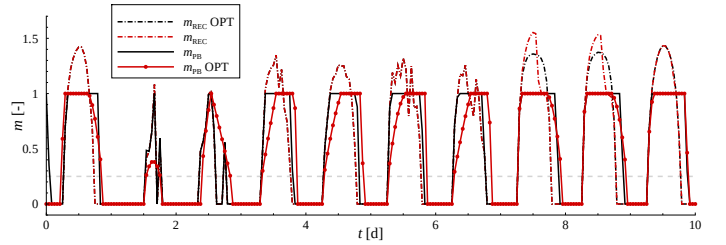

(b)

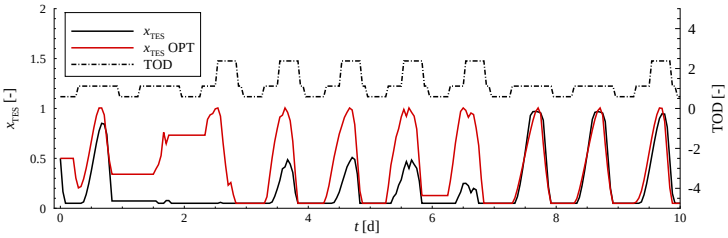

(c)

Figure 6.3: Comparison between reference and optimized solar tower plant operation during a 10-days period, from July the 7th to July the 16th. The considered system features solar multiple SM = 1.5 and storage capacity h_{TES} = 3 eq. hours.

different control strategy. The effects of the optimized control strategy can be clearly understood by considering also Fig. 6.3c, whereby both the storage level and the TOD factor are shown. Being the storage capacity comparatively small, the optimal controller can not manipulate large amounts of energy, and the plant load profile is therefore similar in the two cases. However, the production tends to be shifted towards the afternoon hours of working days (when the TOD factor is highest), by reducing the load during off-peak hours, i.e., by limiting m_{PB} to a value sufficient to prevent storage overloading while avoiding the need of defocusing. Note that the hourly values of m_{PB}, represented by the red dots, never fall in the forbidden region between zero and the minimum load, as expected from the problem formulation.

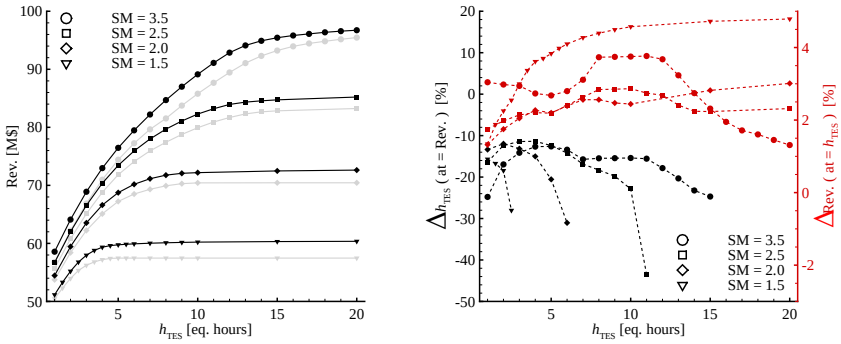

(a) (b)

Figure 6.4: Yearly results for the comparison between reference and optimized solar tower plant operation. The results are shown as a function of the TES system capacity h_{TES}. The symbols refer to the SM values. 6.4a results in terms of harvested revenue Rev, black lines: optimized operation, gray lines: reference operation (these lines correspond to the solid black lines reported in Fig. 6.2a). 6.4b percentage differences among the results shown in Fig. 6.4a; red lines (and red ordinates axis): iso-abscissae comparison (i.e., possible increase in revenue for a given h_{TES}), black lines (and black ordinates axis): iso-ordinates comparison (i.e., possible decrease of h_{TES} for a given revenue).

In order to present a thorough analysis, however, the yearly system performance must be considered. The solution strategy is the same, and the optimal control result has been obtained by separately optimizing each month of operation, and then by summing the resulting monthly revenues. Since the adopted approach assumes perfect knowledge of the weather forecast within the analysis interval, considering monthly intervals may seem inappropriate. However, as discussed in Ref. [20], expanding the forecasting horizon to more than 2 – 3 days has only a minor effect on the yearly revenue, since the storage capacity limitation constrains the amount of energy that the optimizer can shift. The plant yearly revenue as a function of the storage capacity, with and without optimal control and for several SM values, is shown in Fig. 6.4a.

Fig. 6.4b sheds some more light on these results. It can be seen that, for any storage capacity, the optimal operation strategy allows for a positive gain in terms of revenue, ranging approximately from 2% up to 5% (see red lines, and red ordinates axis). Notably, a complementary perspective can be considered, i.e., the operating strategies can be compared for equal revenue yields, thus evaluating the potential reduction in TES system size they allow for, or, in other words, their impact on the system design. Also in this case, the gain achievable thanks to the optimized operation is considerable (see black lines, and black ordinates axis).

To put these conclusions in the right perspective, that is, in order to properly discriminate among an increase in the yearly revenue and a decrease of the capital cost, a financial analysis considering the whole plant life-time is necessary. A detailed financial model has been developed to this end, based on the framework implemented in SAM [26]; the adopted methodology is detailed in A.2. All

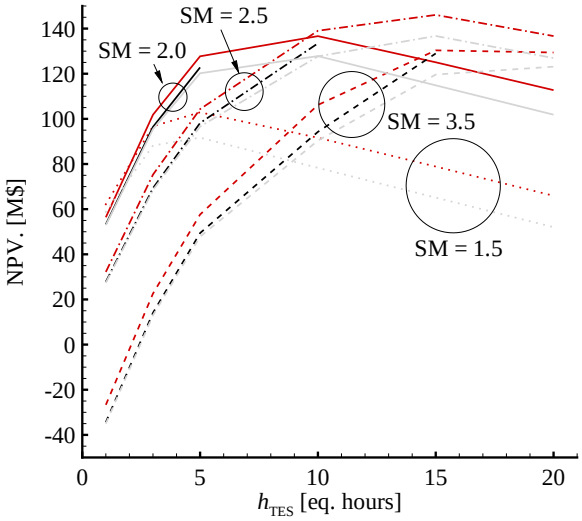

Figure 6.5: Financial comparison between reference and optimized solar tower plant operation strategy: net present value (NPV) as a function of TES system capacity h_{TES}, for several SM values (corresponding to different line formats). Grey lines: reference control strategy; red lines: optimized strategy exploited to increase yearly revenue (see Fig. 6.4b, red lines); black lines: optimized strategy exploited to decrease the investment (see Fig. 6.4b, black lines). The black-dotted line (SM = 1.5) is not shown, being undistinguishable from the corresponding grey-dotted one.

the considered plants are assumed to sell electricity at the same PPA price. The Net Present Value (NPV) of the project is adopted as the financial figure of merit, with the purpose of examining costs and revenues together, in order to evaluate mutually exclusive investment features and decisions [41].

The results of the analysis are summarized in Fig. 6.5, where the NPV is shown as a function of the TES system capacity, for several SM values. It can be noted that all the gray curves, referring to the base case, i.e., to the reference control strategy, reach a maximum NPV value (NPV_{max}) for a given storage capacity value h_{TES}. Referring again to Fig. 6.2a, such h_{TES} value is the one allowing to reach the maximum revenue for the given SM value. In other words, this analysis allows to properly penalize solutions yielding the same revenue with an increasingly large investment.

The red curves show the impact of the optimal operating strategy on the project NPV, accounting for the revenue increase it allows for (see, e.g., Fig. 6.4b, red lines). It can be seen that the location of NPV_{max} in terms of h_{TES} is not varied with respect to the base case, as expected after Fig. 6.4a. In all cases, the financial advantage resulting from a complete analysis is larger if compared to only the yearly revenue. The SM = 1.5 case can be considered as an example: NPV_{max} = 91.5 M$ for h_{TES} = 5 eq. hours is obtained for the base-case, i.e., the gray-dotted line in Fig. 6.5. For the same system (SM = 1.5, h_{TES} = 5 eq. hours), adopting the optimized control strategy allows for an yearly revenue increase of $\approx$ 4%, as shown in Fig. 6.4b. Notably, this figure is coherent with

previously published results [20]. However, this induces a gain of ≈ 11% in terms of NPV, with NPV_{max} = 103 M$, as shown by the red-dotted line in Fig. 6.5.

The black curves account for the impact of the optimal operating strategy on the project NPV as well but, in this case, what is being evaluated is the reduction in the investment it enables (see, e.g., Fig. 6.4b, black lines). As expected, the NPV is in general larger than the one characterizing the base-case, and this gain grows for larger TES system capacity. However, the gain results always lower than in the previous case, approaching the same value in the SM = 3.5 case. The factor determining this situation is the comparatively low specific cost of the storage system which, for a state-of-the-art system with SM = 2.5 and h_{TES} = 15 eq. hours, accounts for approximately 10% of the total installed cost.

Even though these conclusions are strongly influenced by the parameters adopted in the financial analysis, their validity is expected to hold under all the foreseeable realistic scenarios for state-of-the-art systems.

6.6 Conclusions

Concentrated solar power plants with thermal storage are a promising technology, increasingly considered as an option for widespread conversion of renewable energy. In a context of time-varying tariffs, the storage system can be used to shift the production to the most profitable hours, exploiting the dispatchability capabilities of this technology. The aim of the work presented here was to assess the potential of optimal control techniques, applied to the storage operation, to increase the profitability of the plant. To this end, the model of a state-of-the-art central receiver plant has been developed using high-level modelling languages, based on data available in the literature and in the SAM reference software. Optimal control problems have then been formulated and solved. The different operating strategies are compared based on a detailed financial analysis over the project life-time. A wide system design space is considered, and the results are presented for all the foreseeable combinations of solar field size and storage system capacity.

A novel methodology is introduced, which allows to properly assess the potential of optimal control in terms of both the increased revenue and the reduced investment cost it allows for. In other words, it becomes possible to evaluate the influence of the operating strategy on the system design. It is demonstrated that optimal control should be taken into account when estimating the potential plant revenue since its design and sizing phase. This constitutes a new tool in the designer's hands who, depending on the specific project characteristics and financial framework, may be keen on favouring a larger electricity production or a comparatively lower investment cost. In summary, the main findings of the work are:

- For state-of-the art systems operating in a context of time-varying tariffs, it seems profitable to exploit optimal control to the end of increasing electricity production. This is mainly due to the comparatively low impact of the storage system cost on the investment. On a yearly basis, an average gain in the revenue of the order of 5% is obtained with respect to usually adopted short-sighted strategies. However, this figure is amplified to more than 10% in terms of net present value of the investment when applying the complete financial analysis presented here. Notably however, the storage capacity for which maximum profitability occurs seems to be independent from the considered operating strategy.
- The potential of optimal control in terms of investment cost reduction has been unveiled for the first time. For the case-study technology considered, this follows the possibility of harvesting the same revenue with a smaller storage capacity. Even if this solution is

suboptimal for current CSP practice, it might assume practical significance in evaluating plants with different cost structure, e.g., featuring larger storage relative cost, as is case of PV/batteries installations.

- The results have been obtained with open-source software, and a total of about 50 code lines.

A future step of this research might involve the implementation of the proposed methodology as an extension of reference design models, such as the model implemented into the SAM program.

6.7 Acknowledgements

This work has been carried out during E. Casati's research period at Politecnico di Milano, Dipartimento di Elettronica, Informazione e Bioingegneria, supported by the Dutch Technology Foundation STW, Applied Science Division of NWO and the Technology Program of the Ministry of Economic Affairs, grant # 11143. The authors thankfully acknowledge the precious suggestions about JModelica.org from their colleagues at the University of Lund, Sweden: F. Magnusson, J. Åkesson, and C. Andersson. The help received by the NREL staff working on the SAM support forum, in particular by P. Gilman, has also been invaluable.

A.1 Solar Fields Design

This section details the procedure adopted in order to obtain the design of the solar fields considered here. It shows how the field reflective surface A_{SF} and its time-varying optical efficiency η_{opt} are defined, see Eq. 6.1. As described in §6.2, several solar fields characterized by different SM values are designed for the same hypothetical plant power output, location, and so forth, using the data reported in Tab. 2. For a given SM value, the adopted algorithm, based on the DELSOL3 code [30, 31], searches for a system design capable of yielding the highest financial returns, accounting for capital and other costs against the projected electricity production. The main objective of the tool is to optimize the geometric relationships among the main components of the solar power harvesting system, i.e., the solar field, the tower, and the receiver [25]. It is worth noting that all the designed fields share the design boundaries defined by the data in Tab. 2, aiming at reducing the complexity of the treatment and at facilitating the reproducibility of the results. The ranges of variation for the design variables, in particular, have been selected such that reasonable layouts can be obtained regardless of the considered SM value.

The modelled receiver is of the tubular type, with constant absorptivity α_{REC} and emissivity $\epsilon_{coating}$. The main constraint regarding the design of this component is the maximum admissible heat flux on its surface (see "rec. max flux"). Regarding the solar field, a general layout constraint is expressed in terms of the maximum/minimum distance of the farther/closer heliostats row from the tower (see "helio.-tow. distance/H_{TOW}"). The modelled technology relies on square heliostats with a 12 m side (reflective part), whose main optical properties are also reported in Tab. 2. As anticipated in §6.5, these are arranged in a *radially staggered, surround* field which, for the sake of the layout optimization, is discretized in radial and azimuthal zones (see "N rad. zones" and "N azim. zones"). In order to solve the SF design problem, an optimal number of heliostats has to be allocated within each zone. The program evaluates discrete combinations of values for the main design variables, i.e. the diameter of the receiver D_{REC} and its height-over-diameter ratio $(H/D)_{REC}$, and the tower height H_{TOW}, with a grid-spacing based on the search interval and on the number of

Common parameters			
Location	Daggett - CA	Longitude	-116.8
Latitude [°]	34.9		
$W_{\text{el, gross}}$ [MW_E]	115	η_{PB} [%]	40
α_{REC} [%]	94	$\epsilon_{coating}$ [−]	88
rec. max flux [$kW_T\ m^{-2}$]	1000		
(helio. - tow. distance/H_{TOW})$_{min}$ [−]	0.75	(helio. - tow. distance/H_{TOW})$_{max}$ [−]	12
A_{helio} [m^2]	144	image error [mrad]	1.53
N rad. zones [−]	12	N azim. zones [−]	12
non SF land area [m^2]	182109	SF land area multiplier [−]	1.3
N opt. levels	10		
(D_{REC}, $(H/D)_{REC}$, H_{TOW}) [−]			
Design Variable	**LB**	**UB**	
D_{REC} [m]	8	30	
$(H/D)_{REC}$ [m]	0.5	2.5	
H_{TOW} [m]	100	300	

Table 2: Design parameters and variables used within the radially-staggered solar field layout optimization, with relative lower (LB) and upper (UB) bounds. Several quantities appeared in Tab. 6.1, and are reported here for the sake of clarity. For all the three design variables, the defined range of variation is discretized into 10 points. These data are common to all the solar fields designed in this work.

optimization levels (see "N opt. levels").
The most critical step is the evaluation of the flux distribution on the receiver surface as a function of solar position, which DELSOL3 calculates based on sophisticated aiming techniques. This information allows to iterate on the system design, accounting for the maximum flux levels the receiver can withstand, until an optimum layout is determined. The results regarding the geometry of the solar power harvesting system are reported in Tab. 3. The radial step indicates the distance among two subsequent heliostats rows, and it is assumed constant within each field. It can be noted that the relation between the area A_{SF} and the SM value is not linear, reflecting the decrease of the optical performance as the solar field size grows. As detailed in [25], DELSOL3 outputs also a 2D matrix reporting the field optical efficiency appearing in Eq. 6.1, and defined as

$$\eta_{opt}(t, \text{loc, SF}) = (\mathcal{F}_{REC}\ A_{REC})\ (\text{DNI}\ A_{helio}\ N_{helio})^{-1}\ , \tag{17}$$

where $\mathcal{F}_{REC}$ [$kW_T\ m^{-2}$] is the average flux incident on the receiver at the given time, and A_{REC} [m^2] is the receiver surface. In other words, the total radiation incident on the receiver is divided by the total radiation incident on the heliostat field mirrors for a given solar position. This last bit of information is fully specified in terms of Azimuth and Zenith angles which, in turn, can be calculated for the given time of the year (t) and the plant location (loc) by means of standard methods, see, e.g., [28]. The values of η_{opt}, calculated for the fields whose geometry is defined by the data in Tab. 3, are reported in Tab. 4.

	Solar Multiple (SM)			
	1.5	**2.0**	**2.5**	**3.5**
N_{helio} [−]	6435	8012	10979	16058
A_{SF} [m^2]	926640	1153728	1580976	2312352
total land area [km^2]	7.12	6.85	11.65	20.13
D_{REC} [m]	10.5	13	13	15.5
H_{REC} [m]	24.0	23.5	29.5	35.0
A_{REC} [m^2]	792	960	1205	1704
H_{TOW} [m]	144	189	189	211
min dist. from tow. [m]	108	142	142	158
radial step [m]	135	177	177	198
max dist. from tow. [m]	1597	1558	2089	2534

Table 3: Design results for the optimized solar power harvesting system. The adopted parameters and variables are listed in Tab. 2.

Z.	SM [°]	A. [°] 0	30	60	90	120	150	180	210	240	270	300	330
0.5	**1.5**	.680	.680	.680	.680	.680	.680	.680	.680	.680	.680	.680	.680
	2.0	.720	.720	.720	.720	.719	.719	.719	.719	.719	.720	.720	.720
	2.5	.667	.667	.667	.667	.667	.667	.667	.667	.667	.667	.667	.667
	3.5	.640	.640	.640	.640	.640	.640	.640	.640	.640	.640	.640	.640
7	**1.5**	.680	.680	.679	.678	.678	.677	.677	.677	.678	.678	.679	.680
	2.0	.720	.720	.719	.716	.715	.714	.713	.714	.715	.716	.719	.720
	2.5	.669	.667	.666	.664	.664	.663	.663	.663	.664	.664	.666	.667
	3.5	.638	.638	.638	.637	.637	.637	.636	.637	.637	.637	.638	.638
15	**1.5**	.674	.673	.672	.669	.668	.666	.666	.666	.668	.669	.672	.673
	2.0	.714	.714	.710	.706	.703	.700	.699	.700	.703	.706	.710	.714
	2.5	.659	.659	.658	.656	.654	.653	.652	.653	.654	.656	.658	.659
	3.5	.632	.631	.631	.630	.629	.627	.627	.627	.629	.630	.631	.631
30	**1.5**	.659	.659	.656	.652	.647	.645	.643	.645	.647	.652	.656	.659
	2.0	.704	.702	.697	.688	.680	.674	.672	.674	.680	.688	.697	.702
	2.5	.646	.645	.642	.638	.635	.631	.631	.631	.635	.638	.642	.645
	3.5	.617	.616	.615	.612	.611	.609	.609	.609	.611	.612	.615	.616
45	**1.5**	.642	.641	.636	.630	.624	.619	.617	.619	.624	.630	.636	.641
	2.0	0.690	.687	.678	.666	.653	.646	.643	.646	.654	.666	.678	.687
	2.5	.627	.626	.622	.616	.610	.606	.605	.606	.611	.616	.622	.626
	3.5	.599	.598	.595	.591	.589	.586	.585	.586	.589	.593	.595	.598
60	**1.5**	.603	.600	.594	.585	.577	.570	.569	.572	.578	.585	.594	.600
	2.0	.646	.641	.630	.614	.599	.589	.585	.589	.600	.615	.631	.642
	2.5	.588	.585	.579	.572	.564	.558	.557	.559	.564	.573	.580	.586
	3.5	.560	.559	.556	.551	.546	.543	.543	.543	.547	.551	.556	.559
75	**1.5**	.480	.476	.469	.460	.448	.440	.440	.442	.450	.462	.470	.478
	2.0	.499	.494	.483	.464	.447	.432	.431	.434	.449	.466	.485	.496
	2.5	.464	.461	.454	.447	.436	.429	.428	.431	.437	.448	.457	.464
	3.5	.447	.445	.442	.436	.431	.426	.426	.428	.432	.438	.443	.448
85	**1.5**	.313	.308	.301	.294	.283	.275	.280	.278	.286	.299	.304	.311
	2.0	.296	.291	.282	.265	.255	.242	.244	.245	.257	.268	.286	.294
	2.5	.297	.294	.288	.281	.271	.265	.266	.267	.273	.283	.291	.297
	3.5	.292	.292	.290	.283	.278	.273	.275	.276	.281	.286	.292	.294

Table 4: Design results for the optimized solar fields. Field optical efficiency η_{opt} (see Eq. 17), calculated for the fields whose geometry is defined by the data in Tab. 3. The results are reported, for the four solar multiples considered, as a function of Azimuth (A.) and Zenith (Z.) angles, which define the solar position.

General							
N [year]	25	d_r [% year^{-1}]	8.2	i_{infl} [% year^{-1}]	2.5	N_{loan} [years]	20
f_{debt} [%]	50	r_{loan} [% year^{-1}]	8	$r_{inc.\ tax}$ [% year^{-1}]	40	r_{ITC} [% DC+IC]	30
Direct and Indirect Costs (Eqs. 21, 22)							
SI_{coeff} [\$ m^{-2}]	15	SF_{coeff} [\$ m^{-2}]	180	BOP_{coeff} [\$ kW$_E^{-1}$]	350	PB_{coeff} [\$ kW$_E^{-1}$]	1200
TES_{coeff} [\$ kWh$_T^{-1}$]	27	TOW_{fixed} [M\$]	3	$TOW_{scaling}$ [−]	0.0113	REC_{ref} [M\$]	110
$A_{REC,\ ref}$ [m^{-2}]	1571	$REC_{scaling}$ [−]	0.7	contin. [%]	7	r_{EPC} [% DC]	11
r_{land} [\$ m^{-2}]	2.47	$r_{sales\ tax}$ [%]	5	$base_{sales\ tax}$ [% DC]	80		
Operating Income (Eq. 23)							
$O\&M_{cap,coeff}$ [\$ kW$_E^{-1}$]	65	$O\&M_{gen,coeff}$ [\$ MWh$_E^{-1}$]	4	$r_{insurance}$ [% DC+IC]	0.5	$r_{PPA,\ escalation}$ [% year^{-1}]	1
$r_{perf.\ degr.}$ [% year^{-1}]	0.5						

Table 5: Data adopted in the financial analysis. The meaning of the reported quantities is discussed in the body of the appendix.

A.2 Financial Analysis

The financial model presented here has been developed following the SAM framework [26] and the work of [41]. The parameters for the analysis, reported in Tab. 5, are assigned typically encountered values, see, e.g., [10]. The selected figure of merit is the Net Present Value (NPV) of the solar power project, i.e., the sum of the actualized net cash flows along the project life [41], which reads

$$\mathrm{NPV} = \sum_{n=0}^{N} \frac{F_n}{(1+d)^n} = F_0 + \frac{F_1}{(1+d)^1} + \frac{F_2}{(1+d)^2} + \cdots + \frac{F_N}{(1+d)^N} \,. \tag{18}$$

N is the analysis period (i.e., the project life), and d the nominal discount rate

$$d = ((1 + d_r/100)\,(1 + i/100) - 1) \cdot 100 \,, \tag{19}$$

where d_r is the real discount rate, and i is the inflation rate. The F_n terms represent the net after-tax cash flows in the n years: a negative value represents a net outflow, a positive value a net inflow. They are evaluated as

$$F_n = \begin{cases} -(1 - f_{debt}/100)\ (\mathrm{DC{+}IC}) & \text{if } n = 0 \quad (20a) \\ \text{op. inc.}(n) - \text{inc. tax}(n) + \text{tax sav.}(n) + \ldots & \quad (20b) \\ \ldots - \text{debt repaym.}(n) - \text{debt int. paym.}(n) & \text{if } 0 < n \leq N \quad (20c) \end{cases}$$

For the first year of the analysis, i.e. conventionally the 0th year, the financial balance accounts for the debt portion of the investment only, expressed as a fraction f_{debt} of the total installed costs, i.e.,

as shown in Eq. 20a, the sum of direct-costs (DC) and indirect ones (IC), respectively defined as

$$\mathrm{DC} = (\mathrm{SI} + \mathrm{SF} + \mathrm{BOP} + \mathrm{PB} + \mathrm{TES} + \mathrm{TOW} + \mathrm{REC})\left(1 + \frac{\text{contin.}}{100}\right), \tag{21}$$

$$\mathrm{IC} = \mathrm{EPC} + \mathrm{LC} + \mathrm{S_{tax}}\,. \tag{22}$$

The first two terms in Eq. 21 account for the solar field costs, in terms of site improvement SI and of heliostats cost SF, as $\mathrm{SI} = A_{\mathrm{SF}}\ \mathrm{SI_{coeff}}$ and $\mathrm{SF} = A_{\mathrm{SF}}\ \mathrm{SF_{coeff}}$, respectively. Similarly, BOP and PB account for the cost of the Balance Of Plant and of the power block, as $\mathrm{BOP} = W_{\mathrm{el,\,gross}}\ \mathrm{BOP_{coeff}}$ and $\mathrm{PB} = W_{\mathrm{el,gross}}\ \mathrm{PB_{coeff}}$. TES relates the storage system cost to its capacity in terms of thermal energy, i.e $\mathrm{TES} = W_{\mathrm{el,gross}}\ \mathrm{TES_{coeff}}$. The tower cost is evaluated by multiplying a fixed cost component to an exponential function of the tower height, i.e., $\mathrm{TOW} = \mathrm{EXP}\ (\mathrm{TOW_{scaling}}\ H_{\mathrm{TOW}})\ \mathrm{TOW_{fixed}}$. The receiver cost is found by multiplying the cost of a reference component (i.e., $\mathrm{REC_{ref}}$) by the corresponding surface ratio, i.e., $\mathrm{REC} = \mathrm{REC_{ref}}\ (A_{\mathrm{REC}}/A_{\mathrm{REC,\,ref}})^{\mathrm{REC_{scaling}}}$. A contingency factor (i.e. "contin".) is also considered.

As shown in Eq. 22, the indirect costs account for the Engineering-Procurement-Construction Costs (EPC), calculated as a percentage r_{EPC} of the direct costs. The land cost term LC is evaluated by applying the unit cost coefficient r_{land} to the total land area needed (see Tab. 3). The sales tax $\mathrm{S_{tax}}$ is a one-time tax included in the project total installed cost, and therefore in the depreciable basis (see in the following), and is calculated on a fraction of the direct costs as $\mathrm{S_{tax}} = \mathrm{DC}\ (\mathrm{base_{sales\ tax}}/100)\ (r_{\mathrm{sales\ tax}}/100)$.

Regarding the financing scheme, a fraction f_{debt} of the total installed cost is assumed to be borrowed. This initial debt is payed back through annual amounts (i.e. "debt repaym."), calculated by using the levelized mortgage payment methodology, i.e., by assuming constant payments on principal amount over the loan term N_{loan} at the rate r_{loan}. The payment of interests is evaluated by applying the same rate on the remaining debt, through annual amounts (i.e. "debt int. paym.").

For the calculation of the cash flows for the following years of the analysis, i.e., when $0 < n \leq N$, Eq. 20c applies (the dependency from n, common to all terms, is not explicitly indicated in the following in order to improve readability). The first term accounts for the operating income the project generates in the n^{th} year, i.e.,

$$\text{op. inc.} \;=\; \mathrm{Rev} - (\mathrm{O\&M_{cap}} + \mathrm{O\&M_{gen}} + \text{insurance})\,. \tag{23}$$

Rev indicates the yearly revenue from sold electricity, i.e., for the 1^{st} year, the performance indicator used throughout §6.5. Thus, an annual average value for the energy price $\overline{P}_{\mathrm{E}}$ can be defined as $\overline{P}_{\mathrm{E}} = E/\mathrm{Rev}$, with E being the sold energy. These values are used as the basis for the analysis and, for the following years (i.e., for $1 < n \leq N$), the plant revenue is calculated as $\mathrm{Rev} = E_{\mathrm{corr}}/\overline{P}_{\mathrm{E,corr}}$, whereby E_{corr} corrects E accounting, year after year, for the degradation of performance $r_{\mathrm{perf.\ degr.}}$, and $\overline{P}_{\mathrm{E,\,corr}}$ applies the annual PPA price escalation rate $r_{\mathrm{PPA,\,escalation}}$ to $\overline{P}_{\mathrm{E}}$. Furthermore, both quantities are yearly inflated by considering the i_{infl} rate.

The $\mathrm{O\&M_{cap}}$ and $\mathrm{O\&M_{gen}}$ terms in Eq. 23 refer to the operating and maintenance costs related to the plant nameplate power capacity and the generated energy E, and are evaluated by multiplying these quantities by the corresponding coefficients $\mathrm{O\&M_{cap,coeff}}$ and $\mathrm{O\&M_{gen,coeff}}$. Also the annual insurance cost is considered as an operating expense (therefore reducing the taxable income, see the following), and is calculated as a percentage $r_{\mathrm{insurance}}$ of the total installed costs (i.e., DC+iC) . For the years of the analysis following the first, all the quantities appearing between brackets in Eq. 23 are recalculated accounting for inflation.

The second term in Eq. 20c refers to a global annual income tax, which applies to a percentage

$r_{\text{inc. tax}}$ of the taxable income, and reads

$$\text{inc. tax} = (r_{\text{inc. tax}}/100)\ (\text{op. inc.} - \text{debt int. paym.} - \text{depreciation})\ . \tag{24}$$

The depreciation term represents the decrease in value of project assets over the analysis period, and it reduces the taxable income. In the present work, the so-called Modified Accelerated Cost Recovery System depreciation schedule offered by the US Federal government using a five-year life and half-year convention is used, commonly referred to as *5-yr MACRS* [41]. The depreciation is expressed as a percentage of the depreciable basis, corresponding to the total installed costs in this analysis, and it applies to the first five years of the project life as follows: 20%, 32%, 19.2%, 11.52%, 11.52%, and 5.76%.

The third term in Eq. 20c refers to tax savings deriving from tax credits or incentives. In the present analysis, only an Investment Tax Credit equal to a fraction r_{ITC} of the initial investment (i.e. of the total installed costs) is considered. This applies on the first year of the analysis, i.e. for $n = 1$ only.

A.3 Modelica and Optimica listings

Listing 1: Plant model in Modelica.

```
model CSP_tower
 input Real Q_rec_inc_av ;
 input Real m_PB;
 input Real Q_def;
 output Real x_TES;
 Real m_rec_HTF;
 Real Q_rec_inc;
 Real Q_rec_abs, Q_rec_HTF, Q_rec_HTF, Q_lost, W_PB;
 parameter Real alpha_rec = 0.94;
 parameter Real eta_rec_th = 0.88;
 parameter Real eta_des = 1;
 parameter Real f_max_Q_rec_inc = 1.2 ;
 parameter Real T_TES;
 parameter Real x_TES_0 = 0.05;
 equation
 Q_rec_inc  = Q_rec_inc_av - Q_def;
 Q_rec_HTF  = Q_rec_abs * (1 - eta_rec_th);
 m_rec_HTF = Q_rec_HTF;
 W_PB       = m_PB * eta_des;
 T_TES * der(x_TES) = m_rec_HTF - m_PB;
initial equation
 x_TES = x_TES_0;
end CSP_tower;
```

Listing 2: Optimization problem in Optimica.

```
optimization optim(objectiveIntegrand =
  -plant.W_PB*f_TOD + c*du_dt^2 + g*s*(u-plant.f_min_m_PB),
  startTime = 0,finalTime = 7*24*3600);
 CSP_tower plant(T_TES=15*3600);
 parameter Real g = 1;
 parameter Real c = 2250000;
 // Known inputs
 input Real Q_rec_inc_av;
 input Real f_TOD;
 // Unknown control variables
 input Real f(min=0, free=true);
 input Real du_dt (free=true, nominal = 4e-5);
 // Other extra variables
 Real s(free=true);
 Real u(min=0,max=1.0);
equation
 Q_rec_inc_av  = plant.Q_rec_inc_av;
 TOD           = plant.TOD;
 u             = plant.m_PB + s;
 der(u)        = du_dt;
 f             = plant.Q_def;
initial equation
 plant.m_pb=0;
constraint
 s >= 0; s <= u;
 m_PB >= 0; m_PB <= 1;
 Q_def >= 0;
 x_TES >= 0.05; x_TES <= 1;
 Q_rec_inc >=0; Q_rec_inc <= f_max_Q_rec_inc;
 f >= 0; f <= plant.Q_rec_inc_av;
 plant.x_st(finalTime) = 0.05;
end optim;
```

Nomenclature

Q, W	=	thermal and electrical power [various units]
m, P	=	mass flow rate [kg s^{-1}], electricity price [\$ kWh_{el}^{-1}]
t, Rev	=	time [various units], plant yearly revenue [M\$ $year^{-1}$]
T, x	=	temperature [°C], storage level [−]
η, α	=	efficiency and absorptivity [−]
ϵ_{avail}, ϵ_{refl}	=	average heliostats availability and reflectivity [−]
A, H	=	surface [m^2], height [m]
D, h_{TES}	=	diameter [m], storage capacity [eq. full-load hours]
loc	=	plant location [-]

Subscripts & superscripts

E, T	=	electric, thermal
REC, TOW	=	receiver, tower
TES-C, TES-H	=	cold and hot tanks in the TES system
in, out	=	inlet and outlet conditions of a given HTF stream
opt, inc, av	=	optical, incident (radiative flux), available
min, max	=	minimum and maximum
in, fin	=	initial and final

Acronyms

R&D	=	Research & Development
CSP	=	Concentrated Solar Power
TES	=	Thermal Energy Storage
CR	=	Central Receiver (i.e. solar tower)
HTF	=	Heat Transfer Fluid
PPA	=	power purchase agreement
TOD	=	Time Of Day
LCOE	=	Levelized Cost Of Electricity
SAM	=	System Advisory Model
DNI	=	Direct Normal Irradiation [W m^{-2}]
NLP	=	Non-Linear Programming
PB	=	Power Block
SF	=	Solar Field
SM	=	Solar Multiple
O&M	=	Operations and Maintenance
NPV	=	Net Present Value

References

[1] M. Mediavilla, C. de Castro, I. Capellán, L. J. Miguel, I. Arto, and F. Frechoso. The transition towards renewable energies: Physical limits and temporal conditions. *Energy Policy*, 52(0):297 – 311, 2013.

[2] I. Galiana and C. Green. Let the global technology race begin. *Nature*, 462(7273):570–571, 2009.

[3] A. Pifre. A solar printing press. *Nature*, 26,:503–504, 1882.

[4] G. Francia. Pilot plants of solar steam generating stations. *Solar Energy*, 12(1):51 – 64, 1968.

[5] L.C. Spencer. A comprehensive review of small solar-powered heat engines: Part I. A history of solar–powered devices up to 1950. *Solar Energy*, 43(4):191–196, 1989.

[6] R. Pitz-Paal, A. Amin, M. Bettzüge, P. Eames, F. Fabrizi, G. Flamant, F. Garcia Novo, J. Holmes, A. Kribus, H. van der Laan, C. Lopez, P. Papagiannakopoulos, E. Pihl, P. Smith, and H.J. Wagner. Concentrating solar power in Europe, the Middle East and North Africa: Achieving its potential. *Journal of Energy and Power Engineering*, 7(2):219–228, 2013.

[7] P. Denholm and M. Mehos. Quantifying the value of CSP with thermal energy storage. In *SunShot Concentrating Solar Power Program Review 2013*. U.S. Department of Energy (DOE), 2013.

[8] O. Behar, A. Khellaf, and K. Mohammedi. A review of studies on central receiver solar thermal power plants. *Renewable and Sustainable Energy Reviews*, 23(0):12 – 39, 2013.

[9] G. Beckam and P.V Gilli. *Thermal Energy Storage*. Springer–Verlag, 1984.

[10] C.S. Turchi and M.J. Wagner. Power tower reference plant for cost modeling with the system advisor model (SAM). In *Proceedings of the World Renewable Energy Forum, WREF 2012*, volume 4, pages 2598–2605, 2012.

[11] J.E. Pacheco and al. Final test and evaluation results from the Solar Two project. Technical Report SAND2002-0120, Sandia National Lab, Albuquerque, New Mexico, 2002.

[12] E.F. Camacho, F.R. Rubio, M. Berenguel, and L. Valenzuela. A survey on control schemes for distributed solar collector fields. part I: Modeling and basic control approaches. *Solar Energy*, 81(10):1240 – 1251, 2007.

[13] E.F. Camacho, F.R. Rubio, M. Berenguel, and L. Valenzuela. A survey on control schemes for distributed solar collector fields. part II: Advanced control approaches. *Solar Energy*, 81(10):1252–1272, 2007.

[14] B. Prior. Cost and LCOE by generation technology 2009 – 2020. Available online (accessed November 2013): http://www.greentechmedia.com/images/wysiwyg/research-blogs/GTM-LCOE-Analysis.pdf, 2011.

[15] T. Richert, K. Riffelmann, and P. Nava. LCOE versus PPA bid price – how different financing parameters influence their values. In *Proceedings of the* 18^{th} *SolarPACES conference*, Marrakech, Morocco, 11–14 September 2012.

[16] J. García-Barberena, P. García, M. Sanchez, M. J. Blanco, C. Lasheras, A. Padrós, and J. Arraiza. Analysis of the influence of operational strategies in plant performance using Simul-

CET, simulation software for parabolic trough power plants. *Solar Energy*, 86(1):53 – 63, 2012.

[17] K.M. Powell, J.D. Hedengren, and T.F. Edgar. Dynamic optimization of solar thermal systems with storage. In *Proceedings of the AIChE 2012 Annual Meeting*, Pittsburgh, PA, October 28-November 2 2012.

[18] F. Nolteernsting, D. Fischer, J. Gall, and D. Abel. Optimal storage usage in CSP : A dynamic programming approach. In *Proceedings of the* 18^{th} *SolarPACES conference*, Marrakech, Morocco, 11–14 September 2012.

[19] M. Wittmann, H. Breitkreuz, M. Schroedter-Homscheidt, and M. Eck. Case studies on the use of solar irradiance forecast for optimized operation strategies of solar thermal power plants. *IEEE Journal of Selected Topics in Applied Earth Observations and Remote Sensing*, 1(1):18–27, 2008.

[20] M. Wittmann, M. Eck, T. Hirsch, and R. Pitz-Paal. Theoretical economic potential of the Spanish premium tariff for solar thermal power plants. In *Proceedings of the* 14^{th} *SolarPACES conference*, Las Vegas - CA, United States, 2008.

[21] M. Wittmann, M. Eck, R. Pitz-Paal, and H. Müller-Steinhagen. Methodology for optimized operation strategies of solar thermal power plants with integrated heat storage. *Solar Energy*, 85(4):653 – 659, 2011.

[22] E. Lizarraga-Garcia, A. Ghobeity, M. Totten, and A. Mitsos. Optimal operation of a solar-thermal power plant with energy storage and electricity buy-back from grid. *Energy*, 51(0):61 – 70, 2013.

[23] A.H. Slocum, D.S. Codd, J. Buongiorno, C. Forsberg, T. McKrell, J.-C. Nave, C.N. Papanicolas, A. Ghobeity, C.J. Noone, S. Passerini, F. Rojas, and A. Mitsos. Concentrated solar power on demand. *Solar Energy*, 85(7):1519–1529, 2011.

[24] M. Biencinto, R. Bayón, E. Rojas, and L. González. Simulation and assessment of operation strategies for solar thermal power plants with a thermocline storage tank. *Solar Energy*, 103(0):456 – 472, 2014.

[25] M.J. Wagner. Simulation and predictive performance modeling of utility-scale central receiver system power plants. Technical report, 2008.

[26] M.J. Wagner and P. Gilman. Technical manual for the SAM physical trough model. Technical Report NREL/TP-5500-51825, National Renewable Energy Laboratory, U.S. Department of Energy, 2011.

[27] S. Wilcox and W. Marion. Users manual for TMY3 data sets. Technical Report NREL/TP-581-43156, National Renewable Energy Laboratory, U.S. Department of Energy, 2008.

[28] J.A. Duffie and W.A. Beckam. *Solar Engineering of Thermal Processes*. John Wiley & Sons, Inc., 3^{rd} edition, 2006.

[29] R. Pitz-Paal, N.B. Botero, and A. Steinfeld. Heliostat field layout optimization for high-temperature solar thermochemical processing. *Solar Energy*, 85(2):334–343, 2011.

[30] B.L. Kistler. A users manual for DELSOL3: A computer code for calculating the optical performance and optimal system design for solar thermal central receiver plants. Technical Report SAND86-8018, Sandia National Labs, Albuquerque, NM, 1986.

[31] P. Garcia, A. Ferriere, and J.-J. Bezian. Codes for solar flux calculation dedicated to central receiver system applications: A comparative review. *Solar Energy*, 82(3):189–197, 2008.

[32] S. E. Mattsson, H. Elmqvist, and M. Otter. Physical system modeling with Modelica. *Control Engineering Practice*, 6(4):501–510, 1998.

[33] J. Åkesson, C.E. Årzén, M. Gäfvert, T Bergdahl, and H Tummescheit. Modeling and optimization with Optimica and JModelica.org – Languages and tools for solving large-scale

dynamic optimization problems. *Computers and Chemical Engineering*, 34(11):1737–1749, 2010.

[34] The Modelica Association. Modelica - A unified object-oriented language for physical systems modeling - Language specification version 3.2 revision 2. Online - www.modelica.org (Last accessed June 2014), July 30 2013.

[35] J. Åkesson. Optimica - An extension of Modelica supporting dynamic optimization. In *Proceedings* 6^{th} *International Modelica Conference*, pages 57–66, Bielefeld, Germany, Mar. 3–4 2008.

[36] Modelon AB. *JModelica.org User Guide: Version 1.9*, 2013.

[37] Open Source Modelica Consortium. *OpenModelica Users Guide for OpenModelica 1.9.1 Beta2*, 2014.

[38] J. Andersson, J. Åkesson, F. Casella, and M. Diehl. Integration of CasADi and JModelica.org. In C. Clauss, editor, *Proceedings* 8^{th} *International Modelica Conference*, pages 218–231, Dresden, Germany, Mar 20–22 2011. Modelica Association.

[39] F. Magnusson. Collocation methods in JModelica.org. Master's thesis, Department of Automatic Control, Lund University, 2012.

[40] A. Wächter and L. T. Biegler. On the implementation of an interior-point filter line-search algorithm for large-scale nonlinear programming. *Math. Program.*, 106(1):25–57, May 2006.

[41] W. Short, D.J. Packey, and T. Holt. A manual for the economic evaluation of energy efficiency and renewable energy technologies. Technical Report NREL/TP-462-5173, National Renewable Energy Laboratory, U.S. Department of Energy, 1995.

Part II

Fundamental Aspects

7

Flexible Asymmetric Shock Tube (FAST): Commissioning of a High Temperature Ludwieg Tube for Wave Propagation Measurements

Part of the contents of this chapter will appear in:

T. Mathijssen, E. Casati, M. Gallo, N.R. Nannan, C. Zamfirescu, A. Guardone, & P. Colonna
Meas Sci Technol, To be submitted for publication (2014)

Abstract *This chapter describes the commissioning of the Flexible Asymmetric Shock Tube (FAST) setup, designed and built at the Delft University of Technology. The aim of this Ludwieg Tube facility is to measure wave propagation speed in the high pressure side of the tube, with the final objective of providing the first experimental evidence of the rarefaction shock waves in the dense vapor region of fluids formed by complex organic molecules. Measurements can be performed for a variety of fluids, and up to temperature and pressure conditions equal to 400° C and 20 bar, respectively. A fast opening valve induces a pressure disturbance propagating in the tube, which is thus sensed through 4 dynamic pressure transducers. The FAST components and the measurement methodology are described in detail. The fast opening valve is characterized in terms of its opening time. The results regarding a shock wave forming in air are presented, and used to demonstrate and validate the setup capabilities. Preliminary expansion measurements in* D_6 *siloxane are also presented, being of special interest to the end of the envisaged non-classical gas dynamics experiments.*

7.1 Introduction

The branch of gas dynamics investigating exotic specimens such as rarefaction shock waves, and mixed or split waves, is called non-classical [1, 2]. However, the existence of non-classical gas dynamic phenomena in the single-phase vapour region is still an open question in fluid mechanics. Nsotwithstanding a certain number of attempts, experimental evidences are lacking.

The empirical verification of the voluminous theoretical body forming non-classical gas dynamics, contributed by a number of scientists worldwide since the first decades of the 20th century, would constitute a big advancement for science. Furthermore, a comparatively close at hand industrial application already exists in the field of organic Rankine cycle (ORC) turbogenerators [3, 4], a technology for the conversion of thermal energy into electricity presently growing at a fast pace [5].

This work documents the design, construction, and commissioning phases of the flexible asymmetric shock tube (FAST) set-up. This is a dense gas Ludwieg tube conceived and installed at the Delft University of Technology, The Netherlands, with the aim of providing the first experimental proof of the most fascinating and evanescent non-classical gas dynamics effect, namely the rarefaction shock wave (RSW).

The theoretical framework surrounding this research is summarized in §7.2, together with a literature review regarding past experiences in the field of experimental non-classical gas dynamics. A conceptual description of the FAST set-up and of its working principle, and the detailed description of the main components are provided in §7.3. The data acquisition and control infrastructures are presented in §7.4. The results of the preliminary experiments conducted in order to validate the functioning of the FAST are reported and discussed in §7.5, while the conclusions of the work and an putlook to the future are presented in §7.6.

7.2 Fundamentals

The first studies in the field of non-classical gas dynamics were conducted by Nobel-laureate Hans Bethe, in 1942 [6]. An early contribution is also due to Zeldovich [7] and Weyl [8]. Though, it was Thompson who first provided a systematic treatment in its seminal works [1, 9, 10]. A recent review can be found in Ref. [11]. A necessary condition for non-classical behaviour to be physically

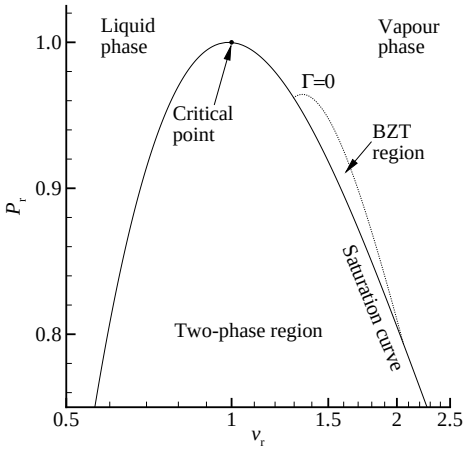

Figure 7.1: Saturation and $\Gamma = 0$ curves in the $v_R - P_R$ plane of reduced specific volume and pressure, as computed by the SW thermodynamic model [19], for siloxane D_6 (dodecamethylcyclohexasiloxane, $C_{12}H_{36}O_6Si_6$): $MW = 444.9$ [g mol^{-1}], $T_{CR} = 372.7$ [°C], $P_{CR} = 9.61$ [bar], $\rho_{CR} = 246.8$ [kg m^{-3}]. Reduced thermodynamic variables are made dimensionless by their critical point values. The non-classical region (BZT region) is bounded by the saturation curve and the $\Gamma = 0$ curve.

admissible is that the fundamental derivative of gas dynamics

$$\Gamma \equiv 1 + \frac{\rho}{c}\left(\frac{\partial c}{\partial \rho}\right)_s = \frac{v^3}{2c^2}\left(\frac{\partial^2 P}{\partial v^2}\right)_s, \tag{7.1}$$

a thermodynamic property of the fluid first introduced by Hayes [12], is negative in part of the covered domain. In definition (8.1), ρ is the density, s is the entropy, P is the pressure, $v = 1/\rho$ is the specific volume, and c is the zero-frequency speed of sound $c \equiv (\partial P/\partial \rho)_s$. If Γ is negative in a finite thermodynamic region, RSWs are admissible, among other so-called non-classical waves [9]. From basic gas dynamics theory [9, 12], an expansion perturbation entirely embedded in the $\Gamma < 0$ region necessarily evolves as a discontinuity, namely as a non-classical rarefaction shock wave, whereas a compression disturbance disintegrates into an isentropic non-classical compression wave. After the names of the above mentioned scientists, substances characterized by thermodynamic states featuring negative values of Γ in the dense vapour phase are called Bethe-Zel'dovich-Thompson (BZT) fluids.

Much attention has recently been devoted to the computation of the negative-Γ region, and to the identification of BZT compounds among both pure fluids, see Ref. [13] for a review, and binary mixtures [14]. Currently, there are three classes of substances predicted to be BZT by the most accurate thermodynamic models available, namely hydrocarbons [15], perfluorocarbons [15–17], and siloxanes [18]. Figure 7.1 shows the saturation curve and the non-classical ($\Gamma < 0$) region of the cyclic siloxane D_6.

Experimental evidence of non-classical gas dynamics is available only for flows displaying liquidvapour phase transition, see Refs. [20–22], or in allotropic phase changes in solid-solid systems [23]. In the single-phase vapour region, only classical gas dynamics phenomena have been

observed so far. Compared to the amount of theoretical and numerical studies on non-classical gas dynamics, a comparatively limited amount of effort has been devoted to experimental assessments, mainly due to the technical difficulties related to the observation of these fleeting waves, as discussed in Refs. [24, 25].

A first attempt has been carried out in the former USSR by Borisov and colleagues in 1983 [26, 27] who claimed to have measured a RSW in Freon-13 (trifluorochloromethane, CCl_3F). Fergason et al. [24, 28] and others [22, 29] refute that this could have been a RSW in the single phase region and provide alternative interpretations of that experiment by pointing towards critical point phenomena and two-phase effects. Recent studies show that the fundamental derivative of gas dynamics indeed is negative in the two-phase critical point region [30] and that rarefaction shockwaves are possible in close-to-critical conditions [31].

In the early 2000's, a shock-tube experiment has been pursued at the University of Colorado at Boulder, with the aim of producing a RSW in perfluorocarbon fluid PP10 (Perfluorofluorene, $C_{13}F_{22}$), see Ref. [24]. The experiment eventually failed because the working fluid underwent thermal decomposition due to the extremely high operating temperature. This put into evidence one of the major obstacles, namely that the BZT thermodynamic region is very close to the thermal decomposition temperature of suitable organic fluids, which is in the range 350–400 °C. In addition, the repeatable rupture of the shock-tube diaphragm proved unattainable due to the relatively small pressure difference and the large acoustic impedance of the fluid [32, 33].

7.3 The FAST Set-Up

Building on the experience acquired during the Boulder experiment, the novel FAST set-up for the generation of RSWs has been conceived, designed and constructed at the Delft University of Technology, The Netherlands, with the participation of an international consortium of academic and industrial partners, as documented in Ref. [25].

Siloxanes have been selected as the working fluid class for the available knowledge regarding their thermal stability [34, 35], thermodynamic properties [19, 36–38], and their use as working fluids in thermal energy conversion systems [39–41]. Moreover, the products of thermal decomposition of siloxanes are non-toxic polymers, whereas thermal decomposition of perfluorocarbons may result in highly corrosive hydrofluoric acid (HF) and possibly other very toxic compounds. Furthermore, the flammability of siloxanes is far lower than that of hydrocarbons.

Few of the compounds of the siloxane family are candidate BZT fluids [18]. Initially, D_6 is chosen as working fluid as the result of a trade-off between the size of the predicted BZT region and the thermal stability of the fluid.

The design of the RSW experiment drove studies aimed at better identifying the thermodynamic region within which non-classical phenomena are admissible, see, e.g., Ref [42]. Given that the experimental conditions are difficult to realize and that the rarefaction shock wave is expected to be weak, therefore more challenging to measure, several authors proposed methods aimed at relaxing the experimental constraints by producing comparatively stronger phenomena [28].

In particular, Guardone et al. [43] presented an analytical procedure to identify the thermodynamic states resulting in the RSW exhibiting the maximum pressure difference, the RSW with maximum Mach number, and the RSW with the largest strength, over the entire dense-vapour thermodynamic region of a given BZT fluid. Uncertainty quantification applied to flow simulations has been preliminarily used, as an aid in determining the optimal experimental conditions [44].

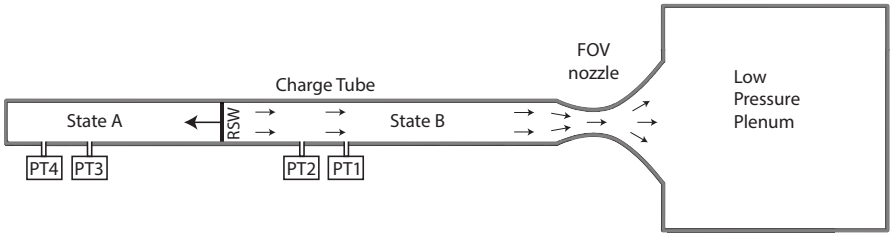

Figure 7.2: Conceptual layout of the FAST dense gas Ludwieg tube setup, representative of a time instance after the opening of the FOV separating the charge tube (CT) from the reservoir (LPP). A rarefaction shock wave (RSW) propagates into the charge tube at supersonic speed W. Past the RSW, the fluid is accelerated from rest conditions A to post-shock conditions B and flows into the reservoir through the nozzle. At the nozzle throat, sonic conditions S are attained.

7.3.1 Working Principle

The working principle of the FAST setup is depicted schematically in Fig. 7.2. The Ludwieg-tube facility is composed of a high-pressure charge tube connected to a low pressure plenum. The charge tube and the reservoir are separated by a fast opening valve. The fluid is initially at rest and the temperature is kept uniform by a suitable thermal control system. The experiment starts when the FOV is opened, thus connecting the charge tube to the reservoir. Depending on the pressure, compression or rarefaction waves will propagate into the charge tube. In case of suitable initial states A (charge tube) and R (reservoir) in a BZT fluid, the rarefaction waves are expected to coalesce forming a RSW. The fluid is accelerated from rest conditions A to condition B, and thus flows into the LPP through a nozzle integrated in the FOV. The nozzle is designed to work in choked conditions in the RSW experiment, in order to prevent disturbances to propagate from the plenum into the charge tube. Fast response absolute dynamic pressure transducers are flush-mounted along the charge tube in order to measure the incident wave.

A time-of-flight (TOF) method can be adopted to determine the speed of the waves travelling in the CT as discussed in Ref. [25]. The wave arrival time is measured at four consecutive stations, i.e. pressure probes PT1 – PT4 in Fig. 7.2. Since the distance between the stations is known, the wave speed can be easily calculated.

This procedure can be first adopted to estimate the speed of sound in the unperturbed state, namely by inducing a weak (acoustic) disturbance propagating through the charge tube. This measurement is expected to be more accurate than the prediction obtained by means of the thermodynamic models available for siloxanes [19].

Stronger pressure waves can be generated in the same way (e.g., by varying the initial pressure levels in the setup) and their speed of propagation measured according to the same principle. In case a RSW is formed, its speed must be greater than the local speed of sound just determined. In other words, by measuring the difference in wave speed between to subsequent experiments, it is possible to detect if a wave is moving at supersonic speed, thus proving that it is indeed a RSW.

Fig. 7.3 shows the RSW and the expansion up to the nozzle throat in the reduced volume-pressure plane, and the flow Mach number profile along the charge tube at time $t = t_1$, i.e. the instant in which the shock is predicted to be fully formed [25].

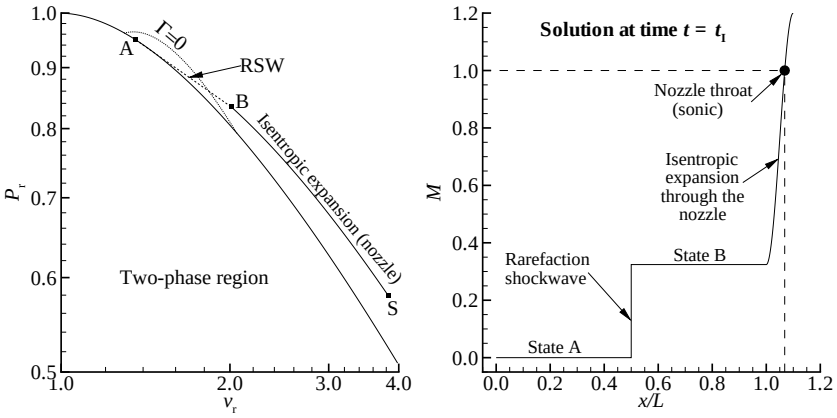

Figure 7.3: Left: Expansion in the charge tube up to the nozzle throat in the v_r-P_r plane. Right: Mach profile at time $t = t_I$ for a fully formed RSW.

The entire setup is constructed out of stainless steel AISI 316Ti, and all connections are sealed using graphite gaskets, making the facility an hermetically closed system, whose schematic layout is shown in Fig. 7.4. In order to attain the desired conditions in the CT, the working fluid is heated and vaporised in the vapour generator (HFT). Once the target pressure is obtained, a valve is opened connecting the HFT with the reference tube (RT), a component used for the thermal control of the charge tube (CT), and the CT itself, where the desired super-heating is thus induced by heating the vapor. Once all temperatures have stabilized, the test can begin. The valve between the HFT and the RT is closed just before the FOV opening to avoid flashing of the liquid in the vapour generator. Most of the fluid in the CT flows to the LPP and condenser (COND) after the FOV is opened, where it condenses and is stored in the return line (RL). For the subsequent experiments, the FOV is closed again and the valve between HFT and RT is opened in order to fill with vapor this last volume together with the CT. This procedure can be repeated until the liquid level in the HFT lies within acceptable limits.

7.3.2 Vapour Generator

The vapour generator, or HFT, is a 5.9 liter vessel designed to bring the working fluid up to the desired thermodynamic conditions, see Fig. 7.5. During normal operation, the HFT contains a liquid-vapour mixture of the working fluid, in conditions of thermodynamic equilibrium (i.e. saturation). A connecting pipe leads to a burst disc that breaks at 27 bar followed by an overpressure valve as safety precaution. At the bottom of the vessel, the liquid can be extracted through a manual valve (connected to flange 1 in Fig. 7.5). The connection to the reference tube is done through flange 7, which can be closed off by similar valve. Another connection leads to the flow return pipe through flange 3, and can be closed off by a pneumatic valve. The flanged connection 8 is used to fill the HFT with liquid. Several other flanges accommodate the required instruments. A PT-100 temperature sensor is installed at flange 2 (TE1.0 in Fig. 7.4), a static pressure transducer with stainless steel membrane at flange 5 (P1.0), and a radar liquid level meter at flange 6 (LL). The vessel

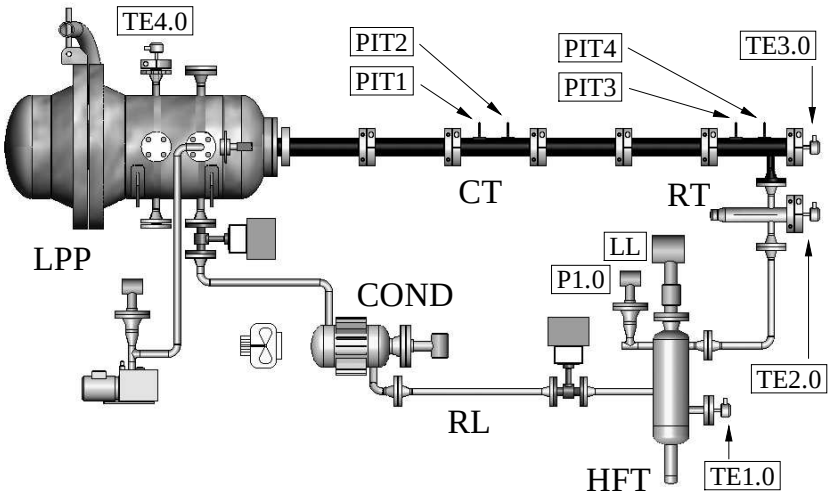

Figure 7.4: Schematic overview of the FAST setup.

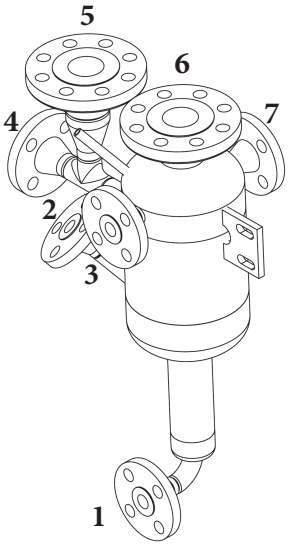

Figure 7.5: Drawing of the vapour generator (HFT). Numbers corresponding to flanged connections: 1. liquid drain, 2. PT-100 T sensor (TE1.0 in Fig. 7.4), 3. to return line (RL), 4. to burst disc, 5. static pressure transducer (P1.0), 6. liquid level meter (LL), 7. reference tube (RT)

is equipped with a 1.5 kW ceramic band heater on the bottom section. To ensure good conducting contact between the band heaters and the wall, a 2 mm graphite layer is inserted between the band heater and the metal wall. Under normal operation conditions, the liquid level is high enough to cover the wall in contact with this heater, which is used as the main supply of thermal energy.

Preliminary tests have highlighted that condensation occurs in the unheated sections, after which the condensate accumulates and cools below saturation conditions. This subcooled liquid periodically flows back in the bulk liquid, temporarily ceasing boiling with a pressure drop as a consequence. This induces a periodic instability, which prevents to maintain the desired stable thermodynamic conditions. In order to overcome this problem, all the walls of the HFT are heated. However, since saturation conditions must be guaranteed in the vessel, the walls are kept at a temperature below the saturation value, such that no super-heating of the vapour occurs. In the middle section of the vessel a 2.8 kW ceramic band heater is used, again with an interposed graphite layer. The pipe leading to the burst disc (flange 4), the pipe leading to the reference tube (flange 7), and the top of the vessel are equipped each with a 6 m long 1 kW heating wire. The entire HFT is covered with a layer of minimum of 50 mm rockwool insulation.

7.3.3 Reference Tube

The reference tube, or RT, is a component used for the thermal control of the charge tube. For this purpose it has the same geometry of a section of the charge tube except for its length, which is 500 mm. It has an internal diameter of 40 mm and 15 mm thick walls. On one end, a PT-100 is mounted to accurately measure the fluid temperature (TE2.0 in Fig. 7.4). Two lines connect the RT tube to

the rest of the setup: one leads to the HFT, while the other leads to the charge tube. The thermal input is provided by a 335 W glass silk heating jacked, which includes a 25 mm glass silk insulation layer.

7.3.4 Charge Tube

The charge tube, or CT, is the long pipe through which pressure waves propagates. The inside diameter is equal to 40 mm, and the inner surface is rectified and electrolytically polished in order to reduce friction effects which cause attenuation in the propagating waves. The 15 mm thick walls enhance an even distribution of the thermal power. It is built up of six elements of 1520 mm length each, joined through custom made male-to-female connections with copper seals. The entire pipe measures 9 m in total, and is placed on sliding supports which allow for thermal expansion. Each section is heated by a 950 W glass silk heating jacket, which includes a 25 mm thick insulation layer. One end of the pipe connects to the fast opening valve which is inserted into the LPP, while at the other end a PT-100 temperature sensor is mounted (TE3.0 in Fig. 7.4). The pressure measurement stations are created by flush-mounting four high frequency pressure transducers along the CT at a distance of 4, 4.3, 8.4 and 8.7 m from the FOV (PIT1−PIT4). The instruments are placed in pairs in order to perform speed of flight measurements at two different locations in the tube. In the case of a RSW in D_6, a RSW is expected to form between the first and second measurement pair [25].

7.3.5 Fast Opening Valve

The most complex piece of equipment of the setup is the fast opening valve, or FOV, contained in the LPP and shown in Fig. 7.6. This custom designed component is able to operate up to 400°C without lubrication, in order to avoid contamination of the working fluid. When the FOV is in the opened position, the working fluid can flow through the venting holes present in the inner and outer body. In the closed position, a sliding cylinder is interposed between these two bodies, obstructing the venting holes. The sliding cylinder is pressed into a perfluoroelastomer compound sealing pad on the flange to ensure the first sealing point. The second sealing is performed by a perfluoroelastomer O-ring placed between the sliding cylinder and the inner body. A high temperature spring built with austenitic nickel-chromium steel is compressed while closing the FOV, and three radial clamps are used to prevent it from being released. To open the FOV, the clamps are actuated, allowing the spring to push the sliding cylinder away, thus leaving the venting holes open. A movable nozzle insert allows to fine-tune the throat section, i.e. the minimum flow passage area, in the range $420 - 600\ mm^2$. A peculiarity of this valve is that the nozzle is located on the high pressure side of the sealing, as opposite to typical solutions adopted in Ludwieg tube facilities [45, 46].

7.3.6 Low Pressure Plenum

After the FOV has been opened, the fluid flows into a 113 liter low pressure plenum (LPP), containing the FOV itself. The LPP has an outer diameter of 406.4 mm and 9.53 mm thick stainless steel walls. The electric motor triggering the FOV and the manual nozzle positioning gear are mounted on the LPP with sealed feedthrough shaft connections. At the bottom, the vessel is connected to the condenser. A lid with a 648 mm diameter flange gives access to the vessel interior for installation of the FOV, sealed by a graphite gasket compressed by 20 Mx50 bolts. The thermal input to the vessel is supplied by four heating jackets with a nominal power of 1450, 425, 960 and 490 W.

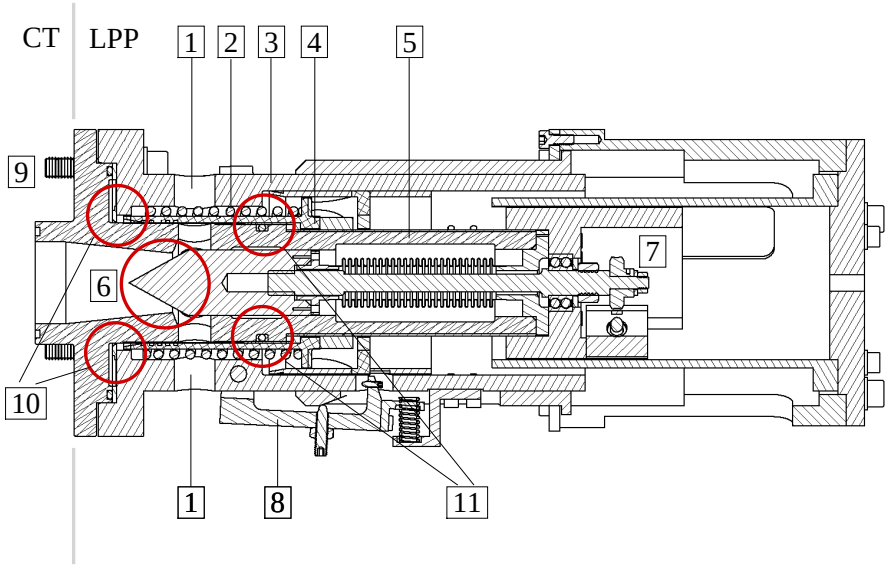

Figure 7.6: Cross-section of the Fast Opening Valve (FOV) at the aperture instance. 1. venting holes (closed), 2. spring (still almost completely compressed, but releasing its force), 3. outer body, 4. sliding cylinder (SC) (obstructing the venting holes, and pushed towards the right by the spring), 5. inner body, 6. nozzle with adjustable throat section, 7. nozzle actuating system, 8. one of the three radial clamps – open position (not engaging the SC, which is thus free to move under the spring force), 9. flanged connection to CT, 10. first sealing element (static pad) – not engaged by the SL (not sealing), 11. second sealing element (dynamic O-ring) – engaged position (compressed between the SL and the inner body, where it is grooved).

7.3.7 Condenser and flow return pipe

A pneumatic valve connects the LPP to the condenser (COND). The condenser is a cylindrical vessel with outer diameter of 168.28 mm, 7.11 mm thick walls, and welded cooling ribs. The condensed liquid flows from the bottom of the condenser into the flow return line (RL). This pipe is connected through another pneumatic valve to the HFT.

7.4 Data Acquisition and Control system

In the following, the control strategy necessary to reach and maintain the desired thermodynamic conditions in the CT is illustrated. A major challenge is the avoidance of hot-spots, which pose a serious danger in terms of decomposition of the working fluid.

7.4.1 Vapour generator control

As anticipated, saturation conditions are enforced during normal operation, and controlled by monitoring the presence of liquid through the level meter measurement (i.e. LL in Fig. 7.4). To this end, the quantity of working fluid initially loaded in the HFT has to be carefully measured. As a consequence, a single thermodynamic quantity is enough to characterize the state of the fluid in the HFT: the pressure and temperature sensors available, i.e. TE1.0 (accuracy 0.1 % of its 400 °C range) and P1.0 (accuracy 0.1 % of its 10 bar range), are used for this scope (with redundancy). The fluid in the HFT can be brought to a different saturation point by increasing/decreasing the thermal input to the HFT, by acting on the heaters (the involved transformation is isochoric). To be noted that the pressure level thus established in the HFT, during normal operation, is common to the RT and the CT (with all the valves opened). Furthermore, the saturation temperature is also estimated from the pressure reading through the equation of state presented in Ref. [19]. A digital PID controller regulates the power supply to the bottom band heater, based on the set-point imposed for the value thus obtained. There are several advantages in performing the control based on this calculated saturation temperature instead than on direct measurements: (i) the controlled variable is expected to promptly reacts since it is based on a pressure measurement (less affected by thermal inertia phenomena), (ii) the same PID parameters can be used throughout the entire operating range, and (iii) the long transient involved when the setup is heated from cold conditions can be managed in a more efficient and safe way. In total nine k-type thermocouples measure the wall temperature at several locations, of which four are used for control purposes and the others for monitoring only. The power supplies to all the secondary heaters are individually controlled in order to maintain their temperatures slightly below the saturation value.

7.4.2 Reference Tube control

The main purpose of the reference tube (RT) is to bring the fluid it contains at the desired conditions of super-heating. In turn, this is directly measured as the difference between the temperature in the RT (from the PT-100 sensor TE2.0 in Fig. 7.4, accuracy 0.1 % of the 400 °C range), and that measured in the HFT (through TE1.0). A PID controller directly regulates this difference, i.e. the super-heating, by acting on the heater equipping the RT.

7.4.3 Charge Tube control

In order to limit the sources of disturbance for the waves propagating inside the CT, the thermal control is conceived such that only the external wall temperature is measured through a total of 10 thermocouples distributed along the CT. The second ends of these sensors are connected to the external wall of the RT, such that the resulting signal is directly the temperature difference between the RT and the CT wall ($\Delta T^{W}_{\text{RT-CT}}$). This arrangement aims at exploiting the geometric equivalence among the CT and the RT: being the temperature of the fluid in the RT accurately measured (TE2.0), if the temperature difference between the external wall of the RT and of the CT is negligible, i.e. $\Delta T^{W}_{\text{RT-CT}} \approx 0$, it follows that the temperature of the fluid in the CT is equal to what is being measured by TE2.0. In other words, it is expected that imposing on the CT wall the same temperature measured on the RT wall will result in the same conditions inside the two volumes. A PID controller modulates the power supply to each individual blanket heater on the CT, aiming at zeroing $\Delta T^{W}_{\text{RT-CT}}$.

7.4.4 Low Pressure Plenum control

The temperature of the vapour contained in the LPP is measured using a PT-100 sensor (TE4.0 in Fig. 7.4). A single PID controller modulates the power supply to each of the blankets covering the LPP, using the temperature as process variable.

7.4.5 Data Acquisition

At each of the measurement stations a fully active four arm Wheatstone bridge absolute transducer measures the pressure at a frequency of 250 kHz with an accuracy of 0.5% of its full scale of 21 bar. The signal is amplified and connected to the synchronous data acquisition board. A PT-100 sensor measures the fluid temperature at the end of the tube (TE3.0 in Fig. 7.4, accuracy 0.1% of its 400°C range).

7.5 Validation

This section presents the results of a series of tests aimed at quantitatively characterizing the performance of the FAST setup.

7.5.1 Tightness characterization

In order to prevent leakage of the working fluid into the ambient, and of air into the setup, this has been designed to be leak-tight both when pressurized and under lower-than-atmospheric pressure conditions. Notably, these requirements must be satisfied within the whole operating temperature range. To this end, two complementary systems are implemented in the facility:

- Pressurization with inert gas, primarily allowing to check the tightness of the system by adopting common techniques (e.g., helium detectors). Furthermore, (part of) the setup can be kept pressurized (e.g. with Nitrogen) while not in use.
- Vacuum system, making it possible to independently vacuum different sections of the setup, in order to get rid of the air or of the inert gas possibly present.

As anticipated, avoiding the contamination of the working fluid with air is of paramount importance in order to reduce the risk of thermal decomposition under high temperature within an oxidizing environment [35]. However, also the contamination by an inert gas has to be avoided. As a matter of fact, since typically adopted gases features speed of sound values more than 1 order of magnitude larger than those of the organic compounds of interest, even the smaller contamination can have a strong influence on the experiments results.

A comprehensive series of tests have been conducted up to temperatures of 300°C, for a duration of 72 hours each. This has allowed to assess that the temperature has a negligible influence on the sealing properties of the equipment. The tightness of the FAST setup has been characterized as follows, in terms of the average leakage rate LR = $\Delta p\ V\ \Delta t^{-1}$ [47], where V is the volume of the whole setup (i.e. 0.143 m^3), and Δp is the pressure drop/rise measured after a time interval Δt (i.e. 259,200 s for all the tests).

- Low p ($\lesssim$ 3 mbar abs.): LR < 5E^{-4} mbar l s^{-1} (air into the system)
- High p ($\gtrsim$ 6000 mbar abs.): LR < 5E^{-2} mbar l s^{-1} (He to the ambient)

These figures are deemed satisfactory. This is particularly true for the results of the vacuum tests which, as explained, were intended to characterize a very critical property of the setup. These conclusions are confirmed by the fact that periodical gas-chromatography analysis performed on working fluid samples to investigate possible decomposition have not unveiled any molecular modification.

7.5.2 Valve Opening Sequence

The opening sequence follows a strict pattern: as soon as the clamps are released, see Fig. 7.6, the spring pushes the slider away, and a small opening is created as the slider leaves the seal and the flow gets choked close to this position. This is seen in an experiment with initially 4.014 bar of N_2 in the CT and vacuum in the LPP, whose results are shown in Fig. 7.7. The small pressure drop of approx. 20 mbar in the signal indicates the initial choking (1). As the slider moves further, the position where the cross-section of the flow is the smallest is changed to a section between the slider and the inner body. This is seen as a second small drop in pressure of approx. 20 mbar (2). Only as the slider passes over the venting hole of the inner body, does the designated nozzle get choked. This corresponds to the large pressure drop in the signal down to approx 2.9 bar (3).

The opening time of the fast opening valve, i.e. t_{FOV}, can be estimated by using the method of characteristics. Fig. 7.8 shows a schematic picture of an instantaneous (left) and non-instantaneous (right) opening. In the ideal case of instantaneous valve opening, all characteristics overlap in a single point. In the real case, where the opening is non-instantaneous, t_{FOV} is finite and the last characteristic starts traveling at a later time instant. Since the seal of the FOV is downstream of the nozzle, the characteristics travel through the nozzle. The nozzle accelerates the fluid, such that the propagation speed in the nozzle is significantly lower than in the rest of the charge tube, with the consequence that the later characteristics are curved in this section [48].

The opening time can be estimated by mapping the pressure signals of the sensors to the position of the valve. For this mapping procedure, the slope of each characteristic has to be determined, which equals the wave propagation speed and is given by the speed of sound minus the speed of the fluid in the laboratory reference frame. As the pressure decreases due to the rarefaction, the local speed of sound decreases, and a flow is started in the opposite direction of the wave propagation, both contributing to a lower wave propagation speed. The propagation speed can be evaluated as a function of the pressure drop. The local speed of sound is evaluated by assuming the expansion is

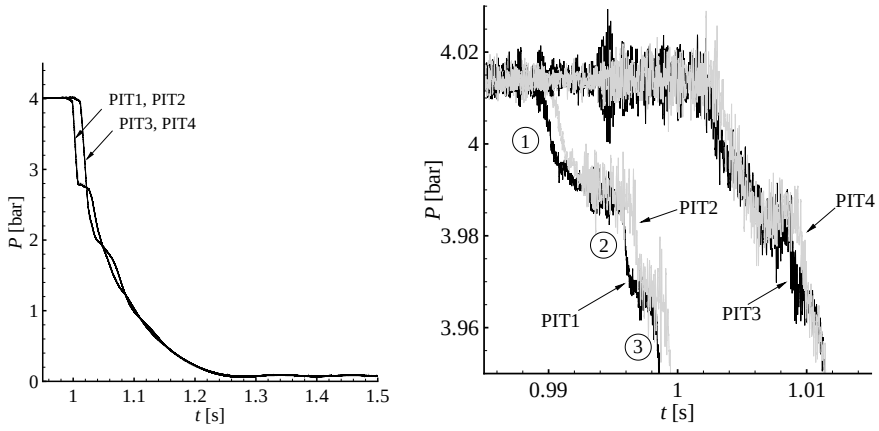

(a) (b)

Figure 7.7: Original signals from an expansion in nitrogen. 7.7a: complete expansion, the two couples of signals, corresponding to the two measurement stations are visible. 7.7b: detail of the very first expansion, it is possible to distinguish the four signals and the subsequent pressure drops corresponding to the FOV opening sequence.

isentropic and the fluid velocity after the expansion can be evaluated by using the Riemann invariant in the undisturbed state in the CT before opening the valve [49]. The estimated value of t_{FOV} does not take the nozzle into account and is thus higher than the actual valve opening time. However, for the formation of an RSW, the characteristics should coalesce, so it is the estimated opening time that we measure using this technique that is important.

Fig. 7.9 shows the signals of the same experiment in N_2 as displayed in Fig. 7.7, but then mapped to the valve position. The signals now overlap initially, giving evidence of a correct mapping procedure. The rarefaction waves propagate through the tube and reflect at the end of the charge tube. Because the reflection of the first rarefaction wave arrives earlier at the sensor location of PT3 than the last unreflected rarefaction wave, a non-simple region is created. This makes signals PT3 and PT4 unuseful for determination of the valve opening sequence. This shows up in the mapped signal as diverting from the other signals because the fluid velocity then is incorrectly evaluated.

In order to have a consistent evaluation without disturbance of the noise, the opening time is in this case defined as the difference in time instance when 5% of the pressure drop has occurred until 95% of the pressure drop, based on the mapped signal. An overview of the performed measurements can be found in table 7.1. The throat area in the nozzle affects the measured opening time as was expected. With a very small throat area of approx. 68mm^2, the opening time measured is between 2.1 and 3.2 ms. With the nominal throat area of approx. 466 mm^2, the opening time measured between 3.5 and 4.5 ms. This can be explained by the fact that the characteristics travel through the nozzle and are curved.

The total opening time, i.e. the duration from the instance the sliding cylinder moves away from the seal until full opening of the valve, increased significantly after many shots in N_2, CO_2, He, and

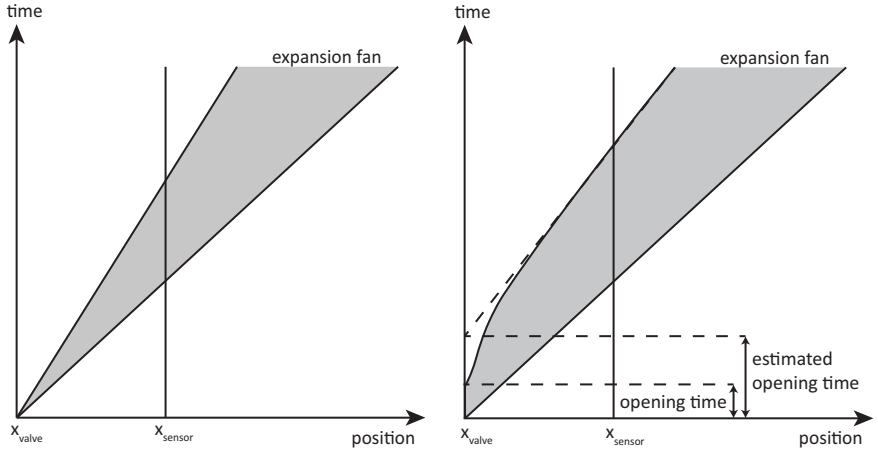

(a) Ideal case: instantaneous valve opening

(b) Real case: non-instantaneous valve opening

Figure 7.8: Position-time diagrams of classical expansion fans. In the ideal case with an instantaneous valve opening and in absence of a nozzle, all characteristics emerge from a single point. In the realistic case, the last characteristic starts at a later time instance than the first one, due to the finite opening time. All characteristics are curved upwards in the nozzle area except the first one, because of the higher flow velocity in the nozzle, which slows down the wave propagation speed.

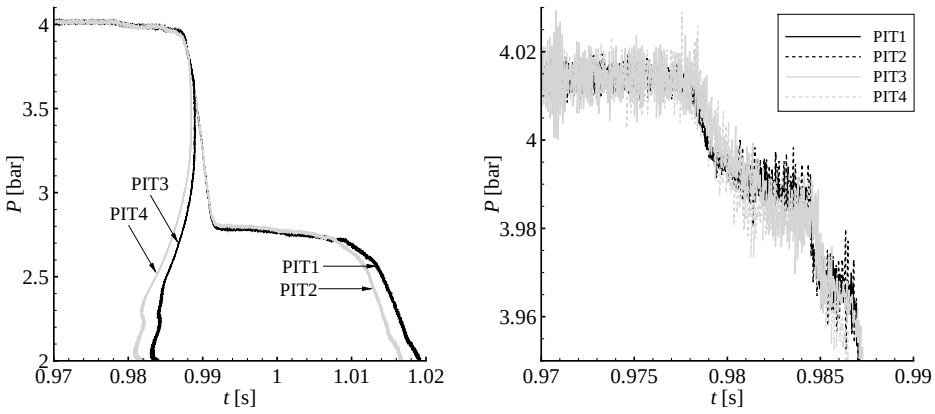

(a)

(b)

Figure 7.9: Portions of the signals from an expansion in nitrogen mapped to the valve position, with two levels of magnification.

number	fluid	CT P [bar]	CT T [°C]	ΔP expansion [bar]	calc. A_{nozzle} [mm^2]	opening time [ms]
1	He	6.503	50	0.32	67	2.53
2	He	8.472	269.9	0.44	72	3.18
3	He	7.292	269.4	0.33	62	2.12
4	He	4.895	22.7	0.28	79	2.65
5	He	6.086	48.9	1.69	438	3.71
6	He	6.005	17.3	1.74	459	3.92
7	He	6.663	99.2	2.01	483	3.56
8	He	5.984	251	1.74	462	5.00
9	He	6.025	200.6	1.95	522	7.64
10	He	6.015	149.4	1.84	489	4.07
11	air	6.976	95	0.27	61	2.18
12	air	7.133	22.0	0.3	67	2.17
13	air	5.39	20	0.23	68	2.3
14	air	4.857	20	0.205	67	2.28
15	air	4.084	18	0.97	418	4.2
16	air	6.148	49.1	1.615	468	4.15
17	air	6.8	99.5	1.76	461	3.96
18	air	6.312	17.6	1.62	456	4.16
19	air	6.449	149.6	1.72	476	4.2
20	air	6.645	201.3	1.81	488	4.58
21	air	7.088	252.4	1.88	473	4.99
22	air	7.011	19.1	1.81	459	4.23
23	CO_2	6.423	50.0	1.59	465	4.58
24	CO_2	5.986	18.0	1.5	471	4.86
25	CO_2	6.636	100.3	1.64	464	4.13
26	CO_2	6.13	149.7	1.5	459	4.4
27	CO_2	6.211	201.2	1.51	456	4.56
28	CO_2	6.337	200.5	1.57	465	4.63
29	CO_2	6.312	249.0	1.56	464	4.5
30	N_2	4.000	25.7	1	443	4.12
31	N_2	4.014	25.8	1.08	481	4.2
32	N_2	1.093	25.3	0.345	576	4.26
33	N_2	1.124	25.4	0.33	531	4.39
34	D_6	1.257	297.0	0.179	330	5.48
35	D_6	2.517	301.1	0.257	254	8.99
36	D_6	1.134	254.1	0.175	363	4.87
37	D_6	1.265	298.0	0.179	328	7.48
38	D_6	2.532	305.1	0.292	286	8.92
39	D_6	1.255	293.7	0.151	278	6.61
40	D_6	1.257	264.2	0.092	169	7.66
41	D_6	1.26	263.2	0.105	193	4.59
42	D_6	1.265	300.1	0.14	254	5.62
43	D_6	1.285	265.1	0.118	214	8.28
44	D_6	2.383	302.3	0.214	220	8.32

Table 7.1: Results from measurements. The nozzle area is calculated using the pressure drop across the expansion (not possible for siloxane D_6). The opening time is inferred from the mapped signal.

air had been performed, attributed to a lack of lubrication. This is not reflected in the measured estimated opening time as given in table 7.1, which is determined using the large pressure drop related to the sliding cylinder passing the venting hole. As soon as the first shot in D_6 was done, the total opening time went down immediately, confirming the hypothesis that D_6 acts as a lubricant. On the other hand, the estimated opening time based on the large pressure drop had increased to 5 to 9 ms. These measurements are affected by a large uncertainty due to inaccuracy of the equation of state in this thermodynamic region.

7.5.3 Wave Speed Measurements

To test the capabilities of the measurement system, a shock in air is generated. The pressure in the CT is lowered to approximately 0.37 bar, while the LPP is kept at atmospheric pressure. The whole setup is at ambient temperature, equal to $\approx 18\ ^{o}$C. Upon opening of the FOV, a compression propagates into the charge tube, eventually forming a shock. The expected location of shock formation is estimated using the knowledge on the opening time of the FOV: with $t_{FOV} = 4.5$ ms, the intersection of the first and last characteristic is expected to occur at ≈ 5.2 m from the FOV. Since partial shock formation speeds up the wave, it is expected that complete formation requires more length. It can indeed be seen that the shock has not yet formed at pressure transducer PT1 and PT2. The shock seems to have formed when it passes at PT3 and PT4, since the pressure is much steeper compared to the one given by PT1 and PT2.

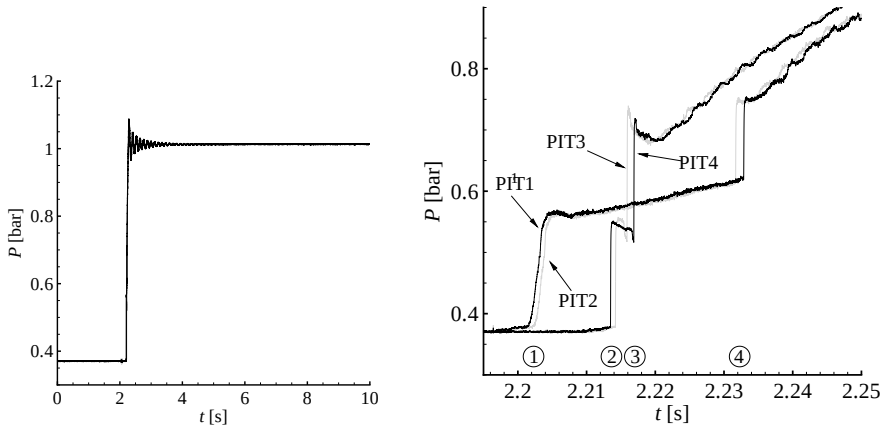

(a) (b)

Figure 7.10: Pressure signals from a compression in air. 7.10: complete compression from below atmospheric up to ambient pressure conditions, the four signals are not distinguishable at this level of detail. 7.10b: detail of the very first compression phase, it is possible to distinguish the four signals, and the shock wave forming $(1-2)$ and then bouncing back $(3-4)$ in the tube.

Since the shock has not formed yet at PT1 and PT2, the compression can be considered a simple compression wave, thus traveling with the speed of the characteristic. By solving the corresponding Riemann problem, values of 341 m s^{-1} before and 488 m s^{-1} after the compression are found as propagation speeds. By using the time-of-flight method, very similar values are found experimentally, as can be seen in Fig. 7.11. Once the shock has formed, it is expected to travel at a velocity of 422 m s^{-1}, this value being in extremely good agreement with the experimental observation. It is demonstrated that the measurement equipment and the devised procedure are best suited to capture steep pressure variations, i.e. shock waves propagating in the CT, which is also the main objective of the setup. Weaker phenomena, such as those involved in speed of sound measurements, are also sensed in a fairly accurate way, but more sophisticated signal analysis techniques than the simple TOF method adopted here are necessary, as detailed also, e.g., in Ref. [50]. The expected pressure after the compression, as calculated by the exact solution of the Riemann problem, is 0.6 bar, which

is also in good agreement with (i.e. approx. 50 mbar above) the experimental observation reported in Fig. 7.10. To be noted also that the expected speed for the RSW is of the order of 100 m s^{-1}, making it comparatively simpler to be detected than the wave just presented.

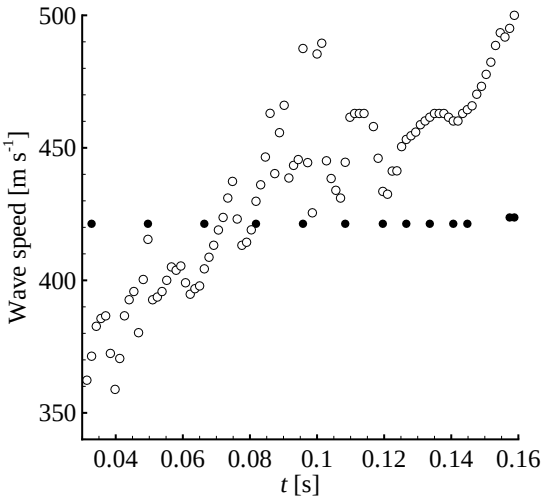

Figure 7.11: Wave speed measurement determined with the time-of-flight method. The black dots are determined by comparing PIT3 with PIT4, while the white dots PIT1 with PIT2.

To fully show the capabilities of the setup, the results of wave speed measurements are presented for an expansion in siloxane D_6 in the classical domain (i.e. outside the BZT region), up to fluid temperatures close to 300 °C. Fig. 7.12 shows several temperature signals as recorded during the test campaign. The setup is heated from cold conditions and, as soon as a temperature of 250 °C is reached, the valve between the HFT and the RT is opened. Part of the liquid is flashed and the temperature of the liquid therefore drops of several degrees. After ≈ 11 hours, the super-heating is set to 5 °C. The first opening of the FOV is performed at ≈ 12 hours. After that, the super-heating is raised to 45 °C, and two more FOV openings are executed. The pressure signals recorded during the second of these experiments are shown in Fig. 7.13. The procedure is thus repeated after having increased the saturation temperature up to 290 °C, with 5 °C of super-heating. The measured fluctuations in temperature in the reference tube and charge tube were of a long period of the order of 2 hours, and with an amplitude of up to 3 °C. Further optimization of the thermal control algorithm is planned for experiments at higher temperatures.

The TOF method, applied only to the PIT1 and PIT2 signals, is used to evaluated the wave speed in this section as a function of the pressure drop, since PIT3 and PIT4 are disturbed by the bouncing rarefaction wave, as shown in Fig. 7.13b. Also in this case, the rarefaction waves travel with a velocity equal to the difference between the speed of sound and the local flow velocity. Since the fluid is initially at rest, the wave speed estimated by the TOF method for a pressure drop close to zero tends to the speed of sound, see Fig. 7.14. Being the thermodynamic conditions in the CT measured, it is possible to obtain an evaluation of the speed of sound also by recurring to the equation of state of siloxane D_6 [19], obtaining a value of 94.8 m s^{-1} (in doing so, the uncertainty in the mea-

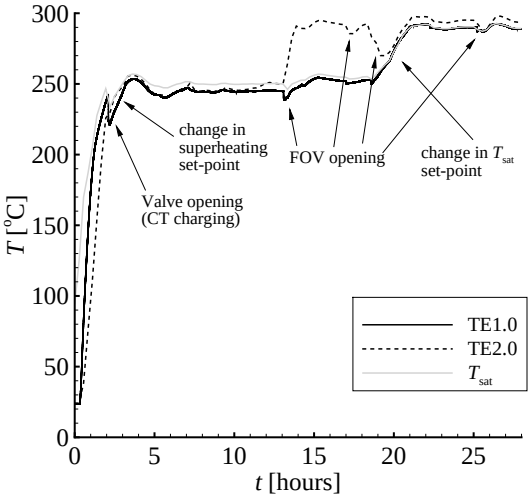

Figure 7.12: Temperature measurements acquired during a test campaign in D_6 siloxane at 1.27 bar and 298 °C. T_{sat} is the saturation temperature calculated starting from the measured pressure. TE1.0 is the temperature measured by the PT-100 in the vapour generator. TE2.0 is the temperature measured by the PT-100 in the reference tube.

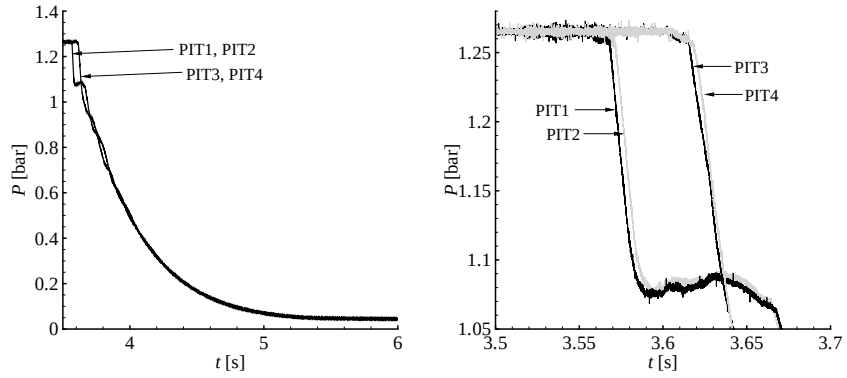

(a) (b)

Figure 7.13: Original signals from an expansion in D_6 siloxane at 1.27 bar and 298 °C. 7.13a: complete expansion, the two couples of signals, corresponding to the two measurement stations are visible. 7.13b: detail of the first expansion, it is possible to distinguish the four signals.

sured quantities has not taken into account). As detailed in Ref. [19], an expanded uncertainty of the order of 6% can be associated to the specific heat capacity of the fluid. Being the epistemic uncertainty associated to the cited thermodynamic model unknown, a first and conservative approach

can consist in attributing the same uncertainty to the speed of sound, as reported in Fig. 7.14. It can be concluded that the facility is effective in performing measurements of wave propagation speed in high temperature organic vapours, with an accuracy comparable with the available thermodynamic models.

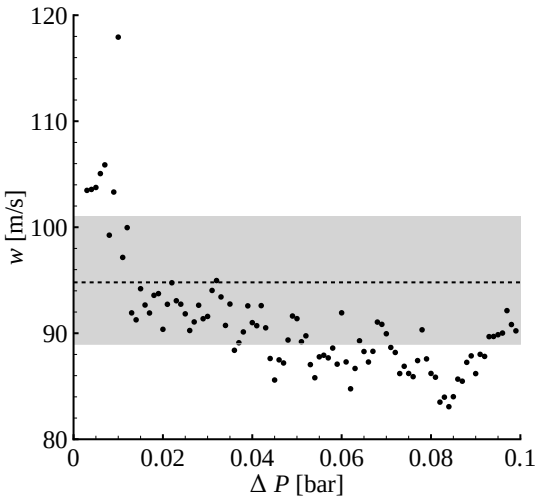

Figure 7.14: Wave Speed in D_6 siloxane as a function of the pressure drop, evaluated with a TOF method applied to the PIT1 and PIT2 pressure signals reported in Fig. 7.13. The dotted line corresponds to the estimation provided by the equation of state presented in Ref. [19], with the shadowed region representing the preliminary assumed expanded uncertainty of 6%.

7.6 Conclusions & Future Work

In this chapter a new Ludwieg tube facility called the FAST is described, that is able to measure speed and intensity of waves propagating through the fluid contained in the tube. The final objective of this setup is to provide the first experimental evidence of the rarefaction shock waves (RSWs) in the dense vapor region of fluids formed by complex organic molecules. The pressure and temperature of the fluid can be regulated independently from each other, such that any thermodynamic state can be achieved within the limits of the facility ($\approx$ 30 bar and 400 °C). The leakage rate of the facility is found to be acceptable, and the fast opening valve is characterized in terms of its aperture time, which is found to be compatible to the end of measuring a RSW in D_6 siloxane. Tests of shock formation in air are presented, and used to validate the functioning of the facility and of the measurement procedure. Preliminary results regarding expansions in D_6, up to fluid temperatures close to 300 °C, further show the capabilities of the FAST of achieving and maintaining the desired thermodynamic conditions, as well as of obtaining wave speed and intensity measurements. As for the next step of the work, the RSW experiment will be attempted.

Nomenclature

s, P	=	specific entropy [kJ kg^{-1} K^{-1}], pressure [bar]
T, v	=	temperature [°K], specific volume [m^3 kg^{-1}]
ρ, c	=	density [kg m^{-3}], speed of sound [m s^{-1}]
A, $\dot{m}$	=	flow passage area [m^2], mass flow rate [kg s^{-1}]
$\dot{V}$	=	volumetric flow rate [m^3 s^{-1}]

Greek symbols

$\Gamma \equiv \frac{v^3}{2c^2}\left(\frac{\partial^2 P}{\partial v^2}\right)_s$	=	fundamental derivative of gas dynamics

Subscripts

CR	=	critical thermodynamic conditions (liquid-vapour)
R	=	reduced (with respect to critical value)

Acronyms

MW	=	Molecular Weight [g mol^{-1}]
ORC	=	Organic Rankine Cycle
FAST	=	Flexible Asymmetric Shock Tube
RSW	=	Rarefaction Shock Wave
BZT	=	Bethe-Zel'dovich-Thompson
FOV	=	Fast Opening Valve
CT	=	Charge Tube
LPP	=	Low Pressure Plenum

References

[1] P. A. Thompson. *Compressible Fluid Dynamics*. McGraw-Hill, 1988.

[2] R. Menikoff and B. J. Plohr. The Riemann problem for fluid flow of real material. *Rev. Mod. Phys.*, 61(1):75–130, 1989.

[3] M.S. Cramer and S. Park. On the suppression of shock-induced separation in Bethe-Zel'dovich-Thompson fluids. *Journal of Fluid Mechanics*, 393:1–21, 1999.

[4] B.P. Brown and B.M. Argrow. Application of Bethe-Zel'dovich-Thompson fluids in organic Rankine cycle engines. *Journal of Propulsion and Power*, 16(6):1118–1124, 2000.

[5] Sylvain Quoilin, Martijn Van Den Broek, Sébastien Declaye, Pierre Dewallef, and Vincent Lemort. Techno-economic survey of Organic Rankine Cycle (ORC) systems. *Renewable and Sustainable Energy Reviews*, 22:168 – 186, 2013.

[6] H. A. Bethe. The theory of shock waves for an arbitrary equation of state. Technical report 545, Office Sci. Res. & Dev., 1942.

[7] Y.B. Zel'dovich. On the possibility of rarefaction shock waves. *Zh. Eksp. Teor. Fiz.*, 4:363–364, 1946.

[8] H. Weyl. Shock waves in arbitrary fluids. *Comm. Pure Appl. Math.*, 2:102–122, 1949.

[9] P. A. Thompson. A fundamental derivative in gasdynamics. *Phys. Fluids*, 14(9):1843–1849, 1971.

[10] P. A. Thompson and K. C. Lambrakis. Negative shock waves. *J. Fluid Mech.*, 60:187–208, 1973.

[11] G. Ben-Dor, O. Igra, T. Elperin, and A. Lifshitz. *Handbook of shockwaves*, volume 1, chapter 3.4 (Theory of shock waves. Rarefaction shocks.), pages 339–411. Academic Press, 2001.

[12] W Hayes. The basic theory of gasdynamic discontinuities. In H. W. Emmons, editor, *Fundamentals of gasdynamics: High speed aerodynamics and jet propulsion*, volume 3, pages 416–481. Princeton University Press, 1960.

[13] P. Colonna, N.R. Nannan, A. Guardone, and T.P van der Stelt. On the computation of the fundamental derivative of gas dynamics using equations of state. *Fluid Phase Equilibria*, 286(1):43–54, 2009.

[14] A. Guardone, P. Colonna, E. Casati, and E. Rinaldi. Non-classical gas dynamics of vapour mixtures. *Journal of Fluid Mechanics*, 741:681–701, 2014.

[15] P.A. Thompson and K.C. Lambrakis. Negative shock waves. *J. Fluid. Mech*, 60:187–208, 1973.

[16] M. S. Cramer. Shock splitting in single-phase gases. *J. Fluid Mech.*, 199:281–296, 1989.

[17] A. Guardone and B. M. Argrow. Nonclassical gasdynamic region of selected fluorocarbons. *Phys. Fluids*, 17(11):116102–1–17, 2005.

[18] P. Colonna, A. Guardone, and N.R. Nannan. Siloxanes: A new class of candidate bethe-zel'dovich-thompson fluids. *Physics of Fluids*, 19(8), 2007.

[19] P. Colonna, N. R. Nannan, and A. Guardone. Multiparameter equations of state for siloxanes: $[(CH_3)_3\text{-Si-}O_{1/2}]_2\text{-}[O\text{-Si-}(CH_3)_2]_{i=1,\dots,3}$ and $[O\text{-Si-}(CH_3)_2]_6$. *Fluid Phase Equilibria*,

263(2):115–130, 2008.

[20] P. A. Thompson, G. A. Carofano, and Y. G. Kim. Shock waves and phase changes in a large heat capacity fluid emerging from a tube. *J. Fluid Mech.*, 166:57–96, 1986.

[21] S. C. Gulen, P. A. Thompson, and H. A. Cho. Rarefaction and liquefaction shock waves in regular and retrograde fluids with near-critical end states. In *Adiabatic waves in liquid-vapor systems*, pages 281–290. Springer-Verlag, 1989.

[22] P. A. Thompson. Liquid-vapor adiabatic phase changes and related phenomena. In A. Kluwick, editor, *Nonlinear Waves in Real Fluids*, pages 147–213. Springer-Verlag, New York, NY, 1991.

[23] A. G. Ivanov and S. A. Novikov. Rarefaction shock waves in iron and steel. *Zh. Eksp. Teor. Fiz.*, 40(6):1880–1882, 1961.

[24] S. H. Fergason, A. Guardone, and B. M. Argrow. Construction and validation of a dense gas shock tube. *J. Thermophys. Heat Tr.*, 17(3):326–333, 2003.

[25] P. Colonna, A. Guardone, N.R. Nannan, and C. Zamfirescu. Design of the dense gas flexible asymmetric shock tube. *Journal of Fluids Engineering, Transactions of the ASME*, 130(3):0345011–0345016, 2008.

[26] A. A. Borisov, S. S. Borisov, AL. A.and Kutateladze, and V. E. Nakoryakov. Rarefaction shock waves near the critic liquid-vapour point. *J. Fluid Mech.*, 126:59–73, 1983.

[27] S. S Kutateladze, V. E. Nakoryakov, and A. A. Borisov. Rarefaction waves in liquid and gas-liquid media. *Ann. Rev. Fluid Mech.*, 19:577–600, 1987.

[28] S.H. Fergason, T.L. Ho, B.M. Argrow, and G. Emanuel. Theory for producing a single-phase rarefaction shock wave in a shock tube. *J Fluid Mech*, 445:37–54, 2001.

[29] M. S. Cramer and R. Sen. Shock formation in fluids having embedded regions of negative nonlinearity. *Phys. Fluids*, 29:2181–2191, 1986.

[30] N. R. Nannan, A. Guardone, and P. Colonna. On the fundamental derivative of gas dynamics in the vapor-liquid critical region of single-component typical fluids. *Fluid Phase Equilib.*, 337:259–273, January 2013.

[31] N. R. Nannan, A. Guardone, and P. Colonna. Critical point anomalies include expansion shock waves. *Physics of Fluids*, 26(021701), 2014.

[32] P. A. Thompson and W. F. Loutrel. Opening time of brittle shock-tube diaphragms for dense fluids. *Rev. Sci. Instrum.*, 44(9):1436–1437, 1973.

[33] A. Guardone. Three-dimensional shock tube flows of dense gases. *J. Fluid Mech.*, 583:423–442, 2007.

[34] G. Angelino and C. Invernizzi. Cyclic methylsiloxanes as working fluids for space power cycles. *Journal of Solar Energy Engineering, Transactions of the ASME*, 115(3):130–137, 1993.

[35] Petar R. Dvornic. High temperature stability of polysiloxanes. *Silicon Compounds: Silanes and Silicones, Gelest Catalog*, pages 419–432, 2004.

[36] P. Colonna, N. R. Nannan, A. Guardone, and E. W. Lemmon. Multiparameter equations of state for selected siloxanes. *Fluid Phase Equilib.*, 244:193–211, 2006.

[37] N.R. Nannan, P. Colonna, C.M. Tracy, R.L. Rowley, and J.J. Hurly. Ideal-gas heat capacities of dimethylsiloxanes from speed-of-sound measurements and ab initio calculations. *Fluid Phase Equilibria*, 257(1):102–113, 2007.

[38] R. N. Nannan and P. Colonna. Improvement on multiparameter equations of state for dimethylsiloxanes by adopting more accurate ideal-gas isobaric heat capacities: Supplementary to P. Colonna, N. R. Nannan, A. Guardone, E. W. Lemmon, Fluid Phase Equilib. 244, 193 (2006). *Fluid Phase Equilib.*, 280(1–2):151–152, 2009. Short Communication.

[39] G. Angelino and P. Colonna. Multicomponent working fluids for organic Rankine cycles (ORCs). *Energy*, 23(6):449–463, 1998. cited By (since 1996) 67.

[40] C. Invernizzi, P. Iora, and P. Silva. Bottoming micro-Rankine cycles for micro-gas turbines. *Applied Thermal Engineering*, 27(1):100–110, 2007.

[41] E. Casati, A. Galli, and P. Colonna. Thermal energy storage for solar-powered organic Rankine cycle engines. *Solar Energy*, 96:205 – 219, 2013.

[42] C. Zamfirescu, A. Guardone, and P. Colonna. Admissibility region for rarefaction shock waves in dense gases. *Journal of Fluid Mechanics*, 599:363–381, 2008.

[43] A. Guardone, C. Zamfirescu, and P. Colonna. Maximum intensity of rarefaction shock waves for dense gases. *Journal of Fluid Mechanics*, 642:127–146, 2010.

[44] P. Congedo, Piero Colonna, Christophe Corre, Jeroen Witteveen, and Gianluca Iaccarino. Backward uncertainty propagation method in flow problems: application to the prediction of rarefaction shock waves. *Comput Method Appl M*, 213–216:314–326, March 2012.

[45] F.F.J. Schrijer and W.J. Bannink. Description and flow assessment of the delft hypersonic ludwieg tube. *Journal of Spacecraft and Rockets*, 47(1), 2010.

[46] H. Knauss, R. Riedel, and S. Wagner. The shock wind tunnel of stuttgart university - a facility for testing hypersonic vehicles. In *9th International Space Planes and Hypersonic Systems and Technologies Conference*, number AIAA 99-4959, 1999.

[47] Robert Charles McMaster. *Nondestructive testing handbook*, volume Volume 1-Leak testing. American Society for Nondestructive Testing, 3 edition, 1997.

[48] D Cagliostro and JA Johnson, III. Starting phenomena in a supersonic tube wind tunnel. *AIAA Journal*, 9(1):101–105, 1971.

[49] Eleuterio F. Toro. *The Riemann Problem for the Euler Equations*. Springer Berlin Heidelberg, Berlin, Heidelberg, 2009.

[50] F.K. Lu, A.A. Ortiz, J.-M. Li, C.H. Kim, and K.-M. Chung. Detection of shock and detonation wave propagation by cross correlation. *Mechanical Systems and Signal Processing*, 23(4):1098 – 1111, 2009.

8

Nonclassical Gasdynamics of Vapour Mixtures

Part of the contents of this chapter appeared in:

A. Guardone, P. Colonna, E. Casati, & E. Rinaldi
Journal of Fluid Mechanics, **741**, 681-701 (2014)

Abstract *The nonclassical gasdynamics of binary mixtures of organic fluids in the vapour phase is investigated for the first time. A predictive thermodynamic model is used to compute the relevant mixture properties, including its critical point coordinates and the local value of the fundamental derivative of gasdynamics* Γ*. The considered model is the improved Peng-Robinson Stryjek-Vera cubic equation of state, complemented by the Wong-Sandler mixing rules. A finite thermodynamic region is found where the non-linearity parameter* Γ *is negative and therefore nonclassical gasdynamics phenomena are admissible. A non monotone dependence of* Γ *on the mixture composition is observed in the case of binary mixtures of siloxane and perfluorocarbon fluids, with the minimum value of* Γ *in the mixture being always larger than that of its more complex component. The observed dependence indicates that non-ideal mixing has a strong influence on the gasdynamics behaviour—either classical or nonclassical—of the mixture. Numerical experiments of the supersonic expansion of a mixture flow around a sharp corner show the transition from the classical configuration, exhibiting an isentropic rarefaction fan centred at the expansion corner, to nonclassical ones, including mixed expansion waves and rarefaction shock waves, if the mixture composition is changed.*

8.1 Introduction

The first scientist who hinted at the possibility of observing rarefaction shock waves in vapours of molecularly complex organic fluids was Nobel-laureate Hans Bethe, in 1942 [1]. Rarefaction shock waves are discontinuous solutions to the Euler equations of compressible flows where the fluid undergoes an irreversible expansion process which results into a discontinuous reduction of density, pressure, temperature and fluid velocity in the direction of propagation of the shock wave. As it is well known, rarefaction shock waves are not physically admissible in dilute gases with constant specific heats.

In a broad theoretical study on the theory of shock waves in arbitrary material, Bethe outlined how the occurrence of rarefaction shock waves depends on a peculiar combination of the thermodynamic properties of the material at the states of interest. He noticed that, according to the van der Waals model [2], rarefaction shock waves would theoretically be possible in the dense vapour of fluids featuring high values of the heat capacity, if the pre- and post-shock states of the fluid are close to the vapour-liquid critical point. Nevertheless, he ruled out this possibility on the ground of what we now know as incorrect physical arguments, see also Ref. [3]. An early contribution is also due to Zeldovich [4] and Weyl [5]. Though, it was Thompson, see also Refs. [3, 6, 7], who first provided a systematic treatment of what is now called non classical gas dynamics. A review article by Kutateladze documents the advancements in non classical gasdynamics until the 80's [8], while a more recent review can be found in Ref. [9].

A necessary condition for non classical behaviour to be physically admissible is that the fundamental derivative of gas dynamics

$$\Gamma \equiv 1 + \frac{\rho}{c}\left(\frac{\partial c}{\partial \rho}\right)_s = \frac{v^3}{2c^2}\left(\frac{\partial^2 P}{\partial v^2}\right)_s, \tag{8.1}$$

a thermodynamic property of the fluid first introduced by Hayes [11], is negative. In definition (8.1), ρ is the density, s is the entropy, P is the pressure, $v = 1/\rho$ is the specific volume, and c is the zero-frequency speed of sound $c \equiv (\partial P/\partial \rho)_s$. If Γ is negative in a finite thermodynamic region, RSWs are admissible, among other so-called non classical waves such as composite and split waves, see, e.g. Ref. [6].

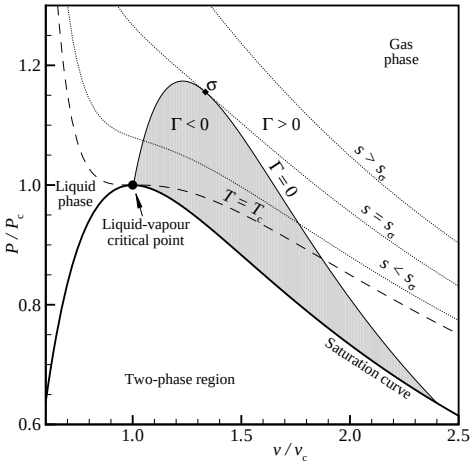

Figure 8.1: From [10]. Liquid-vapour saturation curve (—) and $\Gamma < 0$ region (shaded region) for a BZT fluid in the volume-pressure plane computed from van der Waals model under the assumption of a constant isochoric specific heat c_v and for $c_v/R = 2000$, with R gas constant. Selected isentropes $(\cdots)$ and the critical isotherm $T = T_c$ $(- -)$ are also indicated. Note that the isentropes are concave down in the $\Gamma < 0$ region. The isentrope s_σ is tangent to the $\Gamma = 0$ line in σ.

Substances characterized by thermodynamic states featuring negative values of Γ in the dense vapour phase are called Bethe-Zel'dovich-Thompson (BZT) fluids. The region of negative Γ in the vapour phase is shown in figure 8.1 in the pressure–specific volume thermodynamic diagram of a paradigmatic BZT fluid described by the van der Waals fluid model, where the $\Gamma = 0$ line and the vapour saturation line delimit the negative-Γ region. The studies of Thompson sparked quite some interest in the following years, and many investigations expanded the theory covering several nonclassical phenomena and aspects, see, e.g., Refs. [12–20]. One of the latest developments is related to the investigation of nonclassical phenomena in the vapour-liquid critical point region of any common fluid, see Ref. [21].

Experimental evidence of nonclassical gasdynamics is available only for two-phase vapor-liquid, see Refs. [22–24], or solid-solid systems [25]. In the single-phase vapour region, only classical gasdynamics phenomena have been observed so far. Notably, in the former Soviet Union, Borisov made an attempt to experimentally prove the existence of a rarefaction shock wave (RSW), using a special shock tube [26]. The interpretation of the results of the experiments, arguably a RSW front developing in the tube, has later been confuted in the light of additional knowledge and simulation capability [9, 21, 27]. Theoretical studies [28–33], and new simulation capabilities [34–42], paved the way to a new experimental attempt in 2000 at the University of Boulder [27, 43, 44]. The failed experiment put into evidence one of the major obstacles, namely that the BZT thermodynamic region (the region comprising the states featuring negative-Γ, see figure 8.1) is very close to the thermal decomposition temperature of suitable organic fluids, which is in the range 350–400 °C. In addition, the repeatable rupture of the shock-tube diaphragm proved unattainable due to the relatively small pressure difference and the large acoustic impedance of the fluid [45–47].

Much attention has recently been devoted to the identification of BZT fluids, and to the com-

putation of the negative-Γ region, see Ref. [48] for a review. More recently Colonna and colleagues started a new project aimed at the generation and measurement of a rarefaction shock wave in a newly conceived Ludwieg-tube-type setup [47]. A siloxane fluid, D_6 (dodecamethylcyclohexasiloxane $C_{12}H_{36}O_6Si_6$), has initially been selected as the working fluid. Siloxanes are especially suited for the RSW experiment because of available knowledge on their thermal stability [49], thermodynamic properties [51–54]), and their use as working fluids in thermal energy conversion systems, see, e.g., Refs. [55–57]. Few of the compounds of the siloxane family are candidate BZT fluids [58].

The design of the rarefaction shock wave experiment drove studies aimed at better identifying the thermodynamic region within which nonclassical phenomena are admissible [59], and the maximum pressure difference and shock wave Mach number that can be expected [10]. Given that the experimental conditions are difficult to realize and that the rarefaction shock wave is expected to be weak, therefore more challenging to measure, uncertainty quantification applied to flow simulations has been preliminarily used as an aid in determining the optimal experimental conditions [60].

The present chapter is motivated by several observations about mixtures of organic fluids. Differently from mixtures of ideal gases, thermodynamic properties of dense vapours of multi-component mixtures do not scale linearly with the mole fractions of each compound, as molecular interaction among different molecules plays a major role. Typical hallmarks of non-ideal behaviour of fluids mixtures are the critical temperature, pressure and specific volume of a binary mixture, which usually differ from that of each of the constituents. The same holds for the melting point and for most thermodynamic properties. The fundamental derivative of gasdynamics Γ, being a derived thermodynamic property, is also affected by non-ideal mixing effects, as preliminarily discussed in Ref. [61]. In addition, experiments on the thermal stability of siloxane mixtures [49], and a deeper understanding on the chemistry of thermal decomposition of poly-dymethyl siloxanes [62], show that, at temperatures close to the so-called temperature stability limit, a pure siloxane undergoes a transformation called *rearrangement*, whereby small quantities of other compounds of the same family are formed. Such mixture composition remains then constant at that temperature over time. The composition of the mixture is therefore a new relevant variable in the study of BZT fluids, and, importantly, mixtures of organic fluids are also considered for applications in organic Rankine cycle (ORC) power systems [55, 63–65], one of the possible applications of nonclassical gasdynamics [39].

In the present preliminary study on mixtures as BZT fluids, siloxanes and perfluorocarbons have been considered as constituents. Suitable thermodynamic models for multi-component fluids are briefly discussed in §8.2. Their limitation in terms of accuracy of the predicted Γ values is also addressed. These models are used to estimate the boundaries of the thermodynamic region of admissibility of rarefaction shock waves, and the influence of the mixture composition. In §8.3, exemplary simulation of a supersonic flow expanding over a wedge, whereby the composition of the mixture is varied, are presented to assess the influence of the molecular composition on the gasdynamics behaviour. Concluding remarks and an outlook on future research are given in §8.4.

8.2 Admissibility Region for Rarefaction Shock Waves in Dense gas Mixtures

Modelling non-ideal thermodynamic properties of fluid mixtures—including the determination of the fundamental derivative of gasdynamics Γ—requires to correctly account for the interaction between different molecules, an added degree of difficulty with respect to pure-fluid thermodynamics.

No fundamental and general theory on the interaction of molecules of different type exists yet, therefore no accurate model is available. For these reasons the estimation of mixture properties is affected in general by larger uncertainties, if compared to the estimation of pure-fluid properties. Mixtures of simple molecules, e.g., light gases and simple hydrocarbons, can be modelled with relatively high accuracy, and reference equations of state have been developed [66]. These semi-empirical models rely on large sets of accurate fluid property measurements. Unfortunately, accurate property measurements of complex organic compounds are not available. In order to estimate dense-vapour thermodynamic properties of mixtures of complex organic fluids, simpler so-called predictive equations of state must be adopted, see, e.g., Refs. [67, 68]. These models rely on a small set of data related to the pure constituents, and to parameters describing the interaction between different molecules; these parameters can be determined either experimentally or estimated. Predictive models applicable to mixtures are thermodynamically consistent, but calculated property values are affected by much larger uncertainties if compared to the estimation of pure-fluid properties.

In this study the properties of mixtures of siloxanes and perfluorocarbons are evaluated with either the improved Peng-Robinson Stryjek-Vera cubic equation of state [69], complemented by the Wong-Sandler mixing rules (iPRSV-WS), see Ref. [70, 71], or the PC-SAFT model [72], which is formulated in terms of molecular parameters whose value depends on the molecular arrangement. Since most of the treatment in this chapter is based on the use of the iPRSV-WS model, both the functional form of the equation of state and the derivation of the adopted mixing-rules are recalled in Appendix A.1. These models, together with others, are implemented in an in-house computer library for the calculation of primary and secondary thermodynamic properties of fluids [73].

Information on how the data for the iPRSV-WS model applied to siloxane mixtures were obtained can be found in Ref. [55]. The analytical expression of Γ for this thermodynamic model is reported in Ref. [61]. The application of the PC-SAFT model to linear siloxanes is documented in Ref. [74], and has been extended by the authors to model also cyclic siloxanes. Siloxane/perfluorocabon mixtures are modelled with the iPRSV-WS equation of state starting from experimental values of the critical point of these mixtures [75], and compared to results from the PC-SAFT model. Such a comparison is the only possible assessment at the moment, since no other experimental values are available. Values of Γ for the PC-SAFT mixture model are calculated with analytical expressions obtained by derivation from the equation of state and the isobaric ideal-gas heat capacity relation, see for example Ref. [48] and [21].

Figure 8.2 shows a comparison between the values of Γ calculated along the dew line for the equimolar mixture of propane and pentane using a reference model [66], the iPRSV-WS and the PC-SAFT models. As it is known, see Refs. [76, 77], predictive models fail to accurately estimate properties close to the vapour-liquid critical point, therefore also Γ values at high reduced temperature $\tilde{T} = T/T_c$ deviate from those obtained with the reference model, cf. figure 8.2. A number of evaluations for various fluids modelled by the reference model presented in Ref. [66] revealed that the iPRSV-WS model performs better than the PC-SAFT model in the critical-point region, therefore it has been chosen for the analysis presented in §8.3.

Figure 8.3 shows the negative-Γ region (also termed BZT region) in the P-T thermodynamic plane for several selected organic compounds of the family of siloxanes, cloro-fluorocarbons, perfluorocarbons and their mixtures, calculated with the iPRSV-WS model. The ensemble of fluid thermodynamic states featuring a negative value of Γ in the dense vapour phase is delimited by the dew line on the left and by the concave-upward $\Gamma = 0$ line on the right. An estimate of the temperature at which thermal break-down in stainless steel is likely to occur is also indicated (TSL, Thermal Stability Limit).

As an example, in table 8.1, the molar fraction x, average molecular weight MW, critical pres-

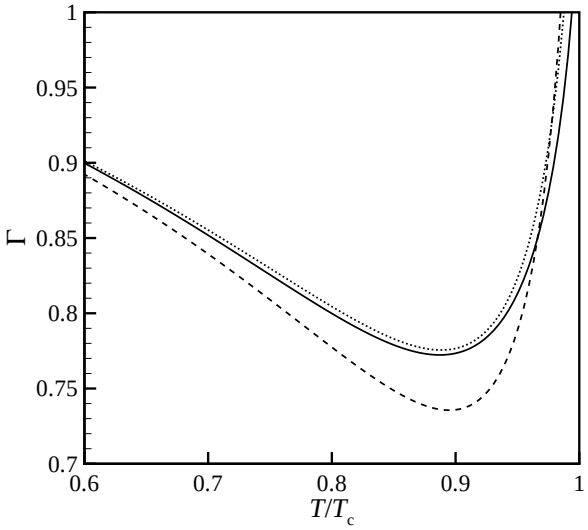

Figure 8.2: Comparison of Γ values along the dew line as a function of the reduced temperature T/T_c for the equimolar mixture of propane and pentane calculated with the reference model presented in Ref. [66] (—), the iPRSV-WS (· · ·), and PC-SAFT (– – –) thermodynamic models.

Table 8.1: Molar fraction x, average molecular weight MW, critical pressure P_c, critical temperature T_c, critical density ρ_c and minimum value of the fundamental derivative of gasdynamics Γ_{min} for a mixture of siloxane fluids MDM and MD_6M.

x		MW	P_c	T_c	ρ_c	Γ_{min}
MDM	MD_6M	[g/mole]	[bar]	[K]	[kg/m^3]	[-]
1.00	0.00	236.5	14.2	564.1	229.38	0.0917
0.75	0.25	329.2	18.0	653.9	288.41	0.5676
0.40	0.60	459.0	11.7	687.5	260.34	0.2567
0.15	0.85	551.7	8.3	690.3	243.09	-0.1187
0.05	0.95	588.8	7.2	689.6	236.65	-0.3040
0.00	1.00	607.3	6.8	689.0	230.64	-0.4001

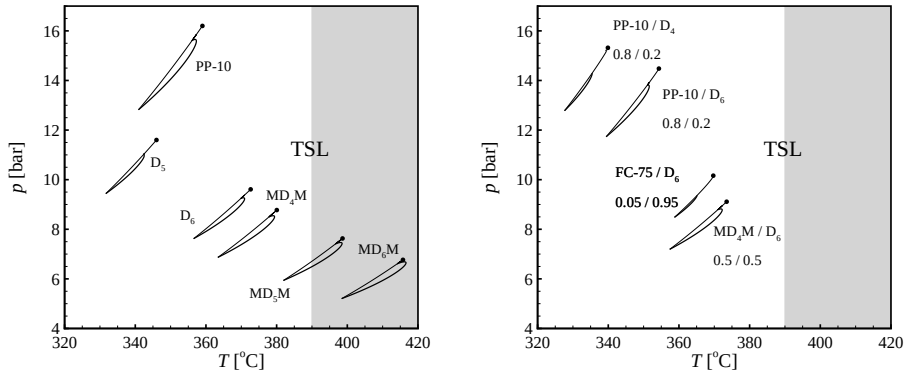

(a) (b)

Figure 8.3: Negative Γ region (or BZT region) in the *P-T* thermodynamic plane for several pure fluids (8.3a) and some selected mixtures (8.3b): values are calculated with the iPRSV-WS thermodynamic model. For each fluid, the circle indicate the critical point. It is relevant to future experiments on non-classical gasdynamic phenomena that the temperature values are close to the estimated thermal stability limit (TSL) for these organic compounds in contact with stainless steel ($\approx 390°C$), while the values of pressure are comparatively moderate. The shaded area indicates the range of temperatures where thermal decomposition in stainless steel can be expected.

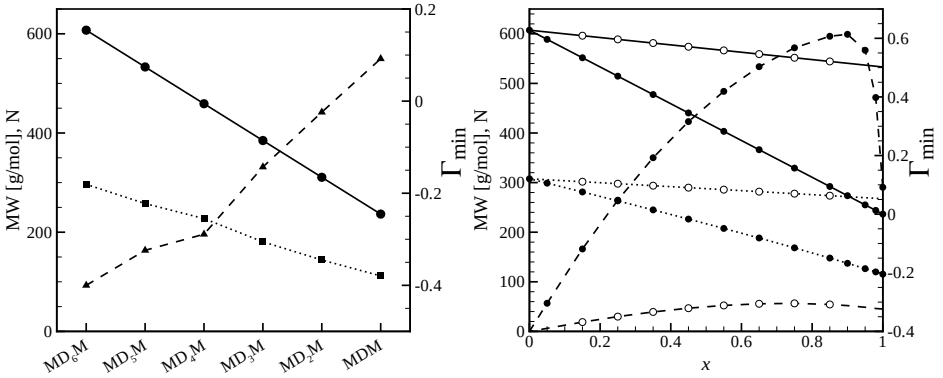

(a) Pure linear siloxanes.

(b) Values for mixtures of MDM/MD_6M (•) and MD_5M/MD_6M (○).

Figure 8.4: Molecular weight MW (—), active degrees of freedom evaluated at the critical temperature N ($\cdots$) and minimum value of Γ along the dew line (- - -) for selected linear siloxanes. Properties are calculated with the iPRSV equation of state for the pure fluids, see Ref. [69], while the equation of state is complemented by the Wong–Sandler mixing rules for the mixtures [78].

sure P_c, critical temperature T_c, critical density ρ_c and minimum value of the fundamental derivative of gasdynamics Γ_{min} for the mixture of siloxane fluids MDM and MD_6M are reported. Thermodynamic properties are calculated using the iPRSV-WS thermodynamic model. As it is well known, the critical point coordinates in table 8.1 depend in a non-linear fashion on the mixture composition x, with the critical pressure, temperature and density exhibiting a local maximum.

Admittedly, the negative-Γ region of fluids MD_5M and MD_6M is partially or completely past the TSL, see figure 8.3. Although mixtures are expected to be more thermally stable than their pure components, such high values of operating temperatures are unrealistic, if stainless steel is the containing material. Moreover, for MD_5M and MD_6M the negative-Γ region is very close to the liquid-vapour saturation point, where the value of Γ is expected to diverge to infinity [21]. In this region, an accurate evaluation of the thermodynamic properties, including Γ, would require the inclusion of a critical point scaling law and of a cross-over model, linking the latter with the analytical EoS. In the present qualitative study, fluid MD_6M was considered in order to maximize the strength of non-classical phenomena for illustration purposes; thermal decomposition and critical point effects are to be carefully assessed before selecting this fluid for the experiments. However, it is remarkable that, similarly to previous studies on non-classical gasdynamics, the present findings are directly applicable to less complex molecules, because the qualitative fluid dynamic behaviour is similar to that of MD_6M.

Results shown in figure 8.4 are a preliminary evaluation of the dependence of the minimum value of Γ on the molecular weight and on the molecular complexity, which is defined here as the equivalent number of active translational, rotational and vibrational degrees of freedom of the molecules at the critical temperature and in the dilute gas limit, see Ref. [79]. The molar composition is also indicated for mixtures. As it is known, in the case of pure fluids the minimum value

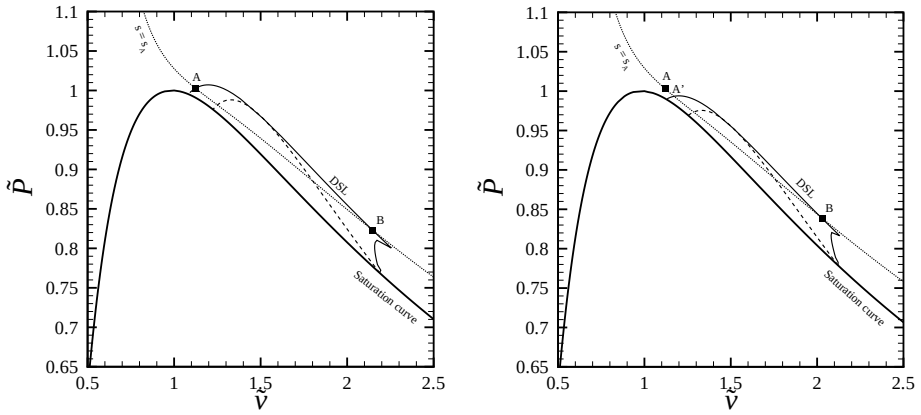

(a) MD6M

(b) MDM(0.05)/MD$_6$M(0.95)

Figure 8.5: Pre- (A) and post-expansion (B) states on the reduced *P*-*v* plane. The negative-Γ region (dashed line) and DSL are also reported.

of Γ along the dew line, Γ_{min}, decreases monotonically with increasing molecular weight and complexity (figure 8.4a). In addition, the extension of the BZT region in the *P*-*T* plane increases with increasing molecular weight and complexity, cf. figure 8.3a.

It is remarkable that the effect of mixing, therefore of intermolecular interaction, alters the non monotone dependency of Γ_{min} from molecular weight and complexity. Figure 8.4b shows that for binary mixtures of the siloxane fluids MDM/MD$_6$M and MD$_5$M/MD$_6$M the estimated value of Γ_{min} does not decrease monotonically with increasing average molecular complexity and weight of the mixture, similarly to what observed for the values of the critical pressure, temperature and density in table 8.1. Indeed, for both the MDM/MD$_6$M and the MD$_5$M/MD$_6$M mixtures, the value of Γ_{min} exhibits a maximum, which is at $x_{MDM} \approx 0.75$ for MDM/MD$_6$M, and at $x_{MD_5M} \approx 0.9$ for MD$_5$M/MD$_6$M. Notably, for the mixture MDM(0.4)/MD$_6$M(0.6) the value of Γ_{min} is largely different, even in sign, from the one predicted for MD$_4$M, which is the homologous pure fluid in terms of molecular weight and complexity. This type of dependency of Γ_{min} on molar composition is predicted also in case of mixtures of alkanes, by using reference equations of state for the calculation of thermodynamic properties.

In the case presented here, the variation of Γ_{min} with the mole fraction of a binary mixture is such that, for any given composition, Γ_{min} is always larger than the molar-fraction averaged value of Γ_{min} of the two pure constituents. Due to the large variety of intermolecular forces, it cannot currently be ruled out that an opposite trend can be observed for different combinations of pure fluids, namely that the mixing of two or more fluids not considered here leads to values of Γ_{min} that are lower than those of the mixture constituents.

From the knowledge of the fundamental derivative of gasdynamics in the vapour phase, the thermodynamic conditions resulting in nonclassical gasdynamics waves can be determined. The conditions for the admissibility of rarefaction shocks are given by the work of Zamfirescu and

colleagues [59], where the method for determining the so called *rarefaction shock region* (RSR) is also reported.

In figure 8.5a the RSR of siloxane fluid MD_6M is shown, together with a representative isentrope $s = s_A$. As detailed in Ref. [59], the RSR is the thermodynamic region that includes all the states that can possibly be upstream and downstream of a rarefaction shock wave. By definition, the RSR embeds the negative-Γ region. For pure fluids, the size of the RSR increases with molecular complexity, similarly to the BZT region. In particular, the RSR is limited by the vapour-liquid saturation (VLE) curve and by the Double Sonic Line (DSL), which is the locus of all fluid states that can be connected by a double-sonic shock, whereby the pre- and post-shock states are sonic. The DSL and the VLE are connected by the two loci representing the upstream state of upstream-sonic downstream-saturated rarefaction shocks and the downstream state of upstream-saturated downstream-sonic rarefaction shock wave.

Each isentrope intersects the DSL in two points A and B, with $v_A < v_B$. At point A the Rayleigh line connecting point A and B is tangent to both the isentrope trough A and the shock adiabat trough A. At point B, it is tangent to the isentrope trough B and the shock adiabat trough A. Therefore, the shock connecting point A and B is a double sonic shock, with sonic state in both point A and B. The RSW connecting point A and B encompasses the largest possible pressure difference, i.e., is the strongest possible RSW originating from the considered isentrope. Note that in figure 8.5a the shock adiabat through A and the isentrope $s = s_A$ are not distinguishable.

The RSR of mixtures is calculated with the same procedure as for pure fluids, with no modifications. An example is given in figure 8.5b, where the RSR for the mixture $MDM(0.05)/MD_6M(0.95)$ is shown. The increase of the MDM percentage in the mixture MDM/MD_6M causes the rarefaction shock region to reduce its size in the *P-v* plane, if compared to the one of pure MD_6M.

8.3 Nonclassical Gasdynamics Behaviour of Dense Gas Mixtures

A preliminary study on the effect of the mixture composition on the gasdynamic behaviour of mixtures of organic fluids is carried out. To this purpose, the supersonic expansion of the dense vapour of a mixture over a corner is simulated.

The selected mixture is composed by MD_6M, a BZT fluid, and MDM, a fluid for which no suitable thermodynamic model predicts a negative-Γ region. To compare results for different mixture composition, a common upstream state was selected in terms of dimensionless quantities. The upstream state features the same value of the Mach number M, reduced pressure $\tilde{P} \equiv P/P_c$, and non-dimensional entropy $\tilde{s} = s/s_\tau$ for all simulations. The locus $s = s_\tau$ is the isentrope tangent to the saturation line, see figure 8.5. The choice of $\tilde{P}$ and $\tilde{s}$ to identify the upstream flow state is motivated by the fact that they identify homologous thermodynamic states in the *P-v* thermodynamic plane, with comparable real gas effects.

The values of M, $\tilde{P}$ and $\tilde{s}$ identifying the upstream states for the simulations are reported in table 8.2. The solid surface past the corner forms an angle of -13.169° with respect to the free-stream direction. These values have been chosen so that in the case of pure MD_6M a rarefaction shock wave with maximum intensity is obtained, which forms an angle of 60° with respect to the free-stream direction, see Ref. [10].

The computer program used to perform the simulations is a parallel solver for the Navier-Stokes equations on unstructured meshes based on a finite volume formulation and implicit time-integration [80]. The code has been recently extended to include real gas properties [81] using a

Table 8.2: Upstream states for the simulations of the supersonic flow of a dense gas mixture over an expansion corner.

M_A	$\tilde{s}_A$	$\tilde{P}_A$
1.15470	1.00276	1.00217

Table 8.3: Upstream and downstream thermodynamic states for the different mixtures considered in the simulations. Z is the compressibility factor defined as $Z = RT/Pv$.

Composition x		Upstream state A				
MDM	MD_6M	$\tilde{T}_A$	$\tilde{\rho}_A$	Γ_A	Z_A	
1.00	0.00	1.0008	0.8630	1.0823	0.3610	
0.75	0.25	1.0133	0.8280	1.1866	0.4510	
0.40	0.60	1.0027	0.9234	1.0741	0.3912	
0.15	0.85	1.0012	0.9059	0.9290	0.3617	
0.05	0.95	1.0008	0.8785	0.8148	0.3577	
0.00	1.00	1.0005	0.8824	0.7310	0.3532	
Composition x		Downstream state B				
MDM	MD_6M	$\tilde{T}_B$	$\tilde{\rho}_B$	Γ_B	Z_B	$\tilde{P}_B$
1.00	0.00	0.9833	0.5279	0.2078	0.5072	0.8461
0.75	0.25	1.0013	0.5172	0.5912	0.5661	0.7764
0.40	0.60	0.9931	0.5698	0.3292	0.5291	0.8284
0.15	0.85	0.9919	0.5342	0.1593	0.5241	0.8485
0.05	0.95	0.9910	0.4920	0.1664	0.5395	0.8382
0.00	1.00	0.9902	0.4660	0.2068	0.5551	0.8231

Table 8.4: Downstream Mach number and pressure, temperature, density, and velocity differences across the expansion waves, where $\Delta(\cdot) = (\cdot)_B - (\cdot)_A$.

Composition x						
MDM	MD_6M	M_B	$\frac{\Delta P}{P_A}$	$\frac{\Delta T}{T_A}$	$\frac{\Delta \rho}{\rho_A}$	$\frac{\Delta u}{u_A}$
1.00	0.00	1.1770	-0.1562	-0.0175	-0.3927	0.4128
0.75	0.25	1.3822	-0.2257	-0.0119	-0.3760	0.3222
0.40	0.60	1.2426	-0.1739	-0.0096	-0.3843	0.3752
0.15	0.85	1.1109	-0.1539	-0.0093	-0.4140	0.4943
0.05	0.95	1.0621	-0.1641	-0.0098	-0.4483	0.6195
0.00	1.00	1.0450	-0.1792	-0.0103	-0.4765	0.7283

general interface to several thermodynamic libraries [73]. An unstructured mesh refinement technique is adopted to increase the accuracy in regions where the solutions exhibit the largest gradients.

Figure 8.6 shows the flow field isobars from flow simulations for different mixtures of MDM/MD_6M, whereby the mole fraction of MDM varies from $x_{MDM} = 1$ in figure 8.6a to $x_{MDM} = 0$ in figure 8.6f, under the assumption of negligible fluid viscosity and thermal conductivity.

Figure 8.6a displays the supersonic flow of a pure MDM vapour. As expected, since $\Gamma > 0$, a classical isentropic expansion fan is observed in this case. It is remarkable that differently from supersonic expansions of a constant specific heats ideal gas, the Mach number M variation across the expansion is non-monotone, as it can be appreciated from figure 8.7a, where the Mach number is depicted for a representative streamline across the expansion wave. The present non monotone behaviour is consistent with the value of the parameter J, namely

$$J(s, \rho, M) = 1 - \Gamma(s, \rho) - \frac{1}{M^2}, \tag{8.2}$$

across the expansion wave. Indeed, for isentropic processes from a given state A one has, see Ref. [82],

$$\frac{dM}{d\rho} = J(s_A, \rho, M)\frac{M}{\rho}. \tag{8.3}$$

As shown in figure 8.7b, in the expansion of pure MDM vapour depicted in figure 8.6a, J can have both negative and positive values and therefore M is non-monotone. Note that for a constant specific heat ideal gas, $J = (1 - \gamma)/2 - 1/M^2 < 0$, with γ ratio of the isobaric and isochoric specific heats, and therefore M always increases monotonically during a supersonic expansion.

A reversed, nonclassical, behaviour is observed for the supersonic expansion of pure MD_6M, shown in figure 8.6f. An oblique nonclassical rarefaction shock wave, which forms an angle of 60° with respect to the upstream flow direction, is observed.

Intermediate situations are observed in the case of mixtures of MDM/MD_6M—shown in figures 8.6b, 8.6c, 8.6d and 8.6e—where the supersonic expansions of mixtures of increasing concentration of the more complex component MD_6M are depicted.

In particular, in figure 8.6b, where the flow of a MDM(0.75)/MD_6M(0.25) mixture is shown, a classical rarefaction fan is observed since $\Gamma > 0$. The angular sector encompassed by the fan is larger than that observed in figure 8.6a for pure fluid MDM, although the final turning angle $\theta_B = -13.169°$ is the same in both conditions. Therefore, since the slope of the limiting characteristic line at the right boundary of the fan is $\lambda(\theta_B) = \tan(\theta_B + \mu(\theta_B))$ where $\sin\mu_B = 1/M_B$, one can conclude that the Mach number at the end of the expansion is larger in this case, as it is confirmed also by the values in table 8.3 and 8.4. The above can be explained by recalling the dependence of the Mach number on the local velocity angle θ given by the Prandtl-Meyer relation, see Ref. [7], namely,

$$d\theta = \frac{\sqrt{M^2 - 1}}{1 - (\Gamma - 1)\, M^2} dM. \tag{8.4}$$

Indeed, despite the larger average molecular weight, along the considered isentrope the value of J for the mixture is always lower than that computed for pure MDM, see figure 8.7b, and the Mach number difference between the upstream and downstream state is larger.

In the conditions depicted in 8.6c and 8.6d, $\Gamma_{min} > 0$, see figure 8.3 and table 8.1, and therefore a classical flow is observed in both cases. In case 8.6c, the Mach number in state B is larger than that observed in case 8.6a, consistently with the Γ and J profiles across the expansion, see figures 8.7c and 8.7b, respectively. As a consequence, the angle encompassed by the rarefaction fan is larger than that observed for pure fluid MDM. The opposite situation is found in the case in 8.6d and the fan is narrower than its pure fluid counterpart.

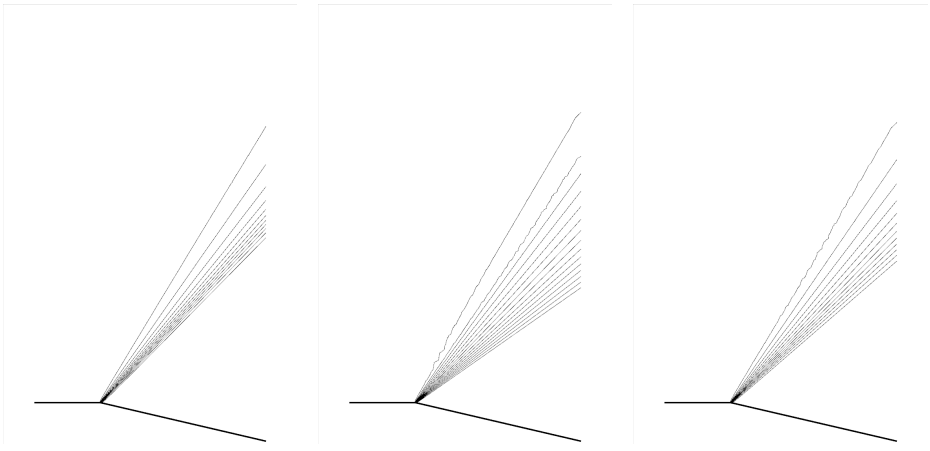

(a) MDM (b) MDM(0.75)/MD_6M(0.25) (c) MDM(0.40)/MD_6M(0.60)

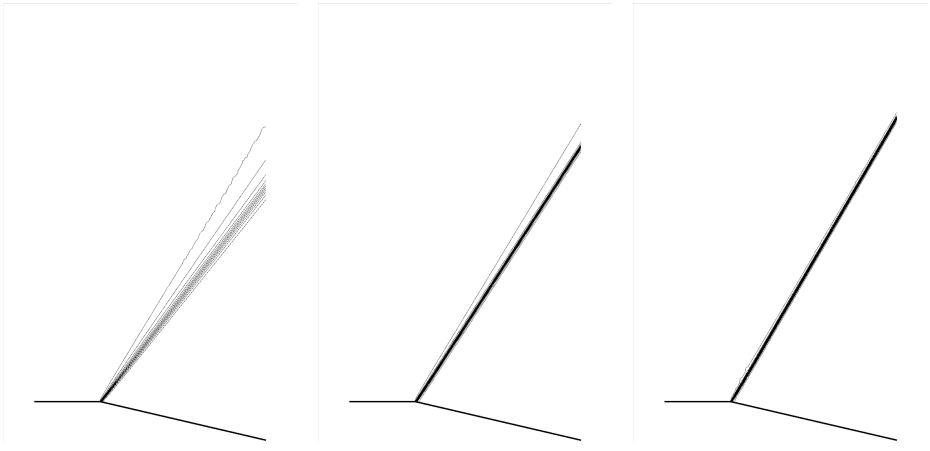

(d) MDM(0.15)/MD_6M(0.85) (e) MDM(0.05)/MD_6M(0.95) (f) MD_6M

Figure 8.6: Simulated flows of dense vapours of MDM/MD_6M expanding over a corner, whereby the mole fraction of MDM varies from 1 (a) to 0 (f). Fifteen levels of isopressure contour lines are plotted in the range $\tilde{P} = [0.8, 1]$. The upstream state features the same Mach number M, reduced pressure $\tilde{P} \equiv P/P_c$ and reduced entropy $\tilde{s} = s/s_\tau$ in all cases. The fluid thermodynamic model is the iPRSV equation of state complemented by the Wong-Sandler mixing rules for the mixtures.

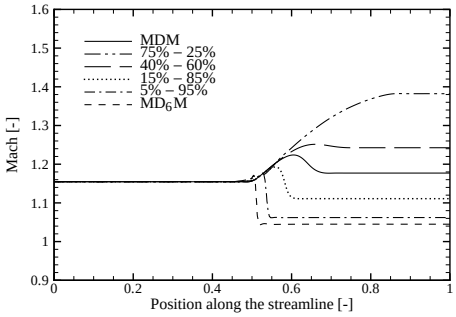

(a) Mach number

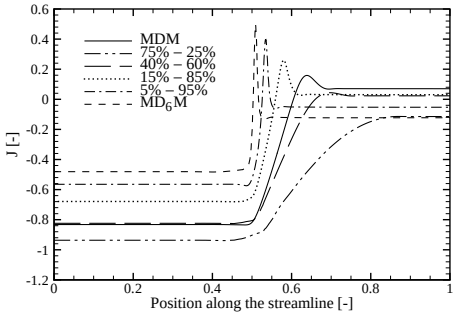

(b) $J = 1 - \Gamma - 1/M^2$

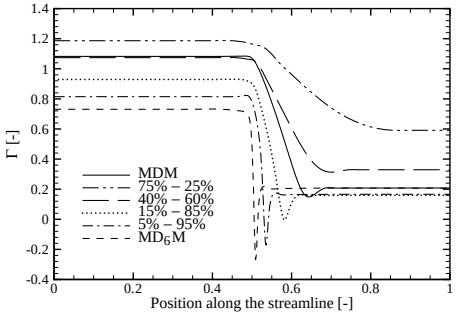

(c) Γ

Figure 8.7: Variation of the Mach number (top), the parameter $J = 1 - \Gamma - 1/M^2$ (middle), and Γ (bottom) along a streamline. Different lines correspond to different compositions of the mixture MDM/MD_6M.

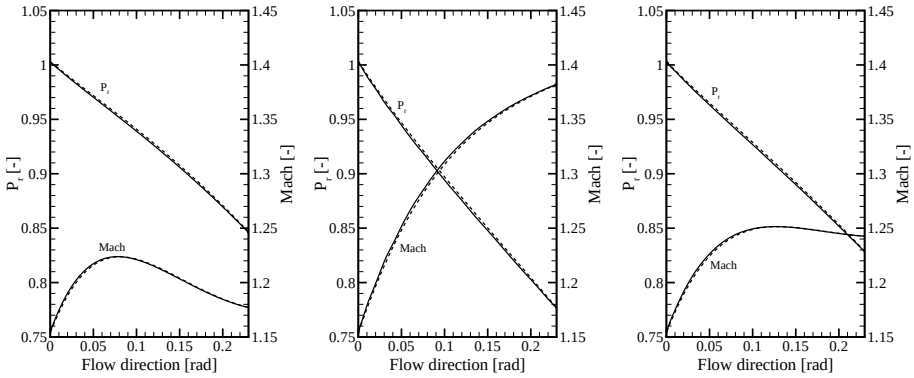

(a) MDM (b) MDM(0.75)/MD_6M(0.25) (c) MDM(0.40)/MD_6M(0.60)

Figure 8.8: Comparison between the numerical integration (- - -) of the Prandtl–Meyer ordinary differential equation (8.4) and numerical simulation (—).

From table 8.1 and figure 8.4, for small concentrations of MDM ($x_{\mathrm{MDM}} < 0.15$), Γ assumes negative values in the vapour phase and nonclassical behaviour is admissible. This is the case of the flow of mixture MDM(0.05)/MD_6M(0.95) in figure 8.6e, where the expansion occurs through a nonclassical composite wave made of a continuous fan that is terminated by a nonclassical rarefaction shock wave, with close-to-sonic downstream state. The expansion is depicted in the thermodynamic plane in figure 8.5b, which displays the pre- and post-expansion states A and B in the reduced *P*-*v* plane. While for the case of the pure fluid MD_6M a single rarefaction shock wave connects the two states, in the case of the mixture MDM(0.05)/MD_6M(0.95), an initial isentropic expansion is observed from state A to state A', which lies on the double sonic line. Then, a rarefaction shock wave expands the fluid from A' to B.

Results are summarized in table 8.4, which displays the downstream Mach number M and the variations of pressure P, the temperature T, the densityρ and the velocity u across the waves for all the considered different mixture compositions. The entropy difference across composite waves and the RSW is very small, due to both the relatively small pressure difference across the shock and the small value of Γ. Indeed, Landau and Lifshitz showed that a Taylor-series expansion of the Rankine-Hugoniot jump conditions delivers the following relation

$$\Delta s \simeq -\frac{\Gamma_{\mathrm{A}}}{6}\frac{c_{\mathrm{A}}^2}{T_{\mathrm{A}}}\left[\frac{\Delta v}{v_{\mathrm{A}}}\right]^3 + o\left(\left[\frac{\Delta v}{v_{\mathrm{A}}}\right]^4\right),$$

where $\Delta(\cdot) = (\cdot)_{\mathrm{B}} - (\cdot)_{\mathrm{A}}$, which is valid for weak shock waves [83]. In the present study, the largest entropy difference was computed by solving the non-linear Rankine-Hugoniot jump conditions for the RSW in MD_6M and it is as small as $\frac{\Delta s}{s_{\mathrm{A}}} \sim 5 \times 10^{-6}$.

To conclude, figure 8.8 reports the comparison of the numerical integration of the Prandtl–Meyer ordinary differential equation (8.4) and the numerical simulations for the three classical expansions of pure fluid MDM and of the mixtures MDM(0.75)/MD_6M(0.25) and MDM(0.40)/MD_6M(0.60). The very good agreement obtained by these two different approaches increases the authors' confidence on the correctness of the presented results. Furthermore, the values of the upstream and

downstream entropy were compared for the three isentropic expansions, for which the exact results is $\frac{\Delta s}{s_A} \equiv 0$ since $s_A \equiv s_B$. Small relative differences of about 10^{-6} confirmed that effects of numerical dissipation were negligible.

8.4 Conclusions

Nonclassical gasdynamic phenomena in dense vapours of organic mixtures have been investigated for the first time. In particular, the effect of non-ideal mixing on the thermodynamic properties relevant to the fluid dynamics was studied.

Predictive equations of state have been used to compute the thermodynamic properties of the mixture, most notably the fundamental derivative of gasdynamics Γ, for mixtures of siloxanes, perfluorocarbons, siloxanes-perfluorocarbons, and cloro- and perfluorocarbons. Some of the exemplary mixtures display thermodynamic regions of negative nonlinearity for certain compositions. The dependence of the minimum value of Γ in the vapour phase from the molar composition has been analyzed in the paradigmatic case of mixtures of linear siloxanes. It is found that Γ_{min} is always greater than the value of Γ_{min} of the most complex molecule in the mixture. In addition the value Γ_{min} of a pure linear siloxane whose molecular weight is intermediate with respect to that of the mixture constituents, is always lower than that of the mixture featuring the same molecular weight or complexity.

Preliminary simulations of a supersonic flow of a dense vapour expanding over a corner are presented. The dense vapour is a binary mixture of linear siloxanes MDM/MD_6M, whereby for each simulation the upstream conditions are kept similar, while the molar composition is varied from $x_{MDM} = 0$ to $x_{MDM} = 1$. The results show how the flow field changes from the classical expansion fan to a rarefaction shock wave, when the composition is MDM(0.05)/MD_6M(0.95). For MDM(0.15)/MD_6M(0.85) a mixed rarefaction shock/fan is predicted. Thermal decomposition of the fluid and critical point effects are to be carefully assessed before selecting the substance for experiments. However, it is remarkable that, similarly to previous studies on non-classical flows, the same gasdynamics behaviour is expected for all considered fluids.

We conclude that for the considered mixtures, mixing compounds of the same fluid family does not enhance non-classical gasdynamic phenomena. Given the variety and complexity of molecular interactions among different molecules, the possibility that the opposite effect occurs for different mixture compositions cannot be ruled out. Limitations with respect to accuracy and predictive character of currently available thermodynamic models for mixtures make the analysis of the possibly large variety of mixtures difficult. In addition, these limitations must be considered also with respect to the results of this study.

Future work will be devoted to the improvement of thermodynamic models suitable for complex organic compounds, possibly also by means of property measurements. Indeed, the main obstacle to such investigation is the lack of experimental thermodynamic data of mixtures of complex organic compounds, or of predictive and accurate thermodynamic models, valid close to the vapour-liquid critical point.

Attention will be dedicated to highly non-ideal mixtures in an attempt to understand if an enhancement of non-classical gasdynamic effects can be achieved by mixing two or more different organic fluids. This possibility—together with thermal stability—would have a large impact on experiments aimed at generating and measuring non-classical gasdynamic phenomena. Siloxane mixtures will also be tested in the experimental facility for generating and measuring rarefaction shock wave at the Delft University of Technology.

Acknowledgments

The authors acknowledge the contribution of their colleague and friend T.P. van der Stelt for development of the mixture thermodynamic models.

A.1 iPRSV-WS Thermodynamic Model

The thermodynamic model adopted for the multi-component fluids is briefly described here. The volumetric equation of state (EoS) is provided by the so-called improved Stryjek-Vera Peng-Robinson (iPRSV) model complemented by a usual polynomial expression for the isobaric ideal-gas specific heat, see Ref. [69], and by the mixing rules proposed by Wong and Sandler [70].

[84], see also [85], proposed to use the Peng Robinson [86] cubic EoS, with the Soave [87] α-function, but with a different temperature and acentric factor dependence in order to improve the correlation of vapor pressures for a wide variety of fluids. Notably, the proposed functional form for α results in the Stryjek-Vera Peng-Robinson (PRSV) EoS featuring a discontinuity in all the properties at the absolute critical temperature, T_c, for water and alcohols, and at temperature $T = 0.7 \cdot T_c$ for all the other fluids. Recently, [69] proposed a modification of the PRSV EoS aimed at eliminating the discontinuity in the prediction of thermodynamic properties.

The iPRSV EoS is similar to the cubic form characteristic of the PRSV EoS,

$$P = \frac{RT}{v-b} - \frac{a}{v^2 + 2bv - b^2}, \tag{5}$$

where,

$$a = \left(0.457235\, R^2\, T_c^2/P_c\right)\alpha, \qquad b = 0.077796\, R\, T_c/P_c, \qquad \alpha = \left[1 + \kappa\left(1 - \sqrt{T_r}\right)\right]^2.$$

Here, $R = \mathcal{R}/\mu$ is the gas constant, with $\mathcal{R}$ the universal gas constant, a is the attractive term, b is the co-volume parameter, P and v are the pressure and the specific volume, respectively. The subscript c indicates properties at the vapour-liquid critical point. The parameter κ depends on the temperature as follows

$$\kappa = \kappa_0 + \kappa_1\left(1 + \sqrt{T_r}\right)(0.7 - T_r), \tag{6}$$

with

$$\kappa_0 = 0.378893 + 1.4897153\omega - 0.17131848\omega^2 + 0.0196554\omega^3, \tag{7}$$

where ω is the acentric factor. The empirical parameter κ_1 in eq. (6) is a pure-component parameter chosen in order to obtain accurate predictions of saturated properties. From low temperatures up to reduced temperatures of $T_r = 0.7$, Stryjek and Vera recommend using values for κ_1 tabulated in their papers [84, 85]. Alternatively, κ_1 can also be obtained by regressing experimental data. According to Stryjek and Vera, for water and alcohols the tabulated values can be applied up to the critical point. For other compounds, slightly better results are obtained with $\kappa_1 = 0$ for $0.7 < T_r < 1$. For super critical temperatures ($T_r \geqslant 1$) they recommend $\kappa_1 = 0$, because there would be no advantage in using eq. (6) in this region. The κ-function therefore introduces a discontinuity in $\alpha(T)$ either at $T_r = 0.7$ or at $T_r = 1$, and in thermodynamic properties dependent upon and derivatives thereof. The iPRSV EoS is obtained by modifying the equation for the calculation of the κ-value, such that it is continuous with the temperature, but by keeping the same parameters κ_0 and κ_1 in the functional form, and in such a way that the same values can be used. This is a notable advantage, because

a large amount of data for these parameters that have been obtained so far can still be used. The κ-function in the iPRSV thermodynamic model is therefore

$$\kappa = \kappa_0 + \kappa_1 \left\{ \sqrt{[A - D(T_r + B)]^2 + E} + A - D(T_r + B) \right\} \sqrt{T_r + C}, \tag{8}$$

where the value of the coefficients are $A = 1.1$, $B = 0.25$, $C = 0.2$, $D = 1.2$ and $E = 0.01$. The accuracy of the iPRSV thermodynamic model is similar or better than that of the model from which is derived. The derivatives of κ with respect to the temperature, that are required for the implementation of a complete thermodynamic model into a computer program, are given in Ref. [69] together with a thorough discussion on the limits of the thermodynamic model.

Wong and Sandler developed a set of mixing rules which satisfy the theoretically correct quadratic composition dependence of the second virial coefficient [70]. The mixing rule is derived by equating the excess Helmholtz energy A^E of an activity coefficient model describing molecular interaction in the liquid phase to that obtained from the EoS at the so-called infinite-pressure state, namely, in the limit of a specific volume approaching the co-volume. The mixing rule contains one additional binary interaction parameter k_{ij} in the cross second virial coefficient, see Eq. 11. The binary interaction parameter can be determined by various approaches, see e.g. Ref. [88]. The Wong-Sandler mixing rule (WSMR) is used extensively in conjunction with the PRSV EoS. For the activity coefficient model, a so-called "solely energetic" model is usually preferred (i.e., a model which does not have an explicit free-volume term). As it is common practice for the PRSV EoS, the NRTL model introduced in Ref. [89] is used here to compute the activity coefficient, see also Ref. [90].

According to the WSMR, the a and b coefficients in (5) are substituted by

$$a_M = RTDb_M, \qquad \text{and} \quad b_M = \frac{Q}{1 - D}, \tag{9}$$

respectively, where

$$D = \frac{A^E_\infty}{C_{EoS}} + \sum_{i=1}^{NC} \frac{x_i a_i}{RT b_i}, \qquad Q = \sum_{i=1}^{NC} \sum_{j=1}^{NC} x_i x_j \left(b - \frac{a}{RT} \right)_{ij}.$$

The parameter C_{EoS} depends upon the equation of state. For the PRSV EOS, it reads

$$C_{EoS} = \frac{\sqrt{2}}{2} \ln\left(\sqrt{2} - 1 \right) \approx -0.62323. \tag{10}$$

The following combining rule has been used

$$\left(b - \frac{a}{RT} \right)_{ij} = \frac{b_i + b_j - a_i + a_j}{2RT} \left(1 - k_{ij} \right). \tag{11}$$

where a and b are the energy and the co-volume parameter. The subscript M refers to mixture properties while i and j refer to the components in the mixture. NC is the number of components.

From the pressure EoS, a complete thermodynamic model can be finally obtained by specifying the relation between the temperature and the specific heat at constant pressure c_P in the dilute gas limit, see e.g. [91]. In the present study, the following functional form of c_P

$$\psi(T) = \lim_{v \to \infty} c_P(T, v) = C_0 + C_1 T + C_2 T^2 + C_3 T^3 \tag{12}$$

with C_0, C_1, C_2 and C_3 constants. The values of the parameters C_0, C_1, C_2 and C_3 are given in Ref. [69] for the fluids of interest here. From the c_P definition (12) and the pressure EoS (5) a

complete thermodynamic model can be obtained. For example, from the reciprocity relation, one immediately computes the energy EoS as

$$e(T,v) = \phi(T) + \int_{v_0}^{v} \left[T \frac{\partial P(T,v)}{\partial v} - P \right] dv \tag{13}$$

where, from the Meyer's law of ideal gas, $\phi(T) = \psi(R) - R = \lim_{v\to\infty} c_v(T,v)$ is the specific heat at constant volume in the dilute gas limit. All thermodynamic variables can be computed from the two pressure and energy EoS (5) and (13), respectively, as detailed, e.g., in Ref. [92].

References

[1] H. A. Bethe. The theory of shock waves for an arbitrary equation of state. Technical report 545, Office Sci. Res. & Dev., 1942.

[2] J. D. van der Waals. *On the continuity of the gaseous and liquid states*, volume XIV. North-Holland, 1988. Reprinted.

[3] P. A. Thompson and K. C. Lambrakis. Negative shock waves. *J. Fluid Mech.*, 60:187–208, 1973.

[4] Y.B. Zel'dovich. On the possibility of rarefaction shock waves. *Zh. Eksp. Teor. Fiz.*, 4:363–364, 1946.

[5] H. Weyl. Shock waves in arbitrary fluids. *Comm. Pure Appl. Math.*, 2:102–122, 1949.

[6] P. A. Thompson. A fundamental derivative in gasdynamics. *Phys. Fluids*, 14(9):1843–1849, 1971.

[7] P. A. Thompson. *Compressilbe Fluid Dynamics*. McGraw-Hill, 1988.

[8] S. S Kutateladze, V. E. Nakoryakov, and A. A. Borisov. Rarefaction waves in liquid and gas-liquid media. *Ann. Rev. Fluid Mech.*, 19:577–600, 1987.

[9] A. Kluwick. *Handbook of shockwaves*, volume 1, chapter 3.4 (Theory of shock waves. Rarefaction shocks.), pages 339–411. Academic Press, 2001.

[10] A. Guardone, C. Zamfirescu, and P. Colonna. Maximum intensity of rarefaction shock waves for dense gases. *J. Fluid Mech.*, 642(1):127–146, January 2010.

[11] W Hayes. The basic theory of gasdynamic discontinuities. In H. W. Emmons, editor, *Fundamentals of gasdynamics: High speed aerodynamics and jet propulsion*, volume 3, pages 416–481. Princeton University Press, 1960.

[12] M.S. Cramer and A. Kluwick. On the propagation of waves exhibiting both positive and negative nonlinearity. *J. Fluid Mech.*, 142:9–37, 1984.

[13] M. S. Cramer and R. Sen. Shock formation in fluids having embedded regions of negative nonlinearity. *Phys. Fluids*, 29:2181–2191, 1986.

[14] M. S. Cramer and R. Sen. Exact solutions for sonic shocks in van der waals gas. *Phys. Fluids*, 30(2):377–385, February 1987.

[15] R. Menikoff and B. J. Plohr. The Riemann problem for fluid flow of real material. *Rev. Mod. Phys.*, 61(1):75–130, 1989.

[16] M. S. Cramer. Negative nonlinearity in selected fluorocarbons. *Phys. Fluids*, 1(11):1894–1897, 1989.

[17] M. S. Cramer and R. Sen. Mixed nonlinearity and double shocks in superfluid helium. *J. Fluid Mech.*, 221:233–261, 1990.

[18] M. S. Cramer and A. B. Crickenberger. The dissipative structure of shock waves in dense gases. *J. Fluid Mech.*, 223:325–355, 1991.

[19] M. S. Cramer. Nonclassical dynamics of classical gases. In A. Kluwick, editor, *Nonlinear Waves in Real Fluids*, pages 91–145. Springer-Verlag, 1991.

[20] A. Kluwick and G. Meyer. Shock regularization in dense gases by viscous-inviscid interac-

tions. *Journal of Fluid Mechanics*, 644:473–507, 2010.

[21] N. R. Nannan, A. Guardone, and P. Colonna. On the fundamental derivative of gas dynamics in the vapor-liquid critical region of single-component typical fluids. *Fluid Phase Equilib.*, 337:259–273, January 2013.

[22] P. A. Thompson, G. A. Carofano, and Y. G. Kim. Shock waves and phase changes in a large heat capacity fluid emerging from a tube. *J. Fluid Mech.*, 166:57–96, 1986.

[23] S. C. Gulen, P. A. Thompson, and H. A. Cho. Rarefaction and liquefaction shock waves in regular and retrograde fluids with near-critical end states. In *Adiabatic waves in liquid-vapor systems*, pages 281–290. Springer-Verlag, 1989.

[24] P. A. Thompson. Liquid-vapor adiabatic phase changes and related phenomena. In A. Kluwick, editor, *Nonlinear Waves in Real Fluids*, pages 147–213. Springer-Verlag, New York, NY, 1991.

[25] A. G. Ivanov and S. A. Novikov. Rarefaction shock waves in iron and steel. *Zh. Eksp. Teor. Fiz.*, 40(6):1880–1882, 1961.

[26] A. A. Borisov, S. S. Borisov, AL. A.and Kutateladze, and V. E. Nakoryakov. Rarefaction shock waves near the critic liquid-vapour point. *J. Fluid Mech.*, 126:59–73, 1983.

[27] S. H. Fergason. *Dense gas shock tube: design and analysis*. Ph.d. thesis, University of Colorado, Boulder, 2001.

[28] D. Chandrasekar and P. Prasad. Transonic flow of a fluid with positive and negative nonlinearity through a nozzle. *Phys. Fluids A*, 3(3):427–438, 1991.

[29] M. S. Cramer, L. M. Tarkenton, and G. M. Tarkenton. Critical Mach number estimates for dense gases. *Phys. Fluids A*, 4(8):1840–1847, 1992.

[30] G.H. Schnerr and S. Molokov. Exact solutions for transonic flows of dense gases in two-dimensional and axisymmetric nozzles. *Phys. Fluids*, 6(10):3465–3472, 1994.

[31] G.H. Schnerr and S. Molokov. Nonclassical effects in two-dimensional transonic flows. *Phys. Fluids*, 7(11):2867–2875, 1995.

[32] A.C. Aldo and B.M. Argrow. Dense gas flow in minimum length nozzles. *J. Fluid Eng.-T. ASME*, 117(2):270–276, 1995.

[33] B.P. Brown and B.M. Argrow. Nonclassical dense gas flows for simple geometries. *AIAA J.*, 36(10):1842–1847, 1998.

[34] G. H. Schnerr and P. Leidner. Numerical investigation of axial cascades for dense gases. In E. L. Chin, editor, *PICAST1–Pacific International Conference on Aerospace Science Technology*, volume 2, pages 818–825, National Cheng Kung University, Taiwan, Republic of China, December 1993.

[35] G. H. Schnerr and P. Leidner. Two-dimensional nozzle flow of dense gases. In *Fluids Engineering Conference*, Washington, DC, 1993.

[36] B. M. Argrow. Computational analysis of dense gas shock tube flow. *Shock Waves*, 6:241–248, 1996.

[37] J.F. Monaco, M.S. Cramer, and L.T. Watson. Supersonic flows of dense gases in cascade configurations. *J. Fluid Mech.*, 330:31–59, 1997.

[38] B.P. Brown and B.M. Argrow. Two-dimensional shock tube flow for dense gases. *J. Fluid Mech.*, 349:95–115, 1997.

[39] B.P. Brown and B.M. Argrow. Application of Bethe–Zel'dovich–Thompson fluids in organic Rankine cycle engines. *J. Propul. Power*, 16(6):1118–1124, 2000.

[40] P. Cinnella and P. M. Congedo. Inviscid and viscous aerodynamics of dense gases. *J. Fluid Mech.*, 580:179–217, 2007.

[41] P. Cinnella and P. M. Congedo. Optimal airfoil shapes for viscous transonic flows of Bethe–

Zel'dovich–Thompson fluids. *Comput. & Fluids*, 37:250–264, 2008.
[42] P. Cinnella. Transonic flows of dense gases over finite wings. *Phys. Fluids*, 20(4), 2008.
[43] S. H. Fergason, T. L. Ho, B. M. Argrow, and G. Emanuel. Theory for producing a single-phase rarefaction shock wave in a shock tube. *J. Fluid Mech.*, 445:37–54, 2001.
[44] S. H. Fergason, A. Guardone, and B. M. Argrow. Construction and validation of a dense gas shock tube. *J. Thermophys. Heat Tr.*, 17(3):326–333, 2003.
[45] P. A. Thompson and W. F. Loutrel. Opening time of brittle shock-tube diaphragms for dense fluids. *Rev. Sci. Instrum.*, 44(9):1436–1437, 1973.
[46] A. Guardone. Three-dimensional shock tube flows of dense gases. *J. Fluid Mech.*, 583:423–442, 2007.
[47] P. Colonna, A. Guardone, N. R. Nannan, and C. Zamfirescu. Design of the dense gas flexible asymmetric shock tube. *J. Fluid Eng.-T. ASME*, 130(3):0345011–0345016, 2008.
[48] P. Colonna, N. R. Nannan, A. Guardone, and T. P van der Stelt. On the computation of the fundamental derivative of gas dynamics using equations of state. *Fluid Phase Equilib.*, 286(1):43–54, 2009.
[49] G. Angelino and C. Invernizzi. Cyclic methylsiloxanes as working fluids for space power cycles. *J. Sol. Energ. - Trans. ASME*, 115(3):130–137, 1993.
[50] P. Colonna. *Fluidi di Lavoro Multi Componenti Per Cicli Termodinamici di Potenza (Multicomponent Working Fluids for Power Cycles)*. PhD thesis, Politecnico di Milano, October 1996.
[51] P. Colonna, N. R. Nannan, A. Guardone, and E. W. Lemmon. Multiparameter equations of state for selected siloxanes. *Fluid Phase Equilib.*, 244:193–211, 2006.
[52] N. R. Nannan, P. Colonna, C. M. Tracy, R. L. Rowley, and J. J. Hurly. Ideal-gas heat capacities of dimethylsiloxanes from speed-of-sound measurements and ab initio calculations. *Fluid Phase Equilib.*, 257(1):102–113, 2007.
[53] P. Colonna, N. R. Nannan, and A. Guardone. Multiparameter equations of state for siloxanes: $[(CH_3)_3\text{-Si-}O_{1/2}]_2$-$[O\text{-Si-}(CH_3)_2]_{i=1,\ldots,3}$ and $[O\text{-Si-}(CH_3)_2]_6$. *Fluid Phase Equilib*, 263(2):115–130, 2008.
[54] R. N. Nannan and P. Colonna. Improvement on multiparameter equations of state for dimethylsiloxanes by adopting more accurate ideal-gas isobaric heat capacities: Supplementary to P. Colonna, N. R. Nannan, A. Guardone, E. W. Lemmon, Fluid Phase Equilib. 244, 193 (2006). *Fluid Phase Equilib.*, 280(1–2):151–152, 2009. Short Communication.
[55] G. Angelino and P. Colonna. Multicomponent working fluids for organic Rankine cycles (ORCs). *Energy*, 23(6):449–463, 1998.
[56] A. Uusitalo, T. Turunen-Saaresti, J. Honkatukia, P. Colonna, and J. Larjola. Siloxanes as working fluids for a mini-ORC systems based on high-speed turbogenerator technology. *Journal of Engineering for Gas Turbines and Power-Transactions of the ASME*, 135(4):042305–1–9, April 2013.
[57] W. Lang, R Almbauer, and P. Colonna. Assessment of waste heat recovery for a heavy-duty truck engine using an ORC turbogenerator. *Journal of Engineering for Gas Turbines and Power-Transactions of the ASME*, 135(4):042313–1–10, April 2013.
[58] P. Colonna, A. Guardone, and N. R. Nannan. Siloxanes: A new class of candidate Bethe–Zel'dovich–Thompson fluids. *Phys. Fluids*, 19(8), 2007.
[59] C. Zamfirescu, A. Guardone, and P. Colonna. Admissibility region for rarefaction shock waves in dense gases. *J. Fluid Mech.*, 599:363–381, 2008.
[60] P. Congedo, Piero Colonna, Christophe Corre, Jeroen Witteveen, and Gianluca Iaccarino. Backward uncertainty propagation method in flow problems: application to the prediction of

rarefaction shock waves. *Comput Method Appl M*, 213–216:314–326, March 2012.
[61] P. Colonna and P. Silva. Dense gas thermodynamic properties of single and multicomponent fluids for fluid dynamics simulations. *J. Fluid Eng.-T. ASME*, 125(3):414–427, 2003.
[62] P. R. Dvornic. *Silicon Compounds: Silanes and Silicones*, chapter High Temperature Stability of Polysiloxanes, pages 419–432. Gelest Inc., 2004.
[63] G. Angelino and P. Colonna. Air cooled siloxane bottoming cycle for molten carbonate fuel cells. In *Fuel Cell Seminar*, pages 667–670, October 2000.
[64] H. Chen, D. Y. Goswami, M. M. Rahman, and E. K. Stefanakos. A supercritical Rankine cycle using zeotropic mixture working fluids for the conversion of low-grade heat into power. *Energy*, 36(1):549–555, 2011.
[65] C. Trapp and P. Colonna. Efficiency improvement in pre-combustion CO_2 removal units with a waste-heat recovery ORC power plant. *Journal of Engineering for Gas Turbines and Power-Transactions of the ASME*, 135(4):042311–1–12, April 2013.
[66] O. Kunz, R. Klimeck, W. Wagner, and M. Jaeschke. The GERG-2004 wide-range equation of state for natural gases and other mixtures. Technical report, GERG Technical Monograph 15, VDI-Verlag, 2007.
[67] S. I. Sandler. *Chemical and Engineering Thermodynamics*. Chemical Engineering Series. John Wiley and Sons, New York, 2nd edition, 1989.
[68] S. I. Sandler. *Models for Thermodynamic and Phase Equilibria Calculations*. CRC Press, 1993.
[69] T. P. van der Stelt, N. R. Nannan, and P. Colonna. The iPRSV equation of state. *Fluid Phase Equilib.*, 330:24–35, September 2012.
[70] D. S. H. Wong and S. I. Sandler. A theoretically correct mixing rule for cubic equations of state. *AIChE J.*, 38:671–680, 1992.
[71] P. Coutsikos et al. Capabilities and limitations of the Wong-Sandler Mixing Rules. *Fluid Phase Equilib.*, 108:59–78, 1995.
[72] J. Gross and G. Sadowski. Perturbed-chain SAFT: An equation of state based on a perturbation theory for chain molecules. *Ind. Eng. Chem. Res.*, 40(4):1244–1260, 2001.
[73] P. Colonna, T. P. van der Stelt, and A. Guardone. FluidProp (Version 3.0): A program for the estimation of thermophysical properties of fluids. `http://www.fluidprop.com/`, 2012. A program since 2004.
[74] N.A. Lai, M. Wendland, and J. Fischer. Description of linear siloxanes with PC-SAFT equation. *Fluid Phase Equilib.*, 283(1-2):22–30, 2009.
[75] A. Armenio. Siloxane/perfuorocarbon mixtures as working fuid for organic Rankine cycle turbogenerators. Master's thesis, Politecnico di Milano - Delft University of Technology, April 2009. ET–2365.
[76] M. M. Abbott. Cubic Equations of State. *AIChE J.*, 19:596–601, 1973.
[77] A. Bymaster, C. Emborsky, A. Dominik, and W.G. Chapman. Renormalization-group corrections to a perturbed-chain statistical associating fluid theory for pure fluids near to and far from the critical region. *Ind. Eng. Chem. Res.*, 47(16):6264–6274, 2008.
[78] D. S. H. Wong and S. I. Sandler. Theoretically correct mixing rule for cubic equations of state. *AIChE J.*, 38(5):671–680, 1992.
[79] P. Colonna and A. Guardone. Molecular interpretation of nonclassical gas dynamics of dense vapors under the van der Waals model. *Phys. Fluids*, 18(5), 2006.
[80] R. Pecnik, V. E. Terrapon, F. Ham, G. Iaccarino, and H. Pitsch. Reynolds-Averaged Navier-Stokes Simulations of the Hyshot II Scramjet. *AIAA J.*, 50(8):1717–1732, 2012.
[81] R. Pecnik, E. Rinaldi, and P. Colonna. Computational fluid dynamics of a radial compres-

sor operating with supercritical CO_2. *Journal of Engineering for Gas Turbines and Power-Transactions of the ASME*, 134:122301, December 2012.

[82] M. S. Cramer and L. M. Best. Steady, isentropic flows of dense gases. *Phys. Fluids A*, 3(1):219–226, 1991.

[83] L. D. Landau and E. M. Lifshitz. *Course of theoretical physics, fluid mechanics*, volume 6. Pergamon Press, Oxford, 1959.

[84] R. Stryjek and J. H. Vera. PRSV: An improved Peng–Robinson equation of state for pure compounds and mixtures. *Canadian Journal of Chemical Engineering*, 64(2):323–333, 1986.

[85] P Proust and J H Vera. PRSV: The Stryjek-Vera modification of the Peng-Robinson equation of state. Parameters for other pure compounds of industrial interest. *The Canadian Journal of Chemical Engineering*, 67(1):170–173, 1989.

[86] D. Y. Peng and D. B. Robinson. A new two-constant equation of state. *Ind. Eng. Chem. Fundam.*, 15(1):59–64, 1976.

[87] G. Soave. Equilibrium constants from a modified Redlich-Kwong equation of state. *Chem. Eng. Sci.*, 27:1197–1203, 1972.

[88] P. Coutsikos, N.S. Kalospiros, and D.P. Tassios. Capabilities and limitations of the Wong-Sandler mixing rules. *Fluid Phase Equilibria*, 108(1-2):59–78, 1995.

[89] H. Renon and J. M. Prausnitz. Local compositions in thermodynamic excess functions for liquid mixtures. *AIChE Journal*, 14(1):135–144, 1968.

[90] P. Ghosh and T. Taraphdar. Prediction of vapor-liquid equilibria of binary systems using PRSV equation of state and Wong-Sandler mixing rules. *Chemical Engineering Journal*, 70(1):15–24, 1998.

[91] H. B. Callen. *Thermodynamics and an introduction to thermostatistics*. Wiley, 2nd edition, 1985.

[92] P. Colonna and P. Silva. Dense gas thermodynamic properties of single and multicomponent fluids for fluid dynamics simulations. *ASME J. Fluids Eng.*, 125:414–427, 2003.

9

Conclusions & Perspectives

This thesis presents the original results of the experimental and numerical research conducted by the author and his colleagues, aimed at investigating the potential of molecularly heavy and complex organic compounds as working fluids for the organic Rankine cycle (ORC) power systems of the future. The material presented is at the basis of several publications on peer-reviewed international journals: five papers are already published, one has been accepted for publication, and two are about to be submitted for publication. The work is divided in self-contained chapters, each addressing a specific sub-topic, with its own concluding remarks. The general conclusions and their practical implications are treated in the following, marked with the ❀ and the ✽ sign, respectively.

The first part of the thesis presents several contributions to the research in the field of energy conversion systems, focusing on ORC turbo-generators.

Chapter 2 presents the first review work covering the historical developments, the status of the art, and the future foreseen for the ORC power systems technology.

- ❀ A comprehensive overview of the applications, technical solutions, and of the ORC plants which reached commercial operation in the last 20 years is presented, with a collection of data harvested within the major manufacturers.
- ✽ The work is intended as a reference for both the Academic and the Industrial audience and, in the authors' opinion, could prove particularly useful in avoiding the repetition of studies/attempts/experiments which have been already carried out in the past. Furthermore, the presented outlook to the future might help in defining the strategic objectives to be pursued in order to advance the ORC power systems field.

Chapter 3 explores the main envisaged research paths in the field of ORC turbo-expanders design, i.e., the development of generalized design methodologies, and the assessment of non-conventional machine architectures.

- ❀ The first critical evaluation of the centrifugal or radial-outflow turbine (ROT) architecture as a candidate technology for ORC systems is presented.
- ❀ It is discussed how the simplifying assumptions usually adopted in the axial turbines practice are typically not applicable for ROT machines. It is concluded that, in order to design efficient ROTs, it is needed that the blade discharge geometric angles, the radial chords, the stage expansion ratios, and the reaction degrees are allowed to vary among each cascade, and that the diameter and the speed of revolution are included among the optimization variables.
- ❀ A novel design methodology for the preliminary sizing of ROTs in the power size range from several MW_E down to few kW_E is presented, which covers most of the applications foreseen today.
- ❀ The in-house mean-line optimization code *zTurbo*, which allows to determine the preliminary design of ORC turbines of various configurations and working with different fluids, is introduced and adopted to verify the novel method by presenting several exemplary design exercises.
- ❀ The design of two 1 MW_E centrifugal turbines is presented, a transonic six-stage and a supersonic three-stage machines. These expanders handle an expansion ratio of 60, and rotate at 3000 RPM. Simplifications derived from the axial-turbines practice are adopted in order to illustrate their consequences. The results of the design exercise carried out with

zTurbo confirm that the adopted assumptions lead to unwanted design features, such as converging meridional channels and large flaring angles on the last stages. The predicted fluid-dynamic efficiency for the transonic and the supersonic machine is around 86% and 81%, respectively.

- The down-scaling potential of the centrifugal architecture is assessed, by applying the novel design methodology to the sizing of two 10 kW_E ROTs, handling an expansion ratio of 45. The design of a 5 stages transonic turbine, and of a 3 stages slightly supersonic one is presented. The proposed design procedure proves valuable in overcoming the criticality previously highlighted. In particular, the resulting meridional channel monotonically diverges maintaining maximum flaring angles lower than 10°. The resulting turbines are projected to exceed a fluid-dynamic efficiency of 79% and 77%, with speed of revolution around 124000 and 15400 RPM, respectively.

- It is demonstrated that the ROT architecture is a promising concept for future ORC power systems, capable of preserving its features and performance when downscaled, for both transonic and slightly supersonic configurations.

- The proposed methodology and tools are virtually applicable to the preliminary design of any ROT expander, working with any reasonable fluid.

Chapter 4 presents the research related with another innovative component, i.e., a so-called direct thermal storage system whereby the same fluid is circulated in the heat source, serves as the thermal storage medium, and acts as the working fluid of the ORC turbo-generator.

- Several options are presented regarding the integration of the thermal storage system into the plant. The most promising solutions seem those decoupling the thermal energy source from the ORC power block. It is demonstrated how, apart from a substantial simplifications in terms of both plant layout and operational strategy, this configuration ensures high exergetic performance of the thermal charge and discharge processes.

- A newly conceived variant of the Rankine cycle is introduced, whereby a flashing evaporation process precedes the power-generating expansion. The properties of the adopted complex-molecule working fluids are such that flashing can lead to saturated or superheated vapor conditions. This characteristic implies further simplifications of the system. The efficiency of an ORC power plant working according to this complete flashing cycle (CFC) may be, under the described assumptions, only marginally lower than what observed for a conventional evaporative ORC power system.

- A case study regarding a 100 kW_E solar plant is presented: the proposed system features a constant-pressure thermocline storage system, with vapour generation through external flashing of the liquid extracted from the storage vessel. The proposed turbo-generator achieves an estimated 25% efficiency, which corresponds to a solar-to-electric value of 18% in design conditions for the complete system. With siloxanes compounds, the estimated values of storage density are around 10 kWh_E for a cubic meter of storage volume, which is around half of what typically achieved with the storage of diathermic oils, but without considering additional filling materials. The advantages in terms of simplification of the plant layout could overcome the relatively low values of storage densities, the need of pressurization, and the specific cost of the fluids. A dynamic model, developed for the complete system, is used to investigate the performance under extreme transient conditions. This allows to preliminary assess the feasibility of remotely controlled operation.

- ❋ Feasible and efficient energy storage systems are foreseen to be the enabler technology for future power plants, such as, notably, those in the field of concentrated solar power (CSP). Furthermore, small-scale distributed CSP plants co-generating heating and cooling power will probably gain an important role. As already said, ORC turbo-generators are good candidates for similar applications but, before this work, no storage system tailored to this technology was investigated. Therefore, this study has the potential to open up new possibilities of dissemination for solar-powered ORC engines.

With Chapter 5, the focus of the analysis is moved from the component- to the system-level, by proposing an innovative methodology for the design of flexible energy conversion systems, which takes dynamic requirements on critical transients into account since a very early phase in the design cycle.

- ❁ The new tool DYNDES is presented, which utilizes a multi-objective optimization approach to search for optimal system designs with potentially conflicting objectives. The main components, notably the heat exchangers in the considered case, are also preliminary sized at this step. The system dynamic performance is thus enforced as an additional design criterion, by testing the previously determined optimal system configurations by simulating the behavior of automatically parametrized dynamic simulations.
- ❁ It is shown how to exclude those designs which do not satisfy given dynamic requirements such as, e.g., the tolerance on network frequency variations as a consequence of a strong load oscillation.
- ❁ The developed methodology is successfully applied to the case study of an ORC-based combined cycle power plant for an off-grid oil platform.
- ❋ The proposed procedures and tools might be valuable for the preliminary design of first-of-a-kind systems with demanding dynamic requirements, also in fields other than energy conversion.

Chapter 6 addresses another important aspect of modern energy systems, i.e. the operating strategy. The paradigmatic case of concentrated solar power plants selling energy in a context of time-varying tariffs is considered. The thermal energy storage (TES) system can be used to shift the production to the most profitable hours, exploiting the dispatchability capabilities of this technology.

- ❁ A simplified model of a state-of-the-art central receiver plant has been developed using high-level modelling languages, and proved to be accurate with respect to the SAM reference software and literature data.
- ❁ Optimal control problems have been formulated and solved using high-level modelling languages. The validity of the analysis is confirmed by previously published results.
- ❁ As a novelty, different operating strategies are compared based on a detailed financial analysis over the project life-time. A wide system design space is considered, and the results are presented for all the foreseeable combinations of solar field size and TES system capacity.
- ❁ A novel methodology is introduced, which allows to properly assess the potential of optimal control in terms of both the increased revenue and the reduced investment cost it allows for.
- ❁ It is demonstrated that optimal control should be taken into account when estimating the potential plant revenue since its design and sizing phase.
- ❁ It is shown that, for state-of-the art systems under the assumptions considered, it is always profitable to exploit optimal control to the end of increasing electricity production. On a yearly basis, an average gain in the revenue of the order of 5% is obtained with respect to

usually adopted short-sighted strategies. However, this figure is amplified to more than 10% in terms of net present value of the investment when applying the complete financial analysis presented here. Notably, the storage capacity for which maximum profitability occurs seems to be independent from the considered operating strategy.

- The potential of optimal control in terms of investment cost reduction has been unveiled for the first time. For the case-study technology considered, this follows the possibility of harvesting the same revenue with a smaller TES capacity.
- The results have been obtained with open-source software, and a total of about 50 code lines, which makes the developed tools quite understandable and user-friendly. The proposed methodology could be easily implemented as an extension of reference design models, such as those available within the SAM program.
- The proposed methodology constitutes a new tool in the designer's hands who, depending on the specific project characteristics and financial framework, may be keen on favouring a larger electricity production or a comparatively lower investment cost. Notably, this could be of particular interest for ORC-based CSP systems operating in the envisaged distributed generation scenario, possibly cogenerating thermal power for heating or cooling purposes.

The second part of the thesis is focused on the experimental and numerical investigation of the non-classical gas dynamic behavior of dense vapors of single- and multi-component organic fluids. Notably, ORC power systems constitute the first foreseen application for the arguments dealt with in this part.

Chapter 7 describes the commissioning the FAST setup, a new Ludwieg tube facility designed and built at the Delft University of Technology with the main purpose of providing the first experimental evidence of the most exotic non-classical gas dynamics effect, i.e., the rarefaction shock wave (RSW) in the dense vapor region of fluids formed by complex organic molecules.

- The setup components and the control & operation strategy devised are proven to be effective to the end of accurately measuring the speed and the intensity of the propagating waves. Results for several ideal gases are presented.
- The fast opening valve, which is the most critical component, is characterized in terms of its opening time, which resulted of the order of $2 - 5$ ms. According to previous studies, this should be small enough to ensure the complete formation of the phenomenon of interest, i.e. a shock wave, within the shock tube. This result is confirmed by analyzing a compression shock wave propagating in air.
- The first published results regarding speed of sound measurements performed in the dense-gas region of a molecularly complex organic compound, i.e. siloxane D_6, are presented.
- The FAST setup and the developed measurement procedure constitute unique tools to the end of proving the existence of the RSW. Furthermore, a number of interesting secondary results can be obtained, such as, notably, speed of sound measurements.

Chapter 8 presents the first theoretical investigation of non-classical gas dynamic phenomena in dense vapours of organic mixtures. In particular, the effect of non-ideal mixing on the thermodynamic properties relevant to the fluid dynamics was studied.

- Predictive equations of state have been used to compute the thermodynamic properties of the mixture, most notably the fundamental derivative of gas dynamics Γ.
- Some of the exemplary mixtures display thermodynamic regions of negative nonlinearity for certain compositions.
- The dependence of the minimum value of Γ in the vapour phase from the molar composition has been analyzed for several paradigmatic mixtures, finding that Γ_{min} is always greater than the value of Γ_{min} of the most complex molecule in the mixture. Further, the value Γ_{min} of a pure component whose molecular weight is intermediate with respect to that of the mixture constituents, is always lower than that of the mixture featuring the same molecular weight or complexity.
- For all the considered mixtures, mixing compounds of the same fluid family does not enhance non-classical gas dynamic phenomena.
- Preliminary simulations of a supersonic flow of a dense vapour expanding over a corner are presented. The dense vapour is a binary mixture of linear siloxanes MDM/MD_6M, whereby for each simulation the upstream conditions are kept similar, while the molar composition is varied from $x_{MDM} = 0$ to $x_{MDM} = 1$. The results show how the flow field changes from the classical expansion fan to a rarefaction shock wave, when the composition is MDM(0.05)/MD_6M(0.95). For MDM(0.15)/MD_6M(0.85) a mixed rarefaction shock/fan is predicted.
- Attention will be dedicated to highly non-ideal mixtures in an attempt to understand if an enhancement of non-classical gas dynamic effects can be achieved by mixing two or more different organic fluids. This possibility—together with thermal stability—would have a large impact on experiments aimed at generating and measuring non-classical gas dynamic phenomena.

Summary

A sharp inversion regarding the current trends of energy consumption and related emissions of global greenhouse gases is needed in order to harmonize our life to the planet resources and, ultimately, in order to survive. It is a shared idea that, to this end, a sustainable energy system has to be conceived, made to be smarter, more decentralized, and more integrated than what we know today. In the author's opinion, energy conversion systems based on the organic Rankine thermodynamic cycle (ORC) have the potential to play a major role in this envisaged framework, and the work hereby documented stems primarily from this belief.

Several contributions are presented, in order to illustrate the original results of numerical and experimental research aimed at investigating the potential of molecularly heavy and complex organic compounds as working fluids for the ORC power systems of the future. This thesis is divided into two main parts, in turn constituted by self-contained chapters, each addressing a specific sub-topic. The material presented is at the basis of several publications on peer-reviewed international journals: five papers are already published, one has been accepted for publication, and two are about to be submitted for publication.

The first part presents the contributions to the research in the field of energy conversion systems, focusing on ORC turbo-generators.

An introductory review on ORC systems, with an overview of their history, the description of the state-of-the-art from both the academic and the industrial perspective, and an outlook to envisaged paths of development is contained in Chapter 2. The cumulative global capacity of ORC systems, which is undergoing a rapid growth started a decade ago, is expected to grow much more in the future. The potential for the conversion into electricity of the thermal power coming from renewable and renewable-like sources is huge, and ORC power systems are one of the most flexible candidate conversion technologies to this end, both in terms of capacity and temperature levels. A comprehensive overview of the applications, technical solutions, and of the ORC plants which reached commercial operation in the last 20 years is presented, with a collection of data harvested within the major manufacturers. The work is intended as a reference for both the Academic and the Industrial audience, and could prove particularly useful in avoiding the repetition of studies/attempts/experiments which have been already carried out in the past.

Chapter 3 documents the original research conducted in the field of ORC turbo-expanders, which constitute the most critical components when efficient systems have to be designed. The variety of possible working fluids, the complex gas dynamic phenomena encountered, and the lack of simplified design methods based on experience on similar machines, make the design of efficient turbines a complicated task. Relevant paths of development may thus be concerned with (i) the development

of generalized design methodologies, and (ii) the assessment of non-conventional machine architectures: the research presented in this chapter aims at exploring both. The first critical evaluation of the radial-outflow turbine (ROT) architecture as a candidate technology for ORC turbo-generators is presented, together with a novel methodological framework for the design of these machines. The results of several design exercises show that the ROT is a promising concept, which allows for the realization of efficient, compact, and reliable turbo-expanders in any power-output level of interest.

Chapter 4 deals with the assessment of a novel thermal storage systems tailored to high-temperature ORC systems for concentrating solar power (CSP) applications, stemming from the observation that the direct storage of the ORC working fluids can be effective thanks to their favourable thermodynamic properties. The concept of complete flashing cycle (CFC) is introduced as a mean of achieving an unmatched system layout simplification, while preserving conversion efficiency. This is a new variant of the Rankine cycle, whereby the vapour is produced by throttling the organic working fluid from liquid to saturated vapour conditions. The main trade-offs appearing in the design phase of such systems, involving the global efficiency, the storage dimensions and pressure, and the expansion ratio across the turbine, are investigated. Also the dynamic performance of an exemplary plant are assessed by mean of simulation, preliminary proving the feasibility of remotely controlled operation. This study has the potential of opening up new possibilities of dissemination for solar-powered ORC engines.

Chapter 5 shifts the focus of the analysis from component- to system-level, presenting a methodology for the optimal design of modern power generation systems, accounting for the increasingly demanding requirements in terms of operational flexibility. The innovative element is the possibility of considering the dynamic performance since a very early phase of the design procedure. The test case presented is the preliminary design of an off-grid power plant serving an off-shore platform, where a gas turbine engine is combined with an ORC power module. The solutions of a stationary model of this combined plant are used to identify its optimal configurations. A dynamic model of each of these systems is thus automatically parameterized, by inheriting its parameters values from the design model results, and used to assess the performance of the modeled system under the transient scenarios of interest. Again, in the considered example it is shown that the proposed combined procedure allows to discriminate among the initial set of solutions, in order to provide the designs that also comply with dynamic requirements. These tools might be valuable for the preliminary design of first-of-a-kind systems with demanding dynamic requirements, also in fields other than energy conversion.

Chapter 6 explores the potential of innovative operating strategies in the context of thermal energy storage management for concentrating solar power plants. As the main novelties, a complete financial analysis is used to this end, and the impact on the system design is investigated. The methodology is applied to a test case, a state-of-the-art central receiver plant with direct storage, using molten salts as working fluid, and selling energy in a context of variable electricity prices. Different operating strategies are compared, and a wide system design space is considered. The potential of these techniques is discussed also under the point of view of investment cost reduction, showing how the same yearly revenue can be harvested with a smaller energy storage, if optimally operated. The novel method is an additional decision tool allowing to treat the storage operation strategy as a new variable in the design of next generation energy systems. This could be of particular interest for ORC-based CSP systems operating in the envisaged distributed generation scenario.

The second part of the thesis is focused on the experimental and numerical investigation of the non-classical gas dynamics behavior of dense vapors of single- and multi-component organic fluids. Notably, ORC power systems constitute the first foreseen application for the arguments dealt with in this part.

Chapter 7 describes the commissioning of the "Flexible Asymmetric Shock Tube" (FAST) experimental setup designed and built at the Delft University of Technology. The aim of this Ludwieg Tube facility is to measure the speed of propagation of pressure waves in organic vapors, with the final objective of providing the first experimental evidence of the most exotic non-classical gas dynamics phenomenon, i.e., the rarefaction shock wave (RSW) in the dense vapor region of fluids formed by complex organic molecules. Furthermore, a number of interesting secondary results can be obtained, such as, notably, speed of sound measurements. The setup components and the control & operation strategy devised are proven to be effective to the end of accurately measuring the speed and the intensity of the propagating waves. Results for several ideal gases are presented. The fast opening valve, which is the most critical component, is characterized in terms of its opening time, which resulted small enough to ensure the complete formation of the phenomenon of interest, i.e. a shock wave, within the shock tube length. This result is confirmed by analyzing a compression shock propagating in air. The preliminary results regarding speed of sound measurements performed in the dense-gas region of a molecularly complex organic compound, i.e. siloxane D_6, are also discussed.

Chapter 8 Presents the first investigation about the non-classical gas dynamics of binary mixtures of organic fluids in the vapour phase, showing how the composition of the mixture is a new relevant variable in the study of BZT fluids. This study has practical implications in that mixtures of organic fluids are considered for applications in ORC power systems, one of the possible applications of non-classical gas dynamics. Furthermore, multicomponent working fluids are often encountered in practice due to impurities, and thermal rearrangement effects. A finite thermodynamic region is predicted where the non-linearity parameter Γ is negative, and therefore non-classical gas dynamics phenomena are admissible. A non monotone dependence of Γ on the mixture composition is observed in the case of binary mixtures of siloxane and perfluorocarbon fluids, with the minimum value of Γ in the mixture being always larger than that of its more complex component. The observed dependence indicates that non-ideal mixing has a strong influence on the gas dynamics behaviour – either classical or non-classical – of the mixture. Numerical experiments of the supersonic expansion of a mixture flow around a sharp corner show the transition from the classical configuration, exhibiting an isentropic rarefaction fan centered at the expansion corner, to non-classical ones, including mixed expansion waves and rarefaction shock waves, if the mixture composition is changed.

Samenvatting

Een scherpe omkering in de huidige trend van energieconsumptie en de gerelateerde emissie van broeikasgassen is nodig om ons leven in harmonie te brengen met de eindige bronnen van onze planeet en om uiteindelijk te overleven. Het doel om dit te bereiken dat door velen gedeeld wordt, is het bedenken van een systeem van duurzame energie dat slimmer, meer gedecentraliseerd en meer geintegreerd is dan nu. Naar de mening van de auteur heeft de organische Rankine thermodynamische cyclus het potentieel om een grote rol te spelen in het voorgenomen kader, en het hierbij gedocumenteerde werk komt voort uit deze overtuiging.

Verschillende bijdragen worden getoond om de originele resultaten te laten zien van numeriek en experimenteel onderzoek met het doel om het potentieel te bestuderen van moleculair zware en complexe organische stoffen als werkvloeistof voor ORC energie systemen van de toekomst. Dit proefschrift is in twee delen gesplitst, die verder onderverdeeld zijn in aparte hoofdstukken, elk hoofdstuk gewijd aan een specifiek sub-onderwerp. Het hierin getoonde materiaal vormt de basis van verschillende publicaties in peer-reviewed internationale tijdschriften: vijf papers zijn reeds gepubliceerd, één is geaccepteerd voor publicatie en twee staan op het punt om ter publicatie verzonden te worden.

Het eerste deel van deze thesis toont de bijdragen aan het onderzoek in veld van energie-omzettings systemen, gericht op ORC turbogeneratoren.

Een inleidende recensie van ORC systemen wordt gegeven in hoofdstuk 2, met daarin een overzicht van hun geschiedenis, beschrijving van de state-of-the-art en het industriële perspectief, en een blik op de voorgestelde ontwikkelingspaden. De cumulatieve globale capaciteit van ORC systemen maakt sinds een decennium geleden een sterke groei door en er wordt verwacht dat deze in de toekomst doorgroeit. Het potentieel van electriciteitsomzetting van thermische energie uit hernieuwbare en gelijksoortige bronnen is enorm, en ORC energie systemen zijn een van de meest flexibele kandidaats-omzettings technologien om dit te doen, zowel wat betreft capaciteit alsmede de temperatuursniveaus. Een uitgebreid overzicht van de toepassingen, technische oplossingen en van de ORC machines die in de laatste 20 jaar commercieel operationeel gemaakt zijn, wordt getoond samen met een data-collectie die van grote fabrikanten afkomstig is. Deze bijdrage is bedoeld als referentie voor zowel het academische als het industriële publiek, en zou bijzonder nuttig kunnen worden om te voorkomen dat studies/pogingen/experimenten herhaald worden die reeds zijn uitgevoerd.

Hoofdstuk 3 documenteert het originele onderzoek gedaan op het gebied van ORC turbo-expanders, die de meest kritieke componenten vormen aangaande het ontwerp van efficiente systemen. De hoeveelheid mogelijke werkvloeistoffen, de aangetroffen complexe gasdynamische fenomenen en het

gebrek aan simpele ontwerpmethoden gestoeld op ervaring van gelijksoortige machines, maken het ontwerp van een efficiente turbine een moeilijke opgave. Relevante ontwikkelingspaden kunnen mogelijk te maken hebben met: (i) de ontwikkeling van gegeneraliseerde ontwerpmethodologin, en (ii) de toetsing van onconventionele machine-bouwstijlen: het gepresenteerde onderzoek in dit hoofdstuk verkent beide doelen. De eerste kritische evaluatie van de opbouw van een radiale uitstroom turbine (ROT) als kandidaatstechnologie voor ORC turbogeneratoren wordt getoond, alsmede een nieuw methodologisch raamwerk voor het ontwerp van zulke machines. De resultaten van verschillende ontwerp-opgaven laten zien dat de ROT een veelbelovend concept is, dat de verwezenlijking van efficiente compacte en betrouwbare turbo-expanders op elk vermogensniveau van belang mogelijk maakt.

Hoofdstuk 4 behandelt de toetsing van nieuwe thermische energie-opslagsystemen specifiek voor hoge temperatuur ORC systemen voor toepassingen met geconcentreerde zonne-energie, afkomstig uit de observatie dat directe opslag van ORC werkvloeistoffen effectief kan zijn door hun gunstige thermodynamische eigenschappen. Het concept van de complete flash cyclus wordt als een middel voorgedragen om een onovertroffen versimpeling van systeemindeling te bewerkstelligen met behoud van efficiëntie. Dit is een nieuwe variant van de Rankine cyclus, waarbij damp geproduceerd wordt door het smoren van vloeistof tot verzadigde damp. De hoofdafwegingen die zich in het ontwerp van zo'n systeem voordoen zijn onderzocht, waaronder de globale efficintie, de opslagdimensies en -druk, en de expansieverhouding over de turbine. Ook de dynamische prestatie van een voorbeeldmachine zijn door middel van simulatie beoordeeld, met als voorlopig resultaat dat het de haalbaarheid van op afstand geregelde bediening aantoont.

Hoofdstuk 5 verschuift de nadruk op de analyse van component naar systeemniveau, waarin een methodologie voor het optimale ontwerp van moderne energie-opwekkingssystemen voorgelegd wordt, waarin de immer meer verlangende eisen op het gebied van operationele flexibiliteit in acht worden genomen. Het innovatieve element is dat de mogelijkheid om de dynamische prestaties vroeg in het ontwerpproces meegenomen kan worden. De voorgestelde proefopstelling is het voorontwerp van een off-grid energiecentrale voor een off-shore platform, waarbij een gasturbine met een ORC energiemodule wordt gecombineerd. De oplossingen van een stationair model van deze centrale zijn gebruikt om de optimale configuratie te bepalen. Een dynamisch model van ieder van deze systemen zijn aldus geparametriseerd door de waarde van haar parameters uit de resultaten van het ontwerpmodel te gebruiken, en de prestatie van het gemodelleerde systeem onder interessante transiente scenarios te bepalen. Nogmaals, in het gebruikte voorbeeld is aangetoond dat de voorgestelde gecombineerde procedure het toelaat om onderscheid te maken tussen de initiele oplossingen om zodoende de ontwerpen eruit te halen die tevens aan de dynamische eisen voldoen. Dit gereedschap zou waardevol kunnen zijn voor het voorontwerp van een eerste systeem met veeleisende dynamische eisen, tevens in andere gebieden dan energie-omzetting.

Hoofdstuk 6 verkent de potentie van innovatieve bedieningsstrategin in de context van opslag van thermische energie voor geconcentreerde zonne-energie centrales. De hoofdnoviteiten zijn dat een complete financile analyse is gebruikt en de impact op het systeemontwerp is onderzocht. De methodologie is toegepast op een testcase, een state-of-the-art centrale opvang-machine met directe opslag, die gesmolten zout als werkvloeistof gebruikt, waarbij energie verkocht wordt afhankelijk van de variabele electriciteitsprijs. Verschillende bedieningsstrategin zijn met elkaar vergeleken, en een brede ontwerpruimte is verkend. De potentie van deze technieken is besproken wat betreft de beperking van investeringskosten, waarbij aangetoond is hoe een gelijk jaarlijks inkomen ge-

realiseerd kan worden met een kleinere energieopslag, als deze optimaal bediend wordt. Deze nieuwe methode is een toegevoegd beslissingsgereedschap dat de opslagbedieningsstrategie als nieuwe variabele in het ontwerp van volgende generatie energiesystemen behandeld kan worden. Die zou specifiek nuttig kunnen zijn voor CSP systemen op basis van een ORC die in de voorziene opwekkingsscenarios werken van gedistribueerde energie-opwekking.

Het tweede deel van deze thesis concentreert zich op het experimentele en numerieke onderzoek van het niet-klassische gasdynamisch gedrag van dichte dampen van organische vloeistoffen bestaande uit een enkelvoudig component of meervoudige componenten. Opvallend is dat ORC energiesystemen de eerste voerziene toepassingen zijn voor de argumenten die in dit deel behandeld worden.

Hoofdstuk 7 beschrijft de ingebruikname van de experimentele opstelling “Flexibele Asymmetrische Schokbuis” (FAST), die aan de Technische Universiteit Delft ontworpen en gebouwd is. Het doel van deze Ludwieg Tube faciliteit is het meten van de propagatiesnelheid van drukgolven in organische dampen, met het uiteindelijke doel om het eerste bewijs te leveren van een van de meest exotische fenomenen uit de niet-klassische gasdynamica, namelijk de expansie schokgolf (RSW) in de dichte-damp regio van vloeistoffen van complexe organische moleculen. Verder kunnen een aantal interessante secundaire resultaten behaald worden, voornamelijk geluidssnelheidsmetingen. De opstellingscomponenten en de bedachte regel & werkingstrategie zijn effectief gebleken om nauwkeuring de snelheid en intensiteit van de propagerende golven te meten. Resultaten van enkele ideale gassen zijn weergegeven. De snel-openende klep, wat het meest kritische component is, is gekarakteriseerd voor zijn openingstijd, met als resultaat dat deze kort genoeg is om complete formatie van het interessante fenomeen, namelijk een schokgolf, binnen de lengte van de schokbuis te realiseren. Dit resultaat wordt bevestigd door een compressie schok te analyseren die door de buis gevuld met lucht reist. De voorlopige resultaten aangaande de geluidssnelheid in de dichte damp regio van een moleculair complexe organische stof, namelijk siloxaan D_6, worden ook behandeld.

Hoofdstuk 8 geeft het eerste onderzoek weer naar niet-klassische gasdynamica van binaire mengsels van organische vloeistoffen in de dampfase, waarin wordt aangetoond hoe de samenstelling van het mengsel een nieuwe relevante variabele is in de studie van BZT vloeistoffen. Dit onderzoek heeft het praktisch oogpunt dat mengsels van organische vloeistoffen worden overwogen als toepassing in ORC energiesystemen, een van de mogelijke toepassingen van niet-klassische gasdynamica. Daarnaast is er regelmatig sprake van een werkvloeistof bestaande uit meerdere componenten vanwege onzuiverheden en thermische her-rangschikkings-effecten. Een eindige thermodynamische regio wordt voorspeld waarin de niet-lineariteitsparameter negatief is, waarin daarom niet-klassische gasdynamica fenomenen toelaatbaar zijn. Een niet-monotone afhankelijkheid van op de mengselsamenstelling is waargenomen in het geval van binaire mengsels van siloxanen en perfluorocarbon vloeistoffen, waarbij de minimumwaarde van in het mengsel altijd groter is dan die van de meer complexe component. De geobserveerde afhankelijkheid laat zien dat het niet ideaal mengen een grote invloed heeft op het gasdynamisch gedrag – zowel klassisch als niet-klassisch – van het mengsel. Numerieke experimenten in de supersone expansie langs een scherpe hoek laten de transitie zien van de klassische configuratie met een isentrope expansie waaier gecentreerd op de hoek, naar niet-klassische configuraties met gemenge waarier-schok expansiegolven en pure expansie-schokgolven zodra de mengselsamenstelling veranderd wordt.

Acknowledgement

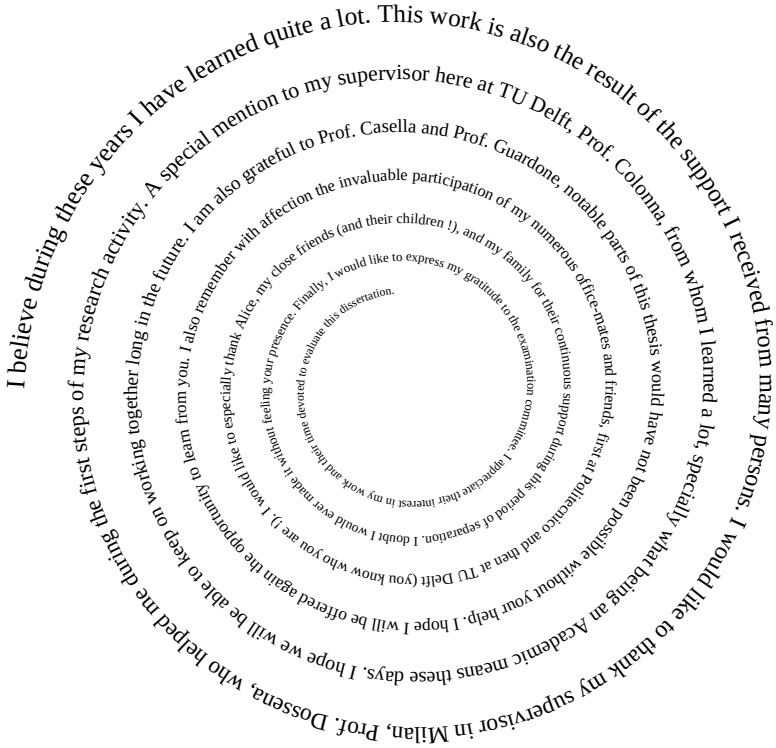

Emiliano Casati
Firenze, June 22, 2014

About the Author

Emiliano I.M. Casati was born in Milan, Italy, on June the 21st – 1982. After a more than reasonably happy childhood, long story short, he received his high-school diploma from Liceo Scientifico Statale G. Galilei - Erba, in Italy. He then enrolled for a BSc in Energy Engineering at Politecnico di Milano University. Before realizing the BSc was done, he found himself involved in the MSc program "Energy Conversion" within the same faculty, which finished at the end of 2008 defending the thesis "Development of aerodynamic probes for pneumatic measurements in turbines operated with dense vapors". The work lasted 18 months as part of a research project involving the company Turboden (presently part of Mitsubishi Heavy Industries); approximately half of the time was spent working at Turboden R&D. He then realized he really enjoyed studying, and thus started working as a post-graduate researcher at Politecnico di Milano for one year, under the supervision of Prof. Dossena. During the hot summer of 2009 he met Prof. Colonna and decided to go for a PhD program under the joint-supervision between TU Delft and Politecnico di Milano. The work started in 2010 and, after four years and few months, here he comes again, but with this nice and well crafted book in addition!

List of publications

Journal articles

M. Pini, G. Persico, E. Casati, & V. Dossena (2013). Preliminary Design of a Centrifugal Turbine for Organic Rankine Cycle Applications". *Journal of Engineering for Gas Turbines and Power-Transactions of the ASME*, vol. 135, pp 04231219.

E. Casati, A. Galli, & P. Colonna (2013). Thermal Energy Storage for Solar Powered Organic Rankine Cycle Engines". *Solar Energy*, vol. 96, pp 205 - 219.

A. Guardone, P. Colonna, E. Casati, & E. Rinaldi (2014). Non-Classical Gasdynamics of Vapour Mixtures". *Journal of Fluid Mechanics*, vol. 741, pp 681-701.

L. Pierobon, E. Casati, F. Casella, F. Haglind, & P. Colonna (2014). Preliminary Design Methodology for Flexible Power Systems Accounting for Dynamic Performance". *Energy*, vol. 68, pp 667-679.

E. Casati, S. Vitale, M. Pini, G. Persico, & P. Colonna (2014). Centrifugal Turbines for Mini-ORC Power Systems". *Journal of Engineering for Gas Turbines and Power-Transactions of the ASME*, in print.

E. Casati, F. Casella, & P. Colonna (2014). Design of CSP Plants with Optimally Operated Thermal Storage". *Submitted for publication.*

T. Mathijssen, E. Casati, M. Gallo, & P. Colonna (2014). Flexible Asymmetric Shock Tube (FAST): Commissioning of an High Temperature Ludwieg Tube for Rarefaction Shock Wave Measurements". *To be submitted for publication.*

P. Colonna, E. Casati, J. Larjola, A. Uusitalo, T. Turunen-Saaresti, C. Trapp, & T. Mathijssen (2014). Organic Rankine Cycle Power Systems: the Path from the Concept to Current Applications and an Outlook to the Future. *To be submitted for publication.*

T. van der Stelt, E. Casati, N. Chan, & P. Colonna (2014). Development of Technical Equations of State for Mixtures of Diphenyl-Diphenyl Ether Used as Heat Transfer Fluids". *Submitted for publication.*

Conference proceedings

E. Casati, P. Colonna, & N. R. Nannan (2011). Supercritical ORC turbogenerators coupled with linear solar collectors". *In Proceedings of the 30th ISES Biennial Solar World Congress 2011*, Kassel - DE. Vol. 5, pp. 40564067.

E. Casati, A. Desideri, F. Casella, & P. Colonna (2012). Preliminary assessment of a novel small

CSP plant based on linear collectors, ORC and direct thermal storage". *In Proceedings of the 18th SolarPACES conference*, Marrakech - MA.

E. Casati, E. Rinaldi, A. Guardone, & P. Colonna (2012). Nonclassical gasdynamics of vapor mixtures". *In Proceedings of the 6th European Congress on Computational Methods in Applied Sciences and Engineering – ECCOMAS 2012*. J. Eberhardsteiner, H. J. Böhm, & F. G. Rammerstorfer (Eds.) – pp. 111. Vienna University of Technology, Vienna - AT.

F. Casella, E. Casati, & P. Colonna (2014). Optimal Operation of Solar Tower Plants with Thermal Storage for System Design". *To be presented at the 19th World Congress of the International Federation of Automatic Control – IFAC 2014*, Cape Town–ZA.

Conference presentations

T. Mathijssen, M. Gallo, E. Casati, & P. Colonna (2012). Flow measurements in a Ludwieg tube type setup for the experimental investigation of rarefaction shock waves: status report". *In Proceedings of the 6th European Congress on Computational Methods in Applied Sciences and Engineering – ECCOMAS 2012*. J. Eberhardsteiner, H. J. Böhm, & F. G. Rammerstorfer (Eds.) – pp. 12. Vienna University of Technology, Vienna - AT.

P. Colonna, M. Gallo, E. Casati, & T. Mathijssen (2013). Flexible asymmetric shock tube (FAST) set-up – Status and first experiences". *Presented at the 2nd International Seminar on ORC Power Systems – ASME ORC-2013*, Rotterdam - NL.

E. Casati, S. Vitale, M. Pini, G. Persico, & P. Colonna (2014). Centrifugal turbines for mini-ORC power systems". *Presented at the 2nd International Seminar on ORC Power Systems – ASME ORC-2013*, Rotterdam - NL.